Black Hole Accretion Disks and Jets: Connecting Simulations and Theory

Black Hole Accretion Disks and Jets:

Connecting Simulations and Theory

A thesis presented

by

Robert Francis Penna

to

The Department of Astronomy

in partial fulfillment of the requirements

for the degree of

Doctor of Philosophy

in the subject of

Astronomy and Astrophysics

Harvard University

Cambridge, Massachusetts

May 2013

Dissertation Advisor: Prof. Ramesh Narayan Robert Francis Penna

Black Hole Accretion Disks and Jets: Connecting Simulations and Theory

Abstract

In recent years, general relativistic magnetohydrodynamic (GRMHD) simulations have produced more realistic models for black hole disks and jets. However the complexity of the simulations has created a disconnect between simulations and theory: it is often unclear whether the simulated physics is correctly described by standard, semi-analytic disk and jet models. In this thesis, we describe new GRMHD simulations of black hole disks and jets. We compare the simulations to standard disk and jet models. We show that GRMHD thin disks are well described by the Novikov-Thorne model, and GRMHD jets are well described by the Blandford-Znajek model. Then, guided by the simulations, we develop two extensions of the standard thin disk model: a radially varying $\alpha(r)$ viscosity prescription and an analytical disk solution with nonzero stress at the innermost stable circular orbit.

Contents

Abstract . . . iii

Citations to Previously Published Work . . . ix

Acknowledgments . . . xi

1 Introduction **1**

1.1 Testing general relativity with astrophysics . . . 1

1.2 Black hole accretion disks . . . 3

1.2.1 The continuum fitting method for measuring black hole spin . . . 3

1.2.2 Accretion disk simulations . . . 5

1.2.3 Simulation results for thin accretion disks . . . 9

1.3 The α viscosity prescription . . . 11

1.3.1 The $\alpha(r)$ viscosity prescription . . . 13

1.3.2 Turbulence scaling laws . . . 17

1.4 Black hole jets . . . 17

1.4.1 The membrane formalism . . . 18

1.4.2 Jet simulations . . . 20

1.5 Chapter summaries . . . 21

2 Thin Accretion Disks: Simulations and the Novikov-Thorne Model **26**

2.1 Introduction . . . 26

2.2 Governing equations . . . 30

2.3 Diagnostics . . . 32

2.3.1 Disk thickness measurement . . . 33

2.3.2 Fluxes of mass, energy, and angular momentum . . . 34

2.3.3 Splitting angular momentum flux into ingoing and outgoing components . . . 35

2.3.4 The magnetic flux . . . 36
2.3.5 Inflow equilibrium . . . 39
2.3.6 Luminosity measurement . . . 40
2.4 Physical models and numerical methods . . . 41
2.4.1 Physical models . . . 41
2.4.2 Numerical methods . . . 46
2.4.3 Numerical model setup . . . 47
2.5 Fiducial model of a thin disk around a non-rotating black hole . . . 49
2.5.1 Initial and evolved disk structure . . . 50
2.5.2 Velocities and the viscous time-scale . . . 51
2.5.3 Fluxes vs. time . . . 56
2.5.4 Disk thickness and fluxes vs. radius . . . 57
2.5.5 Comparison with Gammie (1999) model . . . 59
2.5.6 Luminosity vs. radius . . . 60
2.5.7 Luminosity from disk vs. corona-wind-jet . . . 61
2.6 Convergence with resolution and box size . . . 63
2.7 Dependence on black hole spin and disk thickness . . . 78
2.7.1 Scaling laws vs. a/M and $|h/r|$ . . . 82
2.8 Thin disks with varying magnetic field geometry . . . 90
2.9 Comparisons with other results . . . 98
2.10 Discussion . . . 103
2.11 Conclusions . . . 108
2.A Example solutions and scalings for the Gammie (1999) model . . . 111
2.B Inflow equilibrium timescale in the Novikov-Thorne model . . . 112

3 Beyond Novikov-Thorne Disks I: Torque at the ISCO 118

3.1 Introduction . . . 118
3.2 Physics beyond the standard disk model . . . 120
3.2.1 The inner edge boundary condition . . . 120
3.2.2 The plunging region . . . 123
3.2.3 Vertical gravity . . . 123
3.3 Explicit disk solutions . . . 124

3.3.1 Plunging region . . . 125
3.3.2 Edge region . . . 126
3.3.3 Inner region . . . 127
3.3.4 Middle region . . . 127
3.3.5 Outer region . . . 128
3.4 Comparison with slim disk models . . . 128
3.5 Comparison with GRMHD simulations . . . 130
3.5.1 Hydrostatic equilibrium of GRMHD disks . . . 130
3.5.2 The boundary between disk and corona . . . 131
3.5.3 Effective α . . . 132
3.5.4 Comparison . . . 132
3.6 Conclusions . . . 134
3.A The Kerr metric . . . 136
3.A.1 Geodesics . . . 138
3.B Disk structure equations . . . 139
3.B.1 Definitions . . . 139
3.B.2 Radial structure equations . . . 140
3.B.3 Vertical structure equations . . . 141
3.B.4 Solving for the disk structure . . . 141
3.C Scaling of compression, advection, and boundary stress terms with α and h . . . 142

4 Beyond Novikov-Thorne Disks II: Radial Varying α(r) Viscosity 147

4.1 Introduction . . . 147
4.2 Preliminaries . . . 151
4.2.1 Inertial fluid frame . . . 152
4.2.2 Electric and magnetic fields . . . 154
4.2.3 Shear rate . . . 155
4.2.4 Radial epicyclic frequency . . . 157
4.3 One-dimensional model for $\alpha(r)$ . . . 158
4.3.1 Turbulent α . . . 158
4.3.2 Mean magnetic field stresses . . . 159
4.3.3 Combined model . . . 160

4.4 Details of the simulations . . . 161
4.4.1 Computational method . . . 161
4.4.2 Initial conditions . . . 163
4.4.3 Quasi-steady state . . . 164
4.5 Analysis of simulations A and D . . . 164
4.5.1 The distinction between disk and corona . . . 166
4.5.2 Radial and azimuthal velocities . . . 167
4.5.3 Convergence and steady state . . . 171
4.5.4 Shear and epicyclic frequencies . . . 173
4.5.5 Shakura-Sunyaev viscosity parameter, α . . . 175
4.5.6 Comparison with the one-dimensional $\alpha(r)$ prescription . . . 178
4.6 Analysis of simulations B, C, E, and F . . . 179
4.6.1 Simulation E . . . 183
4.6.2 Simulation B . . . 183
4.6.3 Simulation C . . . 186
4.6.4 Simulation F . . . 186
4.7 α-disk solutions with variable $\alpha(r)$ . . . 192
4.8 Discussion and summary . . . 193

5 Black Hole Jets: Simulations and the Blandford-Znajek Model 201
5.1 Introduction . . . 201
5.2 Preliminaries . . . 202
5.2.1 GRMHD simulations . . . 202
5.3 Simulation jets and jet power . . . 204
5.3.1 Jet Lorentz factor . . . 204
5.3.2 Jet power vs. time . . . 207
5.3.3 Time-averaging . . . 208
5.3.4 Jet power vs. black hole spin . . . 209
5.4 Energy extraction at the horizon . . . 211
5.4.1 First law of black hole thermodynamics . . . 211
5.4.2 Torques and dissipation on the membrane . . . 212
5.5 Electromagnetic fields at the horizon . . . 214

5.5.1 Membrane formalism . . . 214
5.5.2 Comparison of GRMHD and BZ electromagnetic fields . . . 216
5.6 The load region . . . 218
5.7 Summary and conclusions . . . 221
5.A Blandford-Znajek jet power . . . 222
5.B 3D visualizations of GRMHD membranes . . . 223

6 Summary and Future Directions **235**
6.1 Summary . . . 235
6.2 Future directions . . . 236
6.2.1 Tilted disks . . . 239

A A New Equilibrium Torus Solution **241**
A.1 Introduction . . . 241
A.2 New torus solution . . . 243
A.3 Properties of the solution . . . 247
A.3.1 Radius of the outer edge . . . 248
A.3.2 Pressure maximum . . . 248
A.3.3 Bernoulli parameter . . . 250
A.3.4 Thickness . . . 250
A.3.5 Comparison with Chakrabarti's solution . . . 251
A.4 Conclusions . . . 251
A.A Adding a magnetic field . . . 253
A.A.1 Magnetic field solution . . . 253
A.A.2 MHD Bernoulli parameter . . . 254

References **257**

Citations to Previously Published Work

Chapter 2 is based on:

> R. F. Penna, J. C. McKinney, R. Narayan, A. Tchekhovskoy, R. Shafee, and J. E. McClintock, 2010, "Simulations of Magnetized Discs Around Black Holes: Effects of Black Hole Spin, Disc Thickness and Magnetic Field Geometry," MNRAS, **408**, 752-782

Chapter 3 is based on:

> R. F. Penna, A. Sądowski, and J. C. McKinney, 2012, "Thin-disc Theory with a Non-Zero Torque Boundary Condition and Comparisons with Simulations," MNRAS, **420**, 684-698

Chapter 4 is based on:

> R. F. Penna, A. Sądowski, A. K. Kulkarni, and R. Narayan, 2012, "The Shakura-Sunyaev Viscosity Prescription with Variable $\alpha(r)$," MNRAS **428**, 2255-2274

Chapter 5 is based on:

> R.F. Penna, R. Narayan, and A. Sądowski, 2013, "General Relativistic Magnetohydrodynamic Simulations of Blandford-Znajek Jets," MNRAS in prep

Appendix A is based on:

> R. F. Penna, A. K. Kulkarni, and R. Narayan, 2013, "A New Equilibrium Torus Solution and its Relation To GRMHD Accretion Disk Simulations," A&A submitted

For my family.

Acknowledgments

I thank my advisor, Ramesh Narayan, for his support and many inspiring discussions.

I thank my thesis advisory committee: Edo Berger, Jeff McClintock, Paul Nulsen, and Ramesh, for their guidance.

Finally, I thank my loving family: Mom, Dad, Ryan and Amanda, Adam, Elliott, Amber, Iram, and my grandparents. For everything.

Chapter 1

Introduction

1.1 Testing general relativity with astrophysics

It is a remarkable prediction of general relativity that every black hole in the universe is described by the Kerr metric (Kerr 1963; Chandrasekhar 1992):

$$\begin{aligned} ds^2 = &-(1-2Mr/\rho^2)dt^2 - (4Mar\sin^2\theta/\rho^2)dtd\phi + (\rho^2/\Delta)dr^2 \\ &+ \rho^2 d\theta^2 + (r^2 + a^2 + 2Ma^2 r\sin^2\theta/\rho^2)\sin^2\theta d\phi^2, \end{aligned} \tag{1.1}$$

where the metric functions are:

$$\Delta = r^2 - 2Mr + a^2, \tag{1.2}$$

$$\rho^2 = r^2 + a^2\cos^2\theta, \tag{1.3}$$

$$\Sigma^2 = (r^2 + a^2)^2 - a^2\Delta\sin^2\theta. \tag{1.4}$$

The Kerr metric has only two free parameters: M, the mass of the black hole, and a, the spin of the black hole. In this sense, black holes are as simple as elementary particles.[1]

[1] Strictly speaking, the Einstein-Maxwell equations also permit black holes to carry electric charge, but astrophysical holes are expected to be essentially neutral, because stars (black hole progenitors) are neutral, and because a charged black hole, should it be created, would tend to be neutralized by free charges (Wald 1974).

Despite the great mathematical beauty of the Kerr metric, it cannot be the ultimate description of black holes. It has a number of problems. The most well known problem is that there is a curvature singularity near the origin, which is unphysical. There are more subtle problems as well. The metric has an inner horizon at $r_- = M - \sqrt{M^2 - a^2}$ which is unstable (Barrabes et al. 1990). This instability will cause the curvature to blow up at r_- when perturbed. The metric has an event horizon at $r_H = M + \sqrt{M^2 - a^2}$ which carries an entropy $S = k_B \pi (r_H^2 + a^2) c^3/(G\hbar)$ (Hawking 1974). This entropy suggests black holes have a hidden internal structure with a vast number of microstates.

All of these issues point to something deeper than the Kerr metric. The great hope of studying astrophysical black holes is that we will find hints about what lies beyond general relativity.

Let us elaborate on this idea. The detection of an outright departure from general relativity is unlikely. Departures from general relativity are only expected when spacetime curvature is of order the Planck scale, $\ell_p = \sqrt{\hbar G/c^3} \approx 10^{-35}\,\mathrm{m}$. Astrophysical event horizons are not even close to being this strongly curved. Stellar mass black holes have $\sim 10\,\mathrm{km}$ radii and the supermassive black holes in the cores of galaxies are a billion times larger. So our expectations for finding an outright violation of general relativity are low. Indeed, after 97 years of looking, no definitive discrepancies have been found. (One might count dark matter and dark energy, but if the former is a weakly interacting massive particle and the latter is the cosmological constant, as seems likely, then these require nothing beyond the standard field equations.)

We may be in a period of history similar to the 330 year period between Newton and Einstein. During this period, no changes were made to Newton's laws of gravity. However, progress was made in the form of elegant reformulations of Newtonian gravity: Lagrangian mechanics, Hamiltonian mechanics, and the action principle were discovered. Without these intermediate steps, it would have been impossible to make the leap from Newton's theory to general relativity

This resembles the situation today. The laws of general relativity remain unchanged, but there have been several elegant reformulations. For example, the Newman-Penrose formalism recasts general relativity using spinors and is important for gravitational wave research (see, e.g., Stewart 1994). The membrane paradigm, which is used extensively in our work on black hole jets, gives a

dual description of black hole horizons (Thorne et al. 1986). Each reformulation changes how we think about gravity and this has the promise of leading to something deeper, in the same way that the Lagrangian and Hamiltonian reformulations of Newton's theory led to general relativity.

Astrophysics plays a key role. First, observational tests help to determine which reformulations are the most predictive and these often turn out to be the deepest. Second, astrophysics suggests what should be possible. For example, the membrane paradigm was largely developed because astrophysicists studying black hole jets showed black holes are similar to pulsars (Blandford & Znajek 1977), and this suggested the existence of a reformulation making the similarity manifest (Thorne & MacDonald 1982; MacDonald & Thorne 1982).

To summarize, no clear deviations from general relativity have been found, but great progress has been made with the discovery of several elegant reformulations. Astrophysics plays a key role, by eliminating unfruitful directions and suggesting what is possible. It is reasonable to hope these developments represent progress towards a theory beyond general relativity, just as Langrangian and Hamiltonian mechanics paved the way for general relativity.

1.2 Black hole accretion disks

As mentioned at the outset, astrophysical black holes are fully characterized by their mass, M, and spin, a. The theoretical work in this thesis is motivated by observational campaigns to understand the spin parameters, a, of stellar mass black holes. There are two aspects to this: direct measurements of black hole spin, and observations of black hole jets, which may be powered by black hole spin.

1.2.1 The continuum fitting method for measuring black hole spin

Let us first discuss black hole spin measurements. For a more extended review see McClintock et al. (2011, 2013). The best studied systems are galactic X-ray binaries. In these systems, an ordinary, main sequence star orbits a $\sim 10M_{\odot}$ black hole. Fluid from the star is pulled onto the black hole, either because the star overflows its Roche lobe or because it is is shedding material into a wind.

The material from the star is unable to plunge directly onto the black hole because of its large angular momentum. So it is wound up into an accretion disk around the black hole. Turbulence drains the disk of angular momentum and the gas slowly spirals onto the black hole.

The inner regions of the accretion disk are very hot, so that their thermal emission peaks in the X-ray band. X-ray observatories obtain spectra of the inner regions of the disk. If the accretion disk is geometrically thin, then the spectra are well-described by the Novikov-Thorne thin accretion disk model (Novikov & Thorne 1973). If the black hole mass, distance, and disk inclination are known, then the only free parameters are black hole spin and accretion rate, which can be measured. This method of measuring black hole spin is called the continuum fitting method. Since 2006, it has produced 10 black hole spin measurements (see McClintock et al. 2011 for an overview).

At most radii, fluid parcels in a thin accretion disk follow nearly circular geodesics. However, general relativity predicts that inside a certain radius, circular geodesics become unstable: there is an innermost stable circular orbit (ISCO). When fluid parcels approaching the black hole reach the ISCO, there are no more stable circular orbits available, so they plunge into the black hole, following nearly radial trajectories. Gas does not remain long in the plunging region, so the density drops. A thin accretion disk is expected to have a sharp inner edge at the ISCO.

The key that makes black hole spin measurements possible is that the position of the ISCO is a strong function of black hole spin, such that the more rapidly a black hole is spinning, the smaller is the radius of the ISCO, $r_{\rm ISCO}$ (Figure 1.1). There is a limit to how fast black holes can spin, $a_* = a/M = 1$, which is reached when the velocity of the horizon at the equator is c. At this limit, the ISCO and the event horizon coincide (in Boyer-Lindquist coordinates): $r_{\rm ISCO} = r_H = GM/c^2$. If the black hole is not spinning, the ISCO moves out to $r_{\rm ISCO} = 6GM/c^2$. If the black hole and disk are rotating in the opposite sense, then the ISCO is even larger; at $a_* = -1$, the ISCO is at $r_* = 9GM/c^2$. So over the possible range of black hole spins, $-1 \leq a_* \leq 1$, the radius of the ISCO changes by a factor of 9. This is a large change and can be measured observationally.

Anticipating low density inside the ISCO, the Novikov-Thorne model assumes as a boundary condition that the luminosity of the disk vanishes at the ISCO. The peak luminosity is just outside the ISCO. Since the position of the ISCO depends on black hole spin, the luminosity peaks at

a different radius for each value of the spin parameter, a_* (Figure 1.2). Therefore, the observed spectrum depends on a_*. This enables one to measure black hole spin from X-ray spectra.

It is interesting to survey the 10 black hole spins measured using the continuum fitting method (McClintock et al. 2011) (see Table 1.1). All of the measured spins are positive; there are no retrograde disks. This suggests tidal interactions align the black hole progenitor stars with the orbital angular momentum of the system. Second, the spins range from near $a_* \approx 0$ (A0620-00 has spin $a_* = 0.12 \pm 0.19$) to $a_* \approx 1$ (GRS1918+105 and Cyg X-1 have spin > 0.95), with an apparently smooth distribution of intermediate spins. This is interesting for several reasons. First, it has not been proven that the Kerr metric is stable. However, if nature is making Kerr black holes, any instabilities cannot be too severe. Second, the Cosmic Censorship Conjecture (Penrose 1969) forbids $a_* > 1$ (or, equivalently, $r_{\rm ISCO} < GM/c^2$), and all of the measured spins are consistent with this constraint. Finding a system with $a_* > 1$ could indicate physics beyond general relativity.

1.2.2 Accretion disk simulations

Black hole spin measurements are only as reliable as the underlying accretion disk model. A large part of the work in this thesis is devoted to testing and extending the accretion disk theory underlying black hole spin measurements. The Novikov-Thorne model is an analytical model without magnetic fields or turbulence. As such it makes several key assumptions. It assumes the disk has a sharp inner edge at the ISCO, where the luminosity goes to zero. It also folds the complicated physics of magnetic fields and turbulence into an α viscosity parameter. The validity of these assumptions has been questioned (Krolik et al. 2005; Beckwith et al. 2008b).

To test these assumptions, we generate accretion disks using the conservative, general relativistic magnetohydrodynamic (GRMHD) code HARM (Gammie et al. 2003; McKinney 2006a). This code evolves the three-dimensional magnetohydrodynamic (MHD) equations in the Kerr metric. The metric is kept fixed (self-gravity is ignored). It is safe to ignore the disk's self-gravity because the mass of the disk is a small fraction of the mass of the black hole.

The code does not include radiation. To mimic the effect of radiation, we use a physically

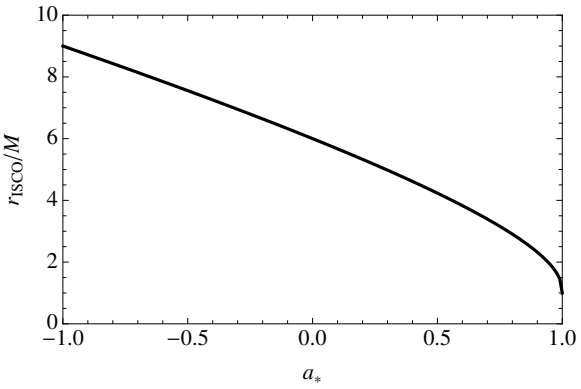

Fig. 1.1.— Radius of the ISCO versus black hole spin, a_*, for equatorial, circular geodesics in the Kerr metric.

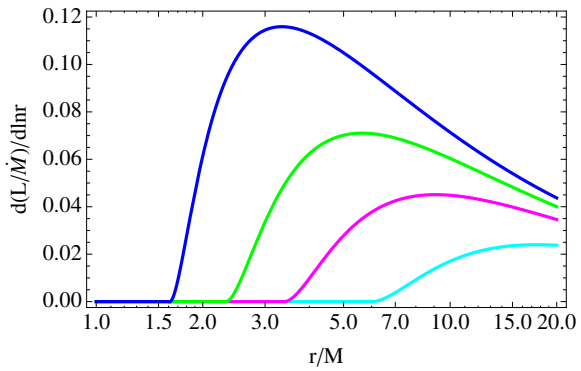

Fig. 1.2.— Luminosity, $dL/d\ln r$, versus radius for Novikov-Thorne disk solutions with $a_* = 0$ (cyan), 0.7 (magenta), 0.9 (green), and 0.98 (blue).

Table 1.1: The masses and spins, measured via continuum-fitting, of ten stellar black holes[ab].

System	a_*	$M/M_\odot$	References
Persistent			
Cyg X-1	> 0.95	14.8 ± 1.0	Gou et al. 2011; Orosz et al. 2011a
LMC X-1	$0.92^{+0.05}_{-0.07}$	10.9 ± 1.4	Gou et al. 2009; Orosz et al. 2009
M33 X-7	0.84 ± 0.05	15.65 ± 1.45	Liu et al. 2008; Orosz et al. 2007
Transient			
GRS 1915+105	> 0.95[b]	10.1 ± 0.6	McClintock et al. 2006; Steeghs et al. 2013
4U 1543–47	0.80 ± 0.10[c]	9.4 ± 1.0	Shafee et al. 2006; Orosz 2003
GRO J1655–40	0.70 ± 0.10[c]	6.3 ± 0.5	Shafee et al. 2006; Greene et al. 2001
XTE J1550–564	$0.34^{+0.20}_{-0.28}$	9.1 ± 0.6	Steiner et al. 2011; Orosz et al. 2011b
H1743–322	0.2 ± 0.3	~ 8[d]	Steiner et al. 2012
LMC X-3	< 0.3[e]	7.6 ± 1.6	Davis & Hubeny 2006; Orosz 2003
A0620–00	0.12 ± 0.19	6.6 ± 0.25	Gou et al. 2010; Cantrell et al. 2010

Notes:

[a] Table reproduced from McClintock et al. (2011), with permission.

[b] Errors are quoted at the 68% level of confidence, except for the three spin limits, which are estimated to be at the 99% level of confidence.

[c] Uncertainties greater than those in papers cited because early error estimates were crude.

[d] Mass estimated using an empirical mass distribution (Özel et al. 2010).

[e] Preliminary result pending improved measurements of M and i.

motivated cooling prescription:

$$\frac{dU}{d\tau} = -\frac{\log(K/K_c)}{\tau_{cool}}. \tag{1.5}$$

This cooling term is added to the energy equation. Whenever the entropy of the gas, $\log(K)$, exceeds a target entropy, $\log(K_c)$, the cooling term removes energy from the gas, on a time scale $\tau_{\rm cool}$, related to the local orbital period. The cooling term only cools, it never heats the gas. We are able to tune the thickness of the accretion disk by varying the free parameter $\log(K_c)$. We generate thick, hot accretion disks by picking a large $\log(K_c)$ and thin, cool accretion disks by picking a small $\log(K_c)$. Then we explore the dependence of disk properties on disk thickness, h/r, and black hole spin, a_*. We also investigate the role of the magnetic field geometry.

The fluid in the code is described by the relativistic MHD stress energy tensor:

$$T^\mu_\nu = (\rho + u + p + b^2)u^\mu u_\nu + (p + b^2/2)\delta^\mu_\nu - b^\mu b_\nu. \tag{1.6}$$

The notation is standard: magnetic field, b^μ, fluid four-velocity u^μ, density ρ, pressure p, and internal energy u (Novikov & Thorne 1973). We pick an ideal gas equation of state: $p = (\Gamma - 1)u$, where we choose $\Gamma = 4/3$ or $5/3$. We find that the choice of Γ does not affect the results significantly. The evolution equations are conservation of rest mass:

$$\nabla_\mu(\rho u^\mu) = 0, \tag{1.7}$$

and conservation of energy-momentum:

$$\nabla_\mu T^\mu_\nu = S_\nu, \tag{1.8}$$

where S_ν is the cooling term (1.5).

Initially, the fluid is confined to an equilibrium torus (Fishbone & Moncrief 1976; Chakrabarti 1985a), with inner edge at $r = 20GM/c^2$. The torus is in hydrostatic equilibrium and rotates around the black hole. We thread the torus with a weak, poloidal magnetic field. This configuration is known to be unstable to the magnetorotational instability (MRI) (Balbus & Hawley 1991, 1998). The MRI causes the fluid to become turbulent. Turbulent stresses transfer angular momentum outwards, allowing gas to accrete inwards. This results in a quasi-steady accretion disk. Only a small fraction of the initial fluid torus is accreted. The torus serves as a reservoir, feeding new gas into the outer edge of the disk as the inner edge of the disk accretes onto the black hole.

The duration of the simulations varies from $t = 20,000GM/c^3 - 200,000GM/c^3$. The inner regions of the disk converge to a quasi-steady solution before the outer parts, because near the black hole the gas velocities are largest and the equilibrium timescales are shortest. Gas at larger radii takes longer to settle down. Given the limited duration of the simulations, we only achieve convergence out to $r \approx 15GM/c^2$ for thin accretion disks. Thick accretion disks have larger radial velocities, hence shorter equilibrium timescales, and we achieve convergence out to $r \approx 100GM/c^2$. In any case, we are only able to probe the innermost regions of accretion disks using these simulations.

We work in spherical coordinates (r, θ, ϕ) and the resolution of the numerical grid is typically either $256 \times 64 \times 32$ (in our earlier work) or $256 \times 128 \times 64$ (in our later work). In either case, we resolve the fast growing mode of the MRI by 10-20 grid cells. We perform a series of convergence tests which suggest our main results do not depend strongly on resolution.

1.2.3 Simulation results for thin accretion disks

Our simulations of thin accretion disks are in good agreement with the Novikov-Thorne model. We confirm that thin accretion disks have a sharp inner edge at the ISCO, at least for $h/r \lesssim 0.1$. Beyond this thickness, the density of the accretion disk increases monotonically down to the event horizon and displays no special features at the ISCO. Thick accretion disks are insensitive to the position of the ISCO because they are sub-Keplerian and have large radial velocities even before reaching the ISCO.

Clearly one should not try to estimate black hole spin from observations of thick accretion disks. Disk thickness roughly corresponds to luminosity: thicker disks are brighter. The cutoff thickness $h/r \approx 0.1$ corresponds to a luminosity of about 50% of the Eddington limit (Kulkarni et al. 2011a). The luminosity of galactic X-ray binaries is highly variable. At times they radiate close to the Eddington limit, while other times they are quiescent (Remillard & McClintock 2006). They can stay in a luminosity state for periods ranging from days to years. Black hole spin measurements (at least when carefully made), use only data for which the source is radiating below 30% of the Eddington limit. This corresponds to $h/r < 0.1$. Our simulations suggest these disks

have a well-defined edge at the ISCO and the Novikov-Thorne model is valid.

In our simulations, thinner accretion disks generate less luminosity from inside the $r_{\rm ISCO}$. Our results suggest that in the razor thin limit, $h/r \to 0$, the Novikov-Thorne model becomes an exact description of the accretion disk. Noble et al. (2010) reach the opposite conclusion. They believe the differences between GRMHD and NT disks are independent of h/r. I they reach different conclusions because they include the corona in their calculations whereas I only include the disk (defined as gas within $2h/r$ of the midplane). The corona has magnetic fields which show up as large stresses and might not obey the zero torque boundary condition in the limit $h/r \to 0$. See Chapter 2 for more discussion on this point.

In applications, disks always have finite thickness and the Novikov-Thorne model is an approximate description. Kulkarni et al. (2011a) have used our simulations to estimate the error in black hole spin measurements. They created mock accretion disk spectra from the simulation data (see Figure 1.3). Then, they fit the spectra to Novikov-Thorne disk solutions using KerrBB, a code for black hole spin measurements. The discrepancy between the actual spin of the simulation and the spin inferred by KerrBB gives an estimate for the theoretical uncertainty in black hole spin measurements. The theoretical error in $r_{\rm ISCO}$ is roughly uniformly distributed, which translates into a smaller error in a_* at high spins (see Figure 1.1). They find typical errors of $\Delta a_* = \pm 0.1$ for spins near $a_* = 0$ and $\Delta a_* = \pm 0.001$ for spins near $a_* = 0.98$. They find a weak dependence on inclination, such that disks observed face-on have somewhat smaller theoretical errors in spin estimates. The Novikov-Thorne model always over-estimates the spin because it ignores light from inside the ISCO and must infer a higher spin to compensate for the excess luminosity (see Figure 1.2).

The theoretical errors in black hole spin measurements are a few times smaller than observational sources of error (Kulkarni et al. 2011a). Observational errors come from uncertainties in black hole mass, distance, and inclinations.

These results increase our confidence in the Novikov-Thorne model as the correct description of thin accretion disks observed in galactic X-ray binaries. This supports efforts to measure black hole spin via the continuum fitting method.

We anticipate future improvements in black hole observations will eventually require better accretion disk models. Therefore, with the simulations as a guide, we have extended the Novikov-Thorne model to include a more realistic viscosity prescription and to allow a nonzero luminosity at the ISCO. These extensions are described in Chapters 3 and 4 of the thesis.

1.3 The α viscosity prescription

The outer parts of an accretion disk have more angular momentum than the inner parts, because fluid parcels follow nearly Keplerian circular orbits. For gas to accrete, it must lose its angular momentum. Early accretion disk models invoked turbulence and magnetic fields as the driver of angular momentum transport (Shakura & Sunyaev 1973). However, these are complicated, nonlinear processes. So analytical accretion disk models fold these effects into a viscosity parameter, α. Based on observational and theoretical clues, one guesses $\alpha \sim 0.1$ (Shakura & Sunyaev 1973).

MHD simulations describe turbulence and magnetic fields self-consistently. A weak seed field in a Keplerian flow generates turbulence and amplifies the magnetic field via the the MRI. There is no need to invoke the α viscosity parameter. Instead, one can measure α from the simulation data. For simplicity, we first review how α is defined in Newtonian physics.

The Newtonian angular momentum flux is (Blackman et al. 2008)

$$F_{r\phi} = r\rho v_\phi v_r - rB_\phi B_r. \tag{1.9}$$

The two terms on the right hand side are the angular momentum transported by gas, $r\rho v_\phi v_r$, and by magnetic fields, $-rB_\phi B_r$.

A useful intuitive picture is to imagine a mean inward flow of accreting matter, with turbulent fluctuations superimposed on top of the mean flow. The turbulent fluctuations remove angular momentum from the mean flow. To implement this intuition, it is useful to split each of the fields v and B into mean and fluctuating pieces. The mean of a quantity, Q, is defined by a density-weighted ϕ-average:

$$\langle Q \rangle = \bar{Q} = \frac{\int Q\rho d\phi}{\int \rho d\phi}. \tag{1.10}$$

The fluctuating part is defined by $q = Q - \bar{Q}$. This gives the splitting

$$Q = \bar{Q} + q. \tag{1.11}$$

Note that $\langle q \rangle = 0$. Applying this splitting to the velocity and magnetic fields in equation (1.9) gives the mean angular momentum flux:

$$\bar{F}_{r\phi} = r\rho \left[\bar{V}_\phi \bar{V}_r - \bar{V}_{A,\phi} \bar{V}_{A,r} + \langle v_\phi v_r \rangle - \langle v_{A,\phi} v_{A,r} \rangle \right], \tag{1.12}$$

where we have replaced the magnetic field with the Alfven velocity $V_A = B/\sqrt{\rho}$.

Each term on the RHS of (1.12) has a simple interpretation. The first term, $r\rho \bar{V}_\phi \bar{V}_r$, is the inward angular momentum flux of the mean flow. The remaining three terms transport angular momentum outwards. There are contributions from large scale magnetic fields, $\bar{V}_{A,\phi} \bar{V}_{A,r}$, small scale magnetic fields, $\langle v_{A,\phi} v_{A,r} \rangle$, and Reynold's stresses, $\langle v_\phi v_r \rangle$. In analytical accretion disk models, these three terms are parametrized by α. To make α dimensionless, we divide by the sound speed squared:

$$\alpha \equiv \frac{-\bar{V}_{A,\phi} \bar{V}_{A,r} + \langle v_\phi v_r \rangle - \langle v_{A,\phi} v_{A,r} \rangle}{c_s^2}. \tag{1.13}$$

One typically asummes $\alpha \sim 0.01 - 0.1$, a constant independent of radius. In MHD simulations in which turbulence is driven by the MRI, one can measure the RHS and compute α.

Our discussion has been Newtonian. There are some subtleties when the flow is relativistic. The splitting into mean and fluctuating terms is less straightforward, because relativistic velocities do not add in the usual way. To give an idea of how this works in the relativistic case, note that the numerator in equation (1.13) is equivalent to $\bar{F}_{\hat{r}\hat{\phi}}$, the $r\phi$ component of $\bar{F}_{ij}$ measured in the fluid frame (the mean velocity term vanishes in the fluid frame, by definition). We may define $\alpha = \bar{F}_{\hat{r}\hat{\phi}}/p$. This expression is made relativistic by replacing F_{ij} with $T_{\mu\nu}$, the relativistic stress-energy tensor. We compute α in the fluid frame using a Lorentz boost.

The indices $\hat{r}\hat{\phi}$ appear to depend on the choice of coordinates. In general relativity, only coordinate-independent quantities are meaningful. The $\hat{\phi}$ direction can be given a coordinate-independent definition in axisymmetric spacetimes such as the Kerr metric because it is related to the Killing tensor generating rotational symmetry. The $\hat{r}$ direction can be given a coordinate-independent definition near the equatorial plane of the Kerr metric, using the symmetry of the

metric under reflections across the equatorial plane. So α can be defined in general relativity, at least near the equatorial plane.

Finally, we note that generalizing equations from laminar flow to turbulence requires some care. Given two observables P and Q, the splitting into mean and turbulent components (equation 1.11) gives

$$\langle PQ \rangle = \langle P \rangle \langle Q \rangle + \langle pq \rangle. \tag{1.14}$$

For laminar flow, $p = q = 0$, so $\langle PQ \rangle = \langle P \rangle \langle Q \rangle$, and the average of the product equals the product of the averages. For turbulent flow, $\langle PQ \rangle \neq \langle P \rangle \langle Q \rangle$ and multiplication does not commute with averaging. So a set of equations describing laminar flow can admit multiple generalizations to turbulent flow because of the ordering ambiguity between multiplication and averaging. This is a bit reminiscent of the operator ordering ambiguities that arise when one passes from a classical Hamiltonian to a quantum Hamiltonian and observables no longer commute. Throughout our work, we are careful to apply multiplications and averages in the correct order. Mixing up the ordering has led to mistakes in the literature. (For example, Noble et al. (2010) underestimated the angular momentum of their simulated disks because their averaging procedure did not eliminate the Reynold's stress from the angular momentum of the mean flow.)

1.3.1 The $\alpha(r)$ viscosity prescription

Our GRMHD accretion disk simulations give a radially varying viscosity parameter, $\alpha(r)$. As gas approaches the black hole, α first increases, peaking somewhere inside the ISCO. Then it decreases on the final plunge to the horizon. The maximum is $\alpha \sim 0.3$ and the value at large radii is $\alpha \sim 0.03$. So α changes by an order of magnitude between the outer and inner regions of the disk. Our simulation data suggest the usual constant α prescription should be replaced with a radially varying $\alpha(r)$ prescription.

Guided by our simulations, we have developed a physically motivated $\alpha(r)$ prescription. This prescription has two components, which correspond to mean magnetic field stresses and turbulent stresses. Mean field stresses dominate inside the ISCO, where plunging gas stretches and amplifies the magnetic field. The MRI requires a weak field to operate, and is thus unable to generate

turbulence efficiently inside the ISCO. Outside the ISCO, turbulent stresses dominate.

Our model for turbulent stresses draws on simulation results of Pessah et al. (2008), who conducted a series of shearing box experiments. These are simulations of a box of fluid which is taken to represent a small patch of an accretion disk. The box is threaded with a weak magnetic field and the MRI develops. One measures α from the simulation. Pessah et al. (2008) performed a series of these simulations, each time varying only the shear rate of the background flow. The shear rate is

$$q = -\frac{d\log\Omega}{d\log r}, \tag{1.15}$$

where Ω is the angular velocity of the flow. So $q = 0$ corresponds to solid body rotation and $q = 3/2$ corresponds to Keplerian rotation.

For $q < 0$, they found no turbulence and $\alpha = 0$. A linear analysis suggests the MRI requires $q > 0$ (Balbus & Hawley 1991, 1998), so this is not too surprising.

As they increased q from 0 to 2, they found

$$\alpha(q) \propto q^n, \tag{1.16}$$

where n is a constant between 2 and 8 (Figure 1.4). Given their resolution, they were not able to pin down n more precisely. The key result is that α is a function of q.

In the Kerr metric, (general) relativistic corrections modify the shear rate (Novikov & Thorne 1973):

$$q(r) = -\gamma^2\mathcal{A}\frac{d\log\Omega}{d\log r}, \tag{1.17}$$

where γ is the Lorentz factor of the gas, and $\mathcal{A}$ is related to frame dragging. In the Newtonian regime at large radii, $\gamma^2\mathcal{A} \to 1$ and equation (1.15) reduces to equation (1.17). However, near the black hole, relativistic effects give a radially varying shear rate, $q(r)$, even for circular geodesics. The shear rate varies from 2 at the ISCO to 3/2 at large radii.

The shear dependence of $\alpha(q)$, combined with the radial dependence of $q(r)$ for circular geodesics in the Kerr metric, gives a radially varying $\alpha(r)$. The best fit to our simulation data is given by

$$\alpha(r) = 0.025\left[\frac{q(r)}{3/2}\right]^6. \tag{1.18}$$

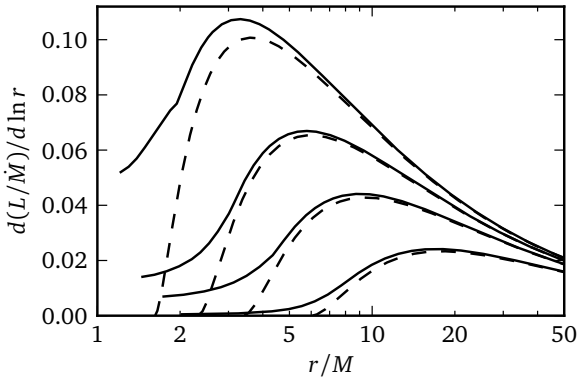

Fig. 1.3.— Novikov-Thorne (dashed) and GRMHD (solid) disk luminosity profiles for $a_* = 0, 0.7, 0.9,$ and 0.98 (bottom to top). The GRMHD disks produce some luminosity inside the ISCO, where the Novikov-Thorne disks produce no luminosity. Figure reproduced from Kulkarni et al. (2011a).

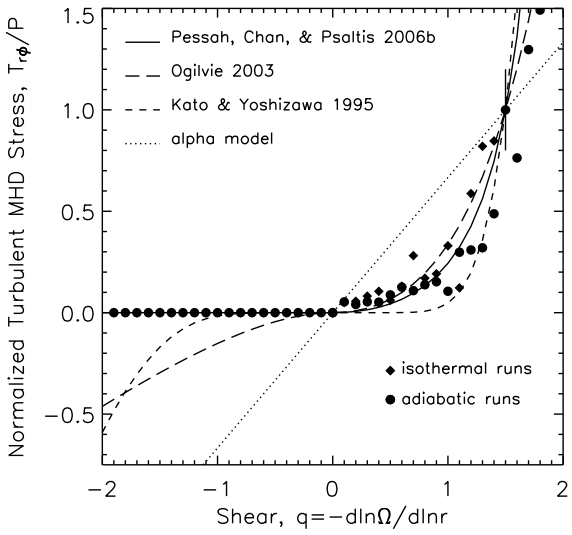

Fig. 1.4.— Each black dot is a shearing box simulation. The α viscosity parameter is plotted against the shear rate, q, of the simulation. Figure reproduced from Pessah et al. (2008) with permission.

The prefactor, 0.025, and the exponent, 6, will probably change as higher resolution simulations become available. They can perhaps be trusted to within a factor of 2. They do not show a strong dependence on black hole spin. Note that while $q(r)$ only varies by about 50% between ISCO and infinity, $\alpha(r)$ varies by an order of magnitude because it scales as q^6.

The accretion disk follows nearly circular geodesics. In this case, $q(r)$ can be computed analytically (Gammie 2004). For the Kerr metric, the result is:

$$\alpha(r) = 0.025 \left(\frac{1 - 2Mr^{-1} + a^2 r^{-2}}{1 - 3Mr^{-1} + 2aM^{1/2} r^{-3/2}} \right)^6 . \tag{1.19}$$

This gives a physically-motivated improvement over the usual $\alpha =$ constant prescription. It applies to the turbulent gas outside the ISCO.

Inside the ISCO, where mean field stresses dominate over turbulent stresses, a separate viscosity prescription is needed. Gammie (1999) has given a one dimensional model for the velocity and magnetic fields inside the ISCO. The magnetic field is stretched by the fluid as it plunges into the black hole. The only free parameters are black hole spin and the magnetic flux threading the horizon. The flow is cold ($p = u = 0$) and there is no radiation. Despite these simplifications, we find that these solutions give a good fit to the mean field stresses observed in the plunging regions of our simulations. We have used the Gammie (1999) model to construct a prescription for $\alpha(r)$ inside the ISCO.

Summing the mean field and turbulent components gives the total $\alpha(r)$ prescription. It gives a good fit to the simulation data. This suggests we understand the physics underlying simulated stresses. One can use our $\alpha(r)$ prescription in place of $\alpha =$ constant in analytical disk models. For most applications, the differences will be smaller than observational precision. The radially varying $\alpha(r)$ and constant α solutions are the same away from the black hole, in the Newtonian regions of the disk. Inside the ISCO, gas follows approximately free-fall geodesics and is fairly insensitive to the viscosity prescription. The viscosity prescription is most important just outside the ISCO, in the the X-ray emitting region relevant for black hole spin measurements. As discussed above, Kulkarni et al. (2011a) have shown that the discrepancies between GRMHD disks and Novikov-Thorne disks with $\alpha =$ constant are currently smaller than the observational errors in black hole spin measurements. Nonetheless, we believe our viscosity prescription will become useful

as observational data improves.

1.3.2 Turbulence scaling laws

Turbulence is a mysterious subject. On the face of it, turbulence is an extremely complicated, nonlinear process. Turbulent accretion disks require weeks of supercomputer effort to simulate. Yet at the end of these arduous computations, simple scaling laws emerge (Figure 1.5). For example, the product of α and the gas-to-magnetic pressure ratio, β, turns out to be a constant, quite independent of initial conditions or details of the accretion flow. One (almost?) always finds $\alpha\beta \approx 0.5$ (Blackman et al. 2008). Similarly, if one splits α into its hydrodynamic and magnetic components, then their ratio gives a (nearly?) universal constant, $\alpha^{\rm mag}/\alpha^{\rm hydro} \approx 4$. We have confirmed that these scaling laws appear in our GRMHD simulations.

The simplicity and universality of these laws suggests a simple explanation should be possible, despite the apparent complexity of turbulence. For now these laws are mysteries. The situation is a bit reminiscent of early work on thermodynamics. A gas is a horribly complicated thing, with $\sim 10^{23}$ particles all interacting through Coulomb forces. And yet, 17th and 18th century experiments uncovered remarkably simple scaling laws: Boyle's Law, Charles' Law, and many others. Why are pV, ρT, and similar combinations so often constant? Only later did statistical mechanics and thermodynamics provide the answer.

The simple scaling laws emerging from MHD simulations may be hints of a deeper, simpler description of turbulence, much as Boyle's Law and Charles' Law hinted at the modern theory of thermodynamics.

1.4 Black hole jets

Our work on thin accretion disks, motivated by black hole spin measurements, comprises the bulk of this thesis (Chapters 2-4). In Chapter 5, the final chapter, we turn to black hole jets.

Of the ten stellar-mass black holes with spins measured via the continuum fitting method,

seven are so-called "transient" systems which have large amplitude outbursts. During outburst they reach close to the Eddington luminosity limit and near peak luminosity they eject blobs of plasma. The blobs move ballistically outward at relativistic speeds (Lorentz factor $\gamma > 2$). Narayan & McClintock (2012) and Steiner et al. (2013) measured the peak radio luminosities of ballistic jet blobs, a proxy for jet power, from five transient systems. They find that the jet power is correlated with black hole spin, increasing by a factor of 1000 as the spin varies from 0.1 to 1. This suggests the blobs may be powered by black hole rotational energy.

The observed scaling of jet power with black hole spin is consistent with the predictions of the Blandford-Znajek (BZ) jet model (Blandford & Znajek 1977; MacDonald & Thorne 1982; Thorne et al. 1986). This model describes how magnetic fields drain a black hole of its rotational energy and drive powerful jets. It builds on earlier proposals for tapping black hole rotational energy using particles (Penrose 1969) and magnetic fields (Ruffini & Wilson 1975), and is a close cousin of the pulsar magnetosphere model of Goldreich & Julian (1969). The similarity between black hole and pulsar jets is particularly transparent in the membrane formulation of the BZ model (MacDonald & Thorne 1982; Thorne et al. 1986).

The BZ model has three free parameters: the angular velocity of the event horizon Ω_H, the angular velocity of magnetic field lines, Ω_F, and the magnetic flux threading the jet, Φ. Early attempts to determine Ω_F (Lovelace et al. 1979; MacDonald & Thorne 1982; Phinney 1983) found (up to factors of order unity) $\Omega_F/\Omega_H \approx 1/2$. If one assumes $\Omega_F/\Omega_H = 1/2$, then the jet power predicted by the BZ model is (Blandford & Znajek 1977; Thorne et al. 1986; Lee et al. 2000; Tchekhovskoy et al. 2010a):

$$P^{\rm BZ} \approx \frac{1}{6\pi}\Omega_H^2\Phi^2. \tag{1.20}$$

The assumption $\Omega_F/\Omega_H = 1/2$ gives maximum jet efficiency. We refer to the BZ model with this assumption as the standard BZ model. Equation (1.20) is consistent with the jet power scaling observed from astrophysical black holes by Narayan & McClintock (2012) and Steiner et al. (2013).

1.4.1 The membrane formalism

MacDonald & Thorne (1982) recast the BZ model in the membrane formalism (see Thorne et al.

1986 for an overview). We will use this formulation for much of our analyses. It allows a local description of the conversion of gravitational energy into magnetic energy at the horizon. Another advantage is that it does not require any mathematics beyond three-dimensional vector algebra, so relations to non-relativistic mechanics are particularly transparent.

There are two pieces to the membrane formalism: we introduce fiducial observers (the ZAMOs), and we switch to a dual description of black holes that treats the horizon as a viscous membrane (but is mathematically equivalent to the usual description of black holes).

Understanding the flow of energy at the horizon presents a conceptual challenge: it is always possible to change the metric at a point to the flat, zero-energy Minkowski metric by a change of reference frame (equivalence principle), so there is no observer-independent way of defining the energy of the gravitational field at a point.[2] The only way to give a local description of black hole energy extraction is to fix an observer. The fiducial choice in the Kerr metric is the zero angular momentum observer (ZAMO) (Bardeen et al. 1972). Quantities measured at infinity do not depend on the choice of local observer. However, introducing the ZAMO is useful because it gives a concrete picture for the intermediate interactions between black hole and jet that result in black hole energy extraction. So we will often work in the ZAMO frame.

It is well-known that to an observer outside a black hole (such as a ZAMO), matter falling into the hole appears to freeze just outside as a result of gravitational redshift. This applies equally well to the matter which first formed the black hole. So the black hole's energy, M, and angular momentum, J, appear spread out in a membrane covering the horizon. The "membrane paradigm" treats this membrane as a surrogate for the black hole. Every interaction of the external world with the black hole becomes concretely realized as an interaction with the membrane. It would be difficult to give a complete discussion of black hole energy extraction without the membrane formalism because we would not be able to say where the black hole energy is located to begin with. Of course, an observer falling into the black hole does not find the hole's energy and angular momentum at the horizon (equivalence principle), but infalling observers are not relevant for

[2] A "quasi-local" energy, defined on surfaces rather than at points, can be defined in at least some cases. See Wang & Yau (2009) for a recent approach and a summary of earlier work.

astrophysics. The fact that different observers see the energy of the gravitational field in different places has been called "black hole complementarity" to highlight its similarity with wave-particle duality in quantum theory (Susskind et al. 1993).

Thorne et al. (1986) give a pedagogical introduction to the membrane formalism. We will develop the material as needed.

1.4.2 Jet simulations

There is now an extensive, decade-old literature on general relativistic magnetohydrodynamic (GRMHD) simulations of black hole jets, which further support and extend the BZ model. Komissarov (2001) presented the first time-dependent simulations of BZ jets and demonstrated that the model is stable. In these simulations, magnetic fields were imposed on the black hole at the outset.

Later simulations (including those in this paper), embed the black hole in a turbulent accretion disk, which then deposits magnetic fields onto the hole self-consistently. A funnel-shaped region develops along the black hole spin axis where the field geometry resembles a split monopole (Hirose et al. 2004). In this region, the flux of magnetic energy at the horizon is sometimes directed outwards, away from the black hole (McKinney & Gammie 2004; De Villiers et al. 2005). The distribution of electromagnetic fields and the angular momentum flux at the horizon are consistent with the BZ model (McKinney & Gammie 2004; McKinney et al. 2012). The flux of energy carried by gas is always directed into the black hole (Komissarov 2005). The strength of the jet is an increasing function of black hole spin (Krolik et al. 2005; McKinney 2005b; Hawley & Krolik 2006) and the energy in the jet can be comparable to the energy in the accretion flow (Hawley & Krolik 2006). The magnetic field geometry is intermediate between the split-monopole and paraboloidal geometries considered by BZ (McKinney & Narayan 2007a,b). The strength of the simulated jet depends on the field geometry in the initial conditions, because this affects the final field strength of the black hole and disk (Beckwith et al. 2008a; McKinney et al. 2012). The simulated scaling of jet power with black hole spin agrees with the BZ prediction (1.20) (Tchekhovskoy et al. 2010a, 2012). If the magnetic field is very strong, the jet can carry off more energy from the black hole

than the accretion flow puts in (Tchekhovskoy et al. 2011). If the magnetic field is very weak, gas accretion can quench jet formation (McKinney et al. 2012). Prograde black holes drive more powerful jets than retrograde holes (Tchekhovskoy & McKinney 2012).

GRMHD simulators often focus on computing jet properties, such as Lorentz factor and opening angle, which are relevant for observations of jets. Simulated jets are found to be similar to the jets observed in active galactic nuclei (Komissarov et al. 2007; Tchekhovskoy et al. 2010a) and gamma ray bursts (Komissarov et al. 2007; Barkov & Komissarov 2008a; Tchekhovskoy et al. 2008; Barkov & Komissarov 2008b; Tchekhovskoy et al. 2009a; Barkov & Komissarov 2010; Tchekhovskoy et al. 2010b; Komissarov 2012). For example, they are relativistic ($\Gamma \sim 1 - 100$, depending on the setup) and well collimated.

We have produced GRMHD simulations of jets from accreting, spinning black holes. We have three main results. First, we quantify the error introduced into the BZ jet power prediction (1.20) by the standard approximations (maximum efficiency, uniform magnetic fields on the horizon, no disk thickness, and no gas accretion). Second, we check that the underlying physics generating simulated jets (torques, dissipation, and electromagnetic fields at the horizon) is correctly described by the membrane formulation of the BZ model. Third, we compute the effective resistance of the load region, where magnetic energy is converted into bulk gas motion. This analysis supports the prediction $\Omega_F/\Omega_H \approx 1/2$ of simple load region models (Lovelace et al. 1979; MacDonald & Thorne 1982; Phinney 1983).

1.5 Chapter summaries

In Chapter 2, we describe three-dimensional GRMHD simulations of accretion disks around black holes with a range of spin parameters, and we use the simulations to assess the validity of the Novikov-Thorne model. Our fiducial initial magnetic field consists of multiple (alternating polarity) poloidal field loops whose shape is roughly isotropic in the disk in order to match the isotropic turbulence expected in the poloidal plane. For a thin disk with an aspect ratio $|h/r| \sim 0.07$ around a non-spinning black hole, we find a decrease in the accreted specific angular momentum of 2.9%

relative to the Novikov-Thorne model and an excess luminosity from inside the ISCO of 3.5%. The deviations in the case of spinning black holes are also of the same order. In addition, the deviations decrease with decreasing $|h/r|$. We therefore conclude that magnetized thin accretion disks in x-ray binaries in the thermal/high-soft spectral state ought to be well-described by the Novikov-Thorne model, especially at luminosities below 30% of Eddington where we expect a very small disk thickness $|h/r| \lesssim 0.05$. We use our results to determine the spin equilibrium of black hole accretion disks with a range of thicknesses and to determine how electromagnetic stresses within the ISCO depend upon black hole spin and disk thickness. We find that the electromagnetic stress and the luminosity inside the ISCO depend on the assumed initial magnetic field geometry. We consider a second geometry with field lines following density contours, which for thin disks leads to highly radially-elongated magnetic field lines. This gives roughly twice larger deviations from Novikov-Thorne for both the accreted specific angular momentum and the luminosity inside the ISCO. Lastly, we find that the disk's corona (including any wind or jet) introduces deviations from Novikov-Thorne in the specific angular momentum that are comparable to those contributed by the disk component, while the excess luminosity of bound gas from within the ISCO is dominated by only the disk component. Based on these indications, we suggest that differences in results between our work and other similar work are due to differences in the assumed initial magnetic field geometry as well as the inclusion of disk gas versus all the gas when comparing the specific angular momentum from the simulations with the Novikov-Thorne model.

In Chapter 3, we present an analytical solution for thin disk accretion onto a Kerr black hole that extends the standard Novikov-Thorne α-disk in three ways: (i) it incorporates nonzero stresses at the inner edge of the disk, (ii) it extends into the plunging region, and (iii) it uses a corrected vertical gravity formula. The free parameters of the model are unchanged. Nonzero boundary stresses are included by replacing the Novikov-Thorne no torque boundary condition with the less strict requirement that the fluid velocity at the innermost stable circular orbit is the sound speed, which numerical models show to be the correct behavior for luminosities below $\sim 30\%$ Eddington. We assume the disk is thin so we can ignore advection. Boundary stresses scale as $\alpha(h/r)$ and advection terms scale as $(h/r)^2$, so the model is self-consistent when $h/r < \alpha$. We compare our solution with slim disk models and GRMHD disk simulations. The model may improve the

accuracy of black hole spin measurements.

In Chapter 4, we discuss $\alpha(r)$. Global simulations of magnetohydrodynamic disks find that α varies with distance from the central object. Also, Newtonian simulations tend to find smaller α's than general relativistic simulations. We seek a one-dimensional model for α that can reproduce these two observations. We are guided by data from six GRMHD disk simulations. The variation of α in the inner, laminar regions of the flow results from stretching of mean magnetic field lines by the flow. The variation of α in the outer, turbulent regions results from the dependence of the magnetorotational instability on the dimensionless shear rate. We give a one-dimensional prescription for $\alpha(r)$ that captures these two effects and reproduces the radial variation of α observed in the simulations. For thin disks, the prescription simplifies to the formula $\alpha(r) = 0.025\,[q(r)/1.5]^6$, where the shear parameter, $q(r)$, is an analytical function of radius in the Kerr metric. The coefficient and exponent are inferred from our simulations and will change as better simulation data becomes available. We conclude that the α-viscosity prescription can be extended to the radially varying α's observed in simulations. It is possible that Newtonian simulations find smaller α's than general relativistic simulations because the shear parameter is lower in Newtonian flows.

In Chapter 5, we revisit the BZ model using GRMHD simulations of magnetized jets from accreting ($h/r \sim 0.3$), spinning ($0 < a_* < 0.98$) black holes. We have three main results. First, we quantify the discrepancies between the BZ jet power and our simulations: assuming maximum efficiency and uniform fields on the horizon leads to a $\sim 10\%$ overestimate of jet power, while ignoring the accretion disk leads to a further $\sim 50\%$ overestimate. Simply reducing the standard BZ jet power prediction by 60% gives a good fit to our simulation data. Our second result is to show that the membrane formulation of the BZ model correctly describes the physics underlying simulated jets: torques, dissipation, and electromagnetic fields on the horizon. This provides intuitive yet rigorous pictures for the black hole energy extraction process. Third, we compute the effective resistance of the load region and show that the load and the black hole achieve near perfect impedance matching. This supports the standard assumption that jets maximize efficiency. Taken together, these results increase our confidence in the BZ model as the correct description of jets observed from astrophysical black holes.

In the Appendix, we provide a new equilibrium torus solution that is more flexible and more physically motivated than the standard solution. The solution is determined by fixing an angular momentum distribution and solving the relativistic Euler equations in the Kerr metric. The solution is isentropic and we assume an ideal gas equation of state. The Bernoulli parameter, rotation rate, and geometrical thickness of the solution can be adjusted independently. The solution tends to have a more negative Bernoulli parameter and a larger radial extent than the standard solution. We show that is it possible for an energetically unbound torus to be thinner than an energetically bound torus. It will be important to check how the results of GRMHD accretion disk simulations depend on the Bernoulli parameter, rotation rate, and geometrical thickness of the initial equilibrium torus. A preliminary check suggests that the longest duration simulations in the literature have not entirely forgotten their initial conditions.

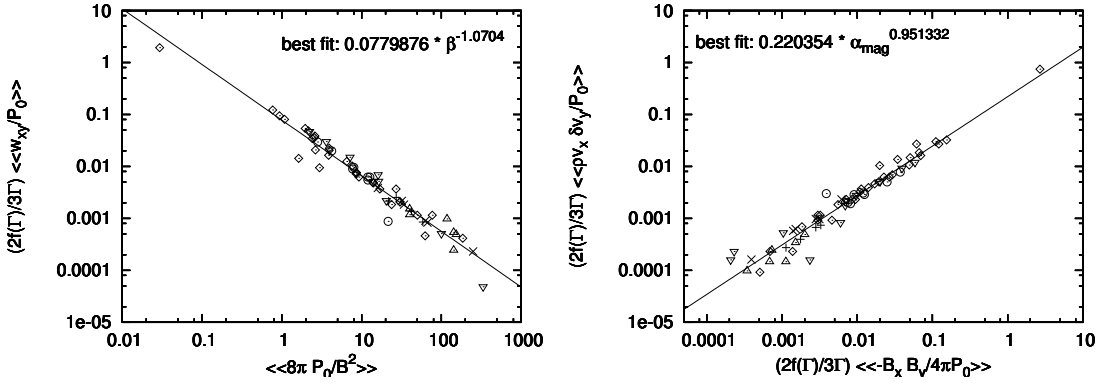

Fig. 1.5.— Each dot is a shearing box simulation. *Left panel:* The viscosity parameter, α, is a constant fraction of β. *Right panel:* The hydrodynamic component of the viscosity is a constant fraction of the magnetic component. Figure reproduced from Blackman et al. (2008).

Chapter 2

Thin Accretion Disks: Simulations and the Novikov-Thorne Model

2.1 Introduction

Accreting black holes (BHs) are among the most powerful astrophysical objects in the Universe. Although they have been the target of intense research for a long time, many aspects of black hole accretion theory remain uncertain to this day. Pioneering work by Bardeen (1970); Shakura & Sunyaev (1973); Novikov & Thorne (1973); Page & Thorne (1974) and others indicated that black hole accretion through a razor-thin disk can be highly efficient, with up to 42% of the accreted rest-mass-energy being converted into radiation. These authors postulated the existence of a turbulent viscosity in the disk, parameterized via the famous α-prescription (Shakura & Sunyaev 1973). This viscosity causes outward transport of angular momentum; in the process, it dissipates energy and produces the radiation. The authors also assumed that, within the inner-most stable circular orbit (ISCO) of the black hole, the viscous torque vanishes and material plunges into the black hole with constant energy and angular momentum flux per unit rest-mass flux. This is the so-called "zero-torque" boundary condition.

Modern viscous hydrodynamical calculations of disks with arbitrary thicknesses suggest that

the zero-torque condition is a good approximation when the height (h) to radius (r) ratio of the accreting gas is small: $|h/r| \lesssim 0.1$ (Paczyński 2000; Afshordi & Paczyński 2003; Shafee et al. 2008b; Sądowski 2009; Abramowicz et al. 2010). Radiatively efficient disks in active galactic nuclei (AGN) and x-ray binaries are expected to have disk thickness $|h/r| < 0.1$ whenever the luminosity is limited to less than about 30% of the Eddington luminosity (McClintock et al. 2006). The above hydrodynamical studies thus suggest that systems in this limit should be described well by the standard relativistic thin disk theory as originally developed by Novikov & Thorne (1973), hereafter NT.

In parallel with the above work, it has for long been recognized that the magnetic field could be a complicating factor that may significantly modify accretion dynamics near and inside the ISCO (Thorne 1974). This issue has become increasingly important with the realization that angular momentum transport in disks is entirely due to turbulence generated via the magnetorotational instability (MRI) (Balbus & Hawley 1991, 1998). However, the magnetic field does not necessarily behave like a local viscous hydrodynamical stress. Near the black hole, the magnetic field may have large-scale structures (MacDonald 1984), which can induce stresses across the ISCO (Krolik 1999; Gammie 1999; Agol & Krolik 2000) leading to changes in, e.g., the density, velocity, and amount of dissipation and emission. Unlike turbulence, the magnetic field can transport angular momentum without dissipation (e.g. Li 2002), or it can dissipate in current sheets without transporting angular momentum. In Agol & Krolik (2000), the additional electromagnetic stresses are treated simply as a freely tunable model parameter on top of an otherwise hydrodynamical model. A more complete magnetohydrodynamical (MHD) model of a magnetized thin disk has been developed by Gammie (1999). In this model, the controlling free parameter is the specific magnetic flux, i.e., magnetic flux per unit rest-mass flux. Larger values of this parameter lead to larger deviations from NT due to electromagnetic stresses, but the exact value of the parameter for a given accretion disk is unknown. For instance, it is entirely possible that electromagnetic stresses become negligible in the limit when the disk thickness $|h/r| \to 0$. The value of the specific magnetic flux is determined by the nonlinear turbulent saturation of the magnetic field, so accretion disk simulations are the best way to establish its magnitude.

The coupling via the magnetic field between a spinning black hole and an external disk, or

between the hole and the corona, wind and jet (hereafter, corona-wind-jet), might also play an important role in modifying the accretion flow near the black hole. The wind or jet (hereafter, wind-jet) can transport angular momentum and energy away from the accretion disk and black hole (Blandford 1976; Blandford & Znajek 1977; McKinney & Gammie 2004; McKinney 2006b; McKinney & Narayan 2007b; Komissarov & McKinney 2007). The wind-jet power depends upon factors such as the black hole spin (McKinney 2005b; Hawley & Krolik 2006; Komissarov et al. 2007), disk thickness (Meier 2001; Tchekhovskoy et al. 2008, 2009a,b, 2010a), and the strength and large-scale behavior of the magnetic field (McKinney & Gammie 2004; Beckwith et al. 2008a; McKinney & Blandford 2009), and these can affect the angular momentum transport through an accretion disk. In this context, we note that understanding how such factors affect disk structure may be key in interpreting the distinct states and complex behaviors observed for black hole X-ray binaries (Fender et al. 2004; Remillard & McClintock 2006). These factors also affect the black hole spin history (Gammie et al. 2004), and so must be taken into account when considering the effect of accretion on the cosmological evolution of black hole spin (Hughes & Blandford 2003; Gammie et al. 2004; Berti & Volonteri 2008).

Global simulations of accretion disks using general relativistic magnetohydrodynamical (GRMHD) codes (e.g. Gammie et al. 2003; De Villiers et al. 2003) currently provide the most complete understanding of how turbulent magnetized accretion flows around black holes work. Most simulations have studied thick ($|h/r| \gtrsim 0.15$) disks without radiative cooling. Such global simulations of the inner accretion flow have shown that fluid crosses the ISCO without any clear evidence that the torque vanishes at the ISCO, i.e., there is no apparent "stress edge" (McKinney & Gammie 2004; Krolik et al. 2005; Beckwith et al. 2008b). Similar results were previously found with a pseudo-Newtonian potential for the black hole (Krolik & Hawley 2002). In these studies, a plot of the radial profile of the normalized stress within the ISCO appears to indicate a significant deviation from the NT thin disk theory (Krolik et al. 2005; Beckwith et al. 2008b), and it was thus expected that much thinner disks might also deviate significantly from NT. A complicating factor in drawing firm conclusions from such studies is that the assumed initial global magnetic field geometry and strength can significantly change the magnitude of electromagnetic stresses and associated angular momentum transport inside the ISCO (McKinney & Gammie 2004; Beckwith

et al. 2008a).

The implications of the above studies for truly thin disks ($|h/r| \lesssim 0.1$) remain uncertain. Thin disks are difficult to resolve numerically, and simulations have been attempted only recently. Simulations of thin disks using a pseudo-Newtonian potential for the black hole reveal good agreement with standard thin disk theory (Reynolds & Fabian 2008). The first simulation of a thin ($|h/r| \approx 0.05$) disk using a full GRMHD model was by Shafee et al. (2008a), hereafter S08. They considered a non-spinning ($a/M = 0$) black hole and an initial field geometry consisting of multiple opposite-polarity bundles of poloidal loops within the disk. They found that, although the stress profile appears to indicate significant torques inside the ISCO, the actual angular momentum flux per unit rest-mass flux through the disk component deviates from the NT prediction by only 2%, corresponding to an estimated deviation in the luminosity of only about 4%. The study by S08 was complemented by Noble et al. (2009), hereafter N09, who considered a thin ($|h/r| \approx 0.1$) disk around an $a/M = 0.9$ black hole and an initial field geometry consisting of a single highly-elongated poloidal loop bundle whose field lines follow the density contours of the thin disk. They found 6% more luminosity than predicted by NT. More recently, Noble et al. (2010), hereafter N10, considered a thin ($|h/r| \approx 0.07$) disk around a non-spinning ($a/M = 0$) black hole and reported up to 10% deviations from NT in the specific angular momentum accreted through the accretion flow.

In this chapter, we extend the work of S08 by considering a range of black hole spins, disk thicknesses, field geometries, box sizes, numerical resolutions, etc. Our primary result is that we confirm S08, viz., geometrically thin disks are well-described by the NT model. We show that there are important differences between the dynamics of the gas in the disk and in the corona-wind-jet. In addition, we find that the torque and luminosity within the ISCO can be significantly affected by the geometry and strength of the initial magnetic field, a result that should be considered when comparing simulation results to thin disk theory. In this context, we discuss likely reasons for the apparently different conclusions reached by N09 and N10.

The equations we solve are given in §2.2, diagnostics are described in §2.3, and our numerical setup is described in §2.4. Results for our fiducial thin disk model for a non-rotating black hole are given in §2.5, and we summarize convergence studies in §2.6. Results for a variety of black

hole spins and disk thicknesses are presented in §2.7 and for thin disks with different magnetic field geometries and strengths in §2.8. We compare our results with previous studies in §2.9, discuss the implications of our results in §2.10, and conclude with a summary of the salient points in §2.11.

2.2 Governing equations

The system of interest to us is a magnetized accretion disk around a rotating black hole. We write the black hole Kerr metric in Kerr-Schild (KS, horizon-penetrating) coordinates (Font et al. 1998; Papadopoulos & Font 1998), which can be mapped to Boyer-Lindquist (BL) coordinates or an orthonormal basis in any frame (McKinney & Gammie 2004). We work with Heaviside-Lorentz units, set the speed of light and gravitational constant to unity ($c = G = 1$), and let M be the black hole mass. We solve the general relativistic magnetohydrodynamical (GRMHD) equations of motion for rotating black holes (Gammie et al. 2003) with an additional cooling term designed to keep the simulated accretion disk at a desired thickness.

Mass conservation gives

$$\nabla_\mu(\rho_0 u^\mu) = 0, \tag{2.1}$$

where ρ_0 is the rest-mass density, corresponding to the mass density in the fluid frame, and u^μ is the contravariant 4-velocity. Note that we write the orthonormal 3-velocity as v_i (the covariant 3-velocity is never used below). Energy-momentum conservation gives

$$\nabla_\mu T^\mu_\nu = S_\nu, \tag{2.2}$$

where the stress energy tensor T^μ_ν includes both matter and electromagnetic terms,

$$T^\mu_\nu = (\rho_0 + u_g + p_g + b^2)u^\mu u_\nu + (p_g + b^2/2)\delta^\mu_\nu - b^\mu b_\nu, \tag{2.3}$$

where u_g is the internal energy density and $p_g = (\Gamma - 1)u_g$ is the ideal gas pressure with $\Gamma = 4/3$ [1]. The contravariant fluid-frame magnetic 4-field is given by b^μ, and is related to the lab-frame 3-field via $b^\mu = B^\nu h^\mu_\nu / u^t$ where $h^\mu_\nu = u^\mu u_\nu + \delta^\mu_\nu$ is a projection tensor, and δ^μ_ν is the Kronecker delta

[1] Models with $\Gamma = 5/3$ show some minor differences compared to models with $\Gamma = 4/3$ (McKinney & Gammie 2004; Mignone & McKinney 2007).

function. We write the orthonormal 3-field as B_i (the covariant 3-field is never used below). The magnetic energy density (u_b) and magnetic pressure (p_b) are then given by $u_b = p_b = b^\mu b_\mu/2 = b^2/2$. Note that the angular velocity of the gas is $\Omega = u^\phi/u^t$. Equation (2.2) has a source term

$$S_\nu = \left(\frac{dU}{d\tau}\right) u_\nu, \tag{2.4}$$

which is a radiation 4-force corresponding to a simple isotropic comoving cooling term given by $dU/d\tau$. We ignore radiative transport effects such as heat currents, viscous stresses, or other effects that would enter as additional momentum sources in the comoving frame. In order to keep the accretion disk thin, we employ the same ad hoc cooling function as in S08:

$$\frac{dU}{d\tau} = -u_g \frac{\log\left(K/K_c\right)}{\tau_{\rm cool}} S[\theta], \tag{2.5}$$

where τ is the fluid proper time, $K = p_g/\rho_0^\Gamma$ is the entropy constant, $K_c = 0.00069$ is set to be the same entropy constant as the torus atmosphere and is the entropy constant we cool the disk towards, and $K_0 \gtrsim K_c$ is the entropy constant of the initial torus[2]. The gas cooling time is set to $\tau_{\rm cool} = 2\pi/\Omega_{\rm K}$, where $\Omega_{\rm K} = (1/M)/[(a/M) + (R/M)^{3/2}]$ is the Keplerian angular frequency and $R = r\sin\theta$ is the cylindrical radius (We consider variations in the cooling timescale in section 2.5.7.). We use a shaping function given by the quantity $S[\theta] = \exp[-(\theta - \pi/2)^2/(2(\theta_{\rm nocool})^2)]$, where we set $\theta_{\rm nocool} = \{0.1, 0.3, 0.45, 0.45\}$ for our sequence of models with target thickness of $|h/r| = \{0.07,\ 0.1,\ 0.2,\ 0.3\}$, although we note that the thickest model with target $|h/r| = 0.3$ has no cooling turned on. The shaping function $S[\theta]$ is used to avoid cooling in the low density funnel-jet region where the thermodynamics is not accurately evolved and where the gas is mostly unbound (see Figure 2.13 in section 2.5.7). In addition, we set the cooling function $dU/d\tau = 0$ if 1) the timestep, dt, obeys $dt > \tau_{\rm cool}$, which ensures that the cooling does not create negative entropy

[2]We intended to have a constant K everywhere at $t = 0$, but a normalization issue led to $K_c \lesssim K_0$. Because of this condition, the disk cools toward a slightly thinner equilibrium at the start of the simulation, after which the cooling proceeds as originally desired by cooling towards the fiducial value $K = K_c$. Our models with $|h/r| \approx 0.07$ are least affected by this issue. Also, since we do not make use of the cooling-based luminosity near $t = 0$, this issue does not affect any of our results. We confirmed that this change leads to no significant issues for either the magnitude or scaling of quantities with thickness by repeating some simulations with the intended $K_c = K_0$. The otherwise similar simulations have thicker disks as expected (very minor change for our thin disk model as expected), and we find consistent results for a given measured thickness in the saturated state.

gas ; or 2) $\log(K/K_c) < 0$, which ensures the gas is only cooled, never heated. Photon capture by the black hole is not included, so the luminosity based upon this cooling function is an upper limit for radiation from the disk. The above cooling function drives the specific entropy of the gas toward the reference specific entropy K_c. Since specific entropy always increases due to dissipation, this cooling function explicitly tracks dissipation. Hence, the luminosity generated from the cooling function should not be considered as the true luminosity, but instead should be considered as representing the emission rate in the limit that all dissipated energy is lost as radiation. Any other arbitrary cooling function that does not track dissipation would require full radiative transfer to obtain the true luminosity.

Magnetic flux conservation is given by the induction equation

$$\partial_t(\sqrt{-g}B^i) = -\partial_j[\sqrt{-g}(B^i v^j - B^j v^i)], \tag{2.6}$$

where $v^i = u^i/u^t$, and $g = \mathrm{Det}(g_{\mu\nu})$ is the determinant of the metric. In steady-state, the cooling is balanced by heating from shocks, grid-scale reconnection, and grid-scale viscosity. No explicit resistivity or viscosity is included.

2.3 Diagnostics

In this section, we describe several important diagnostics that we have found useful in this study. First, since we regulate the disk height via an ad hoc cooling function, we check the scale height of the simulated disk as a function of time and radius to ensure that our cooling function operates properly. Second, the equations we solve consist of seven time-dependent ideal MHD equations, corresponding to four relevant conserved quantities[3]. Using these quantities we construct three dimensionless flux ratios corresponding to the accreted specific energy, specific angular momentum, and specific magnetic flux. Third, we check what the duration of the simulations should be in order to reach a quasi-steady state ("inflow equilibrium") at any given radius. Finally, we describe how

[3]The energy-momentum of the fluid is not strictly conserved because of radiative cooling; however, the fluid component of the energy-momentum equations still proves to be useful. Only energy conservation of the fluid is strongly affected for our types of models.

we compute the luminosity.

When the specific fluxes are computed as a spatial or temporal average/integral, we always take the ratio of averages/integrals of fluxes (i.e. $\int dx F_1 / \int dx F_2$) rather than the average/integral of the ratio of fluxes (i.e. $\int dx (F_1/F_2)$). The former is more appropriate for capturing the mean behavior, while the latter can be more appropriate when investigating fluxes with significant phase shifted correlations between each other. As relevant for this study, the accretion disk has significant vertical stratification and the local value of the ratio of fluxes can vary considerably without any affect on the bulk accretion flow. Similarly, potentially one flux can (e.g.) nearly vanish over short periods, while the other flux does not, which leads to unbounded values for the ratio of fluxes. However, the time-averaged behavior of the flow is not greatly affected by such short periods of time. These cases demonstrate why the ratio of averages/integrals is always performed for both spatial and temporal averages/integrals.

When comparing the flux ratios or luminosities from the simulations against the NT model, we evaluate the percent relative difference $D[f]$ between a quantity f and its NT value as follows:

$$D[f] \equiv 100 \frac{f - f[\mathrm{NT}]}{f[\mathrm{NT}]}. \tag{2.7}$$

For a density-weighted time-averaged value of f, we compute

$$\langle f \rangle_{\rho_0} \equiv \frac{\int\int\int f\, \rho_0(r,\theta,\phi) dA_{\theta\phi} dt}{\int\int\int \rho_0(r,\theta,\phi) dA_{\theta\phi} dt}, \tag{2.8}$$

where $dA_{\theta\phi} \equiv \sqrt{-g} d\theta d\phi$ is an area element in the $\theta - \phi$ plane, and the integral over dt is a time average over the duration of interest, which corresponds to the period when the disk is in steady-state. For a surface-averaged value of f, we compute

$$\langle f \rangle \equiv \frac{\int\int f\, dA_{\theta\phi}}{\int\int dA_{\theta\phi}}. \tag{2.9}$$

2.3.1 Disk thickness measurement

We define the dimensionless disk thickness per unit radius, $|h/r|$, as the density-weighted mean angular deviation of the gas from the midplane,

$$\left|\frac{h}{r}\right| \equiv \left\langle \left| \theta - \frac{\pi}{2} \right| \right\rangle_{\rho_0}. \tag{2.10}$$

(This quantity was called $\Delta\theta_{\rm abs}$ in S08.) Notice that we assume the accretion disk plane is on the equator (i.e. we assume $\langle\theta\rangle_{\rho_0} = \pi/2$). As defined above, $|h/r|$ is a function of r. When we wish to characterize the disk by means of a single estimate of its thickness, we use the value of $|h/r|$ at $r = 2r_{\rm ISCO}$, where $r_{\rm ISCO}$ is the ISCO radius ($r_{\rm ISCO} = 6M$ for a non-spinning BH and $r_{\rm ISCO} = M$ for a maximally-spinning BH; Shapiro & Teukolsky 1983). As we show in §2.5.4, this choice is quite reasonable. An alternative thickness measure, given by the root-mean-square thickness $(h/r)_{\rm rms}$, allows us to estimate how accurate we can be about our definition of thickness. This quantity is defined by

$$\left(\frac{h}{r}\right)_{\rm rms} \equiv \left\langle \left(\theta - \frac{\pi}{2}\right)^2 \right\rangle_{\rho_0}^{1/2}. \tag{2.11}$$

The range of θ for the disk thickness integrals in the above equations is from 0 to π.

2.3.2 Fluxes of mass, energy, and angular momentum

The mass, energy and angular momentum conservation equations give the following fluxes,

$$\dot{M}(r,t) = -\int_\theta \int_\phi \rho_0 u^r dA_{\theta\phi}, \tag{2.12}$$

$$\mathrm{e} \equiv \frac{\dot{E}(r,t)}{\dot{M}(r,t)} = \frac{\int_\theta \int_\phi T^r_t dA_{\theta\phi}}{\dot{M}(r,t)}, \tag{2.13}$$

$$\jmath \equiv \frac{\dot{J}(r,t)}{\dot{M}(r,t)} = -\frac{\int_\theta \int_\phi T^r_\phi dA_{\theta\phi}}{\dot{M}(r,t)}. \tag{2.14}$$

The above relations define the rest-mass accretion rate (sometimes just referred to as the mass accretion rate), $\dot{M}$; the accreted energy flux per unit rest-mass flux, or *specific energy*, e; and the accreted angular momentum flux per unit rest-mass flux, or *specific angular momentum*, $\jmath$. Positive values of these quantities correspond to an inward flux through the black hole horizon.

The black hole spin evolves due to the accretion of mass, energy, and angular momentum, which can be described by the dimensionless spin-up parameter s,

$$s \equiv \frac{d(a/M)}{dt}\frac{M}{\dot{M}} = \jmath - 2\frac{a}{M}\mathrm{e}, \tag{2.15}$$

where the angular integrals used to compute $\jmath$ and e include all θ and ϕ angles (Gammie et al. 2004). For $s = 0$ the black hole is in so-called "spin equilibrium," corresponding to when the dimensionless black hole spin, a/M, does not change in time.

The "nominal" efficiency, corresponding to the total loss of specific energy from the fluid, is obtained by removing the rest-mass term from the accreted specific energy:

$$\tilde{e} \equiv 1 - \mathrm{e}. \tag{2.16}$$

The time-averaged value of $\tilde{e}$ at the horizon ($r = r_{\rm H}$) gives the total nominal efficiency: $\langle \tilde{e}(r_{\rm H}) \rangle$, which is an upper bound on the total photon radiative efficiency.

The range of θ over which the flux density integrals in the above equations are computed depends on the situation. In S08, we limited the θ range to $\delta\theta = \pm 0.2$ corresponding to 2–3 density scale heights in order to focus on the disk and to avoid including the disk wind or black hole jet. In this chapter, we are interested in studying how the contributions to the fluxes vary as a function of height above the equatorial plane. Our expectation is that the disk and corona-wind-jet contribute differently to these fluxes. Thus, we consider different ranges of θ in the integrals, e.g., from $(\pi/2) - 2|h/r|$ to $(\pi/2) + 2|h/r|$, $(\pi/2) - 4|h/r|$ to $(\pi/2) + 4|h/r|$, or 0 to π. The first and third are most often used in later sections.

2.3.3 Splitting angular momentum flux into ingoing and outgoing components

For a more detailed comparison of the simulation results with the NT model, we decompose the flux of angular momentum into an ingoing ("in") term which is related to the advection of mass-energy into the black hole and an outgoing ("out") term which is related to the forces and stresses that transport angular momentum radially outward. These ingoing and outgoing components of the specific angular momentum are defined by

$$\jmath_{\rm in}(r,t) \equiv \frac{\langle (\rho_0 + u_g + b^2/2) u^r \rangle \langle u_\phi \rangle}{\langle -\rho_0 u^r \rangle}, \tag{2.17}$$

$$\jmath_{\rm out}(r,t) \equiv \jmath - \jmath_{\rm in}(r,t). \tag{2.18}$$

By this definition, the "in" quantities correspond to inward transport of the comoving mass-energy density of the disk, $u^\mu u^\nu T_{\mu\nu} = \rho_0 + u_g + b^2/2$. Note that "in" quantities are products of the mean velocity fields $\langle u^r \rangle$ and $\langle u_\mu \rangle$ and not the combination $\langle u^r u_\mu \rangle$; the latter includes a contribution from correlated fluctuations in u^r and u_μ, which corresponds to the Reynolds stress. The residual

of the total flux minus the "in" flux gives the outward, mechanical transport by Reynolds stresses and electromagnetic stresses. One could also consider a similar splitting for the specific energy. The above decomposition most closely matches our expectation that the inward flux should agree with the NT result as $|h/r| \to 0$. Note, however, that our conclusions in this chapter do not require any particular decomposition. This decomposition is different from S08 and N10 where the entire magnetic term $(b^2 u^r u_\phi - b^r b_\phi)$ is designated as the "out" term. Their choice overestimates the effect of electromagnetic stresses, since some magnetic energy is simply advected into the black hole. Also, the splitting used in S08 gives non-monotonic $\jmath_{\rm in}$ vs. radius for some black hole spins, while the splitting we use gives monotonic values for all black hole spins.

2.3.4 The magnetic flux

The no-monopoles constraint implies that the total magnetic flux ($\Phi = \int_S \vec{B} \cdot d\vec{A}$) vanishes through any closed surface or any open surface penetrating a bounded flux bundle. The magnetic flux conservation equations require that magnetic flux can only be transported to the black hole or through the equatorial plane by advection. The absolute magnetic flux ($\int_S |\vec{B} \cdot d\vec{A}|$) has no such restrictions and can grow arbitrarily due to the MRI. However, the absolute magnetic flux can saturate when the electromagnetic field comes into force balance with the matter. We are interested in such a saturated state of the magnetic field within the accretion flow and threading the black hole.

We consider the absolute magnetic flux penetrating a spherical surface and an equatorial surface given, respectively, by

$$\Phi_r(r,\theta,t) = \int_\theta \int_\phi |B^r| dA_{\theta'\phi}, \tag{2.19}$$

$$\Phi_\theta(r,\theta,t) = \int_{r'=r_{\rm H}}^{r'=r} \int_\phi |B^\theta| dA_{r'\phi}. \tag{2.20}$$

Nominally, Φ_r has an integration range of $\theta' = 0$ to $\theta' = \theta$ when measured on the black hole horizon, while when computing quantities around the equatorial plane θ' has the range $\langle\theta\rangle \pm \theta$. One useful normalization of the magnetic fluxes is by the total flux through one hemisphere of the

black hole plus through the equator

$$\Phi_{\rm tot}(r,t) \equiv \Phi_r(r'=r_{\rm H},\theta'=0\ldots\pi/2,t) + \Phi_\theta(r,\theta'=\pi/2,t), \tag{2.21}$$

which gives the normalized absolute radial magnetic flux

$$\tilde{\Phi}_r(r,\theta,t) \equiv \frac{\Phi_r(r,\theta,t)}{\Phi_{\rm tot}(r=R_{\rm out},t=0)}, \tag{2.22}$$

where $R_{\rm out}$ is the outer radius of the computational box. The normalized absolute magnetic flux measures the absolute magnetic flux on the black hole horizon or radially through the equatorial disk per unit absolute flux that is initially available.

The Gammie (1999) model of a magnetized thin accretion flow suggests another useful normalization of the magnetic flux is by the absolute mass accretion rate

$$\dot{M}_G(r,t) \equiv \int_\theta \int_\phi \rho_0 |u^r| dA_{\theta\phi}, \tag{2.23}$$

which gives the normalized specific absolute magnetic fluxes

$$\Xi(r,t) = \frac{\Phi_r(r,t)}{\dot{M}_G(r,t)}, \tag{2.24}$$

$$\Upsilon(r,t) \equiv \sqrt{2}\left|\frac{\Xi(r,t)}{M}\right| \sqrt{\left|\frac{\dot{M}_G(r=r_{\rm H},t)}{{\rm SA}_{\rm H}}\right|}, \tag{2.25}$$

where ${\rm SA} = (1/r^2)\int_\theta\int_\phi dA_{\theta\phi}$ is the local solid angle, ${\rm SA}_{\rm H} = {\rm SA}(r=r_{\rm H})$ is the local solid angle on the horizon, $\Xi(r,t)$ is the radial magnetic flux per unit rest-mass flux (usually specific magnetic flux), and $\Upsilon(r,t)c^{3/2}/G$ is a particular dimensionless normalization of the specific magnetic flux that appears in the MHD accretion model developed by Gammie (1999). Since the units used for the magnetic field are arbitrary, any constant factor can be applied to Ξ and one would still identify the quantity as the specific magnetic flux. So to simplify the discussion we henceforth call Υ the specific magnetic flux. To obtain Equation (2.25), all involved integrals should have a common θ range around the equator. These quantities all have absolute magnitudes because a sign change does not change the physical effect. The quantities $\jmath$, e, $\tilde{e}$, Ξ, and Υ are each conserved along poloidal field-flow lines for stationary ideal MHD solutions (Bekenstein & Oron 1978; Takahashi et al. 1990).

Gammie's (1999) model of a magnetized accretion flow within the ISCO assumes: 1) a thin equatorial flow ; 2) a radial poloidal field geometry (i.e., $|B_\theta| \ll |B_r|$) ; 3) a boundary condition

at the ISCO corresponding to zero radial velocity ; and 4) no thermal contribution. The model reduces to the NT solution within the ISCO for $\Upsilon \to 0$, and deviations from NT's solution are typically small (less than 12% for $\jmath$ across all black hole spins; see Appendix 2.A) for $\Upsilon \lesssim 1$. We have defined the quantity Υ in equation (2.24) with the $\sqrt{2}$ factor, the square root of the total mass accretion rate through the horizon per unit solid angle, and Heaviside-Lorentz units for B^r so that the numerical value of Υ at the horizon is identically equal to the numerical value of the free parameter in Gammie (1999), i.e., their $F_{\theta\phi}$ normalized by $F_{\rm M} = -1$. As shown in that paper, Υ directly controls deviations of the specific angular momentum and specific energy away from the non-magnetized thin disk theory values of the NT model. Even for disks of finite thickness, the parameter shows how electromagnetic stresses control deviations between the horizon and the ISCO. Note that the flow can deviate from NT at the ISCO simply due to finite thermal pressure (McKinney & Gammie 2004). In Appendix 2.6 Table 2.A, we list numerical values of $\jmath$ and $\tilde{e}$ for Gammie's (1999) model, and show how these quantities deviate from NT for a given black hole spin and Υ.

We find Υ to be more useful as a measure of the importance of the magnetic field within the ISCO than our previous measurement in S08 of the α-viscosity parameter,

$$\alpha = \frac{T^{\hat{\phi}\hat{r}}}{p_g + p_b}, \tag{2.26}$$

where $T^{\hat{\phi}\hat{r}} = e^{\hat{\phi}}{}_{\mu} e^{\hat{r}}{}_{\nu} T^{\mu\nu}$ is the orthonormal stress-energy tensor components in the comoving frame, and $e^{\hat{\nu}}{}_{\mu}$ is the contravariant tetrad system in the local fluid-frame. This is related to the normalized stress by

$$\frac{W}{\dot{M}} = \frac{\int\int T^{\hat{\phi}\hat{r}} dA'_{\theta\phi}}{\dot{M} \int_{\phi} dL'_{\phi}}, \tag{2.27}$$

where $dA'_{\theta\phi} = e^{\hat{\theta}}{}_{\mu} e^{\hat{\phi}}{}_{\nu} d\theta^{\mu} d\phi^{\nu}$ is the comoving area element, $dL'_{\phi} = e^{\hat{\phi}}{}_{\nu} d\phi^{\nu}$ evaluated at $\theta = \pi/2$ is the comoving ϕ length element, $\theta^{\mu} = \{0, 0, 1, 0\}$, and $\phi^{\nu} = \{0, 0, 0, 1\}$. This form for W is a simple generalization of Eq. 5.6.1b in NT73, and note that the NT solution for $W/\dot{M}$ is given by Eq. 5.6.14a in NT73. In S08, W was integrated over fluid satisfying $-u_t(\rho_0 + u_g + p_g + b^2)/\rho_0 < 1$ (i.e., only approximately gravitationally bound fluid and no wind-jet). We use the same definition of bound in this chapter. As shown in S08, a plot of the radial profile of $W/\dot{M}$ or α within the ISCO does not necessarily quantify how much the magnetic field affects the accretion flow properties,

since even apparently large values of this quantity within the ISCO do not cause a significant deviation from NT in the specific angular momentum accreted. On the other hand, the Gammie (1999) parameter Υ does directly relate to the electromagnetic stresses within the ISCO and is an ideal MHD invariant (so constant vs. radius) for a stationary flow. One expects that appropriately time-averaged simulation data could be framed in the context of this stationary model in order to measure the effects of electromagnetic stresses.

2.3.5 Inflow equilibrium

When the accretion flow has achieved steady-state inside a given radius, the quantity $\dot{M}(r,t)$ will (apart from normal fluctuations due to turbulence) be independent of time, and if it is integrated over all θ angles will be constant within the given radius[4]. The energy and angular momentum fluxes have a non-conservative contribution due to the cooling function and therefore are not strictly constant. However, the cooling is generally a minor contribution (especially in the case of the angular momentum flux), and so we may still measure the non-radiative terms to verify inflow equilibrium.

The radius out to which inflow equilibrium can be achieved in a given time can be estimated by calculating the mean radial velocity v_r and then deriving from it a viscous timescale $-r/v_r$. From standard accretion disk theory and using the definition of α given in Eq. (2.26), the mean radial velocity is given by

$$v_r \sim -\alpha \left|\frac{h}{r}\right|^2 v_{\rm K}, \tag{2.28}$$

where $v_{\rm K} \approx (r/M)^{-1/2}$ is the Keplerian speed at radius r and α is the standard viscosity parameter given by equation (2.26) (Frank et al. 1992). Although the viscous timescale is the nominal time needed to achieve steady-state, in practice it takes several viscous times before the flow really settles down, e.g., see the calculations reported in Shapiro (2010). In the present chapter, we assume that inflow equilibrium is reached after two viscous times, and hence we estimate the inflow equilibrium

[4]If we integrate over a restricted range of θ, then there could be additional mass flow through the boundaries in the θ direction and $\dot{M}(r,t)$ will no longer be independent of r, though it would still be independent of t.

time, $t_{\rm ie}$, to be

$$t_{\rm ie} \sim -2\frac{r}{v_r} \sim 2M\left(\frac{r}{M}\right)^{3/2}\left(\frac{1}{\alpha|h/r|^2}\right) \sim 5000M\left(\frac{r}{M}\right)^{3/2}, \tag{2.29}$$

where, in the right-most relation, we have taken a typical value of $\alpha \sim 0.1$ for the gas in the disk proper (i.e., outside the ISCO) and we have set $|h/r| \approx 0.064$, as appropriate for our thinnest disk models.

A simulation must run until $t \sim t_{\rm ie}$ before we can expect inflow equilibrium at radius r. According to the above Newtonian estimate, a thin disk simulation with $|h/r| \sim 0.064$ that has been run for a time of $30000M$ will achieve steady-state out to a radius of only $\sim 3M$. However, this estimate is inaccurate since it does not allow for the boundary condition on the flow at the ISCO. Both the boundary condition as well as the effects of GR are included in the formula for the radial velocity given in Eq. 5.9.8 of NT, which we present for completeness in Appendix 2.B. That more accurate result, which is what we use for all our plots and numerical estimates, shows that our thin disk simulations should reach inflow equilibrium within $r/M = 9,\ 7,\ 5.5,\ 5$, respectively, for $a/M = 0,\ 0.7,\ 0.9,\ 0.98$. These estimates are roughly consistent with the radii out to which we have a constant $\jmath$ vs. radius in the simulations discussed in §2.7.

2.3.6 Luminosity measurement

We measure the radiative luminosity of the accreting gas directly from the cooling function $dU/d\tau$. At a given radius, r, in the steady region of the flow, the luminosity per unit rest-mass accretion rate interior to that radius is given by

$$\frac{L(<r)}{\dot{M}(r,t)} = \frac{1}{\dot{M}(r,t)(t_f - t_i)}\int_{t=t_i}^{t_f}\int_{r'=r_{\rm H}}^{r}\int_{\theta=0}^{\pi}\int_{\phi}\left(\frac{dU}{d\tau}\right) u_t\, dV_{tr'\theta\phi}, \tag{2.30}$$

where $dV_{tr'\theta\phi} = \sqrt{-g}dtdr'd\theta d\phi$ and the 4D integral goes from the initial time t_i to the final time t_f over which the simulation results are time-averaged, from the radius $r_{\rm H}$ of the horizon to the radius r of interest, and usually over all θ and ϕ. We find it useful to compare the simulations with thin disk theory by computing the ratio of the luminosity emitted inside the ISCO (per unit rest-mass accretion rate) to the total radiative efficiency of the NT model:

$$\tilde{L}_{\rm in} \equiv \frac{L(<r_{\rm ISCO})}{\dot{M}\tilde{e}[{\rm NT}]}. \tag{2.31}$$

This ratio measures the excess radiative luminosity from inside the ISCO in the simulation relative to the total luminosity in the NT model (which predicts zero luminosity here). We also consider the excess luminosity over the entire inflow equilibrium region

$$\tilde{L}_{\rm eq} \equiv \frac{L(r < r_{\rm eq}) - L(r < r_{\rm eq})[{\rm NT}]}{\dot{M}\tilde{e}[{\rm NT}]}, \tag{2.32}$$

which corresponds to the luminosity (per unit mass accretion rate) inside the inflow equilibrium region (i.e. $r < r_{\rm eq}$, where $r_{\rm eq}$ is the radius out to which inflow equilibrium has been established) subtracted by the NT luminosity all divided by the total NT efficiency. Large percent values of $\tilde{L}_{\rm in}$ or $\tilde{L}_{\rm eq}$ would indicate large percent deviations from NT.

2.4 Physical models and numerical methods

This section describes our physical models and numerical methods. Table 2.1 provides a list of all our simulations and shows the physical and numerical parameters that we vary. Our primary models are labeled by names of the form AxHRy, where x is the value of the black hole spin parameter and y is approximately equal to the disk thickness $|h/r|$. For instance, our fiducial model A0HR07 has a non-spinning black hole ($a/M = 0$) and a geometrically thin disk with $|h/r| \sim 0.07$. We discuss this particular model in detail in §2.5. Table 2.1 also shows the time span (from T_i/M to T_f/M) used to perform the time-averaging, and the last column shows the actual value of $|h/r|$ in the simulated model as measured during inflow equilibrium, e.g., $|h/r| = 0.064$ for model A0HR07.

2.4.1 Physical models

This study considers black hole accretion disk systems with a range of black hole spins: $a/M = 0,\ 0.7,\ 0.9,\ 0.98$, and a range of disk thicknesses: $|h/r| = 0.07,\ 0.13,\ 0.2,\ 0.3$. The initial mass distribution is an isentropic equilibrium torus (Chakrabarti 1985a,b; De Villiers et al. 2003). All models have an initial inner torus edge at $r_{\rm in} = 20M$, while the torus pressure maximum for each model is located between $R_{\rm max} = 35M$ and $R_{\rm max} = 65M$. We chose this relatively large radius for the initial torus because S08 found that placing the torus at smaller radii caused the results to be sensitive to the initial mass distribution. We initialize the solution so that $\rho_0 = 1$ is

the maximum rest-mass density. In S08, we set $q = 1.65$ ($\Omega \propto r^{-q}$ in non-relativistic limit) and $K = 0.00034$ with $\Gamma = 4/3$, while in this chapter we adjust the initial angular momentum profile such that the initial torus has the target value of $|h/r|$ at the pressure maximum. For models with $|h/r| = 0.07,\ 0.13,\ 0.2,\ 0.3$, we fix the specific entropy of the torus by setting, respectively, $K = K_0 \equiv \{0.00034,\ 0.0035,\ 0.009,\ 0.009\}$ in the initial polytropic equation of state given by $p = K_0 \rho_0^{\Gamma}$. The initial atmosphere surrounding the torus has the same polytropic equation of state with nearly the same entropy constant of $K = 0.00069$, but with an initial rest-mass density of $\rho_0 = 10^{-6}(r/M)^{-3/2}$, corresponding to a Bondi-like atmosphere.

Recent GRMHD simulations of thick disks indicate that the results for the disk (but not the wind-jet) are roughly independent of the initial field geometry (McKinney & Narayan 2007a,b; Beckwith et al. 2008a). However, a detailed study for thin disks has yet to be performed.

We consider a range of magnetic field geometries described by the vector potential A_μ which is related to the Faraday tensor by $F_{\mu\nu} = A_{\nu,\mu} - A_{\mu,\nu}$. As in S08, we consider a general multiple-loop field geometry corresponding to N separate loop bundles stacked radially within the initial disk. The vector potential we use is given by

$$A_{\phi,\mathrm{N}} \propto Q^2 \sin\left(\frac{\log(r/S)}{\lambda_{\mathrm{field}}/(2\pi r)}\right)[1 + w(\mathrm{ranc} - 0.5)]\,, \tag{2.33}$$

where ranc is a random number generator for the domain 0 to 1 (see below for a discussion of perturbations.). All other A_μ are initially zero. All our multi-loop and 1-loop simulations have $S = 22M$, and the values of $\lambda_{\mathrm{field}}/(2\pi r)$ are listed in Table 2.1. For multi-loop models, each additional field loop bundle has opposite polarity. We use $Q = (u_g/u_{g,\max} - 0.2)(r/M)^{3/4}$, and set $Q = 0$ if either $r < S$ or $Q < 0$, and $u_{g,\max}$ is the maximum value of the internal energy density in the torus. By comparison, in S08, we set $S = 1.1 r_{\mathrm{in}}$, $r_{\mathrm{in}} = 20M$, $\lambda_{\mathrm{field}}/(2\pi r) = 0.16$, such that there were two loops centered at $r = 28M$ and $38M$. The intention of introducing multiple loop bundles is to keep the aspect ratio of the bundles roughly 1:1 in the poloidal plane, rather than loop(s) that are highly elongated in the radial direction. For each disk thickness, we tune $\lambda_{\mathrm{field}}/(2\pi r)$ in order to obtain initial poloidal loops that are roughly isotropic.

As in S08, the magnetic field strength is set such that the plasma β parameter satisfies $\beta_{\mathrm{maxes}} \equiv p_{g,\max}/p_{b,\max} = 100$, where $p_{g,\max}$ is the maximum thermal pressure and $p_{b,\max}$ is the

maximum magnetic pressure in the entire torus. Since the two maxima never occur at the same location, $\beta = p_g/p_b$ varies over a wide range of values within the disk. This approach is similar to how the magnetic field was normalized in other studies (Gammie et al. 2003; McKinney & Gammie 2004; McKinney 2006b; McKinney & Narayan 2007b; Komissarov & McKinney 2007). It ensures that the magnetic field is weak throughout the disk. Care must be taken with how one normalizes any given initial magnetic field geometry. For example, for the 1-loop field geometry used by McKinney & Gammie (2004), if one initializes the field with a *mean* (volume-averaged) $\bar{\beta} = 100$, then the inner edge of the initial torus has $\beta \sim 1$ and the initial disk is not weakly magnetized.

For most models, the vector potential at all grid points was randomly perturbed by 2% (w in equation 2.33) and the internal energy density at all grid points was randomly perturbed by 10% [5]. If the simulation starts with perturbations of the vector potential, then we compute $\Phi_{\rm tot}$ (used to obtain $\tilde{\Phi}_r$) using the pre-perturbed magnetic flux in order to gauge how much flux is dissipated due to the perturbations. Perturbations should be large enough to excite the non-axisymmetric MRI in order to avoid the axisymmetric channel solution, while they should not be so large as to induce significant dissipation of the magnetic energy due to grid-scale magnetic dissipation just after the evolution begins. For some models, we studied different amplitudes for the initial perturbation in order to ensure that the amplitude does not significantly affect our results. For a model with $|h/r| \sim 0.07$, $a/M = 0$, and a single polarity field loop, one simulation was initialized with 2% vector potential perturbations and 10% internal energy perturbations, while another otherwise similar simulation was given no seed perturbations. Both become turbulent at about the same time $t \sim 1500M$. The magnetic field energy at that time is negligibly different, and there is no evidence for significant differences in any quantities during inflow equilibrium.

[5] In S08, we had a typo saying we perturbed the field by 50%, while it was actually perturbed the same as these models, i.e.: 2% vector potential perturbations and 10% internal energy perturbations.

Table 2.1: Simulation Parameters

Model Name	T_i/M-T_f/M	$\frac{a}{M}$	N_r	N_θ	N_ϕ	$\frac{R_{\rm in}}{r_{\rm H}}$	Y	$\Delta\phi$	$\frac{R_{\rm max}}{M}$	$\frac{R_{\rm out}}{M}$	q	cooling	$\frac{\lambda_{\rm field}}{2\pi r}$	$\frac{h}{r}$
A0HR07	12500-27350	0	256	64	32	0.9	0.13	$\pi/2$	35	50	1.65	yes	0.065	0.064
A7HR07	12500-20950	0.7	256	64	32	0.92	0.13	$\pi/2$	35	50	1.65	yes	0.065	0.065
A9HR07	14000-23050	0.9	256	64	32	0.92	0.13	$\pi/2$	35	50	1.65	yes	0.065	0.054
A98HR07	14000-19450	0.98	256	64	32	0.92	0.13	$\pi/2$	35	50	1.65	yes	0.065	0.059
A0HR1	5050-14150	0	256	64	32	0.9	0.37	$3\pi/4$	45	120	1.94	yes	0.25	0.12
A7HR1	5050-12550	0.7	256	64	32	0.9	0.37	$3\pi/4$	45	120	1.92	yes	0.25	0.09
A9HR1	5050-10000	0.9	256	64	32	0.9	0.37	$3\pi/4$	45	120	1.91	yes	0.25	0.13
A98HR1	12000-13600	0.98	256	64	32	0.9	0.37	$3\pi/4$	45	120	1.91	yes	0.25	0.099
A0HR2	6000-13750	0	256	64	32	0.9	0.65	π	65	200	1.97	yes	0.28	0.18
A7HR2	12000-17900	0.7	256	64	32	0.9	0.65	π	65	200	1.97	yes	0.28	0.16
A9HR2	12000-15200	0.9	256	64	32	0.88	0.65	π	65	200	1.97	yes	0.28	0.21
A98HR2	6100-7100	0.98	256	64	32	0.9	0.65	π	65	200	1.97	yes	0.28	0.18
A0HR3	4700-7900	0	256	64	32	0.9	0.65	π	65	200	1.97	no	0.28	0.35
A7HR3	10000-11900	0.7	256	64	32	0.9	0.65	π	65	200	1.97	no	0.28	0.34
A9HR3	4700-7900	0.9	256	64	32	0.88	0.65	π	65	200	1.97	no	0.28	0.341
A98HR3	4700-7900	0.98	256	64	32	0.9	0.65	π	65	200	1.97	no	0.28	0.307

Table 2.2: Simulation Parameters

Model Name	T_i/M-T_f/M	$\frac{a}{M}$	N_r	N_θ	N_ϕ	$\frac{R_{\rm in}}{r_{\rm H}}$	Y	$\Delta\phi$	$\frac{R_{\rm max}}{M}$	$\frac{R_{\rm out}}{M}$	q	cooling	$\frac{\lambda_{\rm field}}{2\pi r}$	$\frac{h}{r}$
C0	6000-10000	0	512	128	32	0.9	0.15	$\pi/4$	35	50	1.65	yes	0.16	0.052
C1	12500-18900	0	256	64	16	0.9	0.13	$\pi/4$	35	50	1.65	yes	0.065	0.063
C2	12500-22500	0	256	64	64	0.9	0.13	π	35	50	1.65	yes	0.065	0.062
C3	12500-19500	0	256	64	16	0.9	0.13	$\pi/2$	35	50	1.65	yes	0.065	0.061
C4	12500-21700	0	256	64	64	0.9	0.13	$\pi/2$	35	50	1.65	yes	0.065	0.061
C5	12500-20000	0	256	32	32	0.9	0.13	$\pi/2$	35	50	1.65	yes	0.065	0.052
C6	12500-20800	0	256	128	32	0.9	0.13	$\pi/2$	35	50	1.65	yes	0.065	0.065
A0HR07LOOP1	17000-22100	0	256	64	32	0.9	0.13	$\pi/2$	35	50	1.65	yes	0.25	0.048
A0HR3LOOP1	3000-8000	0	256	64	32	0.9	0.65	π	65	200	1.97	no	0.5	0.377

2.4.2 Numerical methods

We perform simulations using the GRMHD code HARM that is based upon a conservative shock-capturing Godunov scheme. One key feature of our code is that we use horizon-penetrating Kerr-Schild coordinates for the Kerr metric (Gammie et al. 2003; McKinney & Gammie 2004; McKinney 2006a; Noble et al. 2006; Mignone & McKinney 2007; Tchekhovskoy et al. 2007), which avoids any issues with the coordinate singularity in Boyer-Lindquist coordinates. Even with Kerr-Schild coordinates, one must ensure that the inner-radial boundary of the computational domain is outside the so-called inner horizon (at $r/M \equiv 1 - \sqrt{1-(a/M)^2}$) so that the equations remain hyperbolic, and one must ensure that there are plenty of grid cells spanning the region near the horizon in order to avoid numerical diffusion out of the horizon.

Another key feature of our code is the use of a 3rd order accurate (4th order error) PPM scheme for the interpolation of primitive quantities (i.e. rest-mass density, 4-velocity relative to a ZAMO observer, and lab-frame 3-magnetic field) (McKinney 2006b). The interpolation is similar to that described in Colella & Woodward (1984), but we modified it to be consistent with interpolating through point values of primitives rather than average values. We do not use the PPM steepener, but we do use the PPM flattener that only activates in strong shocks (e.g. in the initial bow shock off the torus surface, but rarely elsewhere). The PPM scheme attempts to fit a monotonic 3rd order polynomial directly through the grid face where the dissipative flux enters in the Godunov scheme. Only if the polynomial is non-monotonic does the interpolation reduce order and create discontinuities at the cell face, and so only then does it introduce dissipative fluxes. It therefore leads to extremely small dissipation compared to the original schemes used in HARM, such as the 1st order accurate (2nd order error) minmod or monotonized central (MC) limiter type schemes that always create discontinuities (and so dissipative fluxes) at the cell face regardless of the monotonicity for any primitive quantity that is not linear in space.

Simulations of fully three-dimensional models of accreting black holes producing jets using our 3D GRMHD code show that this PPM scheme leads to an improvement in effective resolution by at least factors of roughly two per dimension as compared to the original HARM MC limiter scheme for models with resolution $256 \times 128 \times 32$ (McKinney & Blandford 2009). The PPM method is

particularly well-suited for resolving turbulent flows since they rarely have strong discontinuities and have most of the turbulent power in long wavelength modes. Even moving discontinuities are much more accurately resolved by PPM than minmod or MC. For example, even without a steepener, a simple moving contact or moving magnetic rotational discontinuity is sharply resolved within about 4 cells using the PPM scheme as compared to being diffusively resolved within about 8-15 cells by the MC limiter scheme.

A 2nd order Runge-Kutta method-of-lines scheme is used to step forward in time, and the timestep is set by using the fast magnetosonic wavespeed with a Courant factor of 0.8. We found that a 4th order Runge-Kutta scheme does not significantly improve accuracy, since most of the flow is far beyond the grid cells inside the horizon that determine the timestep. The standard HARM HLL scheme is used for the dissipative fluxes, and the standard HARM Tóth scheme is used for the magnetic field evolution.

2.4.3 Numerical model setup

The code uses uniform internal coordinates $(t, x^{(1)}, x^{(2)}, x^{(3)})$ mapped to the physical coordinates (t, r, θ, ϕ). The radial grid mapping is

$$r(x^{(1)}) = R_0 + \exp(x^{(1)}), \tag{2.34}$$

which spans from $R_{\rm in}$ to $R_{\rm out}$. The parameter $R_0 = 0.3M$ controls the resolution near the horizon. Absorbing (outflow, no inflow allowed) boundary conditions are used. The θ-grid mapping is

$$\theta(x^{(2)}) = [Y(2x^{(2)} - 1) + (1 - Y)(2x^{(2)} - 1)^7 + 1](\pi/2), \tag{2.35}$$

where $x^{(2)}$ ranges from 0 to 1 (i.e. no cut-out at the poles) and Y is an adjustable parameter that can be used to concentrate grid zones toward the equator as Y is decreased from 1 to 0. Roughly half of the θ resolution is concentrated in the disk region within $\pm 2|h/r|$ of the midplane. The HR07 and HR2 models listed in Table 2.1 have 11 cells per $|h/r|$, while the HR1 and HR3 models have 7 cells per $|h/r|$. The high resolution run, C6, has 22 cells per $|h/r|$, while the low resolution model, C5, has 5 cells per $|h/r|$. For $Y = 0.15$ this grid gives roughly 6 times more angular resolution compared to the grid used in McKinney & Gammie (2004) given by equation (8) with

$h = 0.3$. Reflecting boundary conditions are used at the polar axes.

The ϕ-grid mapping is given by $\phi(x^{(3)}) = 2\pi x^{(3)}$, such that $x^{(3)}$ varies from 0 to $1/8, 1/4, 3/8, 1/2$ for boxes with $\Delta\phi = \pi/4, \pi/2, 3\pi/4, \pi$, respectively. Periodic boundary conditions are used in the ϕ-direction. In all cases, the spatial integrals are renormalized to refer to the full 2π range in ϕ, even if our computational box size is limited in the ϕ-direction. We consider various $\Delta\phi$ in order to check whether this changes our results. Previous GRMHD simulations with the full $\Delta\phi = 2\pi$ extent suggest that $\Delta\phi = \pi/2$ is sufficient since coherent structures only extend for about one radian (see Fig. 12 in Schnittman et al. 2006). However, in other GRMHD studies with $\Delta\phi = 2\pi$, the $m = 1$ mode was found to be dominant, so this requires further consideration (McKinney & Blandford 2009). Note that S08 used $\Delta\phi = \pi/4$, while both N09 and N10 used $\Delta\phi = \pi/2$.

The duration of our simulations with the thinnest disks varies from approximately $20000M$ to $30000M$ in order to reach inflow equilibrium and to minimize fluctuations in time-averaged quantities. We ensure that each simulation runs for a couple of viscous times in order to reach inflow equilibrium over a reasonable range of radius. Note that the simulations cannot be run for a duration longer than $t_{\rm acc} \sim M_{\rm disk}(t=0)/\dot{M} \sim 10^5 M$, corresponding to the time-scale for accreting a significant fraction of the initial torus. We are always well below this limit.

Given finite computational resources, there is a competition between duration and resolution of a simulation. Our simulations run for relatively long durations, and we use a numerical resolution of $N_r \times N_\theta \times N_\phi = 256 \times 64 \times 32$ for all models (except those used for convergence testing). In S08 we found this resolution to be sufficient to obtain convergence compared to a similar $512 \times 128 \times 32$ model with $\Delta\phi = \pi/4$. In this chapter, we explicitly confirm that our resolution is sufficient by convergence testing our results (see section 2.6). Near the equatorial plane at the ISCO, the grid aspect ratio in $dr : rd\theta : r\sin\theta d\phi$ is 2:1:7, 1:1:4, 1:1:3, and 1:1:3, respectively, for our HR07, HR1, HR2, and HR3 models. The 2:1:7 grid aspect ratio for the HR07 model was found to be sufficient in S08. A grid aspect ratio of 1:1:1 would be preferable in order to ensure the dissipation is isotropic in Cartesian coordinates, since in Nature one would not expect highly anisotropic dissipation on the scale resolved by our grid cells. However, finite computational resources require a balance between

a minimum required resolution, grid aspect ratio, and duration of the simulation.

As described below, we ensure that the MRI is resolved in each simulation both as a function of space and as a function of time by measuring the number of grid cells per fastest growing MRI mode:

$$Q_{\rm MRI} \equiv \frac{\lambda_{\rm MRI}}{\Delta_{\hat{\theta}}} \approx 2\pi \frac{|v_{\rm A}^{\hat{\theta}}|/|\Omega(r,\theta)|}{\Delta_{\hat{\theta}}}, \tag{2.36}$$

where $\Delta_{\hat{\theta}} \equiv |e^{\hat{\theta}}{}_{\mu} dx^{\mu}|$ is the comoving orthonormal θ-directed grid cell length, $e^{\hat{\nu}}{}_{\mu}$ is the contravariant tetrad system in the local fluid-frame, $|v_{\rm A}^{\hat{\theta}}| = \sqrt{b_{\hat{\theta}} b^{\hat{\theta}}/(b^2 + \rho_0 + u_g + p_g)}$ is the Alfvén speed, $b^{\hat{\theta}} \equiv e^{\hat{\theta}}{}_{\mu} b^{\mu}$ is the comoving orthonormal θ-directed 4-field, and $|\Omega(r,\theta)|$ is the temporally and azimuthally averaged absolute value of the orbital frequency.

During the simulation, the rest-mass density and internal energy densities can become quite low beyond the corona, but the code only remains accurate and stable for a finite value of b^2/ρ_0, b^2/u_g, and u_g/ρ_0 for any given resolution. We enforce $b^2/\rho_0 \lesssim 10^4$, $b^2/u_g \lesssim 10^4$, and $u_g/\rho_0 \lesssim 10^4$ by injecting a sufficient amount of mass or internal energy into a fixed zero angular momentum observer (ZAMO) frame with 4-velocity $u_\mu = \{-\alpha, 0, 0, 0\}$, where $\alpha = 1/\sqrt{-g^{tt}}$ is the lapse. In some simulations, we have to use stronger limits given by $b^2/\rho_0 \lesssim 10$, $b^2/u_g \lesssim 10^2$, and $u_g/\rho_0 \lesssim 10$, in order to maintain stability and accuracy. Compared to our older method of injecting mass-energy into the comoving frame, the new method avoids run-away injection of energy-momentum in the low-density regions. We have confirmed that this procedure of injecting mass-energy does not contaminate our results for the accretion rates and other diagnostics.

2.5 Fiducial model of a thin disk around a non-rotating black hole

Our fiducial model, A0HR07, consists of a magnetized thin accretion disk around a non-rotating ($a/M = 0$) black hole. This is similar to the model described in S08; however, here we consider a larger suite of diagnostics, a resolution of $256 \times 64 \times 32$, and a computational box with $\Delta\phi = \pi/2$. As mentioned in section 2.4.1, the initial torus parameters are set so that the inner edge is at $r = 20M$, the pressure maximum is at $r = 35M$, and $|h/r| \lesssim 0.1$ at the pressure maximum (see

Figure 2.1).

The initial torus is threaded with magnetic field in the multi-loop geometry as described in section 2.4.1. For this model, we use four loops in order to ensure that the loops are roughly circular in the poloidal plane. Once the simulation begins, the MRI leads to MHD turbulence which causes angular momentum transport and drives the accretion flow to a quasi-steady state.

The fiducial model is evolved for a total time of $27350M$. We consider the period of steady-state to be from $T_i = 12500M$ to $T_f = 27350M$ and of duration $\Delta T = 14850M$. All the steady-state results described below are obtained by time-averaging quantities over this steady-state period, which corresponds to about 160 orbital periods at the ISCO, 26 orbits at the inner edge of the initial torus ($r = 20M$), and 11 orbits at the pressure maximum of the initial torus ($r = 35M$).

2.5.1 Initial and evolved disk structure

Figure 2.1 shows contour plots of various quantities in the initial solution projected on the $(R, z) = (r\sin\theta, r\cos\theta)$-plane. Notice the relatively small vertical extent of the torus. The disk has a thickness of $|h/r| \sim 0.06 - 0.09$ over the radius range containing the bulk of the mass. The four magnetic loops are clearly delineated. The plot of $Q_{\rm MRI}$ indicates that the MRI is well-resolved within the two primary loops. The left-most and right-most loops are marginally under-resolved, so a slightly slower-growing MRI mode is expected to control the dynamics in this region. However, the two primary loops tend to dominate the overall evolution of the gas.

Figure 2.2 shows the time-averaged solution during the quasi-steady state period from $T_i = 12500M$ to $T_f = 27350M$. We refer to the disk during this period as being "evolved" or "saturated." The evolved disk is in steady-state up to $r \sim 9M$, as expected for the duration of our simulation. The rest-mass density is concentrated in the disk midplane within $\pm 2|h/r|$, while the magnetic energy density is concentrated above the disk in a corona. The MRI is properly resolved with $Q_{\rm MRI} \approx 6$ in the disk midplane[6]. The gas in the midplane has plasma $\beta \sim 10$ outside the

[6]Sano et al. (2004) find that having about 6 grid cells per wavelength of the fastest growing MRI mode during saturation leads to convergent behavior for the electromagnetic stresses, although their determination of 6 cells was based upon a 2nd order van Leer scheme that is significantly more diffusive than our PPM scheme. Also, the (time-

ISCO and $\beta \sim 1$ near the black hole, indicating that the magnetic field has been amplified beyond the initial minimum of $\beta \sim 100$.

Figure 2.3 shows the time-averaged structure of the magnetic field during the quasi-steady state period. The field has a smooth split-monopole structure near and inside the ISCO. Beyond $r \sim 9M$, however, the field becomes irregular, reversing direction more than once. At these radii, the simulation has not reached inflow equilibrium.

2.5.2 Velocities and the viscous time-scale

Figure 2.4 shows the velocity structure in the evolved model. The snapshot indicates well-developed turbulence in the interior of the disk at radii beyond the ISCO ($r > 6M$), but laminar flow inside the ISCO and over most of the corona. The sudden transition from turbulent to laminar behavior at the ISCO, which is seen also in the magnetic field (Figure 2.3a), is a clear sign that the flow dynamics are quite different in the two regions. Thus the ISCO clearly has an effect on the accreting gas. The time-averaged flow shows that turbulent fluctuations are smoothed out within $r \sim 9M$. Figure 2.5 shows the velocity stream lines using the line integral convolution method to illustrate vector fields. This figure again confirms that the accretion flow is turbulent at radii larger than $r_{\rm ISCO}$ but it becomes laminar inside the ISCO, and it again shows that time-averaging smooths out turbulent fluctuations out to $r \sim 9M$.

Figure 2.6 shows components of the time-averaged velocity that are angle-averaged over $\pm 2|h/r|$ around the midplane (thick dashed lines in Figure 2.8). By limiting the range of the θ integral, we focus on the gas in the disk, leaving out the corona-wind-jet. Outside the ISCO, the radial velocity from the simulation agrees well with the analytical GR estimate (Eq. 2.53 in Appendix 2.B). By making this comparison, we found $\alpha|h/r|^2 \approx 0.00033$. For our disk thickness

averaged or single time value of) vertical field is already (at any random spatial position) partially sheared by the axisymmetric MRI, and so may be less relevant than the (e.g.) maximum vertical field per unit orbital time at any given point that is not yet sheared and so represents the vertical component one must resolve. These issues imply we may only need about 4 cells per wavelength of the fastest growing mode (as defined by using the time-averaged absolute vertical field strength).

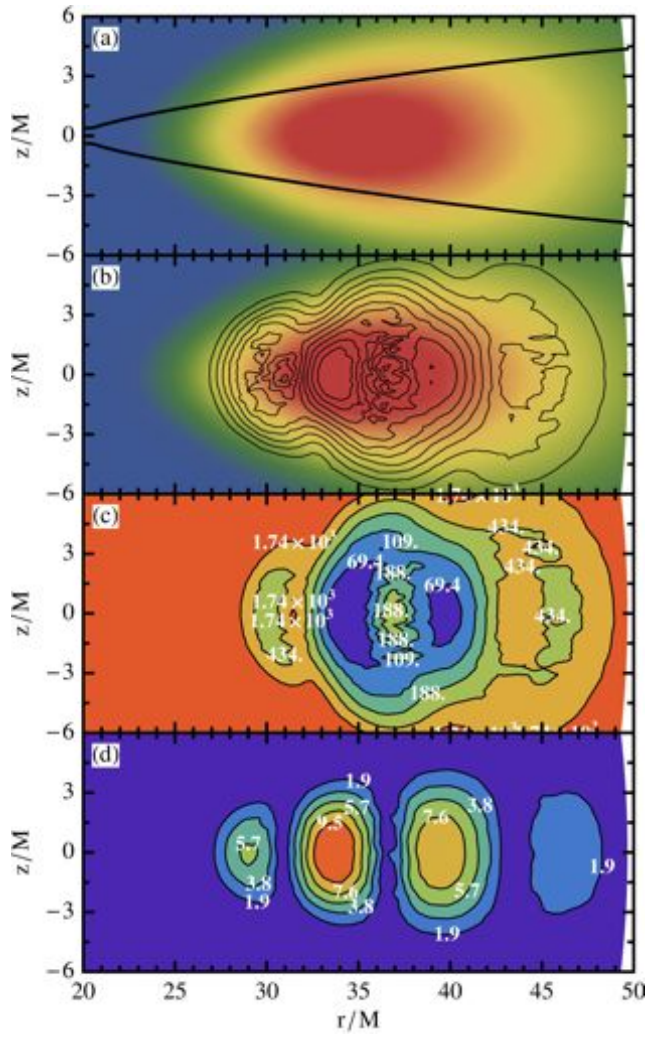

Fig. 2.1.— The initial state of the fiducial model (A0HR07) consists of weakly magnetized gas in a geometrically thin torus around a non-spinning ($a/M = 0$) black hole. Color maps have red as highest values and blue as lowest values. Panel (a): Linear color map of rest-mass density, with solid lines showing the thickness $|h/r|$ of the initial torus. Note that the black hole horizon is at $r = 2M$, far to the left of the plot, so the torus is clearly geometrically thin. Near the pressure maximum $|h/r| \lesssim 0.1$, and elsewhere $|h/r|$ is even smaller. Panel (b): Contour plot of b^2 overlaid on linear color map of rest-mass density shows that the initial field consists of four poloidal loops centered at $r/M = 29$, 34, 39, 45. The wiggles in b^2 are due to the initial perturbations. Panel (c): Linear color map of the plasma β shows that the disk is weakly magnetized throughout the initial torus. Panel (d): Linear color map of the number of grid cells per fastest growing MRI wavelength, $Q_{\rm MRI}$, shows that the MRI is properly resolved for the primary two loops at the center of the disk.

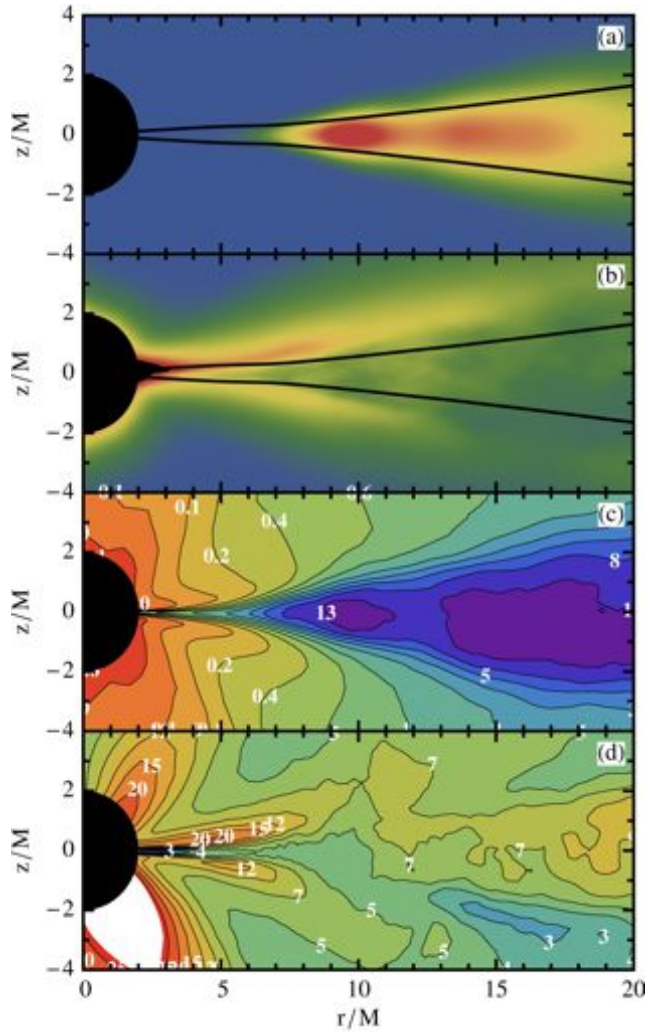

Fig. 2.2.— The evolved state of the fiducial model (A0HR07) consists of a weakly magnetized thin disk surrounded by a strongly magnetized corona. All plots show quantities that have been time-averaged over the period $12500M$ to $27350M$. Color maps have red as highest values and blue as lowest values. Panel (a): Linear color map of rest-mass density, with solid lines showing the disk thickness $|h/r|$. Note that the rest-mass density drops off rapidly inside the ISCO. Panel (b): Linear color map of b^2 shows that a strong magnetic field is present in the corona above the equatorial disk. Panel (c): Linear color map of plasma β shows that the β values are much lower than in the initial torus. This indicates that considerable field amplification has occurred via the MRI. The gas near the equatorial plane has $\beta \sim 10$ far outside the ISCO and approaches $\beta \sim 1$ near the black hole. Panel (d): Linear color map of the number of grid cells per fastest growing MRI wavelength, $Q_{\rm MRI}$.

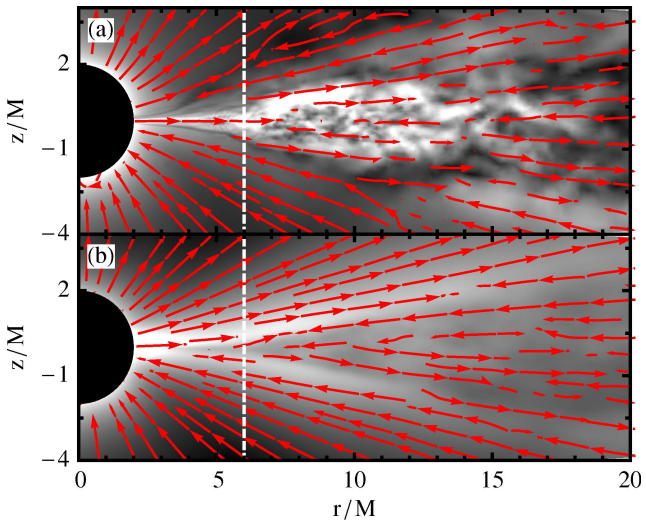

Fig. 2.3.— Magnetic field lines (red vectors) and magnetic energy density (greyscale map) are shown for the fiducial model (A0HR07). Panel (a): Snapshot of the magnetic field structure at time $27200M$ shows that the disk is highly turbulent for $r > r_{\rm ISCO} = 6M$ and laminar for $r < r_{\rm ISCO}$. Panel (b): Time-averaged magnetic field in the saturated state shows that for $r \lesssim 9M$, viz., the region of the flow that we expect to have achieved inflow equilibrium, the geometry of the time-averaged magnetic field closely resembles that of a split-monopole. The dashed, vertical line marks the position of the ISCO.

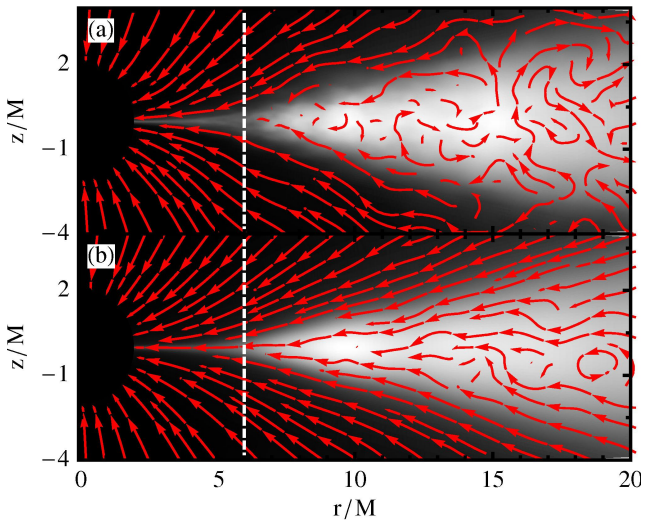

Fig. 2.4.— Flow stream lines (red vectors) and rest-mass density (greyscale map) are shown for the fiducial model (A0HR07). Panel (a): Snapshot of the velocity structure and rest-mass density at time $27200M$ clearly shows MRI-driven turbulence in the interior of the disk. The rest-mass density appears more diffusively distributed than the magnetic energy density shown in Figure 2.3a. Panel (b): Time-averaged streamlines and rest-mass density show that for $r \lesssim 9M$ the velocity field is mostly radial with no indication of a steady outflow. Time-averaging smooths out the turbulent fluctuations in the velocity. The dashed, vertical line marks the position of the ISCO.

$|h/r| = 0.064$, this corresponds to $\alpha \approx 0.08$, which is slightly smaller than the nominal estimate $\alpha \sim 0.1$ we assumed in §2.3.5. As the gas approaches the ISCO, it accelerates rapidly in the radial direction and finally free-falls into the black hole. This region of the flow is not driven by viscosity and hence the dynamics here are not captured by the analytical formula.

Figure 2.6 also shows the inflow equilibrium time $t_{\rm ie}$, which we take to be twice the GR version of the viscous time: $t_{\rm ie} = -2r/v_r$. This is our estimate of the time it will take for the gas at a given radius to reach steady-state. We see that, in a time of $\sim 27350M$, the total duration of our simulation, the solution can be in steady-state only inside a radius of $\sim 9M$. Therefore, in the time-averaged results described below, we consider the results to be reliable only over this range of radius.

2.5.3 Fluxes vs. time

Figure 2.7 shows various fluxes vs. time that should be roughly constant once inflow equilibrium has been reached. The figure shows the mass flux, $\dot{M}(r_{\rm H}, t)$, nominal efficiency, $\tilde{e}(r_{\rm H}, t)$, specific angular momentum, $\jmath(r_{\rm H}, t)$, normalized absolute magnetic flux, $\tilde{\Phi}_r(r_{\rm H}, t)$, (normalized using the unperturbed initial total flux), and specific magnetic flux, $\Upsilon(r_{\rm H}, t)$, all measured at the event horizon ($r = r_H$). These fluxes have been integrated over the entire range of θ from 0 to π. The quantities $\dot{M}$, $\tilde{e}$ and $\jmath$ appear to saturate already at $t \sim 7000M$. However, the magnetic field parameters saturate only at $\sim 12500M$. We consider the steady-state period of the disk to begin only after all these quantities reach their saturated values.

The mass accretion rate is quite variable, with root-mean-square (rms) fluctuations of order two. The nominal efficiency $\tilde{e}$ is fairly close to the NT efficiency, while the specific angular momentum $\jmath$ is clearly below the NT value. The results indicate that torques are present within the ISCO, but do not dissipate much energy or cause significant energy to be transported out of the ISCO. The absolute magnetic flux per unit initial absolute flux, $\tilde{\Phi}_r$, threading the black hole grows to about 1%, which indicates that the magnetic field strength near the black hole is not just set by the amount of magnetic flux in the initial torus. This suggests our results are insensitive to the total absolute magnetic flux in the initial torus. The specific magnetic flux, $\Upsilon \approx 0.86$

on average. Magnetic stresses are relatively weak since $\Upsilon \lesssim 1$, which implies the magnetic field contributes no more than 7% to deviations from NT in $\jmath$ (Gammie 1999) ; see Appendix 2.A. During the quasi-steady state period, the small deviations from NT in $\jmath$ are correlated in time with the magnitude of Υ. This is consistent with the fact that the specific magnetic flux controls these deviations. Also, notice that $\tilde{\Phi}_r$ is roughly constant in time while Υ varies in time. This is clearly because $\dot{M}$ is varying in time and also consistent with the fact that Υ and $\dot{M}$ are anti-correlated in time.

2.5.4 Disk thickness and fluxes vs. radius

Figure 2.8 shows the time-averaged disk thickness of the fiducial model as a function of radius. Both measures of thickness defined in §2.3.1 are shown; they track each other. As expected, our primary thickness measure, $|h/r|$, is the smaller of the two. This thickness measure varies by a small amount across the disk, but it is generally consistent with the following fiducial value, viz., the value $|h/r| = 0.064$ at $r = 2r_{\rm ISCO} = 12M$.

Figure 2.9 shows the behavior of various fluxes versus radius for the full θ integration range (0 to π). We see that the mass accretion rate, $\dot{M}$, and the specific angular momentum flux, $\jmath$, are constant up to a radius $r \sim 9M$. This is exactly the distance out to which we expect inflow equilibrium to have been established, given the inflow velocity and viscous time scale results discussed in §2.5.2. The consistency of these two measurements gives us confidence that the simulation has truly achieved steady-state conditions inside $r = 9M$. Equally clearly, and as also expected, the simulation is not in steady-state at larger radii.

The second panel in Figure 2.9 shows that the inward angular momentum flux, $\jmath_{\rm in}$, agrees reasonably well with the NT prediction. It falls below the NT curve at large radii, i.e., the gas there is sub-Keplerian. This is not surprising since we have included the contribution of the corona-wind-jet gas which, being at high latitude, does not rotate at the Keplerian rate. Other quantities, described below, show a similar effect due to the corona. At the horizon, $\jmath_{\rm in} = 3.286$, which is 5% lower than the NT value. This deviation is larger than that found by S08. Once again, it is because we have included the gas in the corona-wind-jet, whereas S08 did not.

The third panel in Figure 2.9 shows that the nominal efficiency $\tilde{e}$ at the horizon lies below the NT prediction. This implies that the full accretion flow (disk+corona+wind+jet) is radiatively less efficient than the NT model. However, the overall shape of the curve as a function of r is similar to the NT curve. The final panel in Figure 2.9 shows the value of Υ vs. radius. We see that $\Upsilon \approx 0.86$ is constant out to $r \sim 6M$. A value of $\Upsilon \sim 1$ would have led to 7% deviations from NT in $\jmath$, and only for $\Upsilon \sim 6.0$ would deviations become 50% (see Appendix 2.A). The fact that $\Upsilon \sim 0.86 \lesssim 1$ indicates that electromagnetic stresses are weak and cause less than 7% deviations from NT in $\jmath$. Note that one does not expect Υ to be constant[7] outside the ISCO where the magnetic field is dissipating due to MHD turbulence and the gas is forced to be nearly Keplerian despite a sheared magnetic field.

As we have hinted above, we expect large differences between the properties of the gas that accretes in the disk proper, close to the midplane, and that which flows in the corona-wind-jet region. To focus just on the disk gas, we show in Figure 2.10 the same fluxes as in Figure 2.9, except that we have restricted the θ range to $\pi/2 \pm 2|h/r|$. The mass accretion rate is no longer perfectly constant for $r < 9M$. This is simply a consequence of the fact that the flow streamlines do not perfectly follow the particular constant $2|h/r|$ disk boundary we have chosen. The non-constancy of $\dot{M}$ does not significantly affect the other quantities plotted in this figure since they are all normalized by the local $\dot{M}$.

The specific angular momentum, specific energy, and specific magnetic flux are clearly shifted closer to the NT values when we restrict the angular integration range. Compared to the NT value, viz., $\jmath_{\rm NT}(r_{\rm H}) = 3.464$, the fiducial model gives $\jmath(r_{\rm H}) = 3.363$ (2.9% less than NT) when integrating over $\pm 2|h/r|$ around the midplane (i.e., only over the disk gas) and gives $\jmath(r_{\rm H}) = 3.266$ (5.7% less than NT) when integrating over all θ (i.e., including the corona-wind-jet). Even though the mass accretion rate through the corona-wind-jet is much lower than in the disk, still this gas contributes essentially as much to the deviation of the specific angular momentum as the disk gas does. In the

[7]We also find that the ideal MHD invariant related to the "isorotation law" of field lines, $\Omega_F(r) \equiv \left(\int\int d\theta d\phi \sqrt{-g} |v^r B^\phi - v^\phi B^r|\right) / \left(\int\int d\theta d\phi \sqrt{-g} |B^r|\right)$, is Keplerian outside the ISCO and is (as predicted by the Gammie 1999 model) roughly constant from the ISCO to the horizon (see also McKinney & Gammie 2004; McKinney & Narayan 2007a).

case of the specific magnetic flux, integrating over $\pm 2|h/r|$ around the midplane we find $\Upsilon \approx 0.45$, while when we integrate over all angles $\Upsilon \approx 0.86$. The Gammie (1999) model of an equatorial (thin) magnetized flow within the ISCO shows that deviations in the specific angular momentum are determined by the value of Υ. We find that the measured values of Υ are able to roughly predict the measured deviations from NT in $\jmath$.

In summary, a comparison of Figure 2.9 and Figure 2.10 shows that all aspects of the accretion flow in the fiducial simulation agree much better with the NT prediction when we restrict our attention to regions close to the midplane. In other words, the gas in the disk proper, defined here as the region lying within $\pm 2|h/r|$ of the midplane, is well described by the NT model. The deviation of the angular momentum flux $\jmath_{\rm in}$ or $\jmath$ at the horizon relative to NT is $\lesssim 3\%$, similar to the deviation found by S08[8], while the nominal efficiency $\tilde{e}$ agrees to within $\sim 1\%$.

2.5.5 Comparison with Gammie (1999) model

Figure 2.11 shows a comparison between the fiducial model and the Gammie (1999) model of a magnetized thin accretion flow within the ISCO (see also Appendix 2.A). Quantities have been integrated within $\pm 2|h/r|$ of the midplane and time-averaged over a short period from $t = 17400M$ to $t = 18400M$. Note that time-averaging b^2, ρ_0, etc. over long periods can lead to no consistent comparable solution if the value of Υ varies considerably during the period used for averaging. Also, note that the presence of vertical stratification, seen in Figures 2.9 and 2.10 showing that Υ depends upon height, means the vertical-averaging used to obtain Υ can sometimes make it difficult to compare the simulations with the Gammie (1999) model which has no vertical stratification. In particular, using equation (2.24) over this time period, we find that $\Upsilon \approx 0.2\ , 0.3,\ 0.44,\ 0.7,\ 0.8$ for integrations around the midplane of, respectively, $\pm 0.01,\ \pm 0.05,\ \pm 2|h/r|,\ \pm \pi/4,\ \pm \pi/2$, with best matches to the Gammie model (i.e. $b^2/2$ and other quantities match) using an actual value of $\Upsilon = 0.2,\ 0.33,\ 0.47,\ 0.8,\ 0.92$. This indicates that stratification likely causes our diagnostic

[8]The quantities $\jmath_{\rm in}$ and $\jmath$ are nearly equal at the horizon in the calculations reported here whereas they were different in S08. This is because S08 used an alternate definition of $\jmath_{\rm in}$. If we had used that definition here, we would have found a deviation of $\sim 2\%$ in $\jmath_{\rm in}$, just as in S08

to underestimate the best match with the Gammie model once the integration is performed over highly-stratified regions. However, the consistency is fairly good considering how much Υ varies with height.

Overall, Figure 2.11 shows how electromagnetic stresses control the deviations from NT within the ISCO. The panels with $D[\jmath]$ and $D[\mathrm{e}]$ show how the electromagnetic flux starts out large at the ISCO and drops to nearly zero on the horizon. This indicates the electromagnetic flux has been converted into particle flux within the ISCO by ideal (non-dissipative) electromagnetic stresses[9]. The simulated magnetized thin disk agrees quite well with the Gammie solution, in contrast to the relatively poor agreement found for thick disks (McKinney & Gammie 2004). Only the single parameter Υ determines the Gammie solution, so the agreement with the value and radial dependence among multiple independent terms is a strong validation that the Gammie model is working well. Nevertheless, there are some residual deviations near the ISCO where the thermal pressure dominates the magnetic pressure. Even if deviations from NT are present right at the ISCO, the total deviation of the particle flux between the ISCO and horizon equals the deviation predicted by the Gammie (1999) model, as also found in McKinney & Gammie (2004) for thick disks. This indicates that the Gammie (1999) model accurately predicts the effects of electromagnetic stresses inward of the ISCO.

Finally, note that the electromagnetic stresses within the ISCO are ideal and non-dissipative in the Gammie model. Since the flow within the ISCO in the simulation is mostly laminar leading to weak non-ideal (resistive or viscous) effects, the dissipative contribution (which could lead to radiation) can be quite small. An exception to this is the presence of extended current sheets, present near the equator within the ISCO in the simulations, whose dissipation requires a model of the (as of yet, poorly understood) rate of relativistic reconnection.

2.5.6 Luminosity vs. radius

Figure 2.12 shows radial profiles of two measures of the disk luminosity: $L(<r)/\dot{M}$, which is the cumulative luminosity inside radius r, and $d(L/\dot{M})/d\ln r$, which gives the local luminosity at r.

[9]This behavior is just like that seen in ideal MHD jet solutions, but inverted with radius.

We see that the profiles from the simulation are quite close to the NT prediction, especially in the steady-state region. As a way of measuring the deviation of the simulation results from the NT model, we estimate what fraction of the disk luminosity is emitted inside the ISCO; recall that the NT model predicts zero luminosity here. The fiducial simulation gives $L(< r_{\rm ISCO})/\dot{M} = 0.0021$, which is 3.5% of the nominal efficiency $\tilde{e}[{\rm NT}] = 0.058$ of a thin NT disk around a non-spinning black hole. This shows that the excess luminosity radiated within the ISCO is quite small. The relative luminosity within the ISCO is $\tilde{L}_{\rm in} = 3.5\%$ and the relative luminosity within the inflow equilibrium region is $\tilde{L}_{\rm out} = 8.0\%$. Hence, we conclude that, for accretion disks which are as thin as our fiducial model, viz., $|h/r| \sim 0.07$, the NT model provides a good description of the luminosity profile.

2.5.7 Luminosity from disk vs. corona-wind-jet

The fiducial model described so far includes a tapering of the cooling rate as a function of height above the midplane, given by the function $S[\theta]$ (see equation 2.5). We introduced this taper in order to only cool bound ($-u_t(\rho_0 + u_g + p_g + b^2)/\rho_0 < 1$) gas and to avoid including the emission from the part of the corona-wind-jet that is prone to excessive numerical dissipation due to the low resolution used high above the accretion disk. This is a common approach that others have also taken when performing GRMHD simulations of thin disks (N09, N10). However, since our tapering function does not explicitly refer to how bound the gas is, we need to check that it is consistent with cooling only bound gas. We have explored this question by re-running the fiducial model with all parameters the same except that we turned off the tapering function altogether, i.e., we set $S[\theta] = 1$. This is the only model for which the tapering function is turned off.

Figure 2.13 shows a number of luminosity profiles for the fiducial model and the no-tapering model. This comparison shows that, whether or not we include a taper, the results for the luminosity from all the bound gas is nearly the same. Without a tapering, there is some luminosity at high latitudes above $\pm 8|h/r|$ corresponding to emission from the low-density jet region (black solid line). This region is unbound and numerically inaccurate, and it is properly excluded when we use the tapering function. Another conclusion from the above test is that, as far as the luminosity

is concerned, it does not matter much whether we focus on the midplane gas ($(\pi/2) \pm 2|h/r|$) or include all the bound gas. The deviations of the luminosity from NT in the two cases are similar – *changes* in the deviation are less than 1%.

An important question to ask is whether the excess luminosity from within the ISCO is correlated with, e.g., deviations from NT in $\jmath$, since $D[\jmath]$ could then be used as a proxy for the excess luminosity. We investigate this in the context of the simulation with no tapering. For an integration over $\pm 2|h/r|$ around the midplane (which we identify with the disk component), or over all bound gas, or over all the gas (bound and unbound), the excess luminosity inside the ISCO is $\tilde{L}_{\rm in} = 3.3\%,\ 4.4\%,\ 5.4\%$, and the deviation from NT in $\jmath$ is $D[\jmath] = -3.6\%,\ -6.7\%,\ -6.7\%$, respectively. We ignore the luminosity from unbound gas since this is mostly due to material in a very low density region of the simulation where thermodynamics is not evolved accurately. Considering the rest of the results, we see that $D[\jmath]$ is 100% larger when we include bound gas outside the disk compared to when we consider only the disk gas, whereas the excess luminosity increases by only 32%. Therefore, when we compute $\jmath$ by integrating over all bound gas and then assess the deviation of the simulated accretion flow from the NT model, we strongly overestimate the excess luminosity of the bound gas relative to NT. A better proxy for the latter is the deviations from NT in $\jmath$ integrated only over the disk component (i.e. over $\pm 2|h/r|$ around the midplane).

Furthermore, we note that the gas that lies beyond $\pm 2|h/r|$ from the disk midplane consists of coronal gas, which is expected to be optically thin and to emit a power-law spectrum of photons. For many applications, we are not interested in this component but rather care only about the thermal blackbody-like emission from the optically-thick region of the disk. For such studies, the most appropriate diagnostic from the simulations is the radiation emitted within $\pm 2|h/r|$ of the midplane. According to this diagnostic, the excess emission inside the ISCO is only $\tilde{L}_{\rm in} = 3.4\%$ in the model without tapering, and 3.5% in the fiducial model that includes tapering.

Lastly, we consider variations in the cooling timescale, $\tau_{\rm cool}$, which is another free parameter of our cooling model that we generally set to $2\pi/\Omega_{\rm K}$. However, we consider one model that is otherwise identical to the fiducial model except we set $\tau_{\rm cool}$ to be five times shorter so that the cooling rate is five times faster. We find that $\tilde{L}_{\rm in} = 4.2\%$, which is slightly larger than the fiducial

model with $\tilde{L}_{\rm in} = 3.5\%$. Even though the cooling rate is five times faster than an orbital rate, there is only 20% more luminosity from within the ISCO. This is likely due to the flow within the ISCO being mostly laminar with little remaining turbulence to drive dissipation and radiation.

2.6 Convergence with resolution and box size

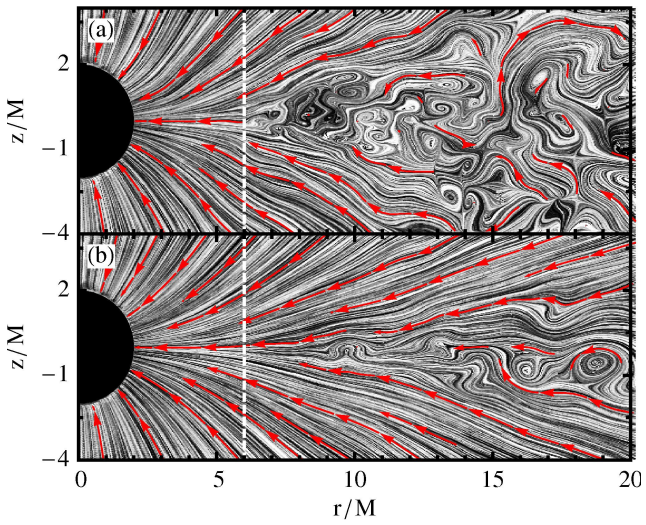

Fig. 2.5.— Flow stream lines are shown for the fiducial model (A0HR07). Panel (a): Snapshot of the velocity structure at time $27200M$ clearly shows MRI-driven turbulence in the interior of the disk. Panel (b): Time-averaged streamlines show that for $r \lesssim 9M$ the velocity field is mostly radial. The dashed, vertical line marks the position of the ISCO.

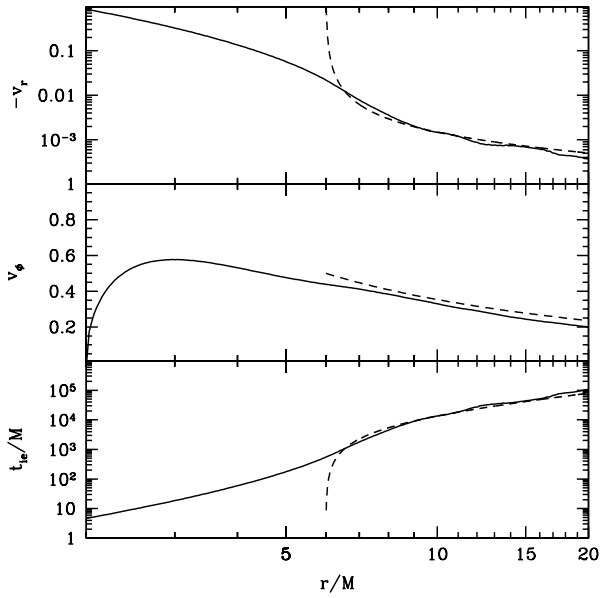

Fig. 2.6.— The time-averaged, angle-averaged, rest-mass density-weighted 3-velocities and viscous timescale in the fiducial model (A0HR07) are compared with the NT model. Angle-averaging is performed over the disk gas lying within $\pm 2|h/r|$ of the midplane. Top Panel: The orthonormal radial 3-velocity (solid line), and the analytical GR estimate given in Eq. 2.53 of Appendix 2.B (dashed line). Agreement for $r > r_{\rm ISCO}$ between the simulation and NT model is found when we set $\alpha|h/r|^2 \approx 0.00033$. At smaller radii, the gas dynamics is no longer determined by viscosity and hence the two curves deviate. Middle Panel: Shows the orthonormal azimuthal 3-velocity v_ϕ (solid line) and the corresponding Keplerian 3-velocity (dashed line). Bottom Panel: The inflow equilibrium time scale $t_{\rm ie} \sim -2r/v_r$ (solid line) of the disk gas is compared to the analytical GR thin disk estimate (dashed line). At $r \sim 9M$, we see that $t_{\rm ie} \sim 2 \times 10^4 M$. Therefore, the simulation needs to be run for this time period (which we do) before we can reach inflow equilibrium at this radius.

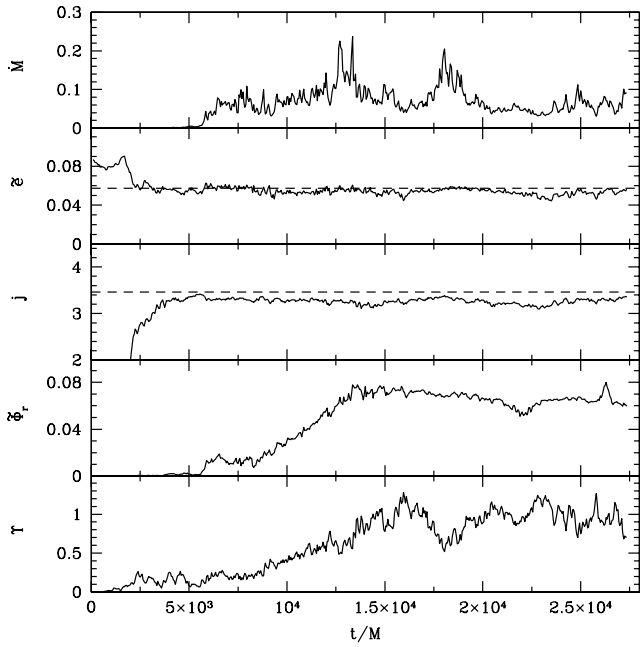

Fig. 2.7.— Shows for the fiducial model (A0HR07) the time-dependence at the horizon of the mass accretion rate, $\dot{M}$ (top panel); nominal efficiency, $\tilde{e}$, with dashed line showing the NT value (next panel); accreted specific angular momentum, $\jmath$, with dashed line showing the NT value (next panel); absolute magnetic flux relative to the initial absolute magnetic flux, $\tilde{\Phi}_r$ (next panel); and dimensionless specific magnetic flux, Υ (bottom panel). All quantities have been integrated over all angles. The mass accretion rate varies by factors of up to four during the quasi-steady state phase. The nominal efficiency is close to, but on average slightly lower than, the NT value. This means that the net energy loss through photons, winds, and jets is below the radiative efficiency of the NT model. The specific angular momentum is clearly lower than the NT value, which implies that some stresses are present inside the ISCO. The absolute magnetic flux at the black hole horizon grows until it saturates due to local force-balance. The specific magnetic flux $\Upsilon \lesssim 1$, indicating that electromagnetic stresses inside the ISCO are weak and cause less than 7% deviations from NT in $\jmath$.

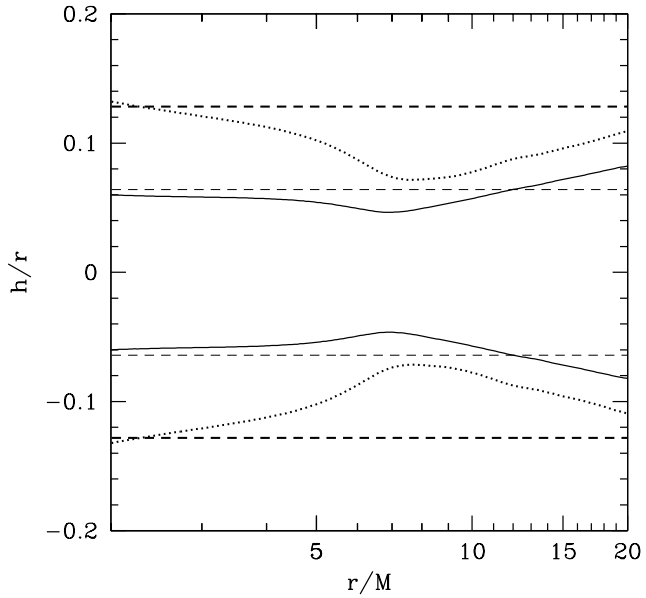

Fig. 2.8.— The time-averaged scale-height, $|h/r|$, vs. radius in the fiducial model (A0HR07) is shown by the solid lines. The above-equator and below-equator values of the disk thickness are $|h/r| \sim 0.04$–0.06 in the inflow equilibrium region $r < 9M$. We use the specific value of $|h/r| = 0.064$ as measured at $r = 2r_{\rm ISCO}$ (light dashed lines) as a representative thickness for the entire flow. Twice this representative thickness (thick dashed lines) is used to fix the θ range of integration for averaging when we wish to focus only on the gas in the disk instead of the gas in the corona-wind-jet. The root mean square thickness $(h/r)_{\rm rms} \sim 0.07$–$0.13$ is shown by the dotted lines.

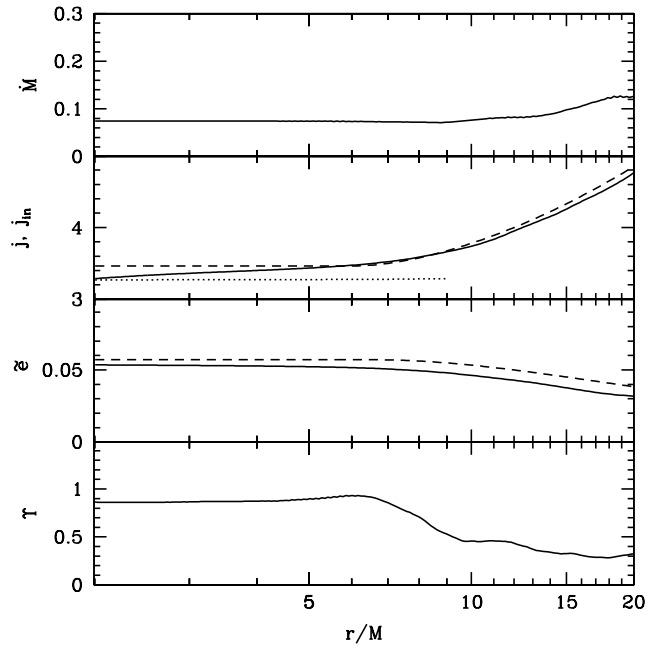

Fig. 2.9.— Mass accretion rate and specific fluxes are shown as a function of radius for the fiducial model (A0HR07). From top to bottom the panels show: Top Panel: mass accretion rate; Second Panel: the accreted specific angular momentum, $\jmath$ (dotted line), $\jmath_{\rm in}$ (solid line), and the NT profile (dashed line); Third Panel: the nominal efficiency $\tilde{e}$ (solid line) and the NT profile (dashed line); Bottom Panel: the specific magnetic flux Υ. For all quantities the integration range includes all θ. The mass accretion rate and $\jmath$ are roughly constant out to $r \sim 9M$, as we would expect for inflow equilibrium. The profile of $\jmath_{\rm in}$ lies below the NT value at large radii because we include gas in the slowly rotating corona. At the horizon, $\jmath$ and $\tilde{e}$ are modestly below the corresponding NT values. The quantity $\Upsilon \sim 0.86$ and is roughly constant out to $r \sim 6M$, indicating that electromagnetic stresses are weak inside the ISCO.

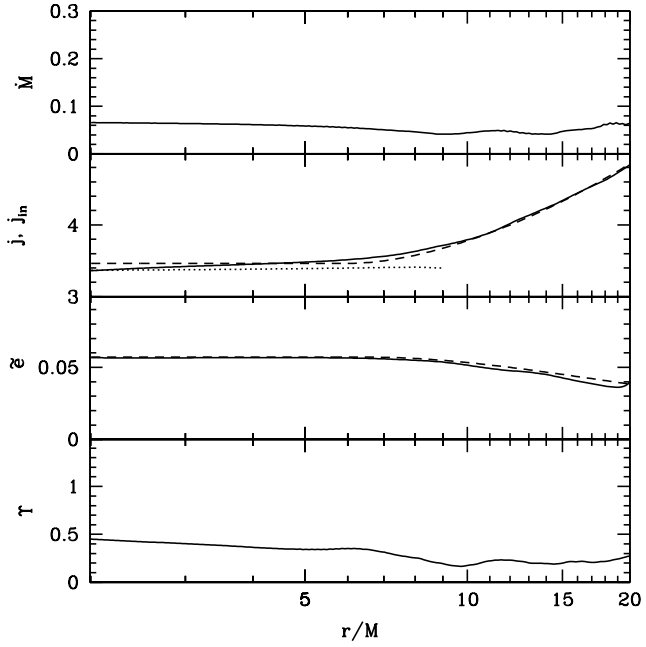

Fig. 2.10.— Similar to Figure 2.9, but here the integration range only includes angles within $\pm 2|h/r| = \pm 0.128$ radians of the midplane. This allows us to focus on the disk gas. The mass accretion rate is no longer constant because streamlines are not precisely radial. The quantities shown in the second and third panels are not affected by the non-constancy of $\dot{M}$ because they are ratios of time-averaged fluxes within the equatorial region and are related to ideal MHD invariants. As compared to Figure 2.9, here we find that $\jmath$, $\jmath_{\rm in}$, and $\tilde{e}$ closely follow the NT model. For example, $\jmath(r_{\rm H}) = 3.363$ is only 2.9% less than NT. This indicates that the disk and coronal regions behave quite differently. As one might expect, the disk region behaves like the NT model, while the corona-wind-jet does not. The specific magnetic flux is even smaller than in Figure 2.9 and is $\Upsilon \sim 0.45$, which indicates that electromagnetic stresses are quite weak inside the disk near the midplane.

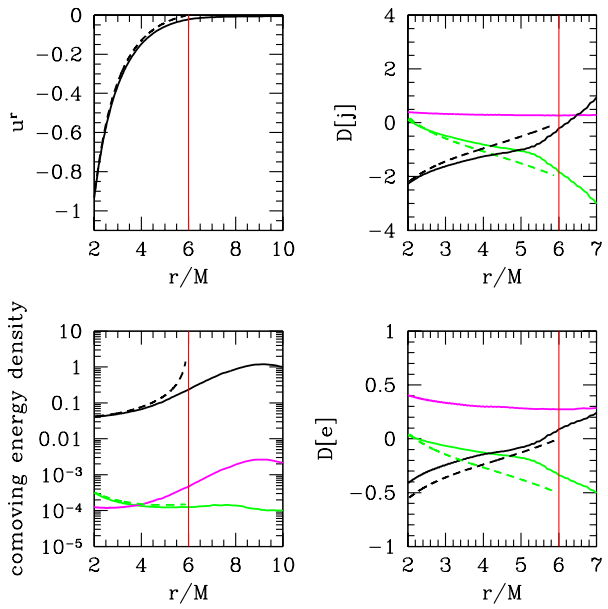

Fig. 2.11.— Comparison between the accretion flow (within $\pm 2|h/r|$ around the midplane) in the fiducial model (A0HR07), shown by solid lines, and the model of a magnetized thin accretion disk (inflow solution) within the ISCO by Gammie (1999), shown by dashed lines. In all cases the red vertical line shows the location of the ISCO. Top-left panel: Shows the radial 4-velocity, where the Gammie solution assumes $u^r = 0$ at the ISCO. Finite thermal effects lead to non-zero u^r at the ISCO for the simulated disk. Bottom-left panel: Shows the rest-mass density (ρ_0, black line), the internal energy density (u_g, magenta line), and magnetic energy density ($b^2/2$, green line). Top-right and bottom-right panels: Show the percent deviations from NT for the simulations and Gammie solution for the specific particle kinetic flux (u_μ, black line), specific enthalpy flux ($(u_g + p_g)u_\mu/\rho_0$, magenta line), and specific electromagnetic flux ($(b^2 u^r u_\mu - b^r b_\mu)/(\rho_0 u^r)$, green line), where for $\jmath$ we use $\mu = \phi$ and for e we use $\mu = t$. As usual, the simulation result for the specific fluxes is obtained by a ratio of flux integrals instead of the direct ratio of flux densities. The total specific flux is constant vs. radius and is a sum of the particle, enthalpy, and electromagnetic terms. This figure is comparable to Fig. 10 for a thick ($|h/r| \sim 0.2$–0.25) disk in McKinney & Gammie (2004). Finite thermal pressure effects cause the fiducial model to deviate from the inflow solution near the ISCO, but the solutions rapidly converge inside the ISCO and the differences between the simulation result and the Gammie model (relative to the total specific angular momentum or energy) are less than 0.5%.

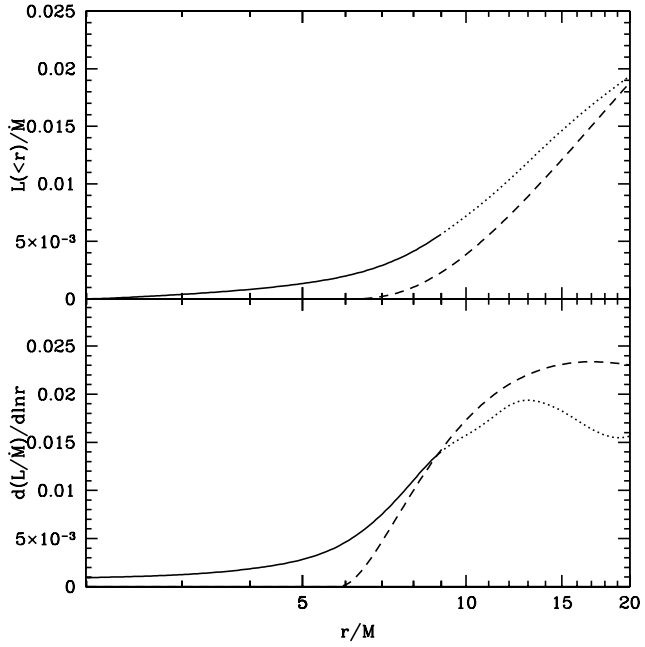

Fig. 2.12.— Luminosity per unit rest-mass accretion rate vs. radius (top panel) and the logarithmic derivative of this quantity (bottom panel) are shown for the fiducial model (A0HR07). The integration includes all θ angles. The simulation result (solid lines, truncated into dotted lines outside the radius of inflow equilibrium) shows that the accretion flow emits more radiation than the NT prediction (dashed lines) at small radii. However, the excess luminosity within the ISCO is only $\tilde{L}_{\rm in} \approx 3.5\%$, where $\tilde{e}$[NT] is the NT efficiency at the horizon (or equivalently at the ISCO).

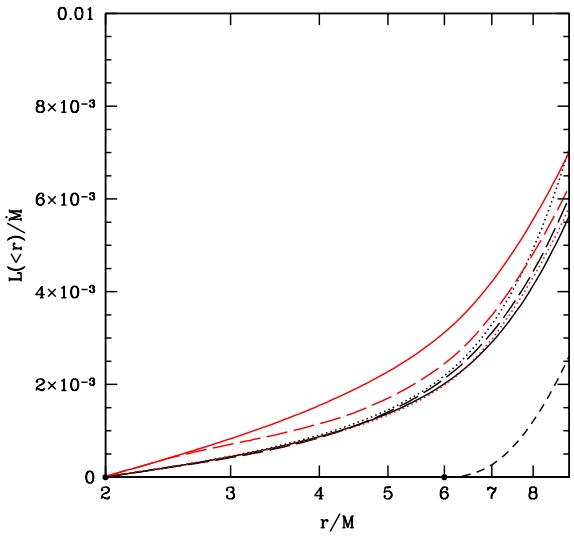

Fig. 2.13.— Shows enclosed luminosity vs. radius for models with different cooling prescriptions and θ integration ranges. The black dashed line corresponds to the NT model. The luminosity for the fiducial model A0HR07, which includes a tapering of the cooling with disk height as described in §2.2, is shown integrated over $\pm 2|h/r|$ from the midplane (black dotted line), integrated over all bound gas (black long dashed line), and integrated over all fluid (black solid line). Essentially all the gas is bound and so the black solid and long dashed lines are indistinguishable. The red lines are for a model that is identical to the fiducial run, except that no tapering is applied to the cooling. For this model the lines are: red solid line: all angles, all fluid; red dotted line: $\pm 2|h/r|$ around the midplane; red long dashed line: all bound gas. The main result is that the luminosity from bound gas is nearly the same (especially at the ISCO) whether or not we include tapering (compare the red long dashed line and the black long dashed line).

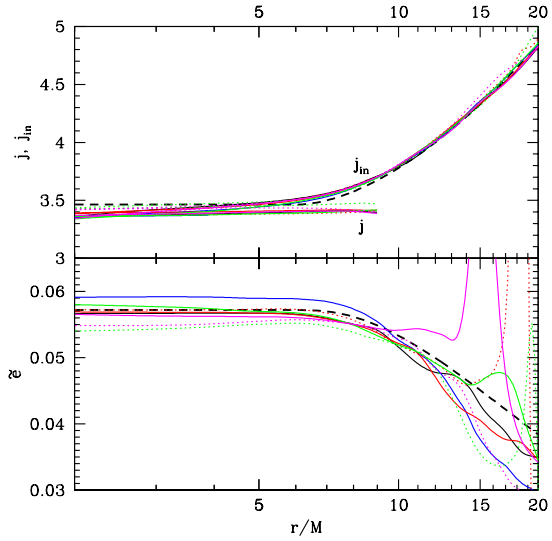

Fig. 2.14.— This plot shows $\jmath$, $\jmath_{\rm in}$, and $\tilde{e}$ for a sequence of simulations that are similar to the fiducial run (A0HR07), viz., $|h/r| \approx 0.07$, $a/M = 0$, but use different radial resolutions, or θ resolutions, or box sizes. The integration range in θ is over $\pm 2|h/r|$ around the midplane. Only the region of the flow in inflow equilibrium, $2M < r < 9M$, is shown in the case of $\jmath$. The different lines are as follows: black dashed line: NT model; black solid line: fiducial model A0HR07; blue solid line: model C0 (S08); magenta dotted line: model C1; magenta solid line: model C2; red dotted line: model C3; red solid line: model C4; green dotted line: model C5; green solid line: model C6. Note that changes in the numerical resolution or other computational parameters lead to negligible changes in the values of $\jmath$, $\jmath_{\rm in}$, and $\tilde{e}$ in the region of the flow that is in inflow equilibrium, $r < 9M$. For $r \gtrsim 9M$, the flow has not achieved steady state, which explains the large deviations in $\tilde{e}$. Only the lowest resolution models are outliers.

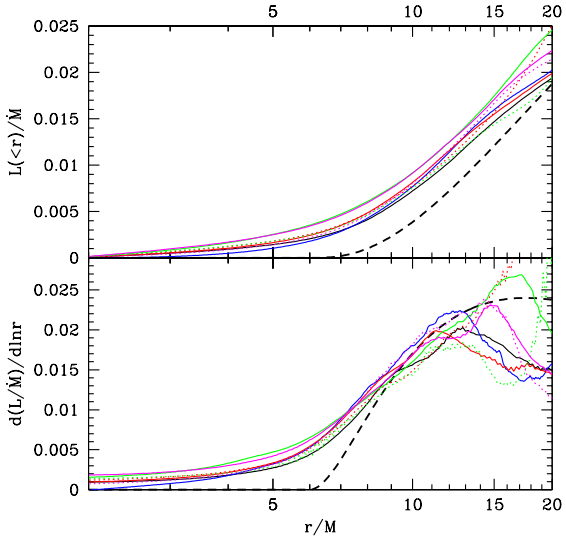

Fig. 2.15.— Similar to Figure 2.14, but for the normalized luminosity, $L(< r)/\dot{M}$, and its logarithmic derivative, $d(L/\dot{M})/d\ln r$, both shown vs. radius. We see that all the models used to test convergence show consistent luminosity profiles over the region that is in inflow equilibrium, $r < 9M$. The well-converged models have $\tilde{L}_{\rm in} \lesssim 4\%$, which indicates only a low level of luminosity inside the ISCO.

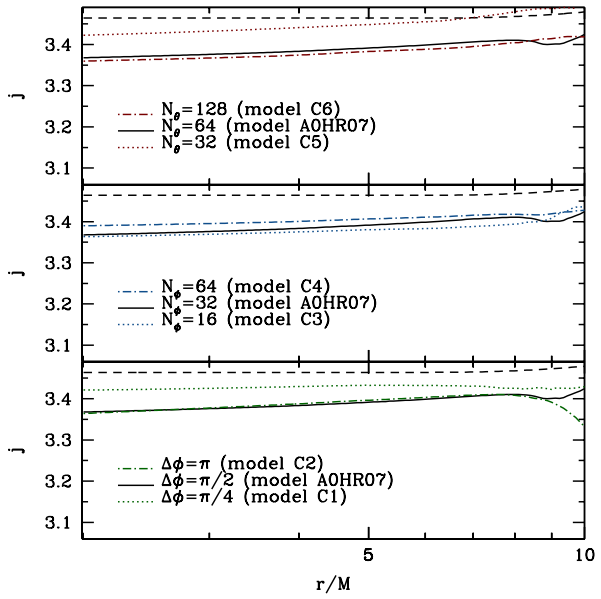

Fig. 2.16.— This is a more detailed version of Figure 2.14, showing j vs r for individually labeled models. The models correspond to the fiducial resolution (solid lines), a higher resolution run (dot-dashed lines), and a lower resolution run (dotted lines). Generally, there are only minor differences between the fiducial and higher resolution models.

Table 2.3: Convergence Study

Model Name	$\lvert h/r\rvert$	$\dot{M}$	$\tilde{e}$	$D[\tilde{e}]$	$\jmath$	$D[\jmath]$	$\jmath_{\rm in}$	$D[\jmath_{\rm in}]$	s	$\tilde{L}_{\rm in}$	$\tilde{L}_{\rm eq}$	$100\tilde{\Phi}_r$	Υ
$\underline{\pm 2\lvert h/r\rvert}$													
A0HR07	0.064	0.066	0.058	-0.829	3.363	-2.913	3.355	-3.153	3.363	0.035	0.080	1.355	0.450
C0	0.052	0.064	0.059	-2.708	3.363	-2.905	3.351	-3.259	3.363	0.019	0.042	0.399	0.359
C1	0.063	0.041	0.056	2.204	3.415	-1.406	3.408	-1.621	3.415	0.034	0.072	0.584	0.223
C2	0.062	0.063	0.058	-0.699	3.360	-3.016	3.333	-3.789	3.360	0.047	0.109	0.925	0.323
C3	0.061	0.026	0.058	-1.969	3.358	-3.060	3.339	-3.610	3.358	0.039	0.087	0.727	0.449
C4	0.061	0.054	0.058	-1.406	3.385	-2.286	3.378	-2.489	3.385	0.019	0.018	0.714	0.296
C5	0.052	0.008	0.055	3.955	3.417	-1.364	3.427	-1.067	3.417	0.034	0.070	0.315	0.322
C6	0.065	0.088	0.059	-3.355	3.355	-3.155	3.333	-3.778	3.355	0.054	0.103	0.933	0.256
$\underline{\text{All } \theta}$													
A0HR07	0.064	0.074	0.054	4.723	3.266	-5.717	3.281	-5.275	3.266	0.035	0.053	6.677	0.863
C0	0.052	0.071	0.057	0.738	3.312	-4.392	3.291	-5.002	3.312	0.032	0.049	2.18	0.480
C1	0.063	0.042	0.055	3.680	3.398	-1.894	3.389	-2.178	3.398	0.037	0.062	0.940	0.142
C2	0.062	0.069	0.056	1.664	3.307	-4.541	3.262	-5.846	3.307	0.053	0.080	5.757	0.710
C3	0.061	0.029	0.057	0.893	3.325	-4.008	3.305	-4.580	3.325	0.042	0.064	1.401	0.309
C4	0.061	0.057	0.057	0.811	3.358	-3.075	3.351	-3.255	3.358	0.020	0.009	2.690	0.359
C5	0.052	0.009	0.053	7.687	3.338	-3.636	3.353	-3.218	3.338	0.039	0.059	0.726	0.243
C6	0.065	0.092	0.058	-1.813	3.334	-3.761	3.306	-4.560	3.334	0.057	0.086	5.091	0.534

The fiducial model described earlier was computed with a numerical resolution of $256 \times 64 \times 32$, using an azimuthal wedge of $\pi/2$. This is to be compared with the simulation described in S08, which made use of a $512 \times 128 \times 32$ grid and used a $\pi/4$ wedge. These two runs give very similar results, suggesting that the details of the resolution and wedge size are not very important. To confirm this, we have run a number of simulations with different resolutions and wedge angles. The complete list of runs is: $256 \times 64 \times 32$ with $\Delta\phi = \pi/2$ (fiducial run, model A0HR07)), $512 \times 128 \times 32$ with $\Delta\phi = \pi/4$ (S08, model C0), $256 \times 128 \times 32$ with $\Delta\phi = \pi/2$ (model C6), $256 \times 32 \times 32$ with $\Delta\phi = \pi/2$ (model C5), $256 \times 64 \times 64$ with $\Delta\phi = \pi/2$ (model C4), $256 \times 64 \times 64$ with $\Delta\phi = \pi$ (model C2), $256 \times 64 \times 16$ with $\Delta\phi = \pi/2$ (model C3), and $256 \times 64 \times 16$ with $\Delta\phi = \pi/4$ (model C1).

Figure 2.14 shows the accreted specific angular momentum, $\jmath$, ingoing component of the specific angular momentum, $\jmath_{\rm in}$, and the nominal efficiency $\tilde{e}$ as functions of radius for all the models used for convergence testing. Figure 2.15 similarly shows the cumulative luminosity $L(<r)/\dot{M}$ and differential luminosity $d(L/\dot{M})/d\ln r$ as functions of radius. The overwhelming impression from these plots is that the sequence of convergence simulations agree with one another quite well. Also, the average of all the runs matches the NT model very well; this is especially true for the steady-state region of the flow, $r < 9M$. Thus, qualitatively, we conclude that our results are well-converged.

For more quantitative comparison, Figure 2.16 shows the profile of $\jmath$ vs r for the various models, this time with each model separately identified. It is clear that $\jmath$ has converged, since there are very minor deviations from our highest resolution/largest box size to our next highest resolution/next largest box size. All other quantities, including $\tilde{e}$, $\jmath_{\rm in}$, and Υ are similarly converged. The model with $N_\phi = 64$ shows slightly *less* deviations from NT in $\jmath$ than our other models. However, it also shows slightly higher luminosity than our other models. This behavior is likely due to the stochastic temporal behavior of all quantities vs. time, but this could also be due to the higher ϕ-resolution causing a weaker ordered magnetic field to be present leading to weaker ideal electromagnetic stresses, smaller deviations from NT in $\jmath$ within the ISCO, but with the remaining turbulent field being dissipated giving a higher luminosity. The N_ϕ resolution appears to be the limit on our accuracy.

Further quantitative details are given in Table 2.3, where we list numerical results for all the convergence test models, with the θ integration performed over both $\pm 2|h/r|$ around the midplane and over all angles. We see that there are some trends as a function of resolution and/or $\Delta\phi$. Having only 32 cells in θ or 16 cells in ϕ gives somewhat poor results, so these runs are under-resolved. However, even for these runs, the differences are not large. Note that Υ reaches a steady-state much later than all other quantities, and our C? (where ? is 0 through 6) models did not run as long as the fiducial model. This explains why Υ is a bit lower for the C? models. Overall, we conclude that our choice of resolution $256 \times 64 \times 32$ for the fiducial run (A0HR07) is adequate to reach convergence.

2.7 Dependence on black hole spin and disk thickness

In addition to the fiducial model and the convergence runs described in previous sections, we have run a number of other simulations to explore the effect of the black hole spin parameter a/M and the disk thickness $|h/r|$ on our various diagnostics: $\jmath$, $\jmath_{\rm in}$, $\tilde{e}$, the luminosity, and Υ. We consider four values of the black hole spin parameter, viz., $a/M = 0,\ 0.7,\ 0.9,\ 0.98$, and four disk thicknesses, viz., $|h/r| = 0.07,\ 0.1,\ 0.2,\ 0.3$. We summarize here our results for this 4×4 grid of models.

Geometrically thick disks are expected on quite general grounds to deviate from the standard thin disk model. The inner edge of the disk, as measured for instance by the location of the sonic point, is expected to deviate from the ISCO, the shift scaling roughly as $|r_{\rm in} - r_{\rm ISCO}| \propto (c_{\rm s}/v_{\rm K})^2$ ($c_{\rm s}$ is sound speed, where $c_{\rm s}^2 = \Gamma p_g/(\rho_0 + u_g + p_g)$). This effect is seen in hydrodynamic models of thick disks, e.g. Narayan et al. (1997) and Abramowicz et al. (2010), where it is shown that $r_{\rm in}$ can move either inside or outside the ISCO; it moves inside when α is small and outside when α is large. In either case, these hydrodynamic models clearly show that, as $|h/r| \to 0$, i.e., as $c_{\rm s}/v_{\rm K} \to 0$, the solution always tends toward the NT model (Shafee et al. 2008b).

While the hydrodynamic studies mentioned above have driven much of our intuition on the behavior of thick and thin disks, it is an open question whether or not the magnetic field plays a significant role. In principle, magnetic effects may cause the solution to deviate significantly from

the NT model even in the limit $|h/r| \to 0$ (Krolik 1999; Gammie 1999). One of the major goals of the present chapter is to investigate this question. We show in this section that, as $|h/r| \to 0$, magnetized disks do tend toward the NT model. This statement appears to be true for a range of black hole spins. We also show that the specific magnetic flux Υ inside the ISCO decreases with decreasing $|h/r|$ and remains quite small. This explains why the magnetic field does not cause significant deviations from NT in thin disks.

Figure 2.17 shows the specific angular momentum, $\jmath$, and the ingoing component of this quantity, $\jmath_{\rm in}$, vs. radius for the 4×4 grid of models. The θ integral has been taken over $\pm 2|h/r|$ around the midplane in order to focus on the equatorial disk properties. The value of $\jmath$ is roughly constant out to a radius well outside the ISCO, indicating that we have converged solutions in inflow equilibrium extending over a useful range of radius. As discussed in section 2.3.5, inflow equilibrium is expected within $r/M = 9,\ 7,\ 5.5,\ 5$, respectively, for $a/M = 0,\ 0.7,\ 0.9,\ 0.98$. This is roughly consistent with the radius out to which the quantity $\jmath$ (integrated over all angles) is constant, and this motivates why in all such plots we only show $\jmath$ over the region where the flow is in inflow equilibrium. The four panels in Figure 2.17 show a clear trend, viz., deviations from NT are larger for thicker disks, as expected. Interestingly, for higher black hole spins, the relative deviations from NT actually decrease.

Figure 2.18 shows the nominal efficiency, $\tilde{e}$, as a function of radius for the 4×4 grid of models. Our thickest disk models ($|h/r| \approx 0.3$) do not include cooling, so the efficiency shown is only due to losses by a wind-jet. We see that the efficiency is fairly close to the NT value for all four thin disk simulations with $|h/r| \sim 0.07$; even in the worst case, viz., $a/M = 0.98$, the deviation from NT is only $\sim 5\%$. In the case of thicker disks, the efficiency shows larger deviations from NT and the profile as a function of radius also looks different. For models with $|h/r| \approx 0.3$, there is no cooling so large deviations are expected.

Figure 2.19 shows the luminosity, $L(< r)/\dot{M}$, vs. radius for our 4×4 grid of models, focusing just on the region that has reached inflow equilibrium. The luminosity is estimated by integrating over all θ angles. Our thickest disk models ($|h/r| \approx 0.3$) do not include cooling and so are not plotted. The various panels show that, as $|h/r| \to 0$, the luminosity becomes progressively closer to

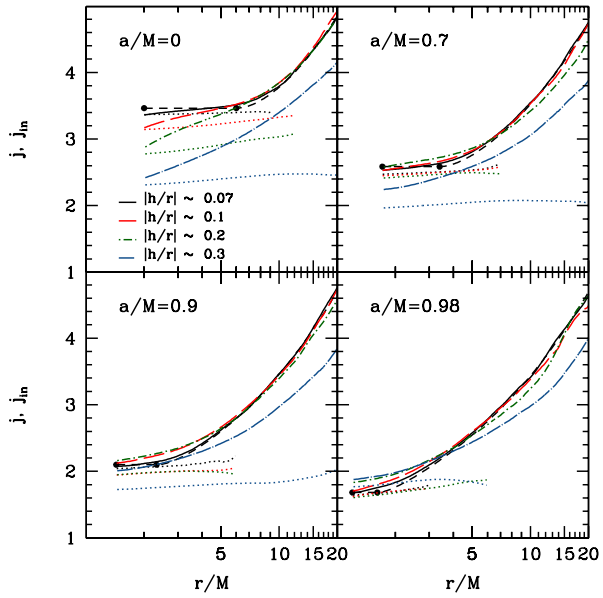

Fig. 2.17.— The net accreted specific angular momentum, $\jmath$ (the nearly horizontal dotted lines), and the ingoing component of this quantity, $\jmath_{\rm in}$ (the sloping curved lines), as a function of radius for the 4×4 grid of models. Each panel corresponds to a single black hole spin, $a/M = 0,\ 0.7,\ 0.9,$ or 0.98, and shows models with four disk thicknesses, $|h/r| \approx 0.07,\ 0.1,\ 0.2,\ 0.3$ (see legend). The θ integral has been taken over $\pm 2|h/r|$ around the midplane. In each panel, the thin dashed black line, marked by two circles which indicate the location of the horizon and the ISCO, shows the NT solution for $\jmath_{\rm in}$. As expected, we see that thicker disks exhibit larger deviations from NT. However, as a function of spin, there is no indication that deviations from NT become any larger for larger spins. In the case of the thinnest models with $|h/r| \approx 0.07$, the NT model works well for gas close to the midplane for all spins.

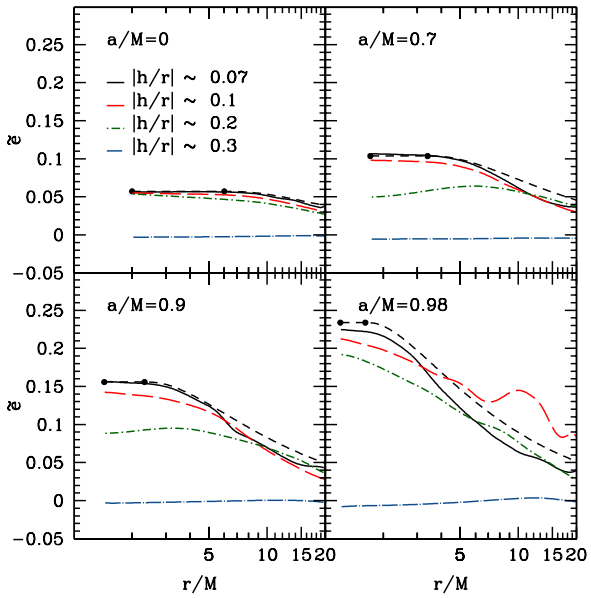

Fig. 2.18.— Similar to Figure 2.17, but for the nominal efficiency, $\tilde{e}$. For thin ($|h/r| \lesssim 0.1$) disks, the results are close to NT for all black hole spins. As expected, the thicker models deviate significantly from NT. In part this is because the ad hoc cooling function we use in the simulations is less accurate for thick disks, and in part because the models with $|h/r| \approx 0.3$ have no cooling and start with marginally bound/unbound gas that implies $\tilde{e} \sim 0$. The $a/M = 0.98$ models show erratic behavior at large radii where the flow has not achieved inflow equilibrium.

the NT result in the steady state region of the flow near and inside the ISCO. Thus, once again, we conclude that the NT luminosity profile is valid for geometrically thin disks even when the accreting gas is magnetized.

A figure (not shown) that is similar to Figure 2.17 but for the specific magnetic flux indicates that $\Upsilon \leq 1$ within $\pm 2|h/r|$ near the ISCO for all black hole spins and disk thicknesses. For our thinnest models, $\Upsilon \leq 0.45$, for which the model of Gammie (1999) predicts that the specific angular momentum will deviate from NT by less than 1.9%, 3.0%, 3.8%, 4.2% for black hole spins $a/M = 0,\ 0.7,\ 0.9,\ 0.98$, respectively (see Appendix 2.A). The numerical results from the simulations show deviations from NT that are similar to these values. Thus, overall, our results indicate that electromagnetic stresses are weak inside the ISCO for geometrically thin disks.

Finally, for all models we look at plots (not shown) of $M(< r)$ (mass enclosed within radius), $\dot{M}(r)$ (total mass accretion rate vs. radius), and $[h/r](r)$ (disk scale-height vs. radius). We find that these are consistently flat to the same degree and to the same radius as the quantity $\jmath(r)$ is constant as shown in Figure 2.17. This further indicates that our models are in inflow equilibrium out to the expected radius.

2.7.1 Scaling laws vs. a/M and $|h/r|$

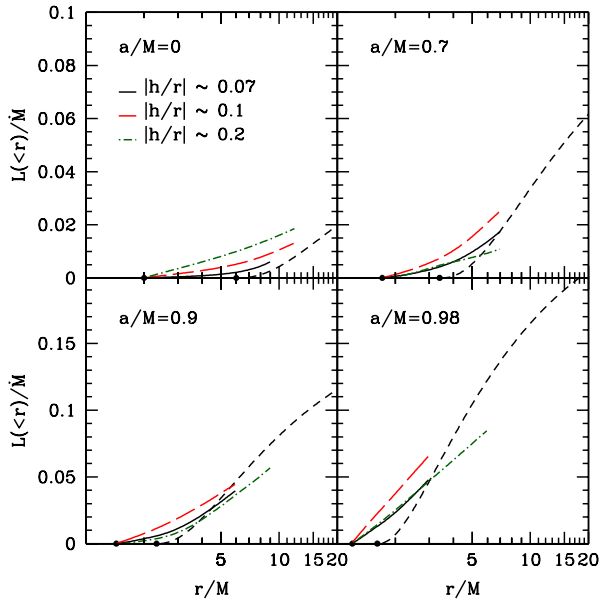

Fig. 2.19.— Similar to Figure 2.17, but for the normalized luminosity, $L(< r)/\dot{M}$. For thin disks, the luminosity deviates only slightly from NT near and inside the ISCO. There is no strong evidence for any dependence on the black hole spin. The region at large radii has not reached inflow equilibrium and is not shown.

Table 2.4: Black Hole Spin and Disk Thickness Study

Model Name	$\lvert h/r\rvert$	$\dot{M}$	$\tilde{e}$	$D[\tilde{e}]$	j	$D[j]$	$j_{\rm in}$	$D[j_{\rm in}]$	s	$\tilde{L}_{\rm in}$	$\tilde{L}_{\rm eq}$	$100\tilde{\Phi}_r$	Υ
$\underline{\pm 2\lvert h/r\rvert}$													
A0HR07	0.064	0.066	0.058	-0.829	3.363	-2.913	3.355	-3.153	3.363	0.035	0.080	1.355	0.450
A7HR07	0.065	0.050	0.107	-2.899	2.471	-4.465	2.527	-2.294	1.220	0.048	0.084	0.919	0.393
A9HR07	0.054	0.045	0.156	-0.157	2.042	-2.762	2.074	-1.213	0.523	0.041	0.082	0.455	0.218
A98HR07	0.059	0.013	0.225	3.897	1.643	-2.335	1.679	-0.199	0.124	0.069	0.127	0.276	0.228
A0HR1	0.12	4.973	0.056	1.470	3.138	-9.424	3.162	-8.724	3.138	0.084	0.134	2.976	0.871
A7HR1	0.09	2.443	0.099	4.808	2.446	-5.447	2.524	-2.409	1.184	0.060	0.108	0.909	0.406
A9HR1	0.13	2.133	0.142	9.014	1.947	-7.261	2.124	1.157	0.402	0.068	0.107	1.064	0.466
A98HR1	0.099	2.372	0.213	8.810	1.626	-3.393	1.703	1.200	0.084	0.062	0.112	0.451	0.254
A0HR2	0.18	48.286	0.055	4.134	2.774	-19.916	2.872	-17.098	2.774	0.167	0.235	2.518	1.235
A7HR2	0.16	31.665	0.049	52.330	2.412	-6.736	2.576	-0.425	1.081	0.050	0.034	0.919	0.631
A9HR2	0.21	40.603	0.090	41.922	1.946	-7.315	2.155	2.624	0.309	0.011	-0.026	0.795	0.557
A98HR2	0.18	29.410	0.191	18.496	1.588	-5.650	1.870	11.117	0.001	0.052	0.068	0.651	0.459
A0HR3	0.350	44.066	-0.003	104.582	2.309	-33.331	2.408	-30.473	2.309	0.000	-0.049	3.039	1.182
A7HR3	0.34	41.045	-0.007	106.384	1.967	-23.970	2.236	-13.549	0.557	0.000	-0.060	1.956	0.746
A9HR3	0.341	35.852	-0.001	100.582	1.722	-17.999	1.998	-4.832	-0.080	0.000	-0.073	1.437	0.543
A98HR3	0.307	24.486	-0.015	106.206	1.783	5.987	1.886	12.102	-0.205	0.000	-0.104	0.369	0.246

We now consider how the magnitude of $\jmath$, $\tilde{e}$, $L(< r_{\rm ISCO})$, and Υ scale with disk thickness and black hole spin. Table 2.4 lists numerical results corresponding to θ integrations over $\pm 2|h/r|$ around the midplane and over all angles[10]. Figure 2.20 shows selected results corresponding to models with a non-rotating black hole for quantities integrated over $\pm 2|h/r|$. We see that the deviations of various diagnostics from the NT values scale roughly as $|h/r|$. In general, the deviations are quite small for the thinnest model with $|h/r| \approx 0.07$.

Next, we consider fits of our simulation data as a function of black hole spin and disk thickness to reveal if, at all, these two parameters control how much the flow deviates from NT. In some cases we directly fit the simulation results instead of their deviations from NT, since for thick disks the actual measurement values can saturate independent of thickness leading to large non-linear deviations from NT. Before making the fits, we ask how quantities might scale with a/M and $|h/r|$. With no disk present, the rotational symmetry forces any scaling to be an even power of black hole spin (McKinney & Gammie 2004). However, the presence of a rotating disk breaks this symmetry, and any accretion flow properties, such as deviations from NT's model, could depend linearly upon a/M (at least for small spins). This motivates performing a linear fit in a/M. Similarly, the thickness relates to a dimensionless speed: $c_{\rm s}/v_{\rm K} \sim |h/r|$, while there are several different speeds in the accretion problem that could force quantities to have an arbitrary dependence on $|h/r|$. Although, in principle, deviations might scale as some power of $|h/r|$, we assume here a linear scaling $\propto |h/r|$. This choice is driven partly by simplicity and partly by Figure 2.20 which shows that the simulation results agree well with this scaling.

These rough arguments motivate obtaining explicit scaling laws for a quantity's deviations from NT as a function of a/M and $|h/r|$. For all quantities we use the full 4×4 set of models, except for the luminosity and efficiency we exclude the two thickest models in order to focus on the luminosity for thin disks with cooling. We perform a linear least squares fit in both a/M and $|h/r|$, and we report the absolute percent difference between the upper 95% confidence limit (C_+) and the best-fit parameter value (f) given by $E = 100|C_+ - f|/|f|$. Note that if $E > 100\%$, then the

[10]Some thicker disk models without cooling show small or slightly negative efficiencies, $\tilde{e}$, which signifies the accretion of weakly unbound gas. This can occur when a magnetic field is inserted into a weakly bound gas in hydrostatic equilibrium.

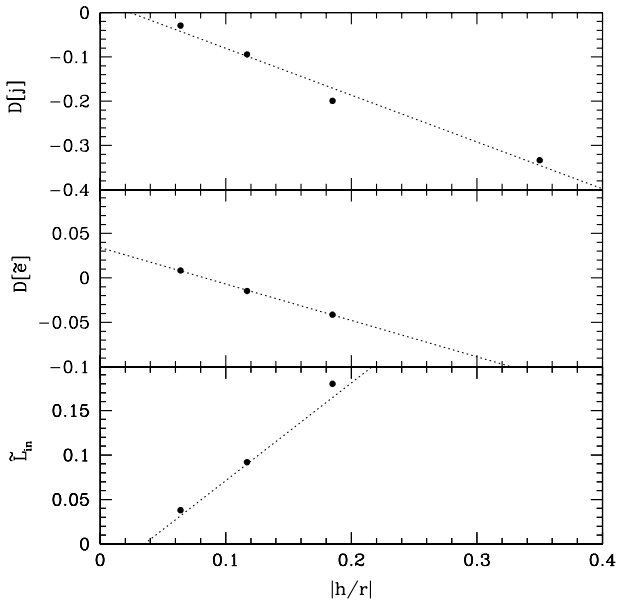

Fig. 2.20.— The relative difference between $\jmath$ in the simulation and in the NT model (top panel), the relative difference between the nominal efficiency, $\tilde{e}$, and the NT value (middle panel), and the luminosity inside the ISCO normalized by the net radiative efficiency of the NT model, $\tilde{L}_{\rm in}$ (bottom panel), where $\tilde{e}$[NT] has been evaluated at the horizon (equivalently at the ISCO). There is a rough linear dependence on $|h/r|$ for all quantities, where a linear fit is shown as a dotted line in each panel. Note that the thicker disk models are not expected to behave like NT, and actually have $\jmath$ roughly similar across all spins. For $|h/r| \approx 0.07$, the excess luminosity from within the ISCO is less than 4% of the total NT efficiency.

best-fit value is no different from zero to 95% confidence (such parameter values are not reported). After the linear fit is provided, the value of E is given for each parameter in order of appearance in the fit. Only the statistically significant digits are shown.

First, we consider how electromagnetic stresses depend upon a/M and $|h/r|$. Gammie (1999) has shown that the effects of electromagnetic stresses are tied to the specific magnetic flux, Υ, and that for $\Upsilon \lesssim 1$ there are weak electromagnetic stresses causing only minor deviations (less than 12% for $\jmath$ across all black hole spins) from NT. Let us consider how Υ should scale with $|h/r|$, where $\Upsilon = \sqrt{2}(r/M)^2 B^r / \left(\sqrt{-(r/M)^2 \rho_0 u^r}\right)$ in the equatorial plane and is assumed to be constant from the ISCO to the horizon. For simplicity, let us study the case of a rapidly rotating black hole. First, consider the boundary conditions near the ISCO provided by the disk, where $c_{\rm s}/v_{\rm K} \sim |h/r|$ and the Keplerian rotation speed reaches $v_{\rm K} \sim 0.5$. This implies $c_{\rm s} \sim 0.5|h/r|$. Second, consider the flow that connects the ISCO and the horizon. The gas in the disk beyond the ISCO has $\beta \sim (c_{\rm s}/v_{\rm A})^2 \sim 10$, but reaches $\beta \sim 1$ inside the ISCO in any GRMHD simulations of turbulent magnetized disks, which gives that $c_{\rm s} \sim v_{\rm A}$. Thus, $v_{\rm A} \sim 0.5|h/r|$. Finally, notice that $\Upsilon \sim 1.4 B^r/\sqrt{\rho_0}$ at the horizon where $u^r \sim -1$ and $r = M$. The Keplerian rotation at the ISCO leads to a magnetic field with orthonormal radial ($|B_r| \sim |B^r|$) and toroidal ($|B_\phi|$) components with similar values near the ISCO and horizon, giving $|B^r| \sim |B_r| \sim |B_\phi| \sim |b|$ and so $\Upsilon \sim 1.4|b|/\sqrt{\rho_0}$. Further, the Alfvén 3-speed is $v_{\rm A} = |b|/\sqrt{b^2 + \rho_0 + u_g + p_g} \sim |b|/\sqrt{\rho_0}$ in any massive disk, so that $\Upsilon \sim 1.4 v_{\rm A} \sim 0.7|h/r|$ for a rapidly rotating black hole. Extending these rough arguments to all black hole spins at fixed disk thickness also gives that $\Upsilon \propto -0.8(a/M)$ for $a/M \lesssim 0.7$. These arguments demonstrate three points: 1) $\Upsilon \gg 1$ gives $b^2/\rho_0 \gg 1$, implying a force-free magnetosphere instead of a massive accretion disk ; 2) $\Upsilon \propto |h/r|$; and 3) $\Upsilon \propto -(a/M)$. Since the local condition for the magnetic field ejecting mass is $b^2/\rho_0 \gg 1$ (see, e.g., Komissarov & Barkov 2009), this shows that $\Upsilon \sim 1$ defines a boundary that the disk component of the flow cannot significantly pass beyond without eventually incurring disruption by the strong magnetic field within the disk.

We now obtain the actual fit, which for an integration over $\pm 2|h/r|$ gives

$$\Upsilon \approx 0.7 + \left|\frac{h}{r}\right| - 0.6\frac{a}{M}, \tag{2.37}$$

with $E = 33\%,\ 70\%,\ 40\%$, indicating a reasonable fit. There is essentially 100% confidence in the sign of the 1st and 3rd parameters and 98% confidence in the sign of the 2nd parameter. This fit is consistent with our basic analytical estimate for the scaling. Since most likely $\Upsilon \leq 0.9$ in the limit that $|h/r| \to 0$ across all black hole spins, the electromagnetic stresses are weak and cause less than 12% deviation from NT in $\jmath$, This means that NT solution is essentially recovered for magnetized thin disks. For an integration over all angles, $\Upsilon \approx 1$ with $E = 35\%$, and there is no statistically significant trend with disk thickness or black hole spin. The value of $\Upsilon \sim 1$ is consistent with the presence of the highly-magnetized corona-wind-jet above the disk component (McKinney & Gammie 2004).

Next, we consider whether our simulations can determine the equilibrium value of the black hole spin as a function of $|h/r|$. The spin evolves as the black hole accretes mass, energy, and angular momentum, and it can stop evolving when these come into a certain balance leading to $d(a/M)/dt = 0$ (see equation 2.15). In spin-equilibrium, the spin-up parameter $s = \jmath - 2(a/M)\mathrm{e}$ has $s = 0$ and solving for a gives the equilibrium spin $a_{\rm eq}/M = \jmath/(2\mathrm{e})$. For the NT solution, s is fairly linear for $a/M > 0$ and $a_{\rm eq}/M = 1$. In appendix 2.A, we note that for $\Upsilon \sim 0.2$–1 that the deviations from NT roughly scale as Υ. Since $\Upsilon \propto |h/r|$, one expects s to also roughly scale with $|h/r|$. This implies that deviations from NT in the spin equilibrium should scale as $|h/r|$. Hence, one should have $1 - a_{\rm eq}/M \propto |h/r|$.

Now we obtain the actual fit. We consider two types of fits. In one case, we fit s (with fluxes integrated over all angles) and solve $s = 0$ for $a_{\rm eq}/M$. This gives

$$s \approx 3.2 - 2.5\left|\frac{h}{r}\right| - 2.9\frac{a}{M}, \tag{2.38}$$

with $E = 8\%,\ 36\%,\ 8\%$, indicating quite a good fit. There is an essentially 100% confidence for the sign of all parameters, indicating the presence of well-defined trends. Solving the equation $s = 0$ for a/M shows that the spin equilibrium value, $a_{\rm eq}/M$, is given by

$$1 - \frac{a_{\rm eq}}{M} \approx -0.08 + 0.8\left|\frac{h}{r}\right|. \tag{2.39}$$

In the other case, we fit $\jmath/(2\mathrm{e})$ and re-solve for $a_{\rm eq}/M$, which gives directly

$$1 - \frac{a_{\rm eq}}{M} \approx -0.10 + 0.9\left|\frac{h}{r}\right|, \tag{2.40}$$

with $E = 9\%,\ 38\%$ with a 99.99% confidence in the sign of the $|h/r|$ term. Both of these procedures give a similar fit (the first fit is statistically better) and agree within statistical errors, which indicates a linear fit is reasonable. For either fit, one should set $a_{\rm eq}/M = 1$ when the above formula gives $a_{\rm eq}/M > 1$ to be consistent with our statistical errors and the correct physics. Note that the overshoot $a_{\rm eq}/M > 1$ in the fit is consistent with a linear extrapolation of the NT dependence of s for $a/M > 0$, which also overshoots in the same way due to the progressively non-linear behavior of s above $a/M \approx 0.95$.

These spin equilibrium fits imply that, within our statistical errors, the spin can reach $a_{\rm eq}/M \to 1$ as $|h/r| \to 0$. Thus, our results are consistent with NT by allowing maximal black hole spin for thin disks[11]. Our results are also roughly consistent with the thick disk 1-loop field geometry study by Gammie et al. (2004). Using our definition of disk thickness, their model had $|h/r| \sim 0.2$–0.25 and they found $a_{\rm eq}/M \sim 0.9$, which is roughly consistent with our scaling law. The fit is also consistent with results for even thicker disks ($|h/r| \sim 0.4$ near the horizon) with $a_{\rm eq}/M \sim 0.8$ (Abramowicz et al. 1978; Popham & Gammie 1998).

Overall, the precise scaling relations given for Υ and $a_{\rm eq}$ should be considered as suggestive and preliminary. More work is required to test the convergence and generality of the actual coefficients. While we explicitly tested convergence for the $a/M = 0$ fiducial model, the other a/M were not tested as rigorously. A potential issue is that we find the saturated state has fewer cells per (vertical magnetic field) fastest growing mode for the axisymmetric MRI in models with $a/M = 0.9, 0.98$ than in models with $a/M = 0, 0.7$ due to the relative weakness of the vertical field in the saturated state for the high spin models. However, both the rough analytical arguments and the numerical solutions imply that electromagnetic stresses scale somewhat linearly with black hole spin. This consistency suggests that many measurements for the simulations, such as Υ and $a_{\rm eq}$, may be independent of smallness of the vertical field. This fact could be due to these quantities being only directly related to the radial and toroidal magnetic field strengths rather than the vertical magnetic field strength. Further, our thick disk models resolve the axisymmetric MRI better than

[11]Here, we do not include black hole spin changes by photon capture, which gives a limit of $a_{\rm eq}/M = 0.998$ (Thorne 1974).

the thinnest disk model. This suggests that the scaling of Υ and $a_{\rm eq}$ with disk thickness may be a robust result.

Lastly, we consider how the specific angular momentum, nominal efficiency, and luminosity from within the ISCO deviate from NT as functions of spin and thickness. Overall, fitting these quantities does not give very strong constraints on the actual parameter values, but we can state the confidence level of any trends. For each of $\tilde{e}$, $\jmath$, $\jmath_{\rm in}$, and $\tilde{L}_{\rm in}$, the deviation from NT as $|h/r| \to 0$ is less than 5% with a confidence of 95%. For $\jmath$ integrated over $\pm 2|h/r|$, $D[\jmath]$ decreases with $|h/r|$ and increases with a/M both with 99% confidence. When integrating $\jmath$ over all angles, $D[\jmath]$ only decreases with $|h/r|$ to 99% confidence. For $\jmath_{\rm in}$ integrated over $\pm 2|h/r|$, $D[\jmath_{\rm in}]$ only increases with a/M with 99.8% confidence and only decreases with $|h/r|$ with 97% confidence. When integrating $\jmath_{\rm in}$ over all angles, $D[\jmath_{\rm in}]$ only increases with a/M to essentially 100% confidence and only decreases with $|h/r|$ to 99.8% confidence. For $\tilde{e}$ integrated over $\pm 2|h/r|$, $D[\tilde{e}]$ only increases with $|h/r|$ with 98% confidence with no significant trend with a/M. When integrating $\tilde{e}$ over all angles, $D[\tilde{e}]$ only increases with a/M with 95% confidence with no significant trend with $|h/r|$. For $\tilde{L}_{\rm in}$, there is a 98% confidence for this to increase with $|h/r|$ with no significant trend with a/M. Overall, the most certain statement that can be made is that our results are strongly consistent with all deviations from NT becoming less than a few percent in the limit that $|h/r| \to 0$ across the full range of black hole spins.

2.8 Thin disks with varying magnetic field geometry

We now consider the effects of varying the initial field geometry. Since the magnetic field can develop large-scale structures that do not act like a local scalar viscosity, there could in principle be long-lasting effects on the accretion flow properties as a result of the initial field geometry. This is especially a concern for geometrically thin disks, where the 1-loop field geometry corresponds to a severely squashed and highly organized field loop bundle with long-range coherence in the radial direction, whereas our fiducial 4-loop model corresponds to nearly circular loops which impose much less radial order on the MRI-driven turbulence. To investigate this question we have simulated a model similar to our fiducial run except that we initialized the gas torus with a 1-loop

type field geometry instead of our usual multi-loop geometry.

Figure 2.21 shows the radial dependence of $\jmath$, $\jmath_{\rm in}$, $\tilde{e}$, and Υ for the two field geometries under consideration, and Table 2.5 reports numerical estimates of various quantities at the horizon. Consider first the solid lines (4-loop fiducial run) and dotted lines (1-loop run) in Figure 2.21, both of which correspond to integrations in θ over $\pm 2|h/r|$ around the midplane. The simulation with 4-loops is clearly more consistent with NT than the 1-loop simulation. The value of $\jmath$ at the horizon in the 4-loop model deviates from NT by -2.9%. Between the times of $12900M$ and $17300M$, the 1-loop model deviates by -5.6%, while at late time over the saturated period the 1-loop model deviates by -7.2%. The long-dashed lines show the effect of integrating over all θ for the 1-loop model. This introduces yet another systematic deviation from NT (as already noted in §2.5.7); now the net deviation of $\jmath$ becomes -10.7% for times $12900M$ to $17300M$ and becomes -15.8% for the saturated state. Overall, this implies that the assumed initial field geometry has a considerable impact on the specific angular momentum profile and the stress inside the ISCO. This also indicates that the saturated state is only reached after approximately $17000M$, and it is possible that the 1-loop model may never properly converge because magnetic flux of the same sign (how much flux is initially available is arbitrary due to the arbitrary position of the initial gas pressure maximum) may continue to accrete onto the black hole and lead to a qualitatively different accretion state (as seen in Igumenshchev et al. (2003) and McKinney & Gammie (2004) for their vertical field model). At early times, the nominal efficiency, $\tilde{e}$, shows no significant dependence on the field geometry, and sits near the NT value for both models. At late time in the 1-loop model, $\tilde{e}$ rises somewhat, which may indicate the start of the formation of a qualitatively different accretion regime.

Table 2.5: Field Geometry Study

Model Name	$\lvert h/r\rvert$	$\dot{M}$	$\tilde{e}$	$D[\tilde{e}]$	$\jmath$	$D[\jmath]$	$\jmath_{\rm in}$	$D[\jmath_{\rm in}]$	s	$\tilde{L}_{\rm in}$	$\tilde{L}_{\rm eq}$	$100\tilde{\Phi}_r$	Υ
$\underline{\pm 2\lvert h/r\rvert}$													
A0HR07	0.064	0.066	0.058	-0.829	3.363	-2.913	3.355	-3.153	3.363	0.035	0.080	1.355	0.450
A0HR07LOOP1	0.048	0.036	0.066	-14.846	3.215	-7.193	3.234	-6.637	3.215	0.049	0.059	6.198	1.281
A0HR3	0.350	44.066	-0.003	104.582	2.309	-33.331	2.408	-30.473	2.309	0.000	-0.049	3.039	1.182
A0HR3LOOP1	0.377	32.577	0.001	98.892	1.823	-47.389	1.984	-42.717	1.823	0.000	-0.049	7.599	2.246
$\underline{\text{All } \theta}$													
A0HR07	0.064	0.074	0.054	4.723	3.266	-5.717	3.281	-5.275	3.266	0.035	0.053	6.677	0.863
A0HR07LOOP1	0.048	0.040	0.075	-31.857	2.915	-15.847	2.928	-15.478	2.915	0.046	0.048	43.935	3.464
A0HR3	0.350	49.207	-0.004	106.180	2.128	-38.572	2.220	-35.919	2.128	0.000	-0.049	4.724	1.331
A0HR3LOOP1	0.377	39.382	-0.001	102.499	1.575	-54.526	1.734	-49.932	1.575	0.000	-0.049	11.444	2.523

Figure 2.22 shows the normalized luminosity. We see that the 1-loop model produces more luminosity inside the ISCO. For times $12900M$ to $17300M$, $\tilde{L}_{\rm in} = 5.4\%$ (integrated over all θ) compared to 3.5% for the 4-loop field geometry. Thus there is 50% more radiation coming from inside the ISCO in this model. At late time during the saturated state, $\tilde{L}_{\rm in} = 4.6\%$ (integrated over all θ). Thus there is approximately 31% more radiation coming from inside the ISCO in this model during the late phase of accretion.

Table 2.5 also reports the results for thick ($|h/r| \approx 0.3$) disk models initialized with the multi-loop and 1-loop field geometries. This again shows that the deviations from NT are influenced by the initial magnetic field geometry and scale with $|h/r|$ in a way expected by our scaling laws. The 1-loop models show deviations from NT in $\jmath$ are larger as related to the larger value of Υ. The deviations from NT are less affected by the initial magnetic field geometry for thicker disks, because the deviations from NT are also driven by thermal effects and Reynolds stresses rather than primarily electromagnetic stresses as for thin disks.

These effects can be partially understood by looking at the specific electromagnetic stress, Υ, shown in Figure 2.21. We find $\Upsilon \approx 0.45$ for the 4-loop field geometry. For times $12900M$ to $17300M$, $\Upsilon \approx 0.71$ in the 1-loop field geometry, and during the saturated state $\Upsilon \approx 1.28$. For times $12900M$ to $17300M$, the 50% larger Υ appears to be the reason for the 50% extra luminosity inside the ISCO in the 1-loop model. The magnetized thin disk model of Gammie (1999) predicts that, for $a/M = 0$, specific magnetic fluxes of $\Upsilon = 0.45,\ 0.71$ should give deviations from NT of $-D[\jmath] = 1.9,\ 3.9$, respectively. These are close to the deviations seen in the simulations, but they are not a perfect match for reasons we can explain. First, the details of how one spatially-averages quantities (e.g., average of ratio vs. ratio of averages) when computing Υ lead to moderate changes in its value, and, for integrations outside the midplane, comparisons to the Gammie model can require slightly higher Υ than our diagnostic reports. Second, the finite thermal pressure at the ISCO leads to (on average over time) a deviation already at the ISCO that is non-negligible compared to the deviation introduced by electromagnetic stresses between the ISCO and horizon. This thermal component is not always important, e.g., see the comparison in Figure 2.11. Still, as found in McKinney & Gammie (2004) for thick disks at least, the deviations from NT contributed by the thermal pressure are of the same order as the deviations predicted by the Gammie model.

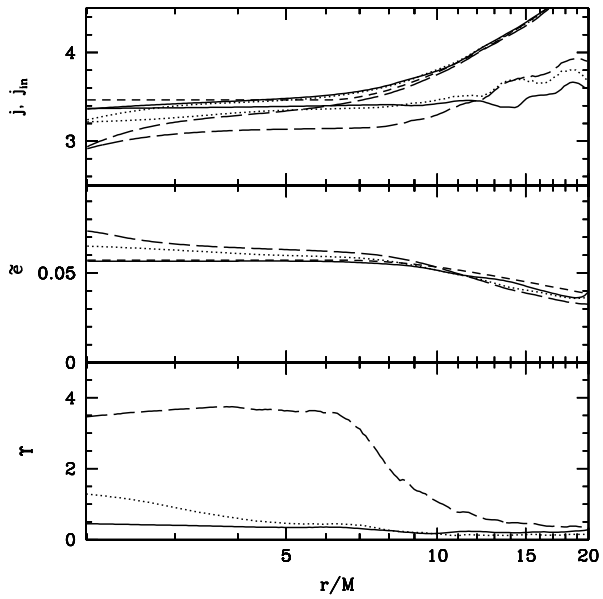

Fig. 2.21.— Radial profiles of $\jmath$ and $\jmath_{\rm in}$ (top panel), $\tilde{e}$ (middle panel), and Υ (bottom panel) are shown for two different initial field geometries. Results for the fiducial 4-loop field geometry (model A0HR07) integrated over $\pm 2|h/r|$ around the midplane are shown by solid lines, for the 1-loop field geometry (model A0HR07LOOP1) integrated over $\pm 2|h/r|$ around the midplane by dotted lines, and the 1-loop model integrated over all angles by long-dashed lines. The short-dashed lines in the top two panels show the NT result. We see that the 1-loop field geometry shows larger deviations from NT in $\jmath$ and Υ compared to the 4-loop geometry. The panels also reemphasize the point that including all θ angles in the angular integration leads to considerable changes in $\jmath$ and Υ due to the presence of magnetic field in the corona-wind-jet.

These results motivate extending the Gammie (1999) model to include a finite (but still small) thermal pressure such that the boundary conditions at the ISCO lead to a non-zero radial velocity.

Within the ISCO, we find that the time-averaged and volume-averaged comoving field strength for the 4-loop geometry roughly follows $|b| \propto r^{-0.7}$ within $\pm 2|h/r|$ of the disk midplane, while at higher latitudes we have a slightly steeper scaling. For times $12900M$ to $17300M$, the 1-loop geometry has $|b| \propto r^{-1.1}$ within $\pm 2|h/r|$ of the disk midplane, and again a slightly steeper scaling in the corona. Other than this scaling, there are no qualitative differences in the distribution of any comoving field component with height above the disk. While the Gammie (1999) solution does not predict a power-law dependence for $|b|$, for a range between $\Upsilon = 0.4$–0.8, the variation near the horizon is approximately $|b| \propto r^{-0.7} - r^{-0.9}$, which is roughly consistent with the simulation results. The slightly steeper slope we obtain for the 1-loop geometry is consistent with a higher specific magnetic flux, although the variations in Υ for integration over different ranges of angle imply stratification and a non-radial flow which the Gammie (1999) model does not account for. This fact and the rise in Υ with decreasing radius seen in Figure 2.21 indicate a non-trivial degree of angular compression as the flow moves towards the horizon. Overall, our results suggest that deviations from NT depend on the assumed field geometry, and that the Gammie (1999) model roughly fits the simulations.

Figure 2.23 shows the same type of plot as in Figure 2.7, but here we compare the fiducial 4-loop model with the 1-loop model. As mentioned above, the 1-loop geometry has a larger deviation in $\jmath$ from the NT value, corresponding to larger stresses inside the ISCO. The absolute magnetic flux (per unit initial total absolute magnetic flux) on the black hole $\tilde{\Phi}_r$ is of order 1/2, suggesting that the inner half of the initial field bundle accreted onto the black hole, while the other half was advected to larger radii. This is consistent with what is seen in simulations of thick tori (McKinney & Gammie 2004; Beckwith et al. 2008a). This suggests that using the 1-loop geometry leads to results that are sensitive to the initial absolute magnetic flux, while the multiple loop geometry leads to results that are insensitive to the initial absolute magnetic flux. Such dependence of the electromagnetic stress on initial magnetic field geometry has also been reported in 3D pseudo-Newtonian simulations by Reynolds & Armitage (2001) and in 3D GRMHD simulations by Beckwith et al. (2008a).

Figure 2.24 shows the electromagnetic stress as computed by equation (2.27) for the multiple loop fiducial model (A0HR07) and the otherwise identical 1-loop model (A0HR07LOOP1). We only show the electromagnetic part of the stress, and within the ISCO this is to within a few percent the same as the total stress obtained by including all terms in the stress-energy tensor. Outside the ISCO, the total stress agrees more with the NT model. The figure shows the full-angle integrated electromagnetic stress, the electromagnetic stress integrated over only $\pm 2|h/r|$, the NT stress, and the Gammie (1999) electromagnetic stress for $\Upsilon = 0.60, 0.89, 0.90, 1.21$ (we choose Υ, the only free parameter of the model, such that the peak magnitude of the stress agrees with the simulation). The chosen Υ values are close to our diagnostic's value of Υ for these models, which demonstrates that the Gammie (1999) model is consistently predicting the simulation's results with a single free parameter. The stress is normalized by the radially dependent $\dot{M}(r)$ that is computed over the same θ integration range. We do not restrict the integration to bound material as done in S08 (in S08, the stress is integrated over $\pm 2|h/r|$ and only for bound material, while in N10 the stress[12] is only over bound material). The stress for the fiducial model was time-averaged over the saturated state, while the 1-loop model was time-averaged from time $12900M$ to $17300M$ in order to best compare with the early phase of accretion for the 1-loop model studied in N10.

Figure 2.24 shows that the simulation and NT stress do not agree well, and it suggests there is an *apparently* large stress within the ISCO. However, as first pointed out by S08 and discussed in section 2.3.4, this stress does not actually correspond to a large deviation from NT in physically relevant quantities such as the specific angular momentum, specific energy, and luminosity. This point is clarified by making a comparison to the Gammie (1999) model's stress, which agrees reasonably well with the simulation stress inside the ISCO. Even though the stress may appear large inside the ISCO, the stress corresponding to the Gammie model with (e.g.) $\Upsilon = 0.60$ only translates into a few percent deviations from NT. This figure also demonstrates that the initial magnetic field geometry affects the amplitude of the stress in the same direction as it affects other quantities and is reasonably well predicted by the Gammie (1999) model. The initial magnetic field

[12]N10's figures 12 and 13 show stress vs. radius, but some of the integrals they computed were not re-normalized to the full 2π when using their simulation ϕ-box size of $\pi/2$, so their stress curves are all a constant factor of 4 times larger than the actual stress (Noble, private communication).

sets the saturated value of Υ, which is directly related to the electromagnetic stresses within the ISCO. The 1-loop model leads to a peak stress (integrated over all angles) within the ISCO that is about 50% larger than the multi-loop model (integrated over all angles), which is likely related to the extra 50% luminosity in the 1-loop model compared to the multi-loop model. The fact that the stress normalization changes with initial field geometry is consistent with other 3D GRMHD simulations of thick disks by Beckwith et al. (2008a). This figure again shows how the stress within the disk ($\pm 2|h/r|$) is much smaller than the total disk+corona+wind+jet (all θ).

Finally, we discuss previous results obtained for other field geometries using an energy-conserving two-dimensional GRMHD code (McKinney & Gammie 2004). While such two-dimensional simulations are unable to sustain turbulence, the period over which the simulations do show turbulence agrees quite well with the corresponding period in three-dimensional simulations. This implies that the turbulent period in the two-dimensional simulations may be qualitatively correct. The fiducial model of McKinney & Gammie (2004) was of a thick ($|h/r| \sim 0.2$–0.25) disk with a 1-loop initial field geometry around an $a/M = 0.9375$ black hole. This model had $\Upsilon \sim 1$ near the midplane within the ISCO and $\Upsilon \sim 2$ when integrated over all θ angles. Their measured value of $\jmath \approx 1.46$ integrated over all angles, $|b| \propto r^{-1.3}$ within the ISCO within the disk midplane (McKinney & Narayan 2007b), along with $\Upsilon \sim 1$–2 are roughly consistent with the Gammie (1999) model prediction of $\jmath \approx 1.5$. Similarly, the strong vertical field geometry model they studied had $\Upsilon \sim 2$ near the midplane within the ISCO and $\Upsilon \sim 6$ integrated over all θ angles. Their measurement of $\jmath \approx -1$ integrated over all angles is again roughly consistent with the model prediction of $\jmath \approx -1.2$ for $\Upsilon \sim 6$. Note that in this model, Υ rises (as usual to reach saturation) with time, but soon after $\Upsilon \gtrsim 2$ in the midplane, the disk is pushed away by the black hole and then Υ is forced to be even larger. Evidently, the accumulated magnetic flux near the black hole pushes the system into a force-free magnetosphere state – not an accretion state. This shows the potential danger of using strong-field initial conditions (like the 1-loop field geometry), since the results are sensitive to the assumed initial flux that is placed on (or rapidly drops onto) the black hole. Even while the disk is present, this particular model exhibits net angular momentum extraction from the black hole. This interesting result needs to be confirmed using three-dimensional simulations of both thick and thin disks.

2.9 Comparisons with other results

The results we have obtained in the present work are consistent with those of Armitage et al. (2001) and Reynolds & Fabian (2008), who carried out pseudo-Newtonian studies, and with the results of S08, who did a full GRMHD simulation. Both of these studies found only minor deviations from NT for thin accretion disks with a multi-loop initial field geometry. However, more recently, N09 and N10 report *apparently* inconsistent results, including factors of up to five larger deviations from NT in the specific angular momentum (2% in S08 versus 10% in N10) for the same disk thickness of $|h/r| \sim 0.07$. They also find a 50% larger deviation from NT in the luminosity (4% in S08 versus 6% in N09). Furthermore, in N10 they conclude that the electromagnetic stresses have no dependence on disk thickness or initial magnetic field geometry, whereas we find that the electromagnetic stresses have a statistically significant dependence on both disk thickness and magnetic field geometry.

We have considered several possible explanations for these differences, as we now describe. We attempt to be exhaustive in our comparison with the setup and results by N09 and N10, because our works and their works seek accuracies much better than order two in measuring deviations from NT. Thus, any deviations between our results by factors of two or more must be investigated further in order to ensure a properly understood and accurate result.

First, we briefly mention some explanations that N10 propose as possible reasons for the discrepant results, viz., differences in 1) numerical algorithm or resolution; 2) box size in ϕ-direction: $\Delta\phi$; 3) amplitude of initial perturbations; 4) accuracy of inflow equilibrium; and 5) duration of the simulations. Our algorithms are similar except that their PPM interpolation scheme assumes primitive quantities are cell averages (standard PPM), while ours assumes they are point values (as required to be applied in a higher-order scheme). They used LAXF dissipative fluxes, while we used HLL fluxes that are about twice more accurate for shocks and may be more accurate in general. On the other hand, they used parabolic interpolation for the Toth electric field, while we use the standard Toth scheme. Given these facts, we expect that the accuracy of our algorithms is similar. Overall, our convergence testing and other diagnostics (see §2.6) confirm that none of their proposed issues can be the cause of differences between S08 and N10.

We have shown that inflow equilibrium must include saturation of the specific magnetic flux, Υ, which generally saturates later in time than other quantities. By running our fiducial model A0HR07 to a time of nearly $30000M$, we ensure that we have a long period of steady state conditions to compute our diagnostic quantities. The fact that we need to run our fiducial thin disk simulation for such a long time to reach inflow equilibrium up to a radius $r \sim 9M$ is completely consistent with our analytical estimate of the time scale calculated using Eq. 2.53 of Appendix 2.B (see the earlier discussion in §2.3.5 and Fig. 2.6). In the comparison between the numerical and analytical results shown in Figure 2.6, we found agreement by setting $\alpha|h/r|^2 \approx 0.00033$ which, for our disk with $|h/r| \approx 0.064$, corresponds to $\alpha \approx 0.08$. With this value of $\alpha|h/r|^2$, we would have to run the simulation until $t \sim 83000M,\ 160000M$, to reach inflow equilibrium out to $15M,\ 20M$, respectively, corresponding to a couple viscous timescales at that radius. N10 state that they reach inflow equilibrium within $r \sim 15M$–$20M$ in a time of only $t \sim 10000M$. Since their disk thickness is $|h/r| \approx 0.06$, even a single viscous timescale would require their simulations to have $\alpha \sim 0.38$ to reach inflow equilibrium up to $r \sim 15M$, and an even larger value of α for $r \sim 20M$. This seems unlikely. We can partially account for their result by considering our 1-loop model, which up to $t \sim 17000M$ has $\alpha|h/r|^2$ twice as large and α about 70% larger than in the fiducial 4-loop run. However, this still falls far short by a factor of roughly 3 of what N10 would require for inflow equilibrium up to $15M$–$20M$. Further, our A0HR07LOOP1 model, which is similar to their model, only reaches a saturated state by $17000M$, and only the Υ quantity indicates that saturation has been reached. If we were to measure quantities from $10000M$ to $15000M$ as in N10, we would have underestimated the importance of magnetic field geometry on the electromagnetic stresses.

Since all these simulations are attempting to obtain accuracies better than factors of two in the results, this inflow equilibrium issue should be explored further. A few possible resolutions include: 1) N10's higher resolution leads to a much larger α; 2) their disk has a larger "effective" thickness, e.g. $|h/r| \sim 0.13$, according to Eq. 5.9.8 in NT (see Eq. 2.53 of Appendix 2.B); 3) some aspects of their solution have not yet reached inflow equilibrium within a radius much less than $r \sim 15M$, such as the value of Υ vs. time that saturates much later than other quantities; or 4) they achieve constant fluxes vs. radius due to transient non-viscous effects – although one should be concerned that the actual value of such fluxes continues to secularly evolve in time and one still requires

evolution on the longer viscous (turbulent diffusion) timescale to reach true inflow equilibrium.

Second, we considered various physical setup issues, including differences in: 1) range of black hole spins considered; 2) range of disk thicknesses studied; 3) ad hoc cooling function; and 4) equation of state. We span the range of black hole spins and disk thicknesses studied by N10, so this is unlikely to explain any of the differences. Some differences could be due to the disk thickness vs. radius profiles established by the ad hoc cooling functions in the two studies. N10's cooling function is temperature-based and allows cooling even in the absence of any dissipation, while ours is based upon the specific entropy and cools the gas only when there is dissipation. Both models avoid cooling unbound gas. In S08 and in the present chapter, we use an ideal gas equation of state with $\Gamma = 4/3$, while N09 and N10 used $\Gamma = 5/3$. The properties of the turbulence do appear to depend on the equation of state (Mignone & McKinney 2007), so it is important to investigate further the role of Γ in thin disks.

Third, the assumed initial field geometry may introduce critical differences in the results. Issues with the initial field geometry include how many field reversals are present, how isotropic the field loops are in the initial disk, how the electromagnetic field energy is distributed in the initial disk, and how the magnetic field is normalized. In S08 and here, we have used a multi-loop geometry in the initial torus consisting of alternating polarity poloidal field bundles stacked radially. We ensure that the field loops are roughly isotropic within the initial torus. We set the ratio of maximum gas pressure to maximum magnetic pressure to $\beta_{\rm maxes} = 100$, which gives us a volume-averaged mean β within the dense part of the torus ($\rho_0/\rho_{0,\rm max} \geq 0.2$) of $\bar{\beta} \sim 800$. Our procedure ensures that all initial local values of β within the disk are much larger than the values in the evolved disk, i.e., there is plenty of room for the magnetic field to be amplified by the MRI.

We have also studied a 1-loop geometry that is similar to the 1-loop geometry used in N09 and N10. Their initial ϕ-component of the vector potential is $A_\phi \propto {\rm MAX}(\rho_0/\rho_{0,\rm max} - 0.25, 0)$ (Noble, private communication). They initialize the magnetic field geometry by ensuring that the volume-averaged gas pressure divided by the volume-averaged magnetic pressure is $\beta_{\rm averages} = 100$ (Noble, private communication). (They stated that the mean initial plasma β is $\bar{\beta} = 100$.) For their thin disk torus model parameters, this normalization procedure leads to a portion of the inner

radial region of the torus to have a local value of $\beta \sim 3 - 8$, which may be a source of differences in our results. Such a small β is lower than present in the saturated disk. N10 make use of an older set of simulations from a different non-energy-conserving code (Hawley & Krolik 2006; Beckwith et al. 2008a) to investigate the effect of other field geometries. The results from this other code have strong outliers, e.g., the KD0c model, and so we are unsure if these other simulations can be used for such a study.

N10 state that they find no clear differences in the electromagnetic stresses for different initial field geometries. As shown in their figures 12 and 13, the Agol & Krolik (2000) model captures the smoothing of the stress outside the ISCO, but it is not a model for the behavior of the stress inside the ISCO. We find that electromagnetic stresses have a clear dependence on both disk thickness and the initial magnetic field geometry, with a trend that agrees with the Gammie (1999) model of a magnetized thin disk. Our Figure 2.24 shows that the stress within the ISCO is reasonably well modelled by the Gammie (1999) model. Our 1-loop thin disk model gives a peak normalized stress (integrated over all angles) of about 3.2×10^{-3} for times $12900M$ to $17300M$, which is comparable to the 1-loop thin disk model in N10 with peak normalized stress (integrated over all angles) of about 2.5×10^{-3} (after correcting for their ϕ-box size). Hence, we are able to account for the results of their 1-loop model.

In addition, we used the specific magnetic flux, Υ, an ideal MHD invariant that is conserved within the ISCO, to identify how electromagnetic stresses scale with disk thickness and magnetic field geometry. In the saturated state, the value of Υ, which controls the electromagnetic stresses, is different for different initial magnetic field geometries. We find that $\jmath$ within the disk ($\pm 2|h/r|$ from the midplane) deviates from NT by -3% in our 4-loop model and -6% in our 1-loop model for times $12900M$ to $17300M$. Integrating over all angles, $\jmath$ deviates by -6% for the 4-loop model and -11% for the 1-loop model for times $12900M$ to $17300M$. Thus, we find a clear factor of two change, depending on the assumed initial field geometry and the range of integration. The excess luminosity is 3.5% for the 4-loop model and 5.4% for the 1-loop model for times $12900M$ to $17300M$. Recalling that N10 find a deviation from NT of about -10% in $\jmath$ (integrated over all angles) and a luminosity excess beyond NT of about 6%, this shows we can completely account for the *apparent* inconsistencies mentioned by N10 by invoking dependence of the results on the initial

field geometry and the presence of extra stress beyond the disk component of the accretion flow.

Fourth, let us consider measurement and interpretation differences. Our ultimate goal is to test how well the NT model describes a magnetized thin accretion disk. The primary quantity that is used to measure this effect in S08 and N10 is the specific angular momentum $\jmath$. However, the measurements are done differently in the two studies. In S08 as well as in this chapter, we focus on the disk gas by limiting the range of θ over which we compute the averaging integrals ($\pm 2|h/r|$ from the midplane). In contrast, N10 compute their integrals over a much wider range of θ which includes both the disk and the corona-wind-jet (Noble, 2010, private communications). We have shown in § 2.5.7 that the disk and corona-wind-jet contribute roughly equally to deviations of $\jmath$ from the NT value. In principle, the luminosity from the corona-wind-jet could be important, but we have shown that the excess luminosity of bound gas within the ISCO is dominated by the disk. This means that the measure used by N10, consisting of integrating over all gas to obtain $\jmath$, cannot be used to infer the excess luminosity of bound gas within the ISCO. Further, the corona would largely emit non-thermal radiation, so for applications in which one is primarily interested in the thermal component of the emitted radiation, one should evaluate the accuracy of the NT model by restricting the angular integration range to the disk component within $\pm 2|h/r|$.

Fifth, let us consider how the results from N10 scale with disk thickness for the specific case of a non-spinning ($a/M = 0$) black hole. We have performed a linear least squares fit of their simulation results, omitting model KD0c which is a strong outlier. For $\jmath$ integrated over all θ, their relative difference follows $D[\jmath] \approx -7 - 45|h/r|$ with confidence of 95% that these coefficients, respectively, only deviate by $\pm 67\%$ and $\pm 89\%$. These fits imply that, as $|h/r| \to 0$, the relative deviation of $\jmath$ from the NT value is about -7%, but they could easily be as low as -2%. Their results do not indicate a statistically significant large deviation from NT as $|h/r| \to 0$. Since the total deviation in $\jmath$ from NT includes the effects of electromagnetic (and all other) stresses, this implies that their models are consistent with weak electromagnetic stresses as $|h/r| \to 0$.

Further, we have already established that the 1-loop geometry gives (at least) twice the deviation from NT compared to the 4-loop geometry, plus there is another factor of two arising from including the corona-wind-jet versus not including it. This net factor of 4 applied to N10's

results implies that $\jmath$ would deviate by about -2% or even as low as -0.5% from NT in the limit $|h/r| \to 0$ if they were to consider a 4-loop field geometry and focus only on the disk gas. Thus, their models show no statistically significant large deviations from NT. In addition, our results in section 2.7.1 show that, whether we consider an integral over all angles or only over the disk, there is no statistically significant large deviation from NT as $|h/r| \to 0$.

In summary, we conclude that the apparent differences between the results obtained in S08 and the present chapter on the one hand, and those reported in N09 and N10 on the other, are due to 1) dependence on initial magnetic field geometry (multi-loop vs 1-loop); 2) dependence upon the initial magnetic field distribution and normalization; and 3) measurement and interpretation differences (disk vs. corona-wind-jet). Note in particular that the 1-loop initial field geometry is severely squashed in the vertical direction and elongated in the radial direction for thin disks, and it is not clear that such a geometry would ever arise naturally. There are also indications from our simulation that the 1-loop geometry may actually never reach a converged state due to the arbitrary amount of magnetic flux accreted onto the black hole due to the single polarity of the initial magnetic field. Finally, if one is trying to test how well simulated thin accretion disks compare with NT, then it is important to restrict the comparison to disk gas near the midplane. One should not expect the gas in the corona-wind-jet to agree with the NT model.

2.10 Discussion

We now discuss some important consequences of our results and also consider issues to be addressed by future calculations. First, we discuss the relevance to black hole spin measurements.

In recent years, black hole spin parameters have been measured in several black hole x-ray binaries by fitting their x-ray continuum spectra in the thermal (or high-soft) spectral state (Zhang et al. 1997; Shafee et al. 2006; McClintock et al. 2006; Davis et al. 2006; Liu et al. 2008; Gou et al. 2009, 2010). This method is based on several assumptions that require testing (Narayan et al. 2008), the most critical being the assumption that an accretion disk in the radiatively-efficient thermal state is well-described by the Novikov-Thorne model of a thin disk. More specifically, in

analyzing and fitting the spectral data, it is assumed that the radial profile of the radiative flux, or equivalently the effective temperature, in the accretion disk closely follows the prediction of the NT model.

Practitioners of the continuum-fitting method generally restrict their attention to relatively low-luminosity systems below 30% of the Eddington luminosity. At these luminosities, the maximum height of the disk photosphere above the midplane is less than 10% of the radius, i.e., $(h/r)_{\rm photosphere} \leq 0.1$ (McClintock et al. 2006). For a typical disk, the photospheric disk thickness is approximately twice the mean absolute thickness $|h/r|$ that we consider in this chapter. Therefore, the disks that observers consider for spin measurement have $|h/r| \lesssim 0.05$, i.e., they are thinner than the thinnest disk ($|h/r|_{\rm min} \sim 0.06$) that we (S08, this chapter) and others (N09, N10) have simulated.

The critical question then is the following: Do the flux profiles of very thin disks match the NT prediction? At large radii the two will obviously match very well since the flux profile is determined simply by energy conservation[13]. However, in the region near and inside the ISCO, analytic models have to apply a boundary condition, and the calculated flux profile in the inner region of the disk depends on this choice. The conventional choice is a "zero-torque" boundary condition at the ISCO. Unfortunately, there is disagreement on the validity of this assumption. Some authors have argued that the magnetic field strongly modifies the zero-torque condition and that, therefore, real disks might behave very differently from the NT model near the ISCO (Krolik 1999; Gammie 1999). Other authors, based either on heuristic arguments or on hydrodynamic calculations, find that the NT model is accurate even near the ISCO so long as the disk is geometrically thin (Paczyński 2000; Afshordi & Paczyński 2003; Shafee et al. 2008a; Abramowicz et al. 2010). Investigating this question was the primary motivation behind the present study.

We described in this chapter GRMHD simulations of geometrically thin ($|h/r| \sim 0.07$) accretion disks around black holes with a range of spins: $a/M = 0,\ 0.7,\ 0.9,\ 0.98$. In all cases, we find that the specific angular momentum $\jmath$ of the accreted gas as measured at the horizon (this

[13]This is why the formula for the flux as a function of radius in the standard thin disk model does not depend on details like the viscosity parameter α (Frank et al. 1992).

quantity provides information on the dynamical importance of torques at the ISCO) shows only minor deviations at the level of $\sim 2\%$–4% from the NT model. Similarly, the luminosity emitted inside the ISCO is only $\sim 3\%$–7% of the total disk luminosity. When we allow for the fact that a large fraction of this radiation will probably be lost into the black hole because of relativistic beaming as the gas plunges inward (an effect ignored in our luminosity estimates), we conclude that the region inside the ISCO is likely to be quite unimportant. Furthermore, our investigations indicate that deviations from the NT model decrease with decreasing $|h/r|$. Therefore, since the disks of interest to observers are generally thinner than the thinnest disks we have simulated, the NT model appears to be an excellent approximation for modeling the spectra of black hole disks in the thermal state.

One caveat needs to be mentioned. Whether or not the total luminosity of the disk agrees with the NT model is not important since, in spectral modeling of data, one invariably fits a normalization (e.g., the accretion rate $\dot{M}$ in the model KERRBB; Li et al. 2005) which absorbs any deviations in this quantity. What is important is the *shape* of the flux profile versus radius. In particular, one is interested in the radius at which the flux or effective temperature is maximum (Narayan et al. 2008; McClintock et al. 2009). Qualitatively, one imagines that the fractional shift in this radius will be of order the fractional torque at the ISCO, which is likely to be of order the fractional error in $\jmath$. We thus guess that, in the systems of interest, the shift is nearly always below 10%. We plan to explore this question quantitatively in a future study.

Another issue is the role of the initial magnetic field topology. We find that, for $a/M = 0$, starting with a 1-loop field geometry gives an absolute relative deviation in $\jmath$ of 7.1%, and an excess luminosity inside the ISCO of 4.9%, compared to 2.9% and 3.5% for our standard 4-loop geometry. Thus, having a magnetic field distribution with long-range correlation in the radial direction seems to increase deviations from the NT model, though even the larger effects we find in this case are probably not a serious concern for black hole spin measurement. Two comments are in order on this issue. First, the 4-loop geometry is more consistent with nearly isotropic turbulence in the poloidal plane and, therefore, in our view a more natural initial condition. Second, the 1-loop model develops a stronger field inside the ISCO and around the black hole and might therefore be expected to produce a relativistic jet with measurable radio emission. However, it is well-known

that black hole x-ray binaries in the thermal state have no detectable radio emission. This suggests that the magnetic field is probably weak, i.e., more consistent with our 4-loop geometry.

Next, we discuss the role of electromagnetic stresses on the dynamics of the gas in the plunging region inside the ISCO. In order to better understand this issue, we have extracted for each of our simulations the radial profile of the specific magnetic flux, Υ. This quantity appears as a dimensionless free parameter (called $F_{\theta\phi}$) in the simple MHD model of the plunging region developed by Gammie (1999). The virtues of the specific magnetic flux are its well-defined normalization and its constancy with radius for stationary flows (Takahashi et al. 1990). In contrast, quantities like the stress W or the viscosity parameter α have no well-defined normalization; W can be normalized by any quantity that has an energy scale, such as ρ_0, $\dot{M}$, or b^2, while α could be defined with respect to the total pressure, the gas pressure, or the magnetic pressure. The numerical values of W or α inside the ISCO can thus vary widely, depending on which definition one chooses. For instance, although S08 found $\alpha \sim 1$ inside the ISCO, the specific angular momentum flux, $\jmath$, deviated from NT by no more than a few percent. Further, Figure 2.24 shows that (even for the multi-loop model) the stress appears quite large within the ISCO, but this is misleading because the effects of the stress are manifested in the specific angular momentum, specific energy, and luminosity – all of which agree with NT to within less than 10% for the multi-loop model. Since W and α do not have a single value within the ISCO or a unique normalization, we conclude that they are not useful for readily quantifying the effects of the electromagnetic stresses within the ISCO.

Gammie's (1999) model shows how the value of Υ is directly related to the electromagnetic stresses within the ISCO. Unfortunately, the actual value of Υ is a free parameter which cannot be easily determined from first principles. It is possible that accretion disks might have $\Upsilon \gg 1$, in which case, the model predicts large deviations from NT. For example, if $\Upsilon = 6$, then for an $a/M = 0$ black hole $\jmath$ is lowered by 56% relative to the NT model. We have used our 3D GRMHD simulations which include self-consistent MRI-driven turbulence to determine the value of Υ for various black hole spins, disk thicknesses, and field geometries. For the multiple-loop field geometry, we find that the specific magnetic flux varies with disk thickness and spin as

$$\Upsilon \approx 0.7 + \left|\frac{h}{r}\right| - 0.6\frac{a}{M}, \tag{2.41}$$

within the disk component, which indicates that electromagnetic stresses are weak and cause less than 8% deviations in $\jmath$ in the limit $|h/r| \to 0$ for all black hole spins. Our rough analytical arguments for how Υ should scale with $|h/r|$ and a/M are consistent with the above formula. Even for the 1-loop field geometry, $\Upsilon \lesssim 1$ for thin disks, so electromagnetic stresses cause only minor deviations from NT for all black hole spins (for $\Upsilon \lesssim 1$, less than 12% in $\jmath$). Not all aspects of the Gammie (1999) model agree with our simulations. As found in McKinney & Gammie (2004), the nominal efficiency, $\tilde{e}$, does not match well and for thin disks is quite close to NT. Since the true radiative efficiency is limited to no more than $\tilde{e}$, this predicts only weak deviations from NT in the total luminosity even if $\jmath$ has non-negligible deviations from NT. Also, this highlights that the deviations from NT in $\jmath$ are due to non-dissipated electromagnetic stresses and cannot be used to directly predict the excess luminosity within the ISCO. The assumption of a radial flow in a split-monopole field is approximately valid, but the simulations do show some non-radial flow and vertical stratification, a non-zero radial velocity at the ISCO, and thermal energy densities comparable to magnetic energy densities. Inclusion of these effects is required for better consistency with simulation results inside the ISCO.

Next, we consider how our results lend some insight into the spin evolution of black holes. Standard thin disk theory with photon capture predicts that an accreting black hole spins up until it reaches spin equilibrium at $a_{\rm eq}/M \approx 0.998$ (Thorne 1974). On the other hand, thick non-radiative accretion flows deviate significantly from NT and reach equilibrium at $a_{\rm eq}/M \sim 0.8$ for a model with $\alpha \sim 0.3$ and $|h/r| \sim 0.4$ near the horizon (Popham & Gammie 1998). GRMHD simulations of moderately thick ($|h/r| \sim 0.2$–0.25) magnetized accretion flows give $a_{\rm eq}/M \approx 0.9$ (Gammie et al. 2004). In this chapter, we find from our multi-loop field geometry models that spin equilibrium scales as

$$\frac{a_{\rm eq}}{M} \approx 1.1 - 0.8\left|\frac{h}{r}\right|, \tag{2.42}$$

where one should set $a_{\rm eq}/M = 1$ if the above formula gives $a_{\rm eq}/M > 1$. This gives a result consistent with the above-mentioned studies of thick disks, and it is also consistent with our rough analytical prediction based upon our scaling of Υ and using the Gammie model prediction for the spin equilibrium. This result also agrees with the NT result in the limit $|h/r| \to 0$ within our statistical errors, and shows that magnetized thin disks can approach the theoretical limit of

$a_{\rm eq}/M \approx 1$, at least in the multi-loop case. In the single-loop field geometry, because of the presence of a more radially-elongated initial poloidal field, we find a slightly stronger torque on the black hole. However, before a time of order $17000M$, the deviations in the equilibrium spin parameter, $a_{\rm eq}/M$, between the 4-loop and 1-loop field geometries appear to be minor, so during that time the scaling given above roughly holds. Of course, it is possible (even likely) that radically different field geometries or anomalously large initial field strengths will lead to a different scaling.

Lastly, we mention a number of issues which we have neglected but are potentially important. A tilt between the angular momentum vector of the disk and the black hole rotation axis might significantly affect the accretion flow (Fragile et al. 2007). We have not accounted for any radiative transfer physics, nor have we attempted to trace photon trajectories (see, e.g. N09 and Noble & Krolik 2009). In principle one may require the simulation to be evolved for hundreds of orbital times at a given radius in order to completely erase the initial conditions (Sorathia et al. 2010), whereas we only run the model for a couple of viscous time scales. New pseudo-Newtonian simulations show that convergence may require resolving several disk scale heights with high resolution (Sorathia et al. 2010), and a similar result has been found also for shearing box calculations with no net flux and no stratification (Stone 2010, private communication). In contrast, we resolve only a couple of scale heights. Also, we have only studied two different types of initial field geometries. Future studies should consider whether alternative field geometries change our results.

2.11 Conclusions

We set out in this study to test the standard model of thin accretion disks around rotating black holes as developed by Novikov & Thorne (1973). We studied a range of disk thicknesses and black hole spins and found that magnetized disks are consistent with NT to within a few percent when the disk thickness $|h/r| \lesssim 0.07$. In addition, we noted that deviations from the NT model decrease as $|h/r|$ goes down. These results suggest that black hole spin measurements via the x-ray continuum-fitting method (Zhang et al. 1997; Shafee et al. 2006; McClintock et al. 2006; Davis et al. 2006; Liu et al. 2008; Gou et al. 2009, 2010), which are based on the NT model, are robust to model uncertainties so long as $|h/r| \lesssim 0.07$. At luminosities below 30% of Eddington, we estimate

disk thicknesses to be $|h/r| \lesssim 0.05$, so the NT model is perfectly adequate.

These results were obtained by performing global 3D GRMHD simulations of accreting black holes with a variety of disk thicknesses, black hole spins, and initial magnetic field geometries in order to test how these affect the accretion disk structure, angular momentum transport, luminosity, and the saturated magnetic field. We explicitly tested the convergence of our numerical models by considering a range of resolutions, box sizes, and amplitude of initial perturbations. As with all numerical studies, future calculations should continue to clarify what aspects of such simulations are converged by performing more parameter space studies and running the simulations at much higher resolutions. For example, it is possible that models with different black hole spins require more or less resolution than the $a = 0$ models, while we fixed the resolution for all models and only tested convergence for the $a = 0$ models.

We confirmed previous results by S08 for a non-spinning ($a/M = 0$) black hole, which showed that thin ($|h/r| \lesssim 0.07$) disks initialized with multiple poloidal field loops agree well with the NT solution once they reach steady state. For the fiducial model described in the present chapter, which has similar parameters as the S08 model, we find 2.9% relative deviation in the specific angular momentum accreted through the disk, and 3.5% excess luminosity from inside the ISCO. Across all black hole spins that we have considered, viz., $a/M = 0,\ 0.7,\ 0.9,\ 0.98$, the relative deviation from NT in the specific angular momentum is less than 4.5%, and the luminosity from inside the ISCO is less than 7% (typically smaller, and much of it is likely lost to the hole). In addition, all deviations from NT appear to be roughly proportional to $|h/r|$.

We found that the assumed initial field geometry modifies the accretion flow. We investigated this effect by considering two different field geometries and quantified it by measuring the specific magnetic flux, Υ, which is an ideal MHD invariant (like the specific angular momentum or specific energy). The specific magnetic flux can be written as a dimensionless free parameter that enters the magnetized thin disk model of Gammie (1999). This parameter determines how much the flow deviates from NT as a result of electromagnetic stresses. We found that Υ allows a quantitative understanding of the flow within the ISCO, while the electromagnetic stress (W) has no well-defined normalization and varies widely within the ISCO. While a plot of the stress may appear to show

large stresses within the ISCO, the actual deviations from NT can be small. This demonstrates that simply plotting W is not a useful diagnostic for measuring deviations from NT. We found that the specific magnetic flux of the gas inside the ISCO was substantially larger when we used a single poloidal magnetic loop to initialize the simulation compared to our fiducial 4-loop run. For $a/M = 0$ and $|h/r| \lesssim 0.07$, the early saturated phase (times $12900M$ to $17300M$) of the evolution for the 1-loop geometry gave 5.6% relative deviation in the specific angular momentum and 5.8% excess luminosity inside the ISCO. These deviations are approximately twice as large as the ones we found for the 4-loop simulation. At late times, the 1-loop model generates significant deviations from NT, which is a result similar to that found in a vertical field model in McKinney & Gammie (2004). However, we argued that the multiple loop geometry we used is more natural than the single loop geometry, since for a geometrically thin disk the magnetic field in the 1-loop model is severely squashed vertically and highly elongated radially. The 1-loop model is also likely to produce a strong radio jet.

More significant deviations from NT probably occur for disks with strong ordered magnetic field, as found in 2D GRMHD simulations by McKinney & Gammie (2004). Of course, in the limit that the magnetic field energy density near the black hole exceeds the local rest-mass density, a force-free magnetosphere will develop and deviations from the NT model will become extreme. We argued that this corresponds to when the specific magnetic flux $\Upsilon \gtrsim 1$ near the disk midplane. Our 1-loop model appears to be entering such a phase at late time after accumulation of a significant amount of magnetic flux. Such situations likely produce powerful jets that are not observed in black hole x-ray binaries in the thermal state. However, transition between the thermal state and other states with a strong power-law component (Fender et al. 2004; Remillard & McClintock 2006) may be partially controlled by the accumulation of magnetic flux causing the disk midplane (or perhaps just the corona) to breach the $\Upsilon \sim 1$ barrier. Such a behavior has been studied in the non-relativistic regime (Narayan et al. 2003; Igumenshchev et al. 2003; Igumenshchev 2009), but more work using GRMHD simulations is required to validate the behavior.

We also found that the apparently different results obtained by N10 were mostly due to measurement and interpretation differences. We found that both the disk and the corona-wind-jet contribute nearly equally to deviations in the total specific angular momentum relative to the

NT model. However, the corona-wind-jet contributes much less to the luminosity than the disk component. Therefore, if one is interested in comparing the luminous portion of the disk in the simulations against the NT model, the only fair procedure is to consider only the disk gas, i.e., gas within a couple of scale heights of the midplane. This is the approach we took in this study (also in S08). N10 on the other hand included the corona-wind-jet gas in their calculation of the specific angular momentum. The dynamics of the coronal gas differs considerably from the NT model. Therefore, while it does not contribute to the luminosity of bound gas, it doubles the deviation of the specific angular momentum from the NT model. In addition, N10 used a 1-loop initial field geometry for their work which, as discussed above, further enhanced deviations.

Acknowledgments

We thank Phil Armitage, the referee, for comments that greatly improved the chapter's presentation, and we thank Scott Noble for detailed discussions about his work. We thank Charles Gammie, Chris Reynolds, Jim Stone, Kris Beckwith, John Hawley, Julian Krolik, Chris Done, Chris Fragile, Martin Pessah, and Niayesh Afshordi for useful discussions. This work was supported in part by NASA grant NNX08AH32G (AT & RN), NSF grant AST-0805832 (AT & RN), NASA Chandra Fellowship PF7-80048 (JCM), an NSF Graduate Research Fellowship (RFP), and by the NSF through TeraGrid resources provided by NCSA (Abe), LONI (QueenBee), NICS (Kraken) under grant numbers TG-AST080025N and TG-AST080026N.

2.A Example solutions and scalings for the Gammie (1999) model

Table 2.6 gives representative solutions for the Gammie (1999) model of a magnetized thin accretion flow. The columns correspond to the black hole spin, a; the specific magnetic flux, Υ; the nominal efficiency, $\tilde{e}$; percent deviation of $\tilde{e}$ from the NT value; the specific angular momentum, $\jmath$; percent deviation of $\jmath$ from NT; and the normalized rate of change of the dimensionless black hole spin,

s (see Eq. 2.15). For $\Upsilon \lesssim 0.5$ and across all black hole spins, the relative change in the specific angular momentum is less than 5% and the relative change in the efficiency is less than 9%. For small values of $\Upsilon \lesssim 1$, the deviations of $\jmath$ and $\tilde{e}$ from NT behave systematically and one can derive simple fitting functions. For $\jmath$ we find

$$\begin{aligned} & \log_{10}\left[-D[\jmath]\right] \\ \approx\ & 0.79 + 0.37(a/M) + 1.60\log_{10}\Upsilon \qquad (2.43) \\ \sim\ & (4/5) + (1/3)(a/M) + (8/5)\log_{10}\Upsilon, \qquad (2.44) \end{aligned}$$

with an L2 error norm of $0.7\%, 0.7\%$, respectively, for the first and second relations, while for $\tilde{e}$ we find

$$\begin{aligned} & \log_{10}\left[D[\tilde{e}]\right] \\ \approx\ & 1.44 + 0.12(a/M) + 1.60\log_{10}\Upsilon \qquad (2.45) \\ \sim\ & (3/2) + (1/10)(a/M) + (8/5)\log_{10}\Upsilon, \qquad (2.46) \end{aligned}$$

with an L2 error norm of $0.9\%, 1\%$, respectively, for the first and second relations. These results indicate that the deviations from NT scale as $\Upsilon^{8/5}$ for $\Upsilon \lesssim 1$. For $\Upsilon \gtrsim 1$, the index on Υ depends on the spin parameter. In the span from $\Upsilon \sim 0.2$ to $\Upsilon \sim 1$, a linear fit across all black hole spins gives $-D[\jmath] \sim -1 + 11\Upsilon$ and $D[\tilde{e}] \sim -4 + 33\Upsilon$, which are rough, though reasonable looking, fits.

2.B Inflow equilibrium timescale in the Novikov-Thorne model

The radius out to which inflow equilibrium is achieved in a given time may be estimated by calculating the mean radial velocity v_r and then deriving from it a viscous timescale $-r/v_r$.

When the flow has achieved steady state, the accretion rate,

$$\dot{M} = -2\pi r \Sigma v_r \mathcal{D}^{1/2}, \qquad (2.47)$$

is a constant independent of time and position. Here we derive an expression for v_r corresponding to the general relativistic NT thin disk model. In what follows, capital script letters denote standard

Table 2.6: Thin Magnetized Inflow Solutions

$\frac{a}{M}$	Υ	$\tilde{e}$	$D[\tilde{e}]$	$\jmath$	$D[\jmath]$	s
0	0.1	0.0576	0.709	3.46	-0.172	3.46
0	0.2	0.0584	2.14	3.45	-0.52	3.45
0	0.3	0.0595	4.08	3.43	-0.991	3.43
0	0.5	0.0624	9.17	3.39	-2.23	3.39
0	1	0.0727	27.1	3.24	-6.57	3.24
0	1.5	0.0859	50.2	3.04	-12.2	3.04
0	6	0.19	232	1.51	-56.4	1.51
0.7	0.1	0.105	1.03	2.58	-0.286	1.33
0.7	0.2	0.107	3.07	2.56	-0.853	1.31
0.7	0.3	0.11	5.8	2.54	-1.61	1.3
0.7	0.5	0.117	12.8	2.49	-3.57	1.26
0.7	1	0.142	36.7	2.32	-10.2	1.12
0.7	1.5	0.172	66.3	2.11	-18.5	0.95
0.7	6	0.477	360	-0.00714	-100	-0.74
0.9	0.1	0.157	1.17	2.09	-0.386	0.576
0.9	0.2	0.161	3.37	2.08	-1.11	0.567
0.9	0.3	0.165	6.29	2.06	-2.07	0.555
0.9	0.5	0.177	13.7	2.01	-4.5	0.524
0.9	1	0.215	38.3	1.84	-12.6	0.423
0.9	1.5	0.262	68.3	1.63	-22.5	0.3
0.9	6	0.845	443	-0.958	-146	-1.24
0.98	0.1	0.236	0.949	1.68	-0.397	0.179
0.98	0.2	0.241	2.86	1.66	-1.2	0.174
0.98	0.3	0.246	5.36	1.64	-2.25	0.168
0.98	0.5	0.261	11.6	1.6	-4.9	0.152
0.98	1	0.309	32.2	1.45	-13.6	0.1
0.98	1.5	0.368	57.1	1.28	-24.1	0.0379
0.98	6	1.21	416	-1.27	-175	-0.862

functions of r and a (cf. eqns. (14) and (35) in Page & Thorne (1974)) which appear as relativistic corrections in otherwise Newtonian expressions. They reduce to unity in the limit $r/M \to \infty$.

The vertically-integrated surface density may be defined as $\Sigma = 2h\rho$, where h is the disk scale-height and ρ is the rest-mass density at the midplane. In equilibrium, density is related to pressure by

$$\frac{dp}{dz} = \rho \times (\text{“acceleration of gravity”}) \tag{2.48}$$

$$= \rho \frac{Mz}{r^3} \frac{\mathcal{B}^2 \mathcal{D} \mathcal{E}}{\mathcal{A}^2 \mathcal{C}}, \tag{2.49}$$

the vertically-integrated solution of which is

$$h = (p/\rho)^{1/2} / |\Omega| \mathcal{A} \mathcal{B}^{-1} \mathcal{C}^{1/2} \mathcal{D}^{-1/2} \mathcal{E}^{-1/2}. \tag{2.50}$$

The pressure may be parameterized in terms of the viscous stress, $|t_{\hat{r}\hat{\phi}}| = \alpha p$, which is a known function of r and a:

$$W = 2h t_{\hat{r}\hat{\phi}} = \frac{\dot{M}}{2\pi} \Omega \frac{\mathcal{C}^{1/2} \mathcal{Q}}{\mathcal{B} \mathcal{D}}. \tag{2.51}$$

The surface density is then

$$\Sigma = \frac{1}{2\pi} \frac{\dot{M}}{\alpha h^2 |\Omega|} \mathcal{A}^2 \mathcal{B}^{-3} \mathcal{C}^{3/2} \mathcal{D}^{-2} \mathcal{E}^{-1} \mathcal{Q}. \tag{2.52}$$

Substituting this in Eq. (2.47), the radial velocity is

$$v_r = -\alpha |h/r|^2 |\Omega| r \mathcal{A}^{-2} \mathcal{B}^3 \mathcal{C}^{-3/2} \mathcal{D}^{3/2} \mathcal{E} \mathcal{Q}^{-1}. \tag{2.53}$$

This result is independent of the exact form of the pressure and opacity and so is valid in all regions of the disk. The inflow equilibrium time may be estimated as $t_{\rm ie} \sim -2r/v_r$.

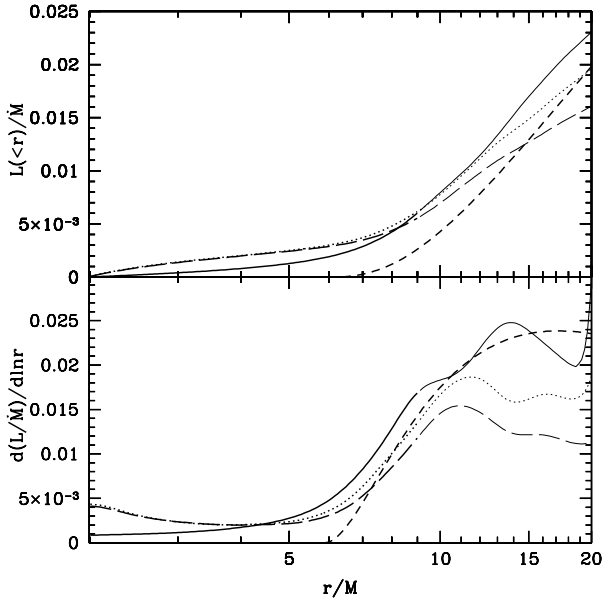

Fig. 2.22.— Similar to Figure 2.21 for the initial 4-loop and 1-loop field geometries, but here we show the luminosity (top panel) and log-derivative of the luminosity (bottom panel). The luminosity is slightly higher for the 1-loop model compared to the 4-loop model.

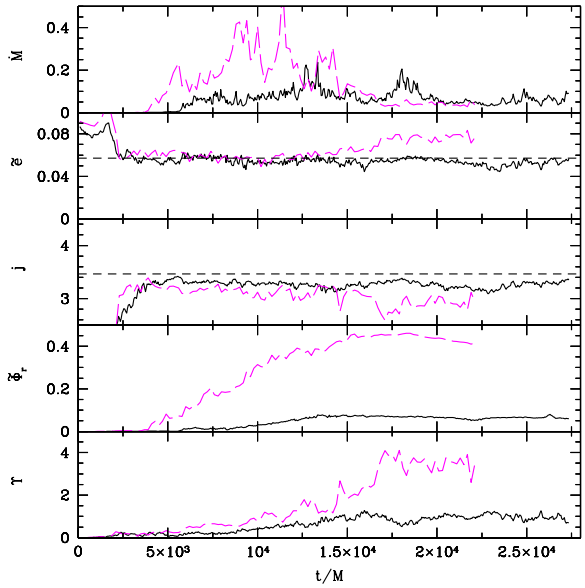

Fig. 2.23.— Similar to Figure 2.7, but here we compare the initial 4-loop fiducial model (black solid lines) and the 1-loop model (dashed magenta lines). The horizontal black dashed lines in the second and third panels show the predictions of the NT model. The mass accretion rate, $\dot{M}$, has larger root-mean-squared fluctuations in the 1-loop model, which is indicative of more vigorous turbulence. The nominal efficiency, $\tilde{e}$, shows no clear difference. The specific angular momentum, $\jmath$, is lower in the 1-loop model compared to the 4-loop model. This indicates that the 1-loop field leads to larger stress within the ISCO. The absolute magnetic flux (per unit initial total absolute flux) on the black hole is larger in the 1-loop model than the 4-loop model. Since $\tilde{\Phi}_r \sim 1/2$ for the 1-loop model, essentially half of the initial loop was advected onto the black hole, while the other half gained angular momentum and has been advected away. This may indicate that the 1-loop geometry is a poor choice for the initial field geometry, since the magnetic flux that ends up on the black hole is determined by the initial conditions. For times $12900M$ to $17300M$, the value of Υ is about twice higher in the 1-loop model, which implies about twice greater electromagnetic stresses within the ISCO.

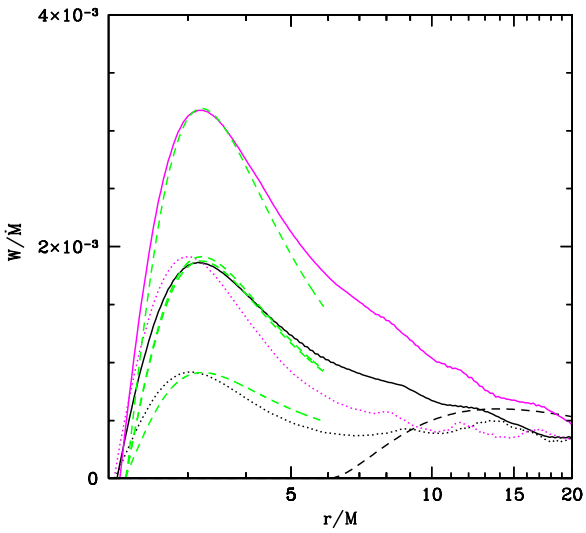

Fig. 2.24.— Normalized electromagnetic stress, $W/\dot{M}$, as a function of radius for the fiducial model (black lines) and the otherwise identical 1-loop model (magenta lines). The solid lines correspond to a θ integration over all angles, while the dotted lines correspond to a θ integration over $\pm 2|h/r|$. The dashed line shows the NT result, while the dashed green lines show the Gammie (1999) result for $\Upsilon = 0.60, 0.89, 0.90, 1.21$ for lines from the bottom to the top. The Gammie (1999) model gives a reasonable fit to the simulation's stress profile within the ISCO. The 1-loop model shows about 50% larger peak normalized stress (integrated over all angles) compared to the multi-loop model (integrated over all angles), which is consistent with the 1-loop model leading to larger deviations from NT (about 50% larger luminosity over the period used for time averaging). The large differences between the solid and dotted lines again highlights the fact that the stress within the disk is much smaller than the stress over all θ that includes the corona+wind+jet. As pointed out in S08, even though such a plot of the electromagnetic stress appears to indicate large deviations from NT within the ISCO, this is misleading because one has not specified the quantitative effect of the non-zero value of $W/\dot{M}$ on physical quantities within the ISCO. Apparently large values of $W/\dot{M}$ do not necessarily correspond to large deviations from NT. For example, quantities such as $\jmath$, e, and the luminosity only deviate by a few percent from NT for the multi-loop model.

Chapter 3

Beyond Novikov-Thorne Disks I: Torque at the ISCO

3.1 Introduction

The standard model for relativistic, thin disk accretion onto a black hole is the Novikov-Thorne (NT) model (Novikov & Thorne 1973; Page & Thorne 1974). It is the relativistic generalization of the Shakura & Sunyaev (1973) α-disk. The black hole is described by the Kerr metric with fixed mass, M, and specific angular momentum, a. The accretion flow is razor thin and confined to the equatorial plane so heat advection is negligible and vertical and radial energy transport can be decoupled. The disk has an inner edge at the innermost stable circular orbit (ISCO) where viscous stresses are assumed to vanish. Mass is accreted at a rate $\dot{M}$ as stresses and radiation transport energy and angular momentum outwards. The NT disk has four free parameters: M, a, $\dot{M}$, and α.

Slim disk models generalize the NT model to include heat advection and coupled radial and vertical energy transport. They are solved numerically by requiring the flow to pass smoothly through a sonic point (Abramowicz et al. 1988; Paczyński 2000; Afshordi & Paczyński 2003; Shafee et al. 2008b; Sądowski 2009; Abramowicz et al. 2010; Sądowski et al. 2011). They have the same free parameters as the NT disk.

General relativistic, magnetohydrodynamic (GRMHD) thin disk simulations (Shafee et al. 2008a; Noble & Krolik 2009; Noble et al. 2010; Penna et al. 2010) incorporate magnetic fields and turbulence is driven by the magnetorotational instability (MRI) (Balbus & Hawley 1991, 1998). Radiation physics is described in an ad-hoc way as a sink term in the energy equation that tends to drive the entropy of the fluid towards a target, K_c. The MRI generates turbulence self-consistently, so the α-viscosity prescription is not used. However the strength of the saturated magnetic stresses, the "effective α," depends on the gas-to-magnetic pressure ratio, β_i, of the initial fields in the simulation. So the target entropy, K_c, plays a similar role to $\dot{M}$, and β_i is analogous to α.

Noble et al. (2010) presented simulations of GRMHD disks with different thicknesses and compared their stress profiles. They argued there is a large stress at the inner edge even in the limit of vanishing disk opening angle $h \to 0$. They concluded magnetized disks cannot be described by the NT model independently of disk thickness. Penna et al. (2010) performed similar simulations but found the stress at the inner edge to be directly proportional to thickness. They argued the NT zero-stress boundary condition is valid in the limit $h \to 0$. We believe the difference is in their definitions of the stress. Noble et al. (2010) included all of the fluid. Penna et al. (2010) made a distinction between the high density disk region and the low density, highly magnetized, coronal region. They included only disk fluid in stress calculations. The corona, if it is included, makes a large contribution to the stress.

The present model only describes the high-density disk region, which is expected to dominate the emission leading to the observed thermal spectral component. The corona is expected to contribute mostly to non-thermal spectral components. So the Penna et al. (2010) result that stress scales with h is the relevant one.

Our model includes a nonzero stress at the inner edge of the disk. Nonzero stress boundary conditions have been previously considered in the context of Newtonian (Shapiro & Teukolsky 1983) and general relativistic (Agol & Krolik 2000) accretion. However, the stress at the inner edge is a free parameter in these models. We eliminate this parameter by identifying the inner edge with the sonic point and relating the stress there to the sound speed. This prescription reduces to the NT zero-torque boundary condition in the razor thin limit $h \to 0$.

In the next section we describe the differences between our model and NT. In §3.3 we give the explicit disk solution. In §3.4 we compare it to slim disk models and in §3.5 we compare it to GRMHD disk simulations. We summarize our main results in §3.6. The Kerr metric and the disk structure equations are summarized in the appendices. A Fortran code which computes our thin disk solutions is available at `https://www.cfa.harvard.edu/~rpenna/thindisk`.

3.2 Physics beyond the standard disk model

Our model extends the NT model in three ways: (i) it incorporates nonzero stresses at the inner edge of the disk, (ii) it extends into the plunging region, and (iii) it uses the correct vertical gravity formula. In this section we discuss each of these developments.

3.2.1 The inner edge boundary condition

The criterion $h \ll \alpha$, where h is the disk opening angle ($h = H/r$) and α is the "effective viscosity" parameter (cf. §3.5), governs the structure of weakly-magnetized GRMHD disk simulations. When the disk is thin, $h \ll \alpha$, the surface density has an inner edge near the sonic point. When the disk is thick, $h \gg \alpha$, advection causes the disk density to increase monotonically down to the event horizon. This is illustrated in Figures 3.1 and 3.2, which show time-averaged rest mass density in the $r - z$ plane for eight GRMHD simulations. Rest mass density drops as the disk approaches the sonic point if and only if $h \ll \alpha$.

Thick disks are non-Keplerian and insensitive to the ISCO. The sonic point and ISCO only coincide if the disk is thin. Abramowicz et al. (2010) find the Boyer-Lindquist radial positions of the sonic point and ISCO deviate by $< 3\%$, independently of α, for $a_* = 0$ slim disks with $\dot{M}/\dot{M}_{\rm edd} < 0.3$.

Summarizing these two observations: the inner edge, sonic point, and ISCO are at the same radius if $h \ll \alpha$ and $\dot{M}/\dot{M}_{\rm edd} < 0.3$. We will assume these conditions hold for thin disks. Under these conditions, energy advection and energy generation by compression, which scale as h^2, can be neglected relative to boundary stresses at the ISCO, which scale as αh. We give a proof in

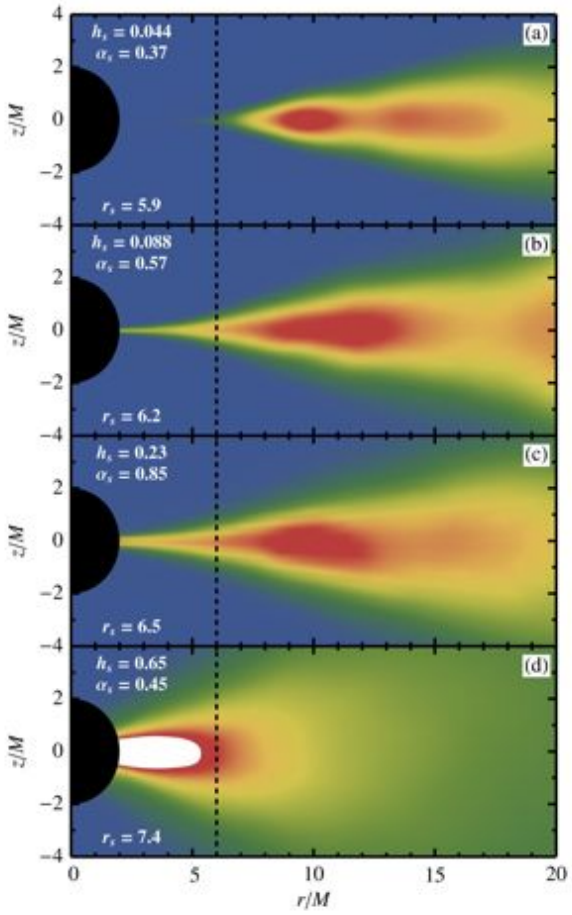

Fig. 3.1.— Time-averaged rest mass density in the $r - z$ plane for four GRMHD simulations with $a_* = 0$ and various disk thicknesses. The dashed vertical line marks the ISCO. The disk opening angle, h, and effective Shakura-Sunyaev viscosity, α, are measured at the sonic point, r_0 (cf. §3.5). The top three panels have $h \ll \alpha$ and the inner edge of the disk is located outside the ISCO. The lowermost panel has $h \gg \alpha$ and the density increases monotonically down to the event horizon. Panels (a) and (b) are the thin and thick $a_* = 0$ simulations of Kulkarni et al. (2011b). Panels (c) and (d) are models A0HR2 and A0HR3, respectively, from Penna et al. (2010).

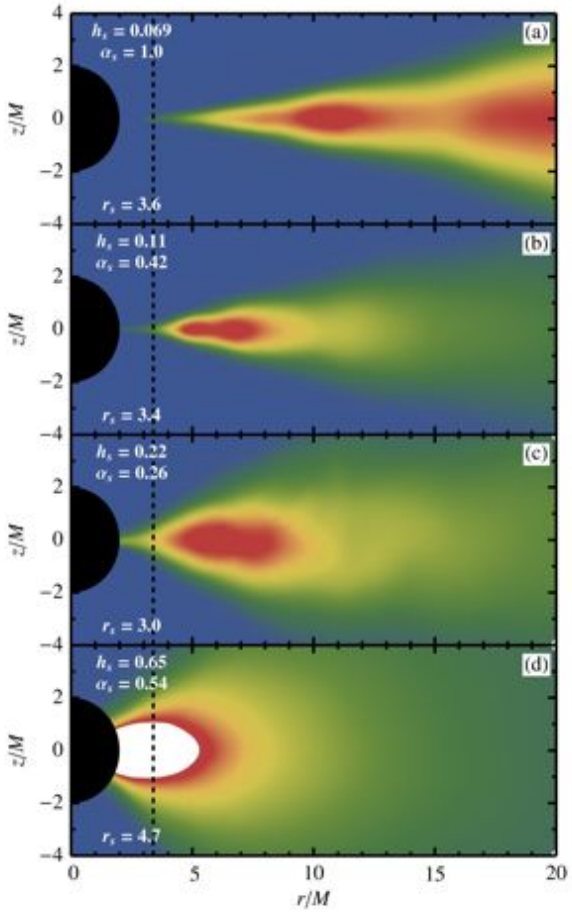

Fig. 3.2.— Same as Figure 3.1 but with $a_* = 0.7$. Panel (a) is the $a_* = 0.7$ simulation of Kulkarni et al. (2011b). Panels (b), (c), and (d) are models A7HR1, A7HR2, and A7HR3, respectively, from Penna et al. (2010).

Appendix 3.C. The NT model ignores boundary stresses at the ISCO, which is valid in the limit $h \to 0$. By including them, we obtain disk solutions with nonzero stress and flux at the ISCO, and radial velocity and surface density profiles that can be extended into the plunging region.

3.2.2 The plunging region

We assume magnetic fields are weak and plunging region stresses are small, so the fluid motion inside the ISCO can be approximated by geodesics. Krolik (1999) argued magnetic fields are always dynamically important inside the ISCO and geodesic trajectories are never a good approximation there. However we will show in §3.5 that our solution gives a good fit to the radial velocity profile of the fiducial $a_* = 0$ GRMHD simulation of Kulkarni et al. (2011b). So GRMHD disks do exist in which the field is sufficiently weak inside the ISCO that geodesic motion is a good approximation.

To solve the geodesic equations (3.21a)-(3.21c) for the fluid motion, we need to fix the fluid energy $E = |u_t|$ and angular momentum $L = u_\phi$. We assume the fluid plunges with constant E and L, so it suffices to fix the fluid energy and angular momentum at the ISCO. Equivalently, it is enough to specify the fluid velocity at the ISCO.

We assume the angular velocity at the ISCO is Keplerian (3.24) and the disk is in the equatorial plane, so $u^\theta = 0$. The radial velocity at the ISCO is the sound speed (cf. §3.2.1):

$$V_0 = \left(h \frac{\mathcal{L}_*}{r} \right)_0 . \tag{3.1}$$

This is the radial velocity in the fluid frame. It is related to u^r by $V = \sqrt{g_{rr}} u^r / \left(1 + \left(\sqrt{g_{rr}} u^r \right)^2 \right)^{1/2}$.

The flow inside the ISCO is now fixed by the disk structure equations. See Appendix 3.B for details.

3.2.3 Vertical gravity

NT gave an incorrect formula for the "vertical gravity" appearing in the pressure balance equation, creating errors in the disk solution. Better formulae for the vertical gravity were found by Eardley & Lightman (1975) and Riffert & Herold (1995). However they assume the disk follows circular

geodesics, so their results break down in the plunging region. Abramowicz et al. (1997) found a more general formula which is valid in the plunging region. We use this result in the disk structure equations (3.40).

3.3 Explicit disk solutions

The model has four free parameters:

$$M = \text{mass of black hole},$$
$$a = \text{specific angular momentum of hole},$$
$$\dot{M} = \text{accretion rate},$$
$$\alpha = \text{Shakura-Sunyaev viscosity}.$$

These are taken to be constants. Following NT, we shall express M in units of $3M_\odot$ and we shall express $\dot{M}$ in units of 10^{17} g/sec:

$$M_* \equiv M/3M_\odot, \quad \dot{M}_* \equiv \dot{M}/10^{17} \text{ g sec}^{-1}.$$

The metric and disk structure equations are summarized in Appendices 3.A and 3.B. In this section we give the solutions for the quantities that appear in the structure equations[1] : flux of radiant energy off the upper surface of the disk, F, surface density, Σ, disk thickness, H, rest mass density in the local rest frame, ρ, temperature, T, and radial velocity in the locally nonrotating frame, $v^{\hat{r}}$. In addition to quantities that appear explicitly in the equations of structure, we calculate the optical depth at the center of the disk,

$$\tau = \bar{\kappa}\Sigma, \tag{3.2}$$

[1] A Fortran code which computes our thin disk solutions is available at `https://www.cfa.harvard.edu/~rpenna/thindisk`.

and the characteristic timescale for the gas to move inward from radius r to the inner edge of the disk,

$$\Delta t(r) = -r/v^{\hat{r}}. \tag{3.3}$$

The disk outside the ISCO can be divided into 4 regions: an "outer region" (large radii) in which gas pressure dominates over radiation pressure, and in which the opacity is predominantly free-free; a "middle region" (smaller radii) in which gas pressure dominates over radiation pressure, but opacity is predominantly due to electron scattering; an "inner region" (even smaller radii) in which radiation pressure dominates over gas pressure, and opacity is predominantly due to electron scattering; and an "edge region" (smallest radii) where gas pressure again dominates over radiation pressure, and opacity is predominantly due to electron scattering.

The NT model does not include the edge region explicitly. However it must exist because the no-torque boundary condition implies radiant flux and radiation pressure go to zero at the ISCO. The NT inner region surface density is singular at the ISCO because of this inconsistency. The edge region surface density is finite in the NT limit.

The solutions are functions of the dimensionless radial coordinate $x = \sqrt{r/M}$. Calligraphic letters denote functions of x and a with value unity far from the hole. A subscript 0 indicates the quantity is evaluated at the ISCO.

3.3.1 Plunging region

$p = p^{(\mathrm{gas})}$, $\bar{\kappa} = \bar{\kappa}_{es}$. In this region the equations of structure (3.37)-(3.44) yield the following radial profiles:

$$F = \left(2 \times 10^{18}\ \mathrm{erg/cm^2\ sec}\right) \left(\alpha^{4/3} M_*^{-3} \dot{M}_* 5/3\right) x^{-26/3} x_0^{4/3} \mathcal{D}^{-5/6} \mathcal{K}^{4/3} \mathcal{F}_0^{4/3} \mathcal{G}_0^{-4/3} v_*^{-5/3}, \tag{3.4a}$$

$$\Sigma = \left(1\ \mathrm{g/cm^2}\right) \left(M_*^{-1} \dot{M}_*\right) x^{-2} \mathcal{D}^{-1/2} v_*^{-1}, \tag{3.4b}$$

$$H = (60\ \mathrm{cm}) \left(\alpha^{1/6} M_*^{1/2} \dot{M}_*^{1/3}\right) x^{8/3} x_0^{-5/6} \mathcal{D}^{-1/6} \mathcal{K}^{1/6} \mathcal{F}_0^{1/6} \mathcal{G}_0^{-1/6} \mathcal{R}_0^{-1/2} v_*^{-1/3} \tag{3.4c}$$

$$\rho = \left(0.01\ \mathrm{g/cm^3}\right) \left(\alpha^{-1/6} M_*^{-3/2} \dot{M}_*^{2/3}\right) x^{-14/3} x_0^{5/6} \mathcal{D}^{-1/3} \mathcal{K}^{-1/6} \mathcal{F}_0^{-1/6} \mathcal{G}_0^{1/6} \mathcal{R}_0^{1/2} v_*^{-2/3} \tag{3.4d}$$

$$T = \left(2 \times 10^5\ \mathrm{K}\right) \left(\alpha^{1/3} M_*^{-1} \dot{M}_*^{2/3}\right) x^{-8/3} x_0^{1/3} \mathcal{D}^{-1/3} \mathcal{K}^{1/3} \mathcal{F}_0^{1/3} \mathcal{G}_0^{-1/3} v_*^{-2/3} \tag{3.4e}$$

$$\tau_{es} = 0.3 \left(M_*^{-1}\dot{M}_*\right) x^{-2}\mathcal{D}^{-1/2} v_*^{-1}, \tag{3.4f}$$

$$\Delta t(r) = \left(1\times 10^{-5}\ \mathrm{sec}\right)(M_*)\, x^2 v_*^{-1}, \tag{3.4g}$$

$$v^{\hat{r}} = -\left(3\times 10^{10}\ \mathrm{cm/sec}\right) v_*. \tag{3.4h}$$

We have defined the dimensionless radial velocity profile:

$$v_* = \left(\left[\mathcal{C}_0^{-1}\mathcal{G}_0^2\mathcal{V}-1\right] + \left(7\times 10^{-3}\right)\left(\alpha^{1/4}M_*^{-3/4}\dot{M}_*^{1/2}\right) x_0^{-7/4}\mathcal{C}_0^{-5/4}\mathcal{D}_0^{-1}\mathcal{G}_0^2\mathcal{V}\right)^{1/2} \tag{3.5}$$

The term in square brackets dominates near the horizon. The term proportional to $\dot{M}$ dominates near the ISCO. At the horizon the radial velocity is c and at the ISCO it is the sound speed. In the limit $\dot{M}/\dot{M}_{\rm edd}\to 0$, we may set $v_* = \left[\mathcal{C}_0^{-1}\mathcal{G}_0^2\mathcal{V}-1\right]^{1/2}$ and the gas is released from rest at the ISCO.

3.3.2 Edge region

$p = p^{(\rm gas)}$, $\bar{\kappa} = \bar{\kappa}_{es}$. In this region the equations of structure (3.37)-(3.44) yield:

$$F = \left(0.6\times 10^{26}\ \mathrm{erg/cm^2\ sec}\right)\left(M_*^{-2}\dot{M}_*\right) x^{-6}\mathcal{B}^{-1}\mathcal{C}^{-1/2}\Phi, \tag{3.6a}$$

$$\Sigma = \left(5\times 10^{4}\ \mathrm{g/cm^2}\right)\left(\alpha^{-4/5}M_*^{-2/5}\dot{M}_*^{3/5}\right) x^{-6/5}\mathcal{B}^{-4/5}\mathcal{C}^{-1/2}\mathcal{D}^{-4/5}\Phi^{3/5}, \tag{3.6b}$$

$$H = \left(3\times 10^{3}\ \mathrm{cm}\right)\left(\alpha^{-1/10}M_*^{7/10}\dot{M}_*^{1/5}\right) x^{21/10}\mathcal{A}\mathcal{B}^{-6/5}\mathcal{C}^{1/2}\mathcal{D}^{-3/5}\mathcal{S}^{-1/2}\Phi^{1/5}, \tag{3.6c}$$

$$\rho = \left(10\ \mathrm{g/cm^3}\right)\left(\alpha^{-7/10}M_*^{-11/10}\dot{M}_*^{2/5}\right) x^{-33/10}\mathcal{A}^{-1}\mathcal{B}^{3/5}\mathcal{D}^{-1/5}\mathcal{S}^{1/2}\Phi^{2/5}, \tag{3.6d}$$

$$T = \left(3\times 10^{8}\ \mathrm{K}\right)\left(\alpha^{-1/5}M_*^{-3/5}\dot{M}_*^{2/5}\right) x^{-9/5}\mathcal{B}^{-2/5}\mathcal{D}^{-1/5}\Phi^{2/5}, \tag{3.6e}$$

$$\tau_{es} = \left(2\times 10^{4}\right)\left(\alpha^{-4/5}M_*^{-2/5}\dot{M}_*^{3/5}\right) x^{-6/5}\mathcal{B}^{-3/5}\mathcal{C}^{1/2}\mathcal{D}^{-4/5}\Phi^{3/5}, \tag{3.6f}$$

$$\frac{\tau_{ff}}{\tau_{es}} = \left(0.6\times 10^{-5}\right)\left(M_*\dot{M}_*^{-1}\right) x^{3}\mathcal{A}^{-1}\mathcal{B}^{2}\mathcal{D}^{1/2}\mathcal{S}^{1/2}\Phi^{-1}, \tag{3.6g}$$

$$\Delta t(r) = \left(0.7\ \mathrm{sec}\right)\left(\alpha^{-4/5}M_*^{8/5}\dot{M}_*^{-2/5}\right) x^{14/5}\mathcal{B}^{-4/5}\mathcal{C}^{1/2}\mathcal{D}^{-3/10}\Phi^{3/5}, \tag{3.6h}$$

$$v^{\hat{r}} = -\left(6\times 10^{5}\ \mathrm{cm/sec}\right)\left(\alpha^{4/5}M_*^{-3/5}\dot{M}_*^{2/5}\right) x^{-4/5}\mathcal{B}^{4/5}\mathcal{C}^{-1/2}\mathcal{D}^{3/10}\Phi^{-3/5}. \tag{3.6i}$$

We have defined a new function:

$$\Phi = \mathcal{Q} + (0.02)\left(\alpha^{9/8}M_*^{-3/8}\dot{M}_*^{1/4}\right) x^{-1}\mathcal{B}\mathcal{C}^{-1/2}\left(x_0^{9/8}\mathcal{C}_0^{-5/8}\mathcal{G}_0\mathcal{V}_0^{1/2}\right), \tag{3.7}$$

which controls the shape of the radiant flux profile, $F(r)$. At large distances, the first term on the RHS is order unity, and the second term decays as x^{-1}. Near the ISCO, the first term goes to

zero, and the second term is nonzero and proportional to $\dot{M}^{1/4}$. So if $\dot{M}/\dot{M}_{\rm edd}$ is small, then the second term is small everywhere and we may substitute $\Phi \to \mathcal{Q}$. This gives the NT flux. Quantities which depend on $\mathcal{S}$ will still differ from NT because our vertical gravity prescription is different (cf. §3.2.3). We may revert to the incorrect NT vertical gravity with the substitution $\mathcal{S} \to \mathcal{E}$. With these two substitutions our model becomes the NT solution outside the plunging region.

3.3.3 Inner region

$p = p^{(\rm rad)}$, $\bar{\kappa} = \bar{\kappa}_{es}$. In this region the equations of structure (3.37)-(3.44) yield:

$$F = \left(0.6 \times 10^{26}\ \mathrm{erg/cm^2\ sec}\right) \left(M_*^{-2}\dot{M}_*\right) x^{-6}\mathcal{B}^{-1}\mathcal{C}^{-1/2}\Phi, \tag{3.8a}$$

$$\Sigma = \left(20\ \mathrm{g/cm^2}\right) \left(\alpha^{-1}M_*\dot{M}_*^{-1}\right) x^{3}\mathcal{A}^{-2}\mathcal{B}^{3}\mathcal{C}^{1/2}\mathcal{S}\Phi^{-1}, \tag{3.8b}$$

$$H = \left(1 \times 10^{5}\ \mathrm{cm}\right) \left(\dot{M}_*\right) \mathcal{A}^{2}\mathcal{B}^{-3}\mathcal{C}^{1/2}\mathcal{D}^{-1}\mathcal{S}^{-1}\Phi, \tag{3.8c}$$

$$\rho = \left(1 \times 10^{-4}\ \mathrm{g/cm^3}\right) \left(\alpha^{-1}M_*\dot{M}_*^{-2}\right) x^{3}\mathcal{A}^{-4}\mathcal{B}^{6}\mathcal{D}\mathcal{S}^{2}\Phi^{-2}, \tag{3.8d}$$

$$T = \left(4 \times 10^{7}\ \mathrm{K}\right) \left(\alpha^{-1/4}M_*^{-1/4}\right) x^{-3/4}\mathcal{A}^{-1/2}\mathcal{B}^{1/2}\mathcal{S}^{1/4}, \tag{3.8e}$$

$$\tau_{es} = 8 \left(\alpha^{-1}M_*\dot{M}_*^{-1}\right) x^{3}\mathcal{A}^{-2}\mathcal{B}^{3}\mathcal{C}^{1/2}\mathcal{S}\Phi^{-1}, \tag{3.8f}$$

$$\frac{p^{(\rm gas)}}{p^{(\rm rad)}} = \left(5 \times 10^{-5}\right) \left(\alpha^{-1/4}M_*^{7/4}\dot{M}_*^{-2}\right) x^{21/4}\mathcal{A}^{-5/2}\mathcal{B}^{9/2}\mathcal{D}\mathcal{S}^{5/4}\Phi^{-2}, \tag{3.8g}$$

$$\Delta t(r) = \left(2 \times 10^{-4}\ \mathrm{sec}\right) \left(\alpha^{-1}M_*^{3}\dot{M}_*^{-2}\right) x^{7}\mathcal{A}^{-2}\mathcal{B}^{3}\mathcal{C}^{1/2}\mathcal{D}^{1/2}\mathcal{S}\Phi^{-1}, \tag{3.8h}$$

$$v^{\hat{r}} = -\left(2 \times 10^{9}\ \mathrm{cm/sec}\right) \left(\alpha M_*^{-2}\dot{M}_*^{2}\right) x^{-5}\mathcal{A}^{2}\mathcal{B}^{-3}\mathcal{C}^{-1/2}\mathcal{D}^{-1/2}\mathcal{S}^{-1}\Phi. \tag{3.8i}$$

$$\tag{3.8j}$$

The boundaries between the edge, inner, and middle regions can be computed from the ratio of pressures (3.8g).

3.3.4 Middle region

$p = p^{(\rm gas)}$, $\bar{\kappa} = \bar{\kappa}_{es}$. The solution is the same as the edge region solution (cf. §3.3.2).

3.3.5 Outer region

$p = p^{(\rm gas)}$, $\bar{\kappa} = \bar{\kappa}_{ff}$. In this region the equations of structure (3.37)-(3.44) yield:

$$F = \left(0.6 \times 10^{26}\ \mathrm{erg/cm^2\ sec}\right) \left(M_*^{-2}\dot{M}_*\right) x^{-6}\mathcal{B}^{-1}\mathcal{C}^{-1/2}\Phi, \tag{3.9a}$$

$$\Sigma = \left(2 \times 10^5\ \mathrm{g/cm^2}\right) \left(\alpha^{-4/5}M_*^{-1/2}\dot{M}_*^{7/10}\right) x^{-3/2}\mathcal{A}^{1/10}\mathcal{B}^{-4/5}\mathcal{C}^{1/2}\mathcal{D}^{-17/20}\mathcal{S}^{-1/20}\Phi^{7/10}, \tag{3.9b}$$

$$H = \left(9 \times 10^2\ \mathrm{cm}\right) \left(\alpha^{-1/10}M_*^{3/4}\dot{M}_*^{3/20}\right) x^{9/4}\mathcal{A}^{19/20}\mathcal{B}^{-11/10}\mathcal{C}^{1/2}\mathcal{D}^{-23/40}\mathcal{S}^{-19/40}\Phi^{3/20}, \tag{3.9c}$$

$$\rho = \left(80\ \mathrm{g/cm^3}\right) \left(\alpha^{-7/10}M_*^{-5/4}\dot{M}_*^{11/20}\right) x^{-15/4}\mathcal{A}^{-17/20}\mathcal{B}^{3/10}\mathcal{D}^{-11/40}\mathcal{S}^{17/40}\Phi^{11/20}, \tag{3.9d}$$

$$T = \left(8 \times 10^7\ \mathrm{K}\right) \left(\alpha^{-1/5}M_*^{-1/2}\dot{M}_*^{3/10}\right) x^{-3/2}\mathcal{A}^{-1/10}\mathcal{B}^{-1/5}\mathcal{D}^{-3/20}\mathcal{S}^{1/20}\Phi^{3/10}, \tag{3.9e}$$

$$\tau_{ff} = \left(2 \times 10^2\right) \left(\alpha^{-4/5}\dot{M}_*^{1/5}\right) \mathcal{A}^{-2/5}\mathcal{B}^{1/5}\mathcal{C}^{1/2}\mathcal{D}^{-3/5}\mathcal{S}^{1/5}\Phi^{1/5}, \tag{3.9f}$$

$$\frac{\tau_{ff}}{\tau_{es}} = 3 \times 10^{-3} \left(M_*^{1/2}\dot{M}_*^{-1/2}\right) x^{3/2}\mathcal{A}^{-1/2}\mathcal{B}^{2/5}\mathcal{D}^{1/4}\mathcal{S}^{1/4}\Phi^{-1/2}, \tag{3.9g}$$

$$\Delta t(r) = \left(2\ \mathrm{sec}\right) \left(\alpha^{-4/5}M_*^{3/2}\dot{M}_*^{-3/10}\right) x^{5/2}\mathcal{A}^{1/10}\mathcal{B}^{-4/5}\mathcal{C}^{1/2}\mathcal{D}^{-7/20}\mathcal{S}^{-1/20}\Phi^{7/10}, \tag{3.9h}$$

$$v^{\hat{r}} = -\left(2 \times 10^5\ \mathrm{cm/sec}\right) \left(\alpha^{4/5}M_*^{-1/2}\dot{M}_*^{3/10}\right) x^{-1/2}\mathcal{A}^{-1/10}\mathcal{B}^{4/5}\mathcal{C}^{-1/2}\mathcal{D}^{7/20}\mathcal{S}^{1/20}\Phi^{-7/10}. \tag{3.9i}$$

$$\tag{3.9j}$$

3.4 Comparison with slim disk models

Slim disk solutions include advection. They are computed numerically subject to the condition that the flow pass smoothly through a sonic point. The position of the sonic point is free to vary. A model for energy transport in the vertical direction, including radiative transport and convection, is coupled to the radial equations. For a complete description see Sądowski et al. (2011).

When in the thin disk regime, $h \ll \alpha$ and $\dot{M}/\dot{M}_{\rm edd} < 0.3$, the sonic point is near the ISCO and advection can be neglected (cf. §3.2.1). This enables the analytical solution of §3.3. So we expect our model and slim disk models to be similar under these conditions. We make this comparison in Figures 3.3 and 3.4. The NT disk is also included.

The disk solutions in Figure 3.3 have $M = 10M_\odot$, $a_* = 0$, $\alpha = 0.1$ and $\dot{M}/\dot{M}_{\rm edd} = 0.3$. Our model and slim disk solutions are in good agreement inside the ISCO where the NT model does

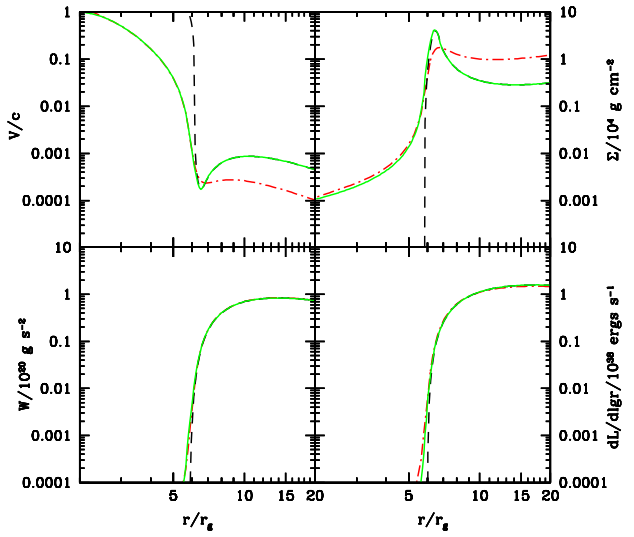

Fig. 3.3.— Radial velocity, surface density, stress, and luminosity versus radius for three disk models: NT (dashed black), slim disk (dot-dashed red), and our generalized thin disk (solid green). These solutions have $M = 10M_{\odot}$, $a_* = 0$, $\alpha = 0.1$, and $\dot{M}/\dot{M}_{\rm edd} = 0.3$. The NT solution terminates at the ISCO but the slim disk and our model continue to the event horizon.

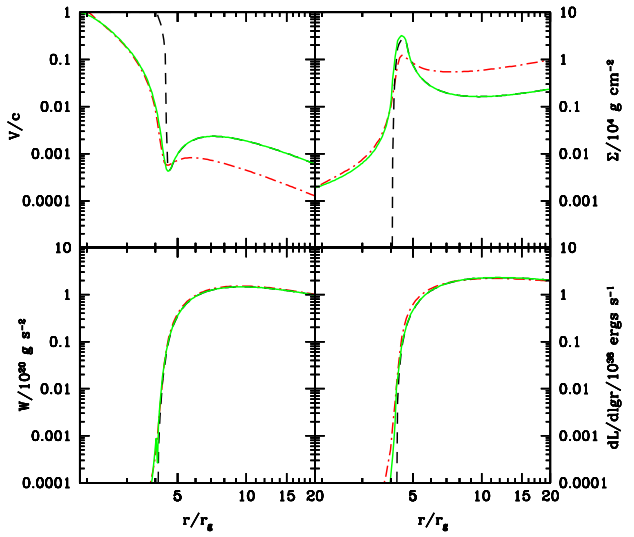

Fig. 3.4.— Same as Figure 3.3 but with $a_* = 0.5$.

not extend. The slim disk surface density is larger outside the ISCO because it includes both radiation and gas pressure (which are comparable there), while the analytical disk models include only radiation pressure at these radii. All three models eventually converge at large radii. Figure 3.4 is the same except with $a_* = 0.5$.

3.5 Comparison with GRMHD simulations

In this section, we compare the fiducial, $a_* = 0$ GRMHD simulation of Kulkarni et al. (2011b) with analytical thin disk solutions. The target entropy in the GRMHD cooling function was $K_c = 0.00034$ and the gas-to-magnetic pressure ratio of the initial fields in the simulation was $\beta_i = 100$. These parameters play similar roles to $\dot{M}$ and α in the thin disk solutions. The simulation reached $t = 26300M$. At large radii, the viscous timescale is long and the solution is not converged. The estimates in Penna et al. (2010) suggest steady state is reached out to $r = 9M$.

3.5.1 Hydrostatic equilibrium of GRMHD disks

In hydrostatic equilibrium, opening angle is related to pressure and density by (3.40):

$$h = \sqrt{\frac{p}{\rho}} \frac{r}{\mathcal{L}_*}, \tag{3.10}$$

where $\mathcal{L}_*^2 = u_\phi^2 - a^2 (u_t - 1)$ (Abramowicz et al. 1997). Our thin disk solutions assume hydrostatic equilibrium even inside the plunging region, so we first check whether this is a good description of GRMHD disks.

A popular definition of opening angle for GRMHD disks is (Penna et al. 2010; Noble et al. 2010; Shafee et al. 2008a):

$$h^{(\mathrm{rms})} \equiv \left(\frac{\int (\theta - \pi/2)^2 \rho \sqrt{-g} dt d\theta d\phi}{\int \rho \sqrt{-g} dt d\theta d\phi} \right)^{1/2}. \tag{3.11}$$

In Figure 3.5, we compare $h^{(\mathrm{rms})}$ for the fiducial GRMHD disk (dotted red) with the RHS of (3.10), the opening angle expected from hydrostatic equilibrium (dot-dashed blue). The later is computed from the rest mass density and total pressure at the midplane. (Replacing midplane values with

density-weighted vertical averages has little effect.) Hydrostatic equilibrium appears to be a bad approximation in the plunging region, where it gives the wrong opening angle by as much as a factor of 4.

The simulation's high density, gas pressure dominated disk is surrounded by a low density, magnetically supported corona. These two regions have different scale heights and the apparent deviations from hydrostatic equilibrium could be a result of mixing them in the definition of opening angle. Our thin disk model only applies to the disk region, so we would like to minimize the contribution of the corona. We can do this by weighting the integrals in (3.11) with higher powers of ρ, because this concentrates attention on high density regions. Unfortunately, the opening angle then depends on this choice: higher powers of ρ give smaller opening angles. To get an invariant measure, we normalize the opening angle as follows. The vertical density profile of a polytropic gas in hydrostatic equilibrium is

$$\rho(z) = \rho(z=0)\left(1 - \frac{(z/r)^2}{\mathcal{H}^2}\right)^N, \tag{3.12}$$

where $\mathcal{H}$ is the opening angle. The simulation has $\Gamma = 1 + 1/N = 4/3$, so $N = 3$. We normalize our definition of opening angle such that it returns $\mathcal{H}$ when given the analytical solution (3.12). So the normalized, ρ^2-weighted opening angle is

$$h_2^{(\mathrm{rms})} \equiv \frac{\sqrt{15}}{3}\left(\frac{\int (\theta - \pi/2)^2 \rho^2 \sqrt{-g} dt d\theta d\phi}{\int \rho^2 \sqrt{-g} dt d\theta d\phi}\right)^{1/2}, \tag{3.13}$$

where $\sqrt{15}/3$ is the the normalization defined by (3.12).

We plot $h_2^{(\mathrm{rms})}$ for the fiducial GRMHD simulation in Figure 3.5 (solid black). It is within 30% of the opening angle expected from hydrostatic equilibrium (dot-dashed blue) at all converged radii. Emphasizing the disk over the corona has removed the discrepancy and shows that hydrostatic equilibrium is a good approximation in the disk region. From now on, we define the GRMHD opening angle to be $h = h_2^{(\mathrm{rms})}$.

3.5.2 The boundary between disk and corona

The boundary between disk and corona can be identified with the contour where the gas-to-magnetic pressure ratio $\beta = 1$, where the pressure switches from predominantly gas to magnetic. This is

plotted in green in Figure 3.6. The corona is located approximately $2h$ away from the midplane (blue contour). The flow is turbulent in the disk and laminar in the corona because strong fields are stabilized against the MRI by magnetic tension (Pessah & Psaltis 2005). Working in the Boussinesq approximation and ignoring magnetic curvature terms, Balbus & Hawley (1991, 1998) argued the MRI cannot operate when $\beta < 1$.

The plunging region inside the ISCO is similar to the corona, although it is highly magnetized for a different reason. The corona is highly magnetized because magnetic buoyancy raises fields out of the disk. The region inside the ISCO is highly magnetized because plunging fluid stretches frozen-in field lines.

3.5.3 Effective α

Viscosity in the simulation is generated by MRI-driven turbulence. We define the effective α:

$$\alpha \equiv \frac{\langle W \rangle}{2 \langle p \rangle hr}. \tag{3.14}$$

The height integrated stress, $\langle W \rangle$, is computed from the GRMHD stress-energy tensor (Penna et al. 2010):

$$\langle W \rangle = \frac{1}{2\pi\Delta t} \int_t^{t+\Delta t} \int_{\pi/2-2h}^{\pi/2+2h} \int_0^{2\pi} T^{\rm GRMHD}_{\hat{r}\hat{\phi}} \sqrt{-g} dt d\theta d\phi. \tag{3.15}$$

The pressure, $\langle p \rangle$, is a ρ^2-weighted height average:

$$\langle p \rangle = \frac{\int p\rho^2 \sqrt{-g} dt d\theta d\phi}{\int \rho^2 \sqrt{-g} dt d\theta d\phi}. \tag{3.16}$$

The effective α is plotted as a function of radius in Figure 3.7. We use $\alpha = 0.3$, the effective α at the ISCO, to compare thin disk solutions with the GRMHD disk.

3.5.4 Comparison

Figure 3.8 compares the GRMHD disk to thin disk solutions with $M = 10M_\odot$. We assume $\dot{M}/\dot{M}_{\rm edd} = 0.5$, which Kulkarni et al. (2011b) estimated to be the effective accretion rate of this simulation. The GRMHD profiles are only shown out to $r = 9M$ because the simulations are

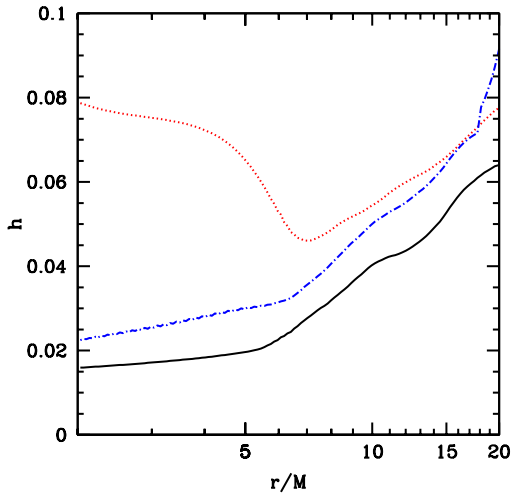

Fig. 3.5.— Unnormalized, ρ-weighted opening angle $h^{(\mathrm{rms})}$ (dotted red), normalized, ρ^2-weighted opening angle $h_2^{(\mathrm{rms})}$ (solid black), and opening angle expected from hydrostatic equilibrium (dot-dashed blue). The opening angle expected from hydrostatic equilibrium is within 30% of $h_2^{(\mathrm{rms})}$ at all converged radii.

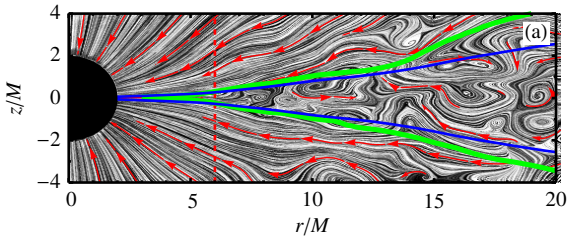

Fig. 3.6.— A snapshot of the velocity streamlines in the saturated state of the fiducial GRMHD disk simulation. The $\beta = 1$ contour (green) divides the high density, weakly magnetized disk from the low density, highly magnetized coronal and plunging regions. Magnetic tension stabilizes strong fields against the MRI, so the corona is laminar and the disk is turbulent. The contour $2h$ (blue) roughly corresponds to $\beta = 1$. The dashed red line marks the ISCO.

not converged beyond this. Simulation data is time-averaged over the steady state period from $t = 21000M - 26300M$ (Kulkarni et al. 2011b; Penna et al. 2010).

The radial velocity and surface density are well-described in the plunging region. This validates the thin disk approximations made in §3.2. In particular, the GRMHD plunging region is well approximated by hydrostatic equilibrium, with inner edge and sonic point at the ISCO, and geodesic motion.

Outside the ISCO the stress is primarily turbulent in origin. Inside the ISCO, it is generated by mean magnetic fields, which are stretched and amplified by the plunging fluid. Magnetic field reconnection at the grid scale and shocks (Beskin & Tchekhovskoy 2005) create luminosity inside the ISCO. The analytical disk models do not contain magnetic fields, so this physics is not captured. This is why the GRMHD stress and luminosity are not well described by the analytical models inside the ISCO. GRMHD disks are thicker inside the ISCO for the same reasons.

3.6 Conclusions

We have developed an analytical model for thin disk accretion in the Kerr metric which generalizes the NT model in three ways: (i) it incorporates nonzero stresses at the inner edge of the disk, (ii) it extends into the plunging region, and (iii) it uses the correct vertical gravity formula. The free parameters are unchanged. Our model is a special case of slim disk solutions, in the regime $h \ll \alpha$ and $\dot{M}_{\rm edd}/\dot{M} < 0.3$. Under these conditions, energy advection is less important than the stress at the inner edge of the disk, and the inner edge, sonic point, and ISCO are at approximately the same position.

The boundary condition is supplied by setting the radial velocity at the ISCO equal to the sound speed. In the limit $h \to 0$, this reduces to the NT zero-stress boundary condition. Outside the ISCO, the stress and radiant flux are the sum of the NT prediction and a correction term which incorporates the stress at the ISCO. Inside the ISCO, fluid plunges into the black hole and the motion is approximately geodesic. This enables us to estimate the pressure, and then the stress and radiant flux, of the plunging gas. Throughout we assume the fluid is in vertical hydrostatic

equilibrium and the stress is described by an α-viscosity. The model compares favorably with slim disk solutions.

We fit our disk solutions to a GRMHD disk simulation. We argued that the $\beta = 1$ contour is a natural boundary between the disk and coronal regions in GRMHD simulations. Fluid in the disk is turbulent. Outside the disk, where the field is strong and the MRI cannot operate, the flow is laminar.

The velocity and surface density are well-modeled inside the ISCO. This validates our assumptions that the fluid is in hydrostatic equilibrium and the velocities are nearly geodesic.

The GRMHD plunging region stress is larger than the stress in hydrodynamic models. The stresses are carried by large scale, mean magnetic fields. Some of this stress is dissipated by magnetic reconnection at the grid scale. The slim and thin disk models do not include magnetic fields, so they cannot model this.

Black hole spin parameters can be measured by modeling X-ray spectra using the NT accretion disk (Zhang et al. 1997; Shafee et al. 2006; Davis et al. 2006; Gou et al. 2009, 2010; Steiner et al. 2009). The NT model assumes advection is negligible, the disk inner edge is at the ISCO, and there are no torques at the ISCO. Slim disk solutions are available which do not make these assumptions. Straub et al. (2011) replaced the NT disk with a slim disk model and revisited the spin estimate of LMC X-3. They were unable to improve the estimate because theoretical improvements in the slim disk model were smaller than observational errors.

Observational errors in black hole spin measurements come from uncertainty in the black hole mass, distance, and disk inclination (McClintock et al. 2006). Current observational uncertainties in spin estimates are at best $\Delta a_* \pm 0.2$ at low spins and $\Delta a_* \pm 0.05$ at high spins (Gou et al. 2009). These estimates are made using data with $\dot{M}/\dot{M}_{\rm edd} < 0.3$. Kulkarni et al. (2011b) created mock data from a GRMHD simulation and fitted it with a NT disk, and computed an estimate of the spin error coming from disk theory. At $\dot{M}/\dot{M}_{\rm edd} \sim 0.5$ and $\alpha \sim 0.3$, they found spin errors of $\Delta a_* \pm 0.2$ at low spins and $\Delta a_* \pm 0.01$ at high spins. Errors increase with luminosity, so the theoretical uncertainties are always smaller than the observational ones.

This means the NT disk is sufficient for spin measurements at present. However, more sophisticated disk models will be needed as black hole mass, distance, and disk inclination measurements improve. In the hierarchy of disk models, the model in this chapter contains more physics than NT but less than a slim disk. Our model and the slim disk are similar when $\dot{M}/\dot{M}_{\rm edd} > 0.3$ and $h < \alpha$, but our model is analytical, so it might be simpler to use in some cases.

McClintock et al. (2006) introduced the selection criterion $\dot{M}/\dot{M}_{\rm edd} < 0.3$ when they measured the spin of the black hole GRS 1915+105. Black hole X-ray binaries have variable luminosities and the NT model is only valid at low luminosities. Of the 22 observations of GRS 1915+105 available to McClintock et al. (2006), five satisfied the $\dot{M}/\dot{M}_{\rm edd} < 0.3$ criterion. These five observations gave a nearly consistent spin parameter $a_* > 0.98$. Observations with $\dot{M}/\dot{M}_{\rm edd} > 0.3$ give inconsistent spin results, but the NT model is not valid in this regime.

Acknowledgments

We thank Stephen Balbus, Ramesh Narayan, and Alexander Tchekhovskoy for discussions. This work was supported by an NSF Graduate Research Fellowship (RFP), NSF grant AST-1041590, NASA grant NNX11AE16G, and by the NSF through TeraGrid resources provided by NCSA (Abe), LONI (QueenBee), and NICS (Kraken) under grant numbers TG-AST080025N and TG-AST080026N.

3.A The Kerr metric

We assume spinning black holes can be described by the Kerr metric and the accretion disk lies in the equatorial plane of the metric. The Kerr metric in Boyer-Lindquist coordinates (t, r, θ, ϕ) in

and near the equatorial plane ($|\theta - \pi/2| \ll 1$) is:

$$ds^2 = -\frac{r^2\Delta}{A}dt^2 + \frac{A}{r^2}\left(d\phi - \omega dt\right)^2 + \frac{r^2}{\Delta}dr^2 + dz^2, \tag{3.17}$$

$$\Delta = r^2 - 2Mr + a^2,$$

$$A = r^4 + r^2a^2 + 2Mra^2,$$

$$\omega = 2Mar/A.$$

Here M and a are the mass and specific angular momentum of the hole. We have replaced the usual angular coordinate by $z = r\cos\theta \simeq r\,(\theta - \pi/2)$. Define the auxiliary parameters:

$$a_* = a/M \quad (\text{note: } -1 \le a_* \le +1), \tag{3.18a}$$

$$x_1 = 2\cos\left(\cos^{-1}\left(a_*\right)/3 - \pi/3\right), \tag{3.18b}$$

$$x_2 = 2\cos\left(\cos^{-1}\left(a_*\right)/3 + \pi/3\right), \tag{3.18c}$$

$$x_3 = -2\cos\left(\cos^{-1}\left(a_*\right)/3\right), \tag{3.18d}$$

and a dimensionless radial coordinate

$$x = (r/M)^{1/2}. \tag{3.19}$$

For simplicity in splitting formulae into Newtonian limits plus relativistic corrections, we shall introduce the following functions of x and a_* with value unity far from the hole:

$$\mathcal{A} = 1 + a_*^2x^{-4} + 2a_*^2x^{-6}, \tag{3.20a}$$

$$\mathcal{B} = 1 + a_*x^{-3}, \tag{3.20b}$$

$$\mathcal{C} = 1 - 3x^{-2} + 2a_*^2x^{-3}, \tag{3.20c}$$

$$\mathcal{D} = 1 - 2x^{-2} + a_*^2x^{-4}, \tag{3.20d}$$

$$\mathcal{E} = 1 + 4a_*^2x^{-4} - 4a_*^2x^{-6} + 3a_*^4x^{-8}, \tag{3.20e}$$

$$\mathcal{F} = 1 - 2a_*x^{-3} + a_*^2x^{-4}, \tag{3.20f}$$

$$\mathcal{G} = 1 - 2x^{-2} + a_*x^{-3}, \tag{3.20g}$$

$$\mathcal{H} = 1 - 2x^{-2} + 2a_*x^{-2}x_0^{-1}\mathcal{F}_0^{-1}\mathcal{G}_0, \tag{3.20h}$$

$$\mathcal{I} = \mathcal{A} - 2a_*x^{-6}x_0\mathcal{F}_0\mathcal{G}_0^{-1}, \tag{3.20i}$$

$$\mathcal{J} = \mathcal{O} - x^{-2}\mathcal{I}^{-1}\Bigg[1 - a_* x_0^{-1}\mathcal{F}_0^{-1}\mathcal{G}_0 + a_*^2 x^{-2}\mathcal{H}\mathcal{I}^{-1} \times \left(1 + 3x^{-2} - 3a_*^{-1}x^{-2}x_0\mathcal{F}_0\mathcal{G}_0^{-1}\right)\Bigg], \tag{3.20j}$$

$$\mathcal{K} = \left|\mathcal{A}\mathcal{J}\left(1 - x^{-4}\mathcal{A}^2\mathcal{D}^{-1}\left(x_0\mathcal{F}_0\mathcal{G}_0^{-1}\mathcal{O} - 2a_* x^{-2}\mathcal{A}^{-1}\right)^2\right)^{-1}\right|, \tag{3.20k}$$

$$\mathcal{O} = \mathcal{H}\mathcal{I}^{-1}, \tag{3.20l}$$

$$\begin{aligned}\mathcal{Q} = \mathcal{B}\mathcal{C}^{-1/2}\frac{1}{x}\Bigg[&x - x_0 - \frac{3}{2}a_*\ln\left(\frac{x}{x_0}\right) \\ &- \frac{3\left(x_1 - a_*\right)^2}{x_1\left(x_1 - x_2\right)\left(x_1 - x_3\right)}\ln\left(\frac{x - x_1}{x_0 - x_1}\right) \\ &- \frac{3\left(x_2 - a_*\right)^2}{x_2\left(x_2 - x_1\right)\left(x_2 - x_3\right)}\ln\left(\frac{x - x_2}{x_0 - x_2}\right) \\ &- \frac{3\left(x_3 - a_*\right)^2}{x_3\left(x_3 - x_1\right)\left(x_3 - x_2\right)}\ln\left(\frac{x - x_3}{x_0 - x_3}\right)\Bigg],\end{aligned} \tag{3.20m}$$

$$\mathcal{R} = \mathcal{F}^2\mathcal{C}^{-1} - a_*^2 x^{-2}\left(\mathcal{G}\mathcal{C}^{-1/2} - 1\right), \tag{3.20n}$$

$$\mathcal{S} = \mathcal{A}^2\mathcal{B}^{-2}\mathcal{C}\mathcal{D}^{-1}\mathcal{R}, \tag{3.20o}$$

$$\mathcal{V} = \mathcal{D}^{-1}\Bigg[1 + x^{-4}\left(a_*^2 - x_0^2\mathcal{F}_0^2\mathcal{G}_0^{-2}\right) + 2x^{-6}\left(a_* - x_0\mathcal{F}_0\mathcal{G}_0^{-1}\right)\Bigg]. \tag{3.20p}$$

A subscript 0 indicates the quantity is evaluated at the innermost stable circular orbit (ISCO). Functions $\mathcal{A}$-$\mathcal{G}$ and $\mathcal{Q}$ are taken from Novikov & Thorne (1973) and Page & Thorne (1974).

3.A.1 Geodesics

The non-zero components of the four-velocity, u^μ, for general equatorial, timelike geodesic motion in the Kerr metric are (Chandrasekhar 1992):

$$u^t = \frac{1}{\Delta}\left[\left(r^2 + a^2 + \frac{2a^2M}{r}\right)E - \frac{2aM}{r}L\right], \tag{3.21a}$$

$$u^r = \frac{1}{r^2}\left[r^2E^2 + \frac{2M}{r}(aE - L)^2 + (a^2E^2 - L^2) - \Delta\right], \tag{3.21b}$$

$$u^\phi = \frac{1}{\Delta}\left[\left(1 - \frac{2M}{r}\right)L + \frac{2aM}{r}E\right], \tag{3.21c}$$

where E and L are the conserved specific energy and angular momentum of the motion. Circular geodesics have energy per unit mass

$$E = |u_t| = \mathcal{G}/\mathcal{C}^{1/2}, \tag{3.22}$$

angular momentum per unit mass

$$L = u_\phi = M^{1/2} r^{1/2} \mathcal{F} / \mathcal{C}^{1/2}, \tag{3.23}$$

and angular velocity

$$\Omega = \frac{u^\phi}{u^t} = \frac{M^{1/2}}{r^{3/2} + a M^{1/2}} = \frac{M^{1/2}}{r^{3/2}} \frac{1}{\mathcal{B}}. \tag{3.24}$$

Circular geodesics are unstable inside the ISCO. The radius of the ISCO is:

$$\begin{aligned} r_0/M &= 3 + Z_2 - \left[(3 - Z_1)\left(3 + Z_1 + 2Z_2\right) \right]^{1/2}, \\ Z_1 &= 1 + \left(1 - a_*^2\right)^{1/3} \left[(1 + a_*)^{1/3} + (1 - a_*)^{1/3} \right], \\ Z_2 &= \left(3a_*^2 + Z_1^2\right)^{1/2} \end{aligned} \tag{3.25}$$

The linear velocity of a circular orbit relative to a locally nonrotating observer (Bardeen et al. 1972) is

$$V_{(\phi)} = \frac{A}{r^2 \Delta^{1/2}} \left(\Omega - \omega \right). \tag{3.26}$$

The Lorentz factor corresponding to this linear velocity is

$$\gamma = \left(1 - V_{(\phi)}^2 \right)^{-1/2}. \tag{3.27}$$

The only nonzero components of the fluid frame shear tensor for the congruence of circular, equatorial geodesics are

$$\sigma_{\hat{r}\hat{\phi}} = \sigma_{\hat{\phi}\hat{r}} = \frac{1}{2} \frac{A}{r^3} \gamma^2 \Omega_{,r}. \tag{3.28}$$

3.B Disk structure equations

3.B.1 Definitions

The stress-energy tensor of a relativistic fluid is

$$\mathbf{T} = \rho(1 + \Pi)\mathbf{u} \otimes \mathbf{u} + \mathbf{t} + \mathbf{u} \otimes \mathbf{q} + \mathbf{q} \otimes \mathbf{u}, \tag{3.29}$$

where ρ is rest mass density in the local rest frame of the baryons (LRF), Π is the specific internal energy in the LRF, $\mathbf{t}$ is the stress tensor in the LRF, and $\mathbf{q}$ is the energy flux relative to the LRF. We make the thin disk approximation $\Pi = 0$ (cf. §3.2.1).

The disk structure equations are expressed in terms of the surface density of the disk,

$$\Sigma = \int_{-H}^{+H} \rho dz = 2\rho H, \tag{3.30}$$

the integrated shear stress,

$$W = \int_{-H}^{+H} t_{\hat{\phi}\hat{r}} dz = 2t_{\hat{\phi}\hat{r}} H, \tag{3.31}$$

the radial velocity of the gas in the locally non-rotating frame,

$$v^{\hat{r}} = \sqrt{g_{rr}} u^r, \tag{3.32}$$

and the the flux of radiant energy off the upper face of the disk,

$$F = q^{\hat{z}}(z = +H) = q^{\hat{z}}(z = -H), \tag{3.33}$$

where the disk scale height, H, is defined by $h = H/r$.

3.B.2 Radial structure equations

The radial structure of the disk is controlled by conservation of baryon number, conservation of angular momentum, and conservation of energy:

$$(\rho u^\mu)_{;\mu} = 0, \tag{3.34}$$

$$\left(T^\mu_\phi\right)_{;\mu} = 0, \tag{3.35}$$

$$(T^\mu_t)_{;\mu} = 0. \tag{3.36}$$

Integrating (3.34) gives the accretion rate of a stationary disk:

$$\dot{M} = -2\pi r \Sigma u^r = (\text{constant independent of } r \text{ and } t). \tag{3.37}$$

Combining angular momentum and energy conservation gives (cf. §3.2.1):

$$F = -\sigma_{n\hat{\phi}} W. \tag{3.38}$$

Combining all three conservation laws gives an integral solution for the flux:

$$4\pi r \frac{(E - \Omega L)^2}{-\Omega_{,r}} F/\dot{M} = \int_{r_0}^{r} (E - \Omega L) L_{,r} dr + C. \tag{3.39}$$

Page & Thorne (1974) give an analytical formula for the integral on the RHS when $r \geq r_0$. The integration constant C is related to the flux at the ISCO. The NT no-torque boundary condition is $C = 0$. We allow nonzero C.

3.B.3 Vertical structure equations

The vertical structure of the disk is controlled by pressure balance (cf. §3.2.3),

$$-\frac{p}{\rho}+h^2\frac{\mathcal{L}_*^2}{r^2}=0, \tag{3.40}$$
$$\mathcal{L}_*^2=u_\phi^2-a^2\left(u_t-1\right),$$

the Shakura-Sunyaev α-viscosity prescription,

$$t_{\hat{\phi}\hat{r}}=\alpha p \tag{3.41}$$

radiative energy transport,

$$bT^4=\bar{\kappa}\Sigma F, \tag{3.42}$$

the equation of state,

$$p=p^{(\mathrm{rad})}+p^{(\mathrm{gas})}, \tag{3.43}$$
$$p^{(\mathrm{rad})}=\frac{1}{3}bT^4,$$
$$p^{(\mathrm{gas})}=\rho\left(T/m_p\right),$$

and the opacity law,

$$\bar{\kappa}=\bar{\kappa}_{ff}+\bar{\kappa}_{es}, \tag{3.44}$$
$$\bar{\kappa}_{ff}=\left(0.64\times10^{23}\right)\left(\frac{\rho}{\mathrm{g/cm^3}}\right)\left(\frac{T}{K}\right)^{-7/2}\frac{\mathrm{cm}^2}{g},$$
$$\bar{\kappa}_{es}=0.40\frac{\mathrm{cm}^2}{\mathrm{g}}.$$

3.B.4 Solving for the disk structure

At this point the disk structure is defined by seven equations (3.37)-(3.44) for nine unknowns $E, L, u^r, W, F, \Sigma, p, h, T, \bar{\kappa}$ and four free parameters $M, a, \dot{M}, \alpha$. The integration constant C is fixed by the boundary condition (3.52).

To close the problem we need two more relations. These are prescriptions for E and L. Outside the ISCO, the disk nearly follows circular geodesics so E and L are (3.22) and (3.23). Inside the ISCO, the disk follows non-circular plunge trajectories with constant E and L defined in §3.2.2.

The fluid flow is slightly non-geodesic because it is acted upon by stresses. These are small deviations because the disk is thin and there are several ways of treating them. The different prescriptions are equivalent in the thin disk limit, so we choose the simplest.

Outside the ISCO, we use the angular velocity of circular geodesics (3.24), but do not enforce $u^r = 0$ (as would be required if the flow were truly geodesic by (3.21b)). We use this angular velocity when computing the shear tensor (3.28).

Inside the ISCO, we use the geodesic velocities (3.21a)-(3.21c), but do not assume the radiant flux integral (3.39) is zero (as would be required if L were truly constant). This eliminates one independent variable from the problem in the plunging region (because u^r is fixed by the geodesic equations) and one of the disk structure equations (because we do not enforce (3.39)).

Throughout most of the plunging region, the angular velocity exceeds the radial velocity, so we use (3.21c) and (3.28) to compute the shear. This fails near the photon orbit, but the thin disk approximations are expected to break down there (§3.2.1).

Explicit solutions are in §3.3.

3.C Scaling of compression, advection, and boundary stress terms with α and h

The law of energy conservation (3.36) can be rewritten (Novikov & Thorne 1973):

$$\rho \frac{d\Pi}{d\tau} + \nabla \cdot \mathbf{q} = -\sigma_{\alpha\beta} t^{\alpha\beta} - \frac{1}{3}\theta t^{\alpha}_{\alpha} - \mathbf{a} \cdot \mathbf{q}. \tag{3.45}$$

We have introduced the convective derivative $d/d\tau \equiv \mathbf{u} \cdot \nabla$, the scalar expansion $\theta \equiv \nabla \cdot \mathbf{u}$, the acceleration vector $\mathbf{a} \equiv \nabla_{\mathbf{u}} \mathbf{u}$, the shear tensor

$$\sigma_{\alpha\beta} \equiv \frac{1}{2}\left(u_{\alpha;\mu} h^{\mu}_{\beta} + u_{\beta;\mu} h^{\mu}_{\alpha}\right) - \frac{1}{3}\theta h_{\alpha\beta}, \tag{3.46}$$

and the projection tensor

$$h_{\alpha\beta} \equiv g_{\alpha\beta} + u_{\alpha} u_{\beta}. \tag{3.47}$$

Each term in (3.45) has a simple physical interpretation. The term $\mathbf{a}\cdot\mathbf{q}$ is a special relativistic correction associated with the inertia of the flowing energy $\mathbf{q}$. We assume $\mathbf{q}$ is directed entirely along z and $u^z = 0$, so $\mathbf{a}\cdot\mathbf{q} = 0$.

The remaining terms on the RHS of (3.45) correspond to energy generation by shear stresses, $-\sigma_{\alpha\beta}t^{\alpha\beta}$, and by compression, $-1/3\theta t^{\alpha}_{\alpha}$. The sink terms on the LHS of (3.45) describe energy advection, $-\rho d\Pi/d\tau$, and radiative losses, $\nabla\cdot\mathbf{q}$.

After height integrating and normalizing by $\dot{M}$, the compression term scales as

$$\frac{\theta t^{\alpha}_{\alpha} h}{\dot{M}} \propto \frac{u^r_{,r} p h}{\rho u^r h} \propto h^2. \tag{3.48}$$

Here $\propto$ means proportionality with respect to h and α, which are considered small. So, for example, $u^r_{,r}/u^r \propto (u^r/r)/u^r \propto 1$. In the first step of (3.48), we inserted the accretion rate (3.37). In the second step, we used the pressure balance relation (3.40).

The height integrated advection term scales as

$$\frac{\rho d\Pi/d\tau h}{\dot{M}} \propto \frac{\rho u^r \Pi_{,r} h}{\rho u^r h} \propto h^2, \tag{3.49}$$

where we have used $\Pi \propto p/\rho \propto h^2$.

The height-integrated stress at the ISCO enters the solution as a boundary condition when integrating the energy equation (3.45). It scales as

$$\frac{\sigma_{n\hat{\phi}} t^{\hat{r}\hat{\phi}} h}{\dot{M}} \propto \frac{\alpha p h}{\rho u^r h} \propto \alpha h. \tag{3.50}$$

In the first step, we used the α-viscosity prescription (3.41). In the second step, we identified the ISCO with the sonic point of the disk (cf. §3.2.1), so $u^r \propto c_s \propto \sqrt{p/\rho} \propto h$ (by 3.40).

Equations (3.48)-(3.50) give the scaling of compression, advection, and boundary stresses with h and α. In the NT limit, $h \to 0$, all three terms vanish. Under the weaker assumption $h \ll \alpha$, compression and advection are small but the stress at the ISCO is important. So we obtain a self-consistent generalization of the NT model by ignoring advection and compression but including the boundary stress at the ISCO, when $h \ll \alpha$.

Dropping advection and compression terms from the energy equation (3.45), we have

$$\frac{dq^z}{dz} = -\sigma_{n\hat{\phi}} t^{\hat{r}\hat{\phi}}, \tag{3.51}$$

which says energy generated by shear stresses is immediately radiated away. Height integrating gives (3.38).

Rewriting the stress at the ISCO (3.50) as a radiant flux using (3.38) fixes the boundary term in the disk solution (3.39):

$$C = \left[\alpha h \gamma \left(E - \Omega L\right) \frac{\mathcal{L}_*}{r}\right]_0 . \tag{3.52}$$

This reduces to the NT choice $C = 0$ in the razor thin limit $h \to 0$. However in general the flux and stress at the ISCO will not be zero.

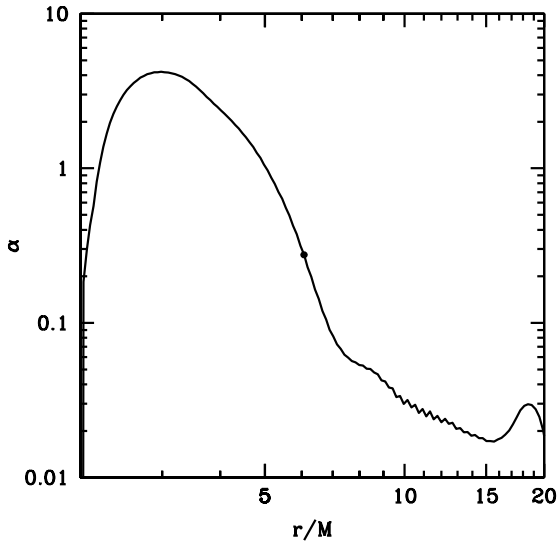

Fig. 3.7.— Effective α of the fiducial GRMHD disk simulation. The ISCO is marked with a black dot. There is a sharp rise inside the ISCO, where the plunging fluid stretches the field lines. Unlike slim disk and thin disk models, the GRMHD disk does not have a constant α.

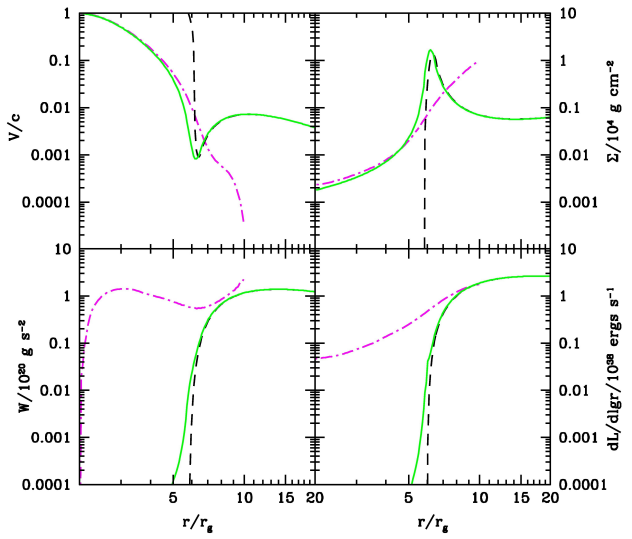

Fig. 3.8.— Radial velocity, surface density, stress, and luminosity versus radius for the fiducial GRMHD disk simulation (dot-dashed red) and NT (dashed black) and generalized thin disk models (solid green) with $\alpha = 0.3$ and $\dot{M}/\dot{M}_{\rm edd} = 0.5$. The GRMHD curves are truncated at $r = 9M$, beyond which the simulations have not reached steady state. (Kulkarni et al. 2011b).

Chapter 4

Beyond Novikov-Thorne Disks II: Radial Varying α(r) Viscosity

4.1 Introduction

Accretion disk magnetic fields and turbulence act as a large scale viscosity, draining angular momentum and energy from accreting gas. The magnitude of this viscosity is uncertain, which adds a free parameter to accretion disk models. For example, Pringle & Rees (1972) leave the ratio of the disk's radial velocity to its circular velocity as a free parameter. They call this ratio $y/100$ and estimate $y \sim 1$. They note that y might be radius dependent and that a strong radial dependence could change qualitative features of the disk. However, other important features of the disk, such as its luminosity, depend weakly or not at all on y, so progress is possible without a detailed model for y.

Shakura & Sunyaev (1973) parametrized the viscosity with α, the ratio of stress to pressure. It is related to Pringle and Rees's y by $y = 100\alpha(h/r)^2$, where h/r is the disk opening angle. [1] They

[1] Pringle & Rees (1972) leave h/r a free parameter which they suppose to be ~ 0.05. Shakura & Sunyaev (1973) use hydrostatic equilibrium to solve for h/r self-consistently.

anticipated that α will be a function of radius, citing experiments of turbulence in Taylor-Coutte flow, flow between rotating cylinders (Taylor 1936). These experiments show that the torque exerted by a turbulent flow on the cylinders depends on the rotation rate of the cylinders and the separation between them. The torque in the experiment is related to α, so α should depend on accretion flow properties that vary with radius. The analogy is too rough to produce a quantitative model, so they assume α is a constant for simplicity.

The most significant theoretical breakthrough towards an understanding of α has been the realization that the magnetorotational instability (MRI) can drive turbulence in ionized accretion disks (Velikhov 1959; Chandrasekhar 1960; Balbus & Hawley 1991, 1998). A weak seed magnetic field and a radially decreasing angular velocity profile are all that are required to trigger the instability and both are present in disks. This makes it possible to run magnetohydrodynamic (MHD) disk simulations without using the α-viscosity prescription.

Nonetheless, because of its relative simplicity, the α-viscosity prescription has not dimmed in importance. Over the past year, more than 300 papers cited the pioneering work of Shakura & Sunyaev (1973) and more than 1000 papers made reference to some disk solution based on the α-viscosity prescription (such as the relativistic thin disk of Novikov & Thorne (1973) or the advection dominated accretion flow (ADAF) of Narayan & Yi (1994)). However, despite its interest, there is still no widely accepted model for the size or shape of α. In applications, it is typically assumed to be a constant between 0.01 and 0.1 (e.g., Gou et al. 2011).

There are two varieties of MHD simulations, local and global, and both provide hints about the size and shape of α. A standard setup for a local simulation is a box of weakly magnetized fluid in the shearing sheet approximation (e.g., Hawley & Balbus 1991; Brandenburg et al. 1995; Hawley et al. 1995, 1996; Stone & Balbus 1996; Brandenburg 2001; Sano et al. 2004). The dimensions of the box are typically a few disk scale heights. The earliest global simulations of MRI turbulent disks used a Newtonian potential (Armitage 1998; Matsumoto 1999; Hawley 2000; Machida et al. 2000) and, later, a pseudo-Newtonian potential (Hawley & Krolik 2001). The first general relativistic global simulations were carried out by De Villiers et al. (2003). A standard setup for global simulations is a torus of fluid in hydrostatic equilibrium, threaded with a weak magnetic field (e.g.,

De Villiers et al. 2003). In local and global simulations, differential rotation triggers the MRI and drives turbulence. When the simulation reaches a quasi-steady state, one can compute the ratio of stress to pressure and so measure α. Local simulations focus on resolving small scale physics, such as saturation of the MRI, while global simulations attempt a complete portrait of the accretion disk.

Global simulations have hinted at the shape of α. Penna et al. (2010) and Penna et al. (2012b) presented general relativistic MHD (GRMHD) simulations of MRI turbulent disks in the Kerr metric, the spacetime of a spinning black hole. They confirmed that the relativistic α-disk model of Novikov & Thorne (1973) gives a good description of the simulation data. This was partly motivated by earlier suggestions that magnetic stresses at the inner edges of MHD disks invalidate the assumptions of α-disk models (e.g., Krolik 1999; Agol & Krolik 2000). The GRMHD simulations produced luminosity inside the innermost stable circular orbit (ISCO), where the Novikov & Thorne (1973) model is entirely dark, but it was a modest contribution to the total luminosity of the disk (on the order of a few percent; Kulkarni et al. 2011b). Later, Penna et al. (2012b) generalized the Novikov & Thorne (1973) model to self-consistently incorporate nonzero luminosity inside the ISCO, bringing it closer to the GRMHD simulations.

Penna et al. (2010) and Penna et al. (2012b) measured the shape of α. For accretion onto a non-spinning black hole, they found α is small at the event horizon, increases to a maximum near the photon orbit, declines to ~ 0.06 near the ISCO, and then continues to decline, albeit more slowly (see, e.g., Figure 7 of Penna et al. 2012b). In a completely different context, MHD simulations of protoplanetary disks, Fromang et al. (2011) found a radially varying α with similar shape. However, the overall size of their α was over an order of magnitude lower, peaking at 0.013 and declining to below 0.002.

The value of α is notoriously difficult to pin down (Pessah et al. 2007). Local simulations find that α is strongly affected by grid scale dissipation as well as stratification (Lesur & Longaretti 2007; Fromang & Papaloizou 2007; Simon & Hawley 2009; Davis et al. 2010). In global and local simulations, α depends non-monotonically on resolution at all but the highest resolutions (Sorathia et al. 2012). In models with net magnetic flux, α scales with increasing flux (Hawley et al. 1995;

Sano et al. 2004; Pessah et al. 2007). Finally, α depends on the initial magnetic field geometry and strength (e.g., Sorathia et al. 2012).

A combination of these effects can probably explain some of the discrepancy between the α values found by Penna et al. (2012b) and Fromang et al. (2011) . The former employed an initially poloidal magnetic field with initial gas-to-magnetic pressure ratio $\beta = 100$ and resolution $256 \times 64 \times 32$ in (r, θ, ϕ). The later employed an initially toroidal field with initial $\beta = 25$ and resolution $512 \times 256 \times 256$. Neither had explicit dissipation or net magnetic flux. Initially toroidal fields tend to beget smaller α's than initially poloidal fields, but α also tends to be inversely related to the initial β. The scaling of α with resolution is non-monotonic (Sorathia et al. 2012). It is not clear whether these effects are large enough to explain why the α's measured from the general relativistic simulations are over an order of magnitude larger than the α's measured from the Newtonian simulations.

In this chapter, we present a one-dimensional model for the shape of α and we show that relativistic corrections enhance the α's measured in GRMHD simulations relative to Newtonian simulations. The one-dimensional model has two components. The first component is generated by large-scale, mean magnetic fields and is based on the model of Gammie (1999). It dominates in the inner regions of accretion flows, where plunging gas stretches and amplifies the frozen-in magnetic field. The second, "turbulent," component describes the dependence of α on the shear rate of the flow. The dependence of α on the shear rate in turbulent flows was earlier emphasized by Godon (1995), Abramowicz et al. (1996), and Pessah et al. (2008). Combining the mean field and turbulent components yields a one-dimensional model for the shape of α.

We use this model to fit the profiles of α versus radius extracted from six GRMHD simulations. The simulations describe thin disks accreting onto a non-spinning black hole at two different resolutions, a thin disk and a thick disk accreting onto a spinning black hole (with dimensionless spin parameter $a/M = 0.7$), and thick disks with two different initial magnetic field topologies accreting onto a nonspinning black hole. We show how the radial variation of α changes the structure of α-disk solutions. Finally, we note that the enhancement of α seen in GRMHD simulations relative to Newtonian simulations can be explained by the dependence of α on shear

rate.

There is another reason α is interesting which we have not yet mentioned. Turbulent fluids can be complicated. They are disordered solutions of nonlinear equations that require great effort to solve numerically. And yet, from fully developed turbulence, simple scaling laws emerge with apparently universal properties. For example, shearing box simulations of MRI-driven turbulence with a Keplerian rotation profile always find that the ratio of Maxwell stress to Reynolds stress is a constant, ≈ 4 (Pessah et al. 2006b). The same ratio appears independently of the magnitude or geometry of the magnetic field. It seems only to depend (in a simple way) on the shear rate of the flow (Hawley et al. 1999; Pessah et al. 2006b). Similarly, the viscosity parameter, α, obeys a remarkable scaling law: $\alpha\beta \approx 1/2$, where β is the gas-to-magnetic pressure ratio (Blackman et al. 2008; Guan et al. 2009; Sorathia et al. 2012). Formulas this simple should have simple explanations; they should not just appear at the end of large numerical calculations, as if by coincidence. We hope that clarifying some of the physics underlying α will improve our understanding of these scaling laws.

This chapter is organized as follows. In §4.2, we give an overview of physics in the Kerr metric. In §4.3, we describe our one-dimensional model for $\alpha(r)$. The GRMHD simulations are described in §§4.4-4.6; we give a broad overview of the simulations in §4.4, analyze the two fiducial simulations in §4.5, and analyze the remaining four simulations in §4.6. In §4.7, we show how a radially varying α affects the structure of α-disk solutions. We conclude with a summary and discussion in §4.8.

4.2 Preliminaries

For our investigation of α, we will need to compute the angular velocity, shear rate, and epicyclic frequency of an accreting gas in the Kerr metric, so we review their definition here. This also helps to establish notation. As an intermediate step, we discuss the transformation between the Boyer-Lindquist and fluid frames.

The Kerr metric in Boyer-Lindquist coordinates is

$$ds^2 = -\left(1 - 2Mr/\Sigma\right) dt^2 - \left(4Mar\sin^2\theta/\Sigma\right) dtd\phi + \left(\Sigma/\Delta\right) dr^2 + \left(r^2 + a^2 + 2Ma^2 r\sin^2\theta/\Sigma\right)\sin^2\theta d\phi^2. \quad (4.1)$$

Here M is the mass of the black hole, a is its angular momentum per unit mass ($0 \leq a \leq M$), and the functions Δ, Σ, and A are defined by

$$\Delta \equiv r^2 - 2Mr + a^2, \quad (4.2)$$

$$\Sigma \equiv r^2 + a^2\cos^2\theta, \quad (4.3)$$

$$A \equiv \left(r^2 + a^2\right)^2 - a^2\Delta\sin^2\theta. \quad (4.4)$$

The accreting, magnetized gas is characterized by its four-velocity, u^μ, density, ρ, pressure, p, and internal energy, u, and by the electromagnetic field, $F^{\mu\nu}$. We set $G = c = 1$.

The angular velocity of the gas is

$$\Omega \equiv \frac{d\phi}{dt} = \frac{u^\phi}{u^t}. \quad (4.5)$$

Circular equatorial geodesics have $\Omega = M^{1/2}/\left(r^{3/2} + aM^{1/2}\right)$, and the motion of a geometrically thin disk is well approximated by circular geodesics outside the ISCO. However, motion inside the ISCO and the motion of thick disks are not Keplerian, so we leave Ω unspecified for now.

4.2.1 Inertial fluid frame

We would like to evaluate the shear rate and epicyclic frequency in the inertial fluid frame, rather than the Boyer-Lindquist, ZAMO, or any other frame, because the physics is simplest there. Also, this is the frame where α is defined. In this frame, the equivalence principle lets us ignore gravitational forces at the center of the fluid parcel we are following. Tidal forces and other gravitational forces that become important over large distances will not concern us because shear rate and epicyclic frequency are local measurements.

Measurements in the Boyer-Lindquist frame, $(dt, dr, d\theta, d\phi)$, are related to measurements in the inertial fluid frame, $\left(\omega^{\hat{t}}, \omega^{\hat{r}}, \omega^{\hat{\theta}}, \omega^{\hat{\phi}}\right)$, by the the transformation matrix $\omega^\mu_{\hat{\mu}}$ (Krolik et al. 2005;

Beckwith et al. 2008b; Kulkarni et al. 2011a):

$$\omega^{\mu}_{\hat{t}} = \left(u^t, u^r, u^\theta, u^\phi\right), \tag{4.6}$$

$$\omega^{\mu}_{\hat{r}} = \frac{s}{N_1}\left(u_r u^t, 1 + u^r u_r + u^\theta u_\theta, 0, u_r u^\phi\right), \tag{4.7}$$

$$\omega^{\mu}_{\hat{\theta}} = \frac{1}{N_2}\left(u_\theta u^t, u_\theta u^r, 1 + u_\theta u^\theta, u_\theta u^\phi\right), \tag{4.8}$$

$$\omega^{\mu}_{\hat{\phi}} = \frac{1}{N_3}\left(-\ell, 0, 0, 1\right), \tag{4.9}$$

where,

$$\begin{aligned}
s &= -C_0/\left|C_0\right|, & \ell &= u_\phi/u_t, \\
N_1 &= g_{rr}\sqrt{g_{tt}C_1^2 + g_{rr}C_0^2 + g_{\phi\phi}C_2^2 + 2g_{t\phi}C_1C_2}, & C_0 &= u^t u_t + u^\phi u_\phi, \\
N_2 &= \sqrt{g_{\theta\theta}\left(1 + u^\theta u_\theta\right)}, & C_1 &= u^r u_t, \\
N_3 &= \sqrt{g_{tt}\ell^2 - 2g_{t\phi}\ell - g_{\phi\phi}}, & C_2 &= u^r u_\phi.
\end{aligned} \tag{4.10}$$

Hatted indices refer to fluid frame quantities and unhatted indices refer to Boyer-Lindquist frame quantities. In the orthonormal fluid frame the metric is the Minkowski metric, $\eta_{\hat{a}\hat{b}} = \mathrm{diag}(-1, 1, 1, 1)$. So hatted indices are raised and lowered with the Minkowski metric and unhatted indices are raised and lowered with the Kerr metric.

The fluid frame basis (4.6)-(4.9) was constructed using a Gram-Schmidt process. There is some arbitrariness in the orientation of the frame, but we followed standard conventions. Equation (4.6) for $\omega_{\hat{t}}$ is necessary because the Lorentz factor in the fluid frame should satisfy $\gamma = -u_{\hat{t}} = -\omega^{\mu}_{\hat{t}} u_\mu = 1$. The next step in the Gram-Schmidt process is to define $\omega_{\hat{\phi}}$ such that it is orthogonal to $\omega_{\hat{t}}$ and has no component along dr or $d\theta$. Finally, $\omega_{\hat{r}}$ and $\omega_{\hat{\theta}}$ are constructed. Notice that $\omega_{\hat{r}}$ has a nonzero component along $d\phi$, and $\omega_{\hat{\theta}}$ has components along all four Boyer-Lindquist directions. This is unavoidable. However, the most important directions for the physics, $\omega_{\hat{r}}$ and $\omega_{\hat{\phi}}$, are aligned as closely as possible with their Boyer-Lindquist analogues.

The arbitrariness in the construction of the fluid frame leads to an ambiguity in the definition of α. One usually avoids quantities with these sorts of ambiguities. But, as discussed in §4.1, α is too useful for accretion disk modeling and turbulence theory to abandon. So our strategy is to define α in the most natural way possible and see where this leads.

If the poloidal velocity is much smaller than the azimuthal velocity, as usually happens everywhere except in the innermost regions of the disk, the fluid frame basis simplifies (Novikov & Thorne 1973):

$$\omega^{\hat{t}} = u_t dt + u_\phi d\phi, \tag{4.11}$$

$$\omega^{\hat{r}} = \mathcal{D}^{-1/2} dr, \tag{4.12}$$

$$\omega^{\hat{\theta}} = r\, d\theta, \tag{4.13}$$

$$\omega^{\hat{\phi}} = \gamma r \mathcal{A}^{1/2} \left(d\phi - \Omega dt \right). \tag{4.14}$$

The Lorentz factor is $\gamma = \sqrt{-g_{tt}} u^t$ and

$$\mathcal{A} = 1 + a^2 r^{-2} + 2 M a^2 r^{-3}, \quad \mathcal{D} = 1 - 2 M r^{-1} + a^2 r^{-2}. \tag{4.15}$$

The relativistic factors $\mathcal{A}, \mathcal{D}$, and γ are unity at large radii. In fact, in this limit, the fluid frame basis is exactly aligned with the Boyer-Lindquist frame. So the ambiguities in the general relativistic definition of α discussed earlier are not important in the outer regions of the disk. There remains a potential ambiguity in the construction of the Boyer-Lindquist r and θ coordinates, even when the gas is nonrelativistic, because the black hole's spin axis breaks the spherical symmetry of spacetime. But this is also negligible far from the black hole where frame dragging is weak.

4.2.2 Electric and magnetic fields

All observers interact with the same electromagnetic field. They might measure its components, $F_{\mu\nu}$, differently, depending on their reference frames, but the underlying object is the same multilinear map, $\mathbb{F}$.

The electric and magnetic fields are not so universal: each observer splits the electromagnetic field into different electric and magnetic components. An observer with four-velocity u^μ measures electric and magnetic fields

$$e^\mu = u_\nu F^{\nu\mu}, \quad b^\mu = u_\nu {}_* F^{\mu\nu}, \tag{4.16}$$

where the dual Faraday tensor is ${}_* F^{\mu\nu} = \epsilon^{\mu\nu\kappa\lambda} F_{\kappa\lambda}/2$, the Levi-Civita symbol is $\epsilon^{\mu\nu\kappa\lambda} = -\left[\mu\nu\kappa\lambda\right]/\sqrt{-g}$, and $[\mu\nu\kappa\lambda]$ is the completely antisymmetric symbol, equal to either $0, -1$, or $+1$.

The electric and magnetic fields e^μ and b^μ transform as tensors, so they can be evaluated in any frame. In general, all four components are nonzero. The four-velocity of the observer, u^μ, appears in (4.16), so each observer interacts with different electric and magnetic fields. Following standard convention, we denote the Boyer-Lindquist observer's splitting E^μ and B^μ, and we denote the fluid frame's splitting e^μ and b^μ. In Boyer-Lindquist coordinates $B^t = E^t = 0$, and in the fluid frame $e^{\hat{t}} = b^{\hat{t}} = 0$, by the antisymmetry of $F^{\mu\nu}$. The remaining nonzero components in these frames are the usual three-vectors of special relativity.

In ideal MHD, $e^\mu = 0$, so the fluid frame splitting of $F_{\mu\nu}$ is usually the simplest. For calculations, Boyer-Lindquist coordinates are sometimes more convenient than the fluid frame. So it is common to work with b^μ, the fluid frame observer's magnetic field expressed in Boyer-Lindquist coordinates. This is legitimate, because b^μ is a 4-vector, but no observer would measure b^t, b^r, b^θ, or b^ϕ. Physically meaningful quantities are $b^{\hat{r}}, b^{\hat{\theta}}$, and $b^{\hat{\phi}}$.

It is possible to convert between B^μ and b^μ directly, without reference to $F^{\mu\nu}$. In Boyer-Lindquist coordinates, the formulae are:

$$b^t = B^\mu u^\nu g_{\mu\nu}, \quad b^i = \frac{B^i + b^t u^i}{u^t}, \tag{4.17}$$

$$B^\mu = b^\mu u^t - b^t u^\mu. \tag{4.18}$$

In these equations, i runs over r, θ, ϕ, and μ, ν run over t, r, θ, ϕ.

4.2.3 Shear rate

The shear rate is a measure of how rapidly the angular velocity of an accretion disk varies with radius. It is $r\Omega_{,r}/2$ in Newtonian gravity. More generally, one can define the special relativistic shear tensor

$$\sigma_{\alpha\beta} \equiv \frac{1}{2}\left(u_{\alpha,\mu}h^\mu_\beta + u_{\beta,\mu}h^\mu_\alpha\right) - \frac{1}{3}\Theta h_{\alpha\beta}, \tag{4.19}$$

where $h_{\alpha\beta} = g_{\alpha\beta} + u_\alpha u_\beta$ is the projection tensor and $\Theta = u^\alpha{}_{;\alpha}$ is the expansion scalar (Novikov & Thorne 1973). Then the shear rate is the $\hat{r}\hat{\phi}$ component of this tensor measured in the fluid frame: $\sigma_{n\hat{\phi}}$. The shear tensor so defined is trace-free and symmetric. To obtain the general relativistic version, one should replace partial derivatives in equation (4.19) with covariant derivatives. We

do not require this generality because in the inertial fluid frame the laws of physics take on their special relativistic form without gravity, by the equivalence principle.

To obtain a simple formula for the shear rate, let us assume the poloidal velocity is small and the flow is axisymmetric. Then we can ignore the expansion scalar, Θ, use equations (4.11)-(4.14) for the fluid frame transformation, and ignore derivatives with respect to $\hat{\phi}$. The fluid frame projection tensor is $h_{\hat{\alpha}\hat{\beta}} = \mathrm{diag}\,(0,1,1,1)$, so the shear rate is

$$\sigma_{n\hat{\phi}} = \frac{1}{2} u^{\hat{\phi}}{}_{,\hat{r}}, \tag{4.20}$$

which resembles the Newtonian shear rate, $r\Omega_{,r}/2$. In the fluid frame, $u^{\hat{\phi}}(r) = 0$, so the derivative is [2]:

$$\sigma_{n\hat{\phi}} = \frac{1}{2} \lim_{d\hat{r}\to 0} \frac{u^{\hat{\phi}}(r + d\hat{r})}{d\hat{r}}. \tag{4.21}$$

We use equations (4.11)-(4.14) to rewrite fluid frame measurements in terms of Boyer-Lindquist measurements, obtaining:

$$\sigma_{n\hat{\phi}} = \frac{1}{2} \gamma^2 \mathcal{A} r\, \Omega_{,r}. \tag{4.22}$$

This is the product of the Newtonian shear rate $r\Omega_{,r}/2$ with a relativistic correction, $\gamma^2\mathcal{A}$. Novikov & Thorne (1973) state this formula without proof. It describes the rate of change of a disk's angular velocity with radius, assuming the azimuthal velocity dominates the poloidal velocity.

A dimensionless measure of the shear rate is

$$q = -2\sigma_{n\hat{\phi}}/\Omega = -\gamma^2 \mathcal{A} \frac{d\log\Omega}{d\log r}. \tag{4.23}$$

Positive q corresponds to angular velocity decreasing with radius. Solid body rotation is $q = 0$. Accretion disks generally have positive q, although q changes sign near the photon orbit in black hole disks. Flows with positive q are unstable to the MRI (Velikhov 1959; Chandrasekhar 1960; Balbus & Hawley 1991), and the value of α is a function of q (Pessah et al. 2008). Flows with $q > 2$ are Rayleigh (hydrodynamically) unstable. The MRI has been analyzed in the $q > 2$ regime

[2] We abuse notation for clarity. The commutators of fluid frame basis elements do not vanish in general, so they are not coordinate induced: there is no "$\hat{r}$" coordinate satisfying $d\hat{r} = e^{\hat{r}}$.

by Balbus (2012)[3]. Circular geodesics in Newtonian gravity have $q = 3/2$. Circular, equatorial geodesics in the Kerr metric have (Gammie 2004)

$$q = \frac{3}{2}\frac{1 - 2Mr^{-1} + a^2r^{-2}}{1 - 3Mr^{-1} + 2aM^{1/2}r^{-3/2}}. \tag{4.24}$$

which becomes 3/2 at large radii. The fact that α is a function of q, and in the Kerr metric q is a function of radius, is the basis for the turbulent component of the one-dimensional α model in §4.3.

4.2.4 Radial epicyclic frequency

The radial epicyclic frequency is the frequency at which a radially displaced fluid parcel will oscillate. As a function of q, it is (Pringle & King 2007)

$$\kappa = \sqrt{2(2-q)}\Omega. \tag{4.25}$$

This expression is valid in the inertial fluid frame provided we use the relativistic expressions for Ω and q, equations (4.5) and (4.23).

Circular geodesics at the ISCO have $\kappa = 0$ by definition, which makes it easy to see that they have $q = 2$. A thin accretion disk starts with $q = 3/2$ at large radii and then q increases until it reaches 2 at the inner edge. The radial dependence of κ^2 for circular, equatorial Kerr geodesics is (Gammie 2004)

$$\kappa^2 = \frac{1}{r^3}\frac{1 - 6M/r + 8aM^{1/2}r^{-3/2} - 3a^2/r^2}{1 - 3Mr^{-1} + 2aM^{1/2}r^{-3/2}}. \tag{4.26}$$

The epicyclic frequency is zero at the ISCO, and imaginary inside the ISCO, signaling the instability of circular geodesics. In §4.5 and §4.6, we compute the epicyclic frequency of simulated GRMHD accretion disks as a function of radius. The inner edge of the disk can be identified with the minimum κ. Only for thin disks does κ have a sharp minimum at the ISCO. In general, pressure gradient forces and magnetic stresses smear out the inner edge of the disk and displace it from the ISCO.

[3]Note that our simulated disks have $q < 2$ at all radii. The scaled epicyclic frequency reaches a minimum near the ISCO and increases in the plunging region.

4.3 One-dimensional model for $\alpha(r)$

In this section we define a one-dimensional prescription for the dependence of α on radius. Our model is the sum of two components: a turbulent component that dominates in the outer regions of the disk and a large scale magnetic field component that dominates in the inner regions of the disk. We discuss each component separately before combining them into a single prescription for $\alpha(r)$. We will fit this $\alpha(r)$ prescription to data from GRMHD simulations in §§4.4-4.6.

The standard α viscosity prescription is

$$T_{\hat{r}\hat{\phi}} = \alpha p, \tag{4.27}$$

where $T_{\hat{r}\hat{\phi}}$ is the fluid frame stress, p is pressure, and α is a constant (Shakura & Sunyaev 1973). There are two equivalent ways to modify this prescription. One can add extra factors multiplying the RHS of equation (4.27) and keep α a constant, or one can keep equation (4.27) unchanged but define α to be a function of radius, $\alpha = \alpha(r)$. We chose the later convention because it makes it easy to adapt old α-disk solutions to the new prescription: just insert $\alpha(r)$ wherever α appears. Both approaches have been used in the past so it requires a bit of care to compare results. For example, Abramowicz et al. (1996) discussed the dependence of α on q, while Pessah et al. (2008) modified (4.27) and kept α a constant.

4.3.1 Turbulent α

We have seen in §4.2.3 that q can be a function of radius, either through relativistic corrections to the Newtonian shear rate, or through the dependence of Ω on radius. It turns out α is a function of q, and so it too can depend on radius. That α depends on q is perhaps not surprising. MHD flows are unstable to the MRI and have finite α when $q > 0$, but they are stable against the MRI and have vanishing α when $q < 0$. Some dependence of α on q must connect these two regimes.

Pessah et al. (2008) examined the dependence of α on q numerically. They used nonrelativistic shearing box simulations with resolution $32 \times 192 \times 32$ in $r \times \phi \times z$, zero net magnetic flux, and initial gas-to-magnetic pressure ratio $\beta = 200$. They ran a series of simulations in which they varied q from $q = -1.9$ up to $q = 1.9$ in steps of $\Delta q = 0.1$. Each simulation ran 150 orbits and they

measured α by averaging the data from the last 100 orbits. For $q > 0$, they found the power-law scaling

$$\alpha \propto q^n, \tag{4.28}$$

where n is between 2 and 8. Higher resolution simulations are needed to determine n more precisely. For $q < 0$, they found $\alpha = 0$, as expected from the MRI stability criterion.

Between the inner edge of a thin accretion disk and the outer, non-relativistic regions, q only varies by 50% (cf. §4.2.3), but α can vary by much more if the exponent in equation (4.28) is large. For $n = 8$, the change in α is a factor of 10.

To get a quantitative prescription for $\alpha(r)$, we need $q(r)$. So first we solve standard α-disk equations with constant $\alpha = \alpha_0$. This gives $q(r)$. Then we define $\alpha(r) = \alpha_0 \left[q(r)/1.5\right]^n$. The exponent is a free parameter to be determined from MHD simulations. Now one could iterate: feed $\alpha(r)$ back into the α-disk equations, and re-evaluate $q(r)$. For simplicity, we do not iterate. We check our model for $\alpha(r)$ against GRMHD simulation data in §§4.4-4.6, but the simulation data are too noisy to justify computing $\alpha(r)$ more precisely for now.

The α-disk solutions we use are the relativistic slim disk solutions of Abramowicz et al. (1988); Sądowski (2011). This is a family of one-dimensional solutions for black hole accretion with four free parameters: black hole mass and spin, accretion rate, and α. At low accretion rates they reduce to the standard thin disks of Shakura & Sunyaev (1973) and Novikov & Thorne (1973), and at high accretion rates they become advection dominated and are similar to slim disks (Abramowicz et al. 1988; Sądowski 2011)

This prescription for $\alpha(r)$ neglects the contribution of large scale, mean magnetic fields, which can exist even in laminar flow. These are important near and inside the inner edge of the disk, where the flow acquires a large radial velocity and stretches the frozen-in magnetic field. We discuss this contribution to $\alpha(r)$ in the next section.

4.3.2 Mean magnetic field stresses

Penna et al. (2010) observed large scale, mean field stresses in GRMHD simulations of black hole

accretion disks, and they showed that a one dimensional model developed by Gammie (1999) could fit the data.

Gammie (1999) solved for the motion of a fluid with a frozen-in magnetic field as it plunges into a Kerr black hole along the equatorial plane. The inner boundary of the flow is at the event horizon and the outer boundary of the flow is at r_B, where the flow is assumed to have zero radial velocity and Keplerian angular velocity. The governing equations are mass, angular momentum, and energy conservation, and Maxwell's equations. There is no dissipation and the pressure and internal energy of the gas are neglected. The solutions are time-independent, axisymmetric, and vertically averaged. They provide the rest mass density, velocities, and magnetic field of the flow as a function of radius. The free parameters are a/M, r_B, and the amount of magnetic flux threading the horizon. Following Penna et al. (2010), we parametrize the flux threading the horizon by

$$\Upsilon = \frac{\int |B^r| dA}{\sqrt{M\dot{M}}}, \tag{4.29}$$

which is dimensionless. A "magnetically arrested disk" corresponds to $\phi_{\rm BH} \equiv \sqrt{\pi}\Upsilon \gtrsim 50$ (Narayan et al. 2003; Tchekhovskoy et al. 2011; Narayan et al. 2012).

Gammie's code for generating solutions numerically using the shooting method is available on the web. [4] The solutions are expressed in terms of B^i, but b^μ follows from equations (4.17)-(4.18), and the stress, $-b_{\hat{r}}b_{\hat{\phi}}$, follows from equations (4.6)-(4.9).

4.3.3 Combined model

Combining the turbulent and mean field contributions to $\alpha(r)$ gives the one-dimensional prescription

$$\alpha(r) = \alpha_0 \left[\frac{q(r)}{3/2}\right]^n - \alpha_1 \frac{b_{\hat{r}}(r) b_{\hat{\phi}}(r)}{\rho(r)^\Gamma}, \quad (q > 0). \tag{4.30}$$

If there are no large scale fields and $q = 3/2$, then $\alpha(r) = \alpha_0$, a constant. If $q < 0$, then one should only include the second term on the RHS. The Gammie (1999) solutions do not include gas pressure so we have divided the mean field stress by $\rho(r)^\Gamma$, which is proportional to pressure for a polytropic gas. This is a crude substitute for the pressure but it gives an acceptable fit to the simulations discussed below.

[4] `http://rainman.astro.illinois.edu/codelib/codes/inflow/src/`

Given M, a/M, $\dot{M}$, α_0, Γ, Υ, and r_B, the slim disk equations provide $q(r)$, and the Gammie (1999) equations provide $b_{\hat{r}}(r), b_{\hat{\phi}}(r)$, and $\rho(r)$.

The remaining free parameters are α_1 and n. These parameters can be inferred from MHD simulations. Note that α_0 and n control the size and shape of the turbulent contribution to $\alpha(r)$, and α_1 and r_B control the size and shape of the mean field contribution to $\alpha(r)$.

In §§4.4-4.6, we estimate values for these four parameters by fitting the $\alpha(r)$ prescription to data from six GRMHD simulations. As an example, Figure 4.1 shows $\alpha(r)$, as prescribed by equation (4.30), for the parameters of Model A in Table 4.4 (solid red curve). The mean magnetic field contribution to $\alpha(r)$ (long-dashed green curve) dominates inside the ISCO, where the plunging fluid stretches and amplifies the magnetic field. The turbulent contribution to $\alpha(r)$ (dashed blue curve) dominates outside the ISCO, where mean magnetic fields are weak. At large radii, the shear parameter becomes 3/2 and α becomes constant. Data from a GRMHD simulation (gray points; cf. §4.5.5) are in good agreement with the one-dimensional prescription for $\alpha(r)$.

In the next three sections, we detail our GRMHD simulations and their connection to the $\alpha(r)$ prescription.

4.4 Details of the simulations

4.4.1 Computational method

The simulations were carried out with the 3D GRMHD code HARM (Gammie et al. 2003; McKinney 2006a; McKinney & Blandford 2009), which solves the ideal MHD equations for the motion of a magnetized gas in the Kerr metric, the spacetime of a rotating black hole. The equation of motion of the gas is taken to be $u = p/(\Gamma - 1)$, where u and p are the internal energy and pressure and Γ is the adiabatic index. The code conserves energy to machine precision, so any energy lost at the grid scale by, e.g., turbulent dissipation or numerical reconnection, is returned to the gas, increasing its entropy.

Table 4.1 gives a summary of the six simulations, which we have labeled A–F. Simulations A,

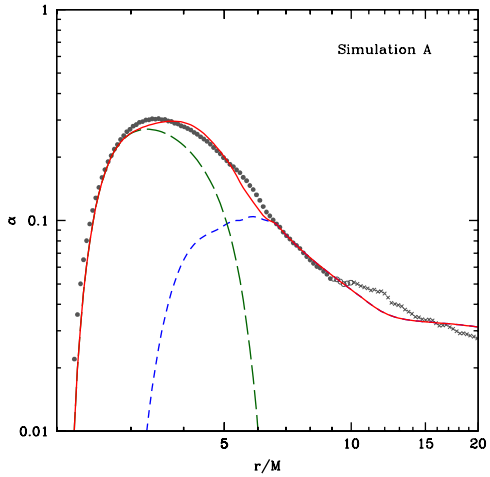

Fig. 4.1.— The $\alpha(r)$ prescription defined by equation (4.30), for parameters $\alpha_0 = 0.025$, $\alpha_1 = 100$, $n = 6$, and $r_B = 6M$ (solid red curve). This prescription is the sum of two terms, a mean magnetic field component (long-dashed green), which dominates inside the ISCO, and a turbulent component (dashed blue), which dominates outside the ISCO. These two components are based on the one-dimensional models of Gammie (1999) and Sądowski (2011), respectively. At large radii, $\alpha(r)$ converges to $\alpha_0 = 0.025$, a constant. This model is a good description of the data from simulation A (gray points; cf. §4.5). Data from inside $r_{\rm strict}$ are marked with filled circles, data from between $r_{\rm strict}$ and $r_{\rm loose}$ are marked with open circles, and data from outside $r_{\rm loose}$ are marked with crosses (cf. §4.5.5).

B, and C are thin, radiatively efficient disks, and simulations D, E, and F are thick, radiatively inefficient disks. The spin parameter is $a/M = 0.7$ for simulations B and E, and $a/M = 0$ for the others.

Most of the simulations have been described in previous papers, so our overview of the simulations in this section can be brief. Simulations B and C are two of the models discussed by Kulkarni et al. (2011a). Simulations A, B, and C were analyzed by Zhu et al. (2012) (where they are labeled E, B, and C, respectively). Finally, simulations D and F were studied by Narayan et al. (2012) (where they are called SANE and MAD). The only simulation that has not appeared before is E, but it only differs from D in that it has $a/M = 0.7$ and a duration of $100,000M$.

The resolution of simulations B and C in $r \times \theta \times \phi$ is $256 \times 64 \times 32$, and the resolution of the other simulations is $256 \times 128 \times 64$. The radial grid is logarithmically spaced to concentrate attention on the inner regions of the flow. The inner boundary of the grid is between the Cauchy horizon and event horizon, and outflow boundary conditions are used there, so the event horizon behaves as a true horizon. The polar grid is squeezed towards the equatorial plane to concentrate resolution on the turbulent, high density regions of the flow, at the expense of the laminar, coronal regions. Simulations D, E, and F use a version of the grid developed by Tchekhovskoy et al. (2011), in which the θ resolution near the pole increases with increasing radius so as to follow the formation of jets, which collimate at large distances. The azimuthal grid is uniform and extends from 0 to $\phi_{\rm max}$, where $\phi_{\rm max}$ is either $\pi/2$ (simulations A, B, and C) or 2π (simulations D, E, and F).

The properties of the six simulations are summarized in Table 4.1.

4.4.2 Initial conditions

Initially, the gas orbits the black hole in a torus in hydrostatic equilibrium (De Villiers et al. 2003; Penna et al. 2010, 2012a). The thickness of the torus can be adjusted to give either thin or thick accretion disks. A weak poloidal magnetic field threads the torus. All of the simulations start with a sequence of poloidal loops, except F, which starts from a single magnetic loop. When there are multiple loops, the black hole accretes flux of alternating polarity over time and little net flux builds up on the hole. In simulation F, the center of the loop at $r = 300M$ does not reach the black

hole over the duration of the simulation, so the black hole acquires a large net flux. In all of the simulations, the magnetic field is normalized so that the initial gas-to-magnetic pressure ratio has minimum $\beta = 100$.

4.4.3 Quasi-steady state

The initial condition is unstable to the MRI. Differential rotation of the torus triggers the MRI and the gas becomes turbulent after ~ 10 orbits. Turbulence transports angular momentum and energy outwards and the gas accretes inwards. At late times in the simulation, gas in the disk near the midplane is turbulent. Magnetic buoyancy lifts fields above and below the disk, forming a highly magnetized corona. The corona is mostly laminar because the MRI requires $\beta > 1$.

Figure 4.2 shows the fluid frame magnetic field at the end of simulations A and D. The field has been azimuthally averaged but not time averaged. The coordinates are $x/M = r\sin(\theta)$ and $z/M = r\cos(\theta)$. The turbulent region of simulation A is thinner than the turbulent region of simulation D. The turbulent region of simulation D extends nearly to the polar axes.

4.5 Analysis of simulations A and D

In this section we discuss our analysis of simulations A and D. These describe a prototypical thin disk and a prototypical thick disk around non-spinning black holes. We discuss the remaining four simulations in §4.6

Our goal for this section, achieved in §4.5.6, is to extract $\alpha(r)$ profiles from the simulation data and compare them with the one-dimensional prescription defined by equation (4.30). As a first step, we discuss the distinction between disk and coronal fluid. We only include disk fluid in our calculations. Then we discuss the radial range of fluid that can be considered to have reached a quasi-steady state. We only include quasi-steady data in our calculations. We examine the shear rate and epicyclic frequency of the simulations, because these play an important role in determining α. Finally, we compute $\alpha(r)$ and compare it with our prescription from §4.3

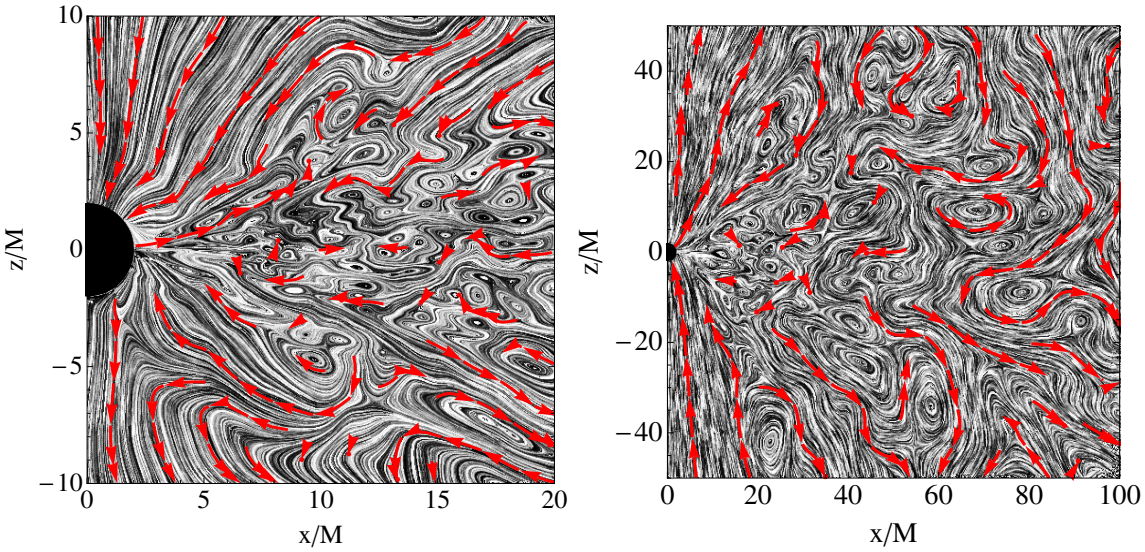

Fig. 4.2.— *Left panel:* Black, white, and red streamlines show the poloidal, fluid frame magnetic field $(b^{\hat{r}}, b^{\hat{\theta}})$ for simulation A. The field has been azimuthally averaged to make the streamlines appear continuous in this two-dimensional projection (this makes the flow appear slightly less turbulent). Turbulent twisting of the magnetic field can be seen on different scales. When the field is twisted on the smallest scale, the grid scale, there is reconnection and dissipation. The density scale height of the disk is $h/r \sim 0.1$ (cf. §4.5.1). Fluid in the disk region of the flow is turbulent. Magnetic buoyancy lifts magnetic fields out of the disk where they settle in a highly magnetized coronal region. The coronal region is mostly laminar, because magnetic tension is quenching the MRI. On very large scales, the magnetic field has an approximately dipolar structure. *Right panel:* Same as left panel, but for simulation D. This accretion flow is much thicker and the flow only becomes laminar near the polar axes.

4.5.1 The distinction between disk and corona

We would like to separate the disk component of the flow from the coronal component so that we can focus our analysis on the disk. There are several reasons to do this. For one, the stress has a different character in the corona and disk regions of the flow. In the corona, the stress is mostly generated by mean magnetic fields, while in the disk, the stress is generated largely by turbulence. So including coronal stresses in the model would add new difficulties. For this reason, and also for simplicity, we focus on the disk region of the flow.

There are other reasons to isolate the disk from the corona. At least in thin accretion disks, the emission from the corona and disk are different. The disk has a thermal spectrum and the corona has a power law spectrum. So the distinction is sensible for observations. Accretion disk models which use the α-viscosity prescription tend to focus on the disk region of the flow and ignore the corona. Another reason to separate out the disk region is that our numerical grid concentrates θ resolution at the midplane and leaves the polar regions poorly resolved. So the simulation data are unreliable in the corona.

We therefore only include fluid within one density scale height of the midplane in our analysis. The density scale height is defined as,

$$\frac{h}{r} = \frac{\int_0^{\pi}\int_0^{\phi_{\rm max}}\int_{t_1}^{t_2} |\theta-\pi/2|\,\rho u^t \sqrt{-g} dt d\theta d\phi}{\int_0^{\pi}\int_0^{\phi_{\rm max}}\int_{t_1}^{t_2} \rho u^t \sqrt{-g} dt d\theta d\phi}. \tag{4.31}$$

where ρ is rest mass density in the fluid frame, and ρu^t is rest mass density in Boyer-Lindquist coordinates. The time integral is over the steady state period of the flow, as explained below. Another popular definition for the scale height is $(h/r)_{\rm rms} = \left(\int (\theta-\pi/2)^2\,\rho\sqrt{-g}dtd\theta d\phi / \int \rho\sqrt{-g}dtd\theta d\phi\right)^{1/2}$. We have no reason to favor one definition over another, though it should be noted that $(h/r)_{\rm rms}$ can be a factor of ~ 2 bigger than h/r (Penna et al. 2010).

We also add a density-weighting to vertical averages, to further emphasize midplane fluid. That is, the density weighted vertical average of $\mathcal{O}$ is $\int \mathcal{O}\rho u^t \sqrt{g_{\theta\theta}} d\theta / \int \rho u^t \sqrt{g_{\theta\theta}} d\theta$.

The top panel of Figure 4.3 shows $\log(\alpha)$ as a function of x and z for simulation A. We explain how α is obtained from the simulation in §4.5.5, but we show this plot here to illustrate the distinction between the disk and the corona. Black dashed curves mark one scale height above

the midplane. Note that α has a very different character above and below the disk region. In the coronal regions α is much larger than in the disk. The middle panel of Figure 4.3 shows the ratio of Maxwell stress to Reynolds stress on a logarithmic scale. Maxwell stresses are much more significant in the corona. The different character of the flow in these two regions is one of the reasons we only include disk fluid within one h/r of the midplane in our calculations.

Figure 4.4 shows the same quantities for simulation D. Again, α and the Maxwell stress are much larger outside the disk. However, the shape of this region does not track h/r as it did in simulation A. In fact, the high α, high Maxwell stress region has a parabolic shape, bounded by roughly $z/M = (r/6M)^2$. This looks like a jet. For simplicity and consistency, we will restrict our calculations to the fluid within one h/r of the midplane for all of the simulations. We have checked that our results do not depend on the details of this cutoff, as long as we do not include the "jet" region.

4.5.2 Radial and azimuthal velocities

To extract smooth results from turbulent data, it is necessary to average the data over at least a viscous time, which smooths out turbulent fluctuations (Narayan et al. 2012). As a first step, we need the radial velocity of the simulations. To compute the shear rate and epicyclic frequency of the gas (and thus α), we need the azimuthal velocity of the gas. We compute these two components of the velocity in this section. We will not need the θ component of the velocity. It is much smaller than the radial and azimuthal components in the disk region of the flows.

In a thin accretion disk, the gas closely follows circular geodesics as it spirals toward the ISCO. The radial velocity of the gas is significantly smaller than the azimuthal velocity. In a standard thin disk, the radial velocity is suppressed by a factor of $\alpha(h/r)^2$. In the ADAF solution, which describes a very thick accretion flow, the radial velocity is suppressed by a factor of α relative to the azimuthal velocity. These relations hold approximately for the GRMHD simulations as well.

The radial velocity most relevant for turbulence is the one measured by the zero angular momentum observer (ZAMO) of Bardeen et al. (1972). This is a local, inertial frame attached to observers with zero angular momentum. As a result of frame dragging, ZAMO observers appear to

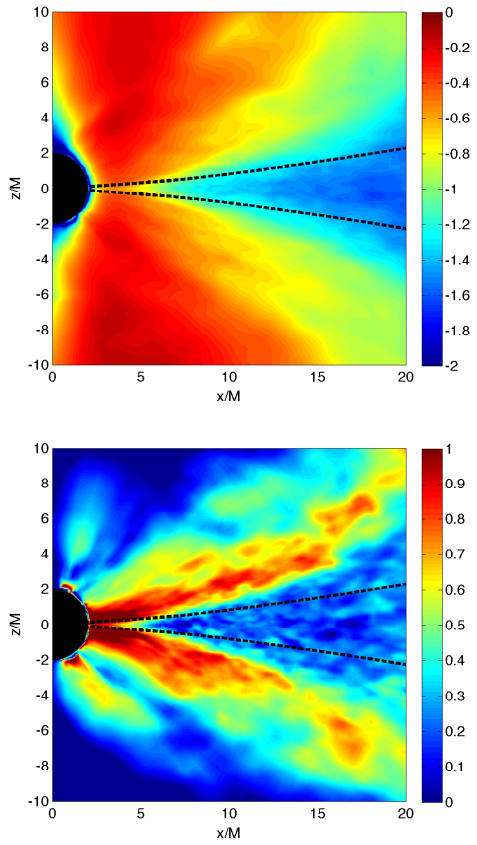

Fig. 4.3.— *Top panel:* $\log(\alpha)$ in the $r-\theta$ plane for simulation A. The data has been time-averaged over $t = 7,000M - 20,000M$. Dashed black lines indicate one density scale height above and below the midplane (cf. §4.5.1). We refer to the low α region within one scale height of the midplane as the disk, and the high α region outside one scale height as the corona. We restrict our calculations to the disk, for the reasons discussed in §4.5.1. We show this plot here to illustrate the difference between the disk and the corona. We explain how α is obtained from the simulation in §4.5.5. *Bottom panel:* Time-averaged ratio of Maxwell stress to Reynolds stress on a log scale, in the $r-\theta$ plane, for simulation A. Coronal fluid is more magnetically dominated than disk fluid. This is expected, as magnetic buoyancy lifts magnetic fields into the corona.

Table 4.1: GRMHD simulation parameters

Simulation	a/M	h/r	Initial loops	$n_r \times n_\theta \times n_\phi$	$\phi_{\rm max}$	Duration
A	0	0.1	Multiple	$256 \times 128 \times 64$	π	$20,000M$
B	0.7	0.05	Multiple	$256 \times 64 \times 32$	$\pi/2$	$27,000M$
C	0	0.05	Multiple	$256 \times 64 \times 32$	$\pi/2$	$27,000M$
D	0	0.3	Multiple	$256 \times 128 \times 64$	2π	$200,000M$
E	0.7	0.3	Multiple	$256 \times 128 \times 64$	2π	$100,000M$
F	0	0.3	Single	$264 \times 126 \times 60$	2π	$100,000M$

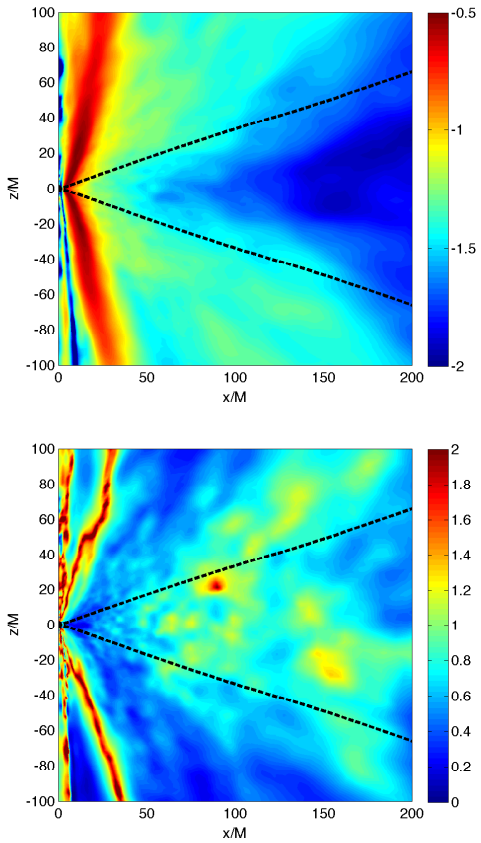

Fig. 4.4.— Same as Figure 4.3, except for simulation D. Unlike simulation A, the highly magnetized region does not have the same shape as the disk scale height. In fact, the former has a paraboloidal, jet-like shape, approximately $z/M = (r/6M)^2$.

rotate with respect to observers at infinity. The ZAMO frame is at rest with respect to the local spacetime.

The radial velocity in the ZAMO frame is

$$v_r = \frac{\sqrt{A}}{\Delta}\frac{u^r}{u^t}, \tag{4.32}$$

where Δ and A are defined by equations (4.2) and (4.4).

The top left panel of Figure 4.5 shows the radial velocity as a function of radius for simulation A. The data has been averaged over the disk region of the flow, with a density weighting, as discussed in §4.5.1. It has been time-averaged over the quasi-steady state period of the flow, which we explain below. The ISCO is at $r = 6M$. Inside the ISCO, the gas is approximately in free fall and the radial velocity increases rapidly as the gas approaches the black hole. Outside the ISCO, the motion is more nearly circular. In this region, the radial velocity is suppressed relative to the azimuthal velocity as predicted by standard disk theory. Because the radial velocity is small, it takes a long time for the simulation to reach a quasi-steady state. Once steady state is reached, it requires a time average extending over many orbital periods to smooth out turbulent fluctuations and obtain reliable results. We take up these issues in the next section.

The top right panel of Figure 4.5 shows the radial velocity as a function of radius for simulation D. The radial velocity is much larger than the radial velocity of A, because this accretion flow is geometrically thick. For this reason, the data from this simulation is in quasi-steady state out to a larger radius. Also, the larger radial velocity smears out the inner edge of the accretion disk. There is no longer a sudden transition between slow and fast radial velocity, at the ISCO or at any other radius.

The bottom left panel of Figure 4.5 shows the angular velocity

$$\Omega = \frac{d\phi}{dt} = \frac{u^\phi}{u^t}, \tag{4.33}$$

of simulation A as a function of radius. Again, we have included only fluid within one scale height of the midplane, taken the density-weighted vertical average, and time averaged over the steady state portion of the flow. The dashed line shows the angular velocity of circular geodesics in the equatorial plane, $\Omega = M^{1/2}/(r^{3/2} + aM^{1/2})$. The flow follows circular geodesics except for

$r \lesssim 5M$, where the radial velocity is increasing rapidly. The angular velocity peaks around $3M$. At this radius, the shear parameter q must go to zero, so the turbulent contribution to α becomes negligible.

The bottom right panel of Figure 4.5 shows the angular velocity of simulation D. It is also nearly Keplerian outside the ISCO. This is perhaps surprising, because the angular velocity of the self-similar ADAF solution is very sub-Keplerian. The initial torus of the GRMHD simulation persists at large radii over the duration of the simulation and continues to feed nearly Keplerian gas into the inner regions of the flow. This acts as a very strong boundary condition, which may limit the solution's ability to converge to the ADAF solution. The ADAF solution is self-similar and describes an accretion flow with infinite extent but, as we will see, the simulation is only converged out to $r = 100M$. A longer duration simulation, which has reached quasi-steady state out to a larger radius, might be expected to have a more ADAF-like angular velocity. Nonetheless, the radial velocity of simulation D does appear to be converging to the ADAF prediction, as shown by Narayan et al. (2012).

4.5.3 Convergence and steady state

Following Narayan et al. (2012), we divide the data from simulation D into six "time chunks" which are logarithmically spaced in time. Each time chunk is about twice as long as the previous one. They are summarized in Table 4.3. This logarithmic spacing is useful since most of the quantities we are interested in show power-law behavior as a function of both time and radius. Note that there is no overlap between chunks, and hence each chunk provides independent information. Because the duration of simulation A is only $20,000M$, we use a single time chunk, spanning $t = 7,000M - 20,000M$.

For each time chunk, we compute the time-averaged radial velocity profile $v_r(r)$ of the gas within one scale-height of the mid-plane. We estimate the viscous time at radius r by (Novikov & Thorne 1973; Penna et al. 2010):

$$t_{\rm visc}(r) = \frac{r}{|v_r(r)|}. \tag{4.34}$$

Following Narayan et al. (2012), we then define two criteria, one "strict" and one "loose," to

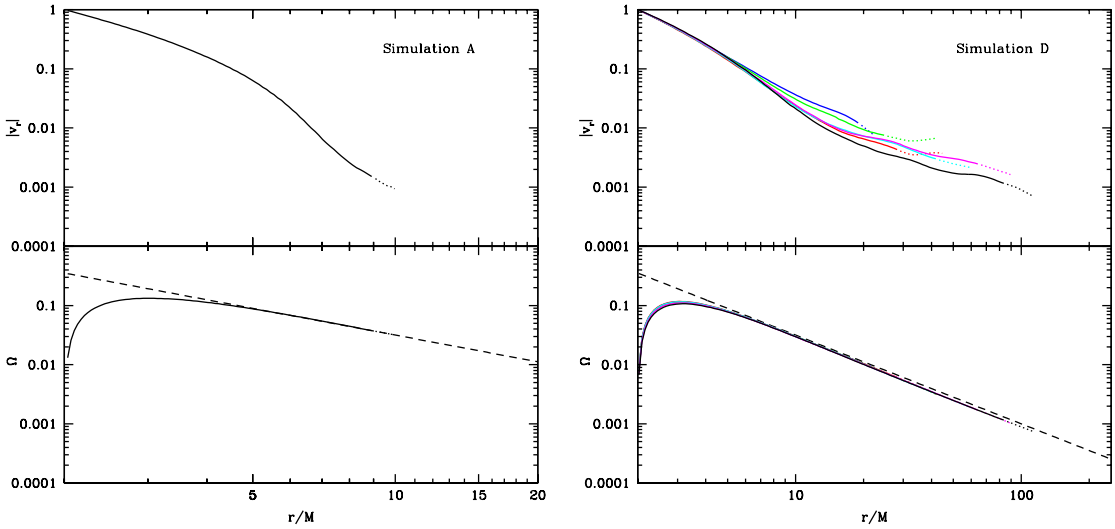

Fig. 4.5.— *Top left:* Radial velocity as a function of radius for simulation A. The solid line extends to $r = r_{\rm strict}$ and the dashed line extends to $r = r_{\rm loose}$ (estimated convergence radii of §4.5.3). The radial velocity increases suddenly around the ISCO at $r = 6M$, inside of which there are no stable circular orbits for the gas to follow. *Top right:* Radial velocity as a function of radius for simulation D. Colors correspond to time chunks 1 (blue), 2 (green), 3 (red), 4 (cyan), 5 (magenta), and 6 (black) (see §4.5.3). *Bottom left:* Angular velocity as a function of radius for simulation A. The dashed black curve shows the angular velocity of circular, equatorial geodesics. The simulated flow is nearly geodesic outside the ISCO. The angular velocity has a maximum near the photon orbit at $r = 3M$, so the shear parameter (and hence the turbulent contribution to α) will be zero here. *Bottom right:* Angular velocity as a function of radius for simulation D. This flow is slightly sub-Keplerian outside the ISCO.

estimate the radius range over which the flow has achieved inflow equilibrium:

$$t_{visc}(r_{\rm strict}) = t_{\rm chunk}/2, \tag{4.35}$$

$$t_{visc}(r_{\rm loose}) = t_{\rm chunk}, \tag{4.36}$$

where $t_{\rm chunk}$ is the duration of the chunk. The values of $t_{\rm chunk}$, $r_{\rm strict}$, and $r_{\rm loose}$ for the various time chunks are summarized in Tables 4.2 and 4.3. We only trust data from inside $r_{\rm loose}$. Data from inside $r_{\rm strict}$ are considered particularly reliable.

4.5.4 Shear and epicyclic frequencies

Now we compute the dimensionless shear parameter, q, and the epicyclic frequency, κ, as a function of radius. The shear parameter is computed from $q = -2\sigma_{\hat{n\phi}}/\Omega$. The epicyclic frequency is computed from the shear parameter using equation (4.25). The data are vertically averaged over the gas within one scale height of the midplane using the density weighting. The data are time averaged over the time chunks listed in Tables 4.2 and 4.3.

The top left panel of Figure 4.6 shows the shear parameter as a function of radius for simulation A out to $r_{\rm strict}$ (solid curve) and $r_{\rm loose}$ (dotted curve). The analytical shear parameter for circular, equatorial Kerr geodesics is shown for comparison (dashed curve). At large radii, the analytical q converges to the shear parameter of non-relativistic Keplerian flow, $q = 3/2$. At the ISCO, general relativistic corrections increase the shear parameter to $q = 2$. The GRMHD shear parameter is about 10% larger than the analytical shear parameter outside the ISCO. Inside the ISCO, the analytical q blows up as it approaches the photon orbit. The GRMHD shear parameter goes to zero near the photon orbit and is negative very close to the black hole.

The top right panel of Figure 4.6 shows the shear parameter as a function of radius for simulation D. Results are shown for each of the time chunks. All of the time chunks are consistent out to $r_{\rm loose}$ to within several percent. This gives us confidence that the simulation has converged to a quasi-steady solution. The GRMHD shear parameter is similar to the shear parameter of simulation A. It is about 10% larger than the analytical q outside the ISCO, turns over inside the ISCO, and drops to zero near the photon orbit. There is good agreement between the GRMHD

Table 4.2: Convergence radii for simulations A, B, and C

Simulation	Time Range (M)	$t_{\rm chunk}/M$	$r_{\rm strict}/M$	$r_{\rm loose}/M$
A	7,000-20,000	13,000	9	10
B	20,000-27,000	7,000	6.5	7
C	20,000-27,000	7,000	6.5	7

Table 4.3: Time chunks for simulation D

Chunk	Time Range (M)	$t_{\rm chunk}/M$	$r_{\rm strict}/M$	$r_{\rm loose}/M$
I	3,000-6,000	3,000	19	23
II	6,000-12,000	6,000	25	43
III	12,000-25,000	13,000	29	45
IV	25,000-50,000	25,000	43	62
V	50,000-100,000	50,000	66	92
VI	100,000-200,000	100,000	86	113

and analytical shear parameters out to $r_{\rm loose} \sim 100M$.

The bottom left panel of Figure 4.6 shows the epicyclic frequency as a function of radius for simulation A. The bottom right panel shows the same quantity for simulation D. In both cases, outside the ISCO, the epicyclic frequency of the simulation is about 10% lower than the epicyclic frequency of Keplerian flow. In both cases the epicyclic frequency has a minimum near the ISCO. The minimum of the epicyclic frequency roughly marks the most unstable radius in the flow, because $\kappa = 0$ corresponds to marginal stability. So it is consistent with standard disk theory that the minimum of κ is near the ISCO. Simulation D has a broader and shallower minimum, indicating the inner edge of this disk has been "smeared out" by the larger radial velocity of the flow.

4.5.5 Shakura-Sunyaev viscosity parameter, α

Finally, we compute the dimensionless viscosity parameter, α. The GRMHD stress-energy tensor is a combination of Reynolds and Maxwell terms:

$$T_{\mu\nu} = T^{(\rm rey)}_{\mu\nu} + T^{(\rm mag)}_{\mu\nu}, \tag{4.37}$$

where,

$$T^{(\rm rey)}_{\mu\nu} = (\rho + u)u_\mu u_\nu + p h_{\mu\nu}, \tag{4.38}$$

$$T^{(\rm mag)}_{\mu\nu} = \frac{1}{2}\left(b^2 u_\mu u_\nu + b^2 h_{\mu\nu} - 2 b_\mu b_\nu\right), \tag{4.39}$$

and $h_{\mu\nu} = g_{\mu\nu} + u_\mu u_\nu$ is the projection tensor. To each term there is an associated stress, which is the $r\phi$ component of the tensor measured in the fluid frame. So the Reynolds stress is $T^{(\rm rey)}_{\hat{r}\hat{\phi}}$ and the Maxwell stress is $T^{(\rm mag)}_{\hat{r}\hat{\phi}}$. An important difference between the two is that the Reynolds stress requires turbulence whereas the Maxwell stress can be generated by turbulence or large scale magnetic fields and thus can be nonzero even in laminar flow.

We define α as the ratio of total stress to total pressure:

$$\alpha = \frac{T^{(\rm rey)}_{\hat{r}\hat{\phi}} + T^{(\rm mag)}_{\hat{r}\hat{\phi}}}{p + b^2/2}. \tag{4.40}$$

We have chosen to include $b^2/2$ in the denominator because it keeps $\alpha < 1$. As a result of this choice, part of the observed dependence of α on q is inherited via the magnetic pressure because

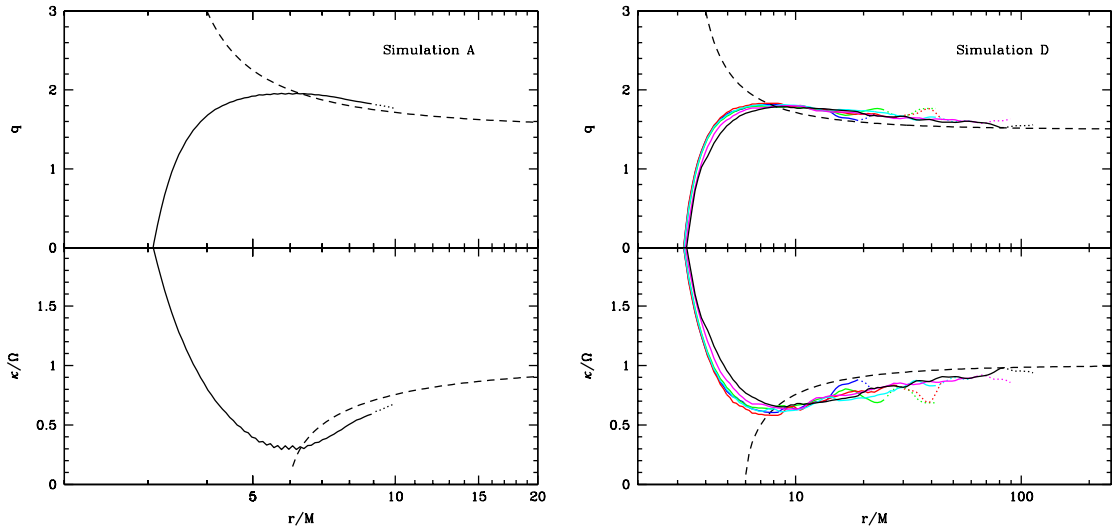

Fig. 4.6.— *Top left:* Dimensionless shear parameter, q, as a function of radius for simulation A (solid and dotted curves) and for Keplerian flow (dashed). The simulation data are plotted out to $r_{\rm loose}$ (dotted curves) and out to $r_{\rm strict}$ (solid curves). The simulated shear parameter turns over near the ISCO. *Top right:* Dimensionless shear parameter as a function of radius for simulation D. Colors are as in Figure 4.5. *Bottom left:* Epicyclic frequency as a function of radius for simulation A. The epicyclic frequency has its minimum near the ISCO, as expected. *Bottom right:* Epicyclic frequency as a function of radius for simulation D. The minimum is still near the ISCO, but it is broader and shallower than the minimum in the epicyclic frequency of simulation A. The larger radial velocity of simulation D has "smeared out" the inner edge of the disk.

the magnetic pressure is amplified by shear. This is significant inside the ISCO where the magnetic pressure is comparable to or exceeds the gas pressure.

We compute the Maxwell and Reynolds stresses in the rest frame of the mean flow,

$$\bar{u}^\mu = \frac{1}{\phi_{\rm max}} \int_0^{\phi_{\rm max}} u^\mu d\phi, \tag{4.41}$$

rather than in the rest frame of the instantaneous flow, u^μ. The mean flow is the ϕ-averaged instantaneous flow. There are some subtleties in the distinction between these two frames. The Reynolds stress vanishes in the rest frame of the instantaneous flow, u^μ, by definition of the fluid frame, but not in the rest frame of the mean flow, $\bar{u}^\mu$. This is our primary reason for choosing $\bar{u}^\mu$ to define the inertial fluid frame when computing α . The electric field vanishes in the rest frame of the instantaneous flow, by the assumption of ideal MHD, and not in the rest frame of the mean flow, but for simplicity we assume the electric field can be neglected in both frames.

One could include a time average in the definition of the mean flow, equation (4.41). Penna et al. (2010) included a $100M$ time average. That is, they averaged the instantaneous flow over all of ϕ and over $100M$ in time to obtain the mean flow. At large radii, $100M$ is much smaller than the orbital timescale, so this extra averaging has little effect. However, inside the ISCO, $100M$ is larger than the orbital timescale. In this case, the time-averaged mean flow tends to give larger α. The reason is that time-averaging increases the discrepancy between the mean and instantaneous flows by adding contributions to the mean flow from earlier and later times. This discrepancy propagates into α when the stress tensor is boosted to the rest frame of the mean flow.

Figure 4.7 shows $\alpha(r)$ for simulation A with and without a $100M$ time averaging in the definition of $\bar{u}^\mu$. Including the time averaging increases α and the effect is greatest inside the ISCO. In fact, the peak α exceeds unity when the mean flow is defined with a time average. This would imply the stresses carry more energy than the total energy of the gas and magnetic fields, which is unphysical. To avoid these sorts of contradictions, we do not include any time averaging in equation (4.41).

The middle panel of Figure 4.8 shows the ratio of Maxwell stress to Reynolds stress in simulation A. Outside the ISCO, the ratio tracks the prediction of the linearized MRI, $(4-q)/q$

(Pessah et al. 2006b). In fact, it is slightly larger, as is consistent with shearing box simulations of MRI turbulence (Pessah et al. 2006b). Inside the ISCO, the Maxwell stress is an order of magnitude larger than the Reynolds stress. The flow is mostly laminar inside the ISCO, so Reynolds stress is weak, and the plunging fluid stretches the magnetic field, so the Maxwell stress is strong. The bottom panel of Figure 4.8 shows the product $\alpha\beta$. It approaches the expected value of ≈ 0.5 in the disk (Blackman et al. 2008; Guan et al. 2009; Sorathia et al. 2012).

The top panel of Figure 4.9 shows $\alpha(r)$ for the six time chunks of simulation D. Outside the ISCO, the various time chunks agree to within 30%, which provides an estimate for the contribution of turbulent noise to the error in our α measurements. Inside the ISCO, where the flow is more nearly laminar, the agreement between the time chunks is better.

The bottom panel of Figure 4.9 shows the ratio of Maxwell to Reynolds stress as a function of radius for simulation D. Inside about $r = 22M$, the ratio is consistent with the ratio of simulation A. Outside $r = 22M$, the ratio begins to grow with radius. It is not clear what causes this. It may indicate that simulation D has not reached quasi-steady state at these radii yet. Figure 4.4 shows highly magnetized, irregular clumps of fluid in the disk region, even after time-averaging the data over the last time chunk. In a true quasi-steady state, one would expect time averaging to eliminate these clumps.

4.5.6 Comparison with the one-dimensional $\alpha(r)$ prescription

Finally, we compare $\alpha(r)$ of the simulations with the one-dimensional prescription for $\alpha(r)$ of §4.3, as defined by equation (4.30) and the parameters listed in Table 4.4.

Figure 4.1 shows the agreement between the GRMHD $\alpha(r)$ from simulation A and the $\alpha(r)$ prescription. Figure 4.10 shows the agreement between simulation D and the $\alpha(r)$ prescription. The interpretation of the GRMHD $\alpha(r)$ in terms of a mean magnetic field component in the inner regions, and a turbulent component in the outer regions, appears to match the data. It is more difficult to fit simulation D because the $\alpha(r)$ prescription relies on a sharp distinction between the laminar, magnetically dominated inner regions of the flow, and the turbulent, weakly magnetized outer regions. This distinction is cleanest in thin disks, like simulation A, which have a clear inner

edge at the ISCO. In thick disks, like simulation D, the inner edge of the disk is smeared out by the radial velocity of the flow, so the separation of α into two independent components is less sound.

The shape of $\alpha(r)$ does not depend strongly on all of the parameters in Table 4.4. The mass of the black hole in the GRMHD simulations is dimensionless. It is listed in Table 4.4 because it goes into the slim disk solutions that underlie the one-dimensional $\alpha(r)$ prescription. We set $M/M_{\odot} = 10$ arbitrarily and this choice has a negligible effect on $\alpha(r)$.

The accretion rate also enters through the slim disk part of $\alpha(r)$. Our estimates of $\dot{M}/\dot{M}_{\rm edd}$ for the GRMHD simulations are based on the analysis of Zhu et al. (2012), who used h/r as a proxy for the accretion rate. This gives rough estimates, which is all we need because the dependence of $\alpha(r)$ on the accretion rate is also very weak.

The magnetic flux threading the horizon, Υ, is measured directly from the GRMHD simulations. It slightly affects the shape of $\alpha(r)$ inside the ISCO.

The four parameters that strongly control the shape of $\alpha(r)$ are α_0, α_1, n and r_B. It is encouraging that $\alpha_0 = 0.025$, and $n = 6$ give good fits to both simulations. In other words, both simulations have $\alpha(r) \sim 0.025$ at large radii, and $\alpha \propto q^6$ (and $q > 0$) in the turbulent disk.

Mean magnetic fields are only important inside the ISCO of simulation A, so we set $r_B = 6M$ in this case. The region where mean magnetic fields are important in simulation D is broader, so we set $r_B = 30M$ in this case.

4.6 Analysis of simulations B, C, E, and F

In this section we present data from four more GRMHD simulations. This gives information about the dependence of the viscosity parameters α_0, α_1, n, and r_B, on black hole spin, resolution, and the amount of magnetic flux threading the black hole. Of these effects, the dependence on flux threading the black hole is the most dramatic.

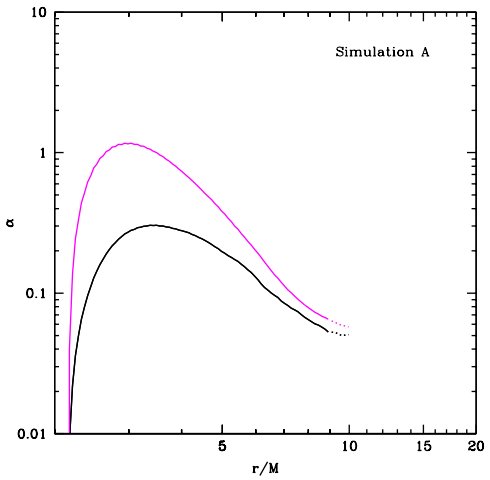

Fig. 4.7.— Dimensionless viscosity parameter, α, as a function of radius for simulation A, with (magenta) and without (black) a $100M$ time-average in the definition of the mean fluid frame, $\bar{u}^\mu$. Outside the ISCO, $100M$ is shorter than an orbital period, so the effect is small. Inside the ISCO, $100M$ is several orbital periods, so the effect is large.

Table 4.4: Parameters for $\alpha(r)$ fits to the GRMHD simulations

Simulation	$M/M_\odot$	a/M	$\dot{M}/\dot{M}_{\rm edd}$	Υ	α_0	α_1	n	r_B
A	10	0	0.5	0.6	0.025	100	6	$r_{\rm ISCO}$
B	10	0.7	0.2	3	0.025	10	6	$r_{\rm ISCO}$
C	10	0	0.2	6	0.025	1	6	$r_{\rm ISCO}$
D	10	0	1	5	0.025	0.5	6	30M
E	10	0.7	1	10	0.025	0.5	6	30M
F	10	0	1	30	0.025	0.1	6	30M

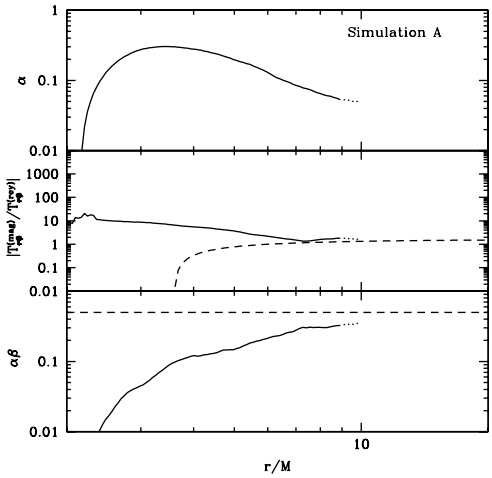

Fig. 4.8.— *Top panel:* Dimensionless viscosity parameter, α, as a function of radius for simulation A. The data has been time averaged from $t = 7,000M$ to $20,000M$. Solid and dotted curves correspond to $r \leq r_{\rm strict}$ and $r \leq r_{\rm loose}$, *Middle panel:* Time-averaged ratio of Maxwell to Reynolds stress for simulation A (solid and dotted curves). The dashed curve is the the prediction from a linearized MRI analysis, $4/q(r) - 1$ (Pessah et al. 2006b), for Keplerian $q(r)$, equation (4.24). *Bottom panel:* Product $\alpha\beta$ for simulation A (solid and dotted curves). The dashed line at $\alpha\beta = 0.5$ is the expected value for saturated MRI turbulence (Blackman et al. 2008; Guan et al. 2009; Sorathia et al. 2012). The simulated product falls below this value inside the ISCO where the flow is mostly laminar.

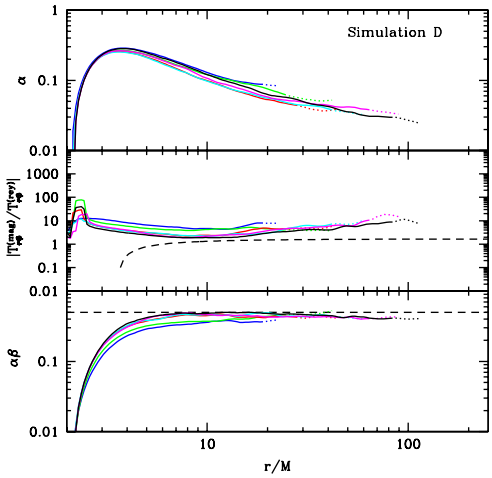

Fig. 4.9.— Same as Figure 4.8 but for simulation D. Colors and line types are as in Figure 4.5.

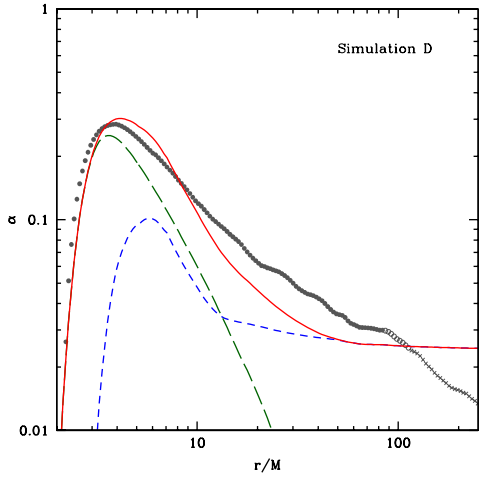

Fig. 4.10.— Same as Figure 4.1 but for simulation D.

4.6.1 Simulation E

Simulation E is identical to simulation D except the black hole has spin parameter $a/M = 0.7$ and the duration is $100,000M$. We have divided the simulation data into time chunks as we did for simulation D, but there is one less time chunk because the duration is half as long. The time chunks and radii of convergence estimates are listed in Table 4.5.

Figure 4.11 shows the radial and angular velocities as a function of radius for the five time chunks. After the first three time chunks, around $t = 25,000$, the radial velocity drops by about a factor of 2. Then it holds steady (to within a few percent) for the final two time chunks. So even at $t = 25,000M$, the simulation is still settling down. The radial velocity at the end of simulation E is about 30% lower than the radial velocity at the end of simulation D. As a result, simulation E has converged over a smaller range of radii; we find $r_{\rm loose} = 60M$ for the last time chunk (simulation D had $r_{\rm loose} = 90M$ over the same time interval.)

Figure 4.12 shows the dimensionless shear parameter and epicyclic frequency as a function of radius. Outside the ISCO, the shear parameter is about 20% larger than the shear parameter of circular geodesics and the epicyclic frequency is about 20% smaller, similar to the results from simulation D. The minimum epicyclic frequencies of the two simulations are also comparable. Simulation D had $\kappa/\Omega \sim 0.6$ and simulation E has $\kappa/\Omega \sim 0.5$.

Figure 4.13 compares $\alpha(r)$ as computed from the last time chunk of the simulation against $\alpha(r)$ computed from the one-dimensional viscosity prescription with $\alpha_0 = 0.025$, $\alpha_1 = 0.5$, $n = 6$, and $r_B = 30M$. This is the same choice of parameters that gave a good fit to simulation D. It is interesting that they fit simulation E as well. This suggests the parameters of the modified viscosity prescription do not depend strongly on black hole spin.

4.6.2 Simulation B

This simulation is identical to simulation A, except the black hole is spinning with spin parameter $a/M = 0.7$ and the resolution is $256 \times 64 \times 32$ rather than $256 \times 128 \times 64$.

The left panel of Figure 4.14 shows the GRMHD $\alpha(r)$. The $\alpha(r)$ prescription is shown for the

Table 4.5: Time chunks for simulation E

Chunk	Time Range (M)	$t_{\rm chunk}/M$	$r_{\rm strict}/M$	$r_{\rm loose}/M$
I	3,000-6,000	3,000	9.5	15
II	6,000-12,000	6,000	15	20
III	12,000-25,000	13,000	22	31
IV	25,000-50,000	25,000	31	44
V	50,000-100,000	50,000	44	60

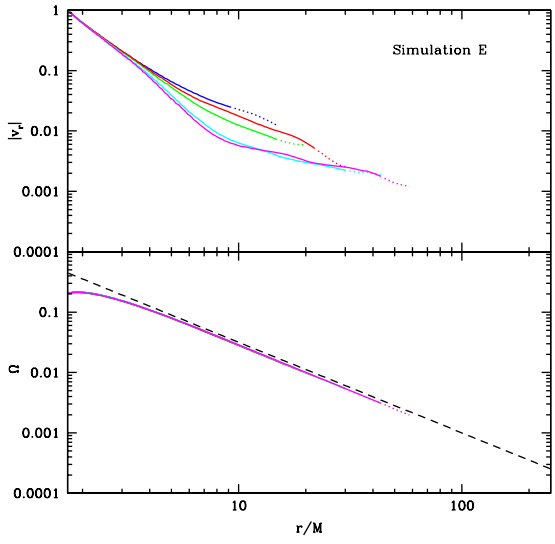

Fig. 4.11.— Same as Figure 4.5 but for simulation E.

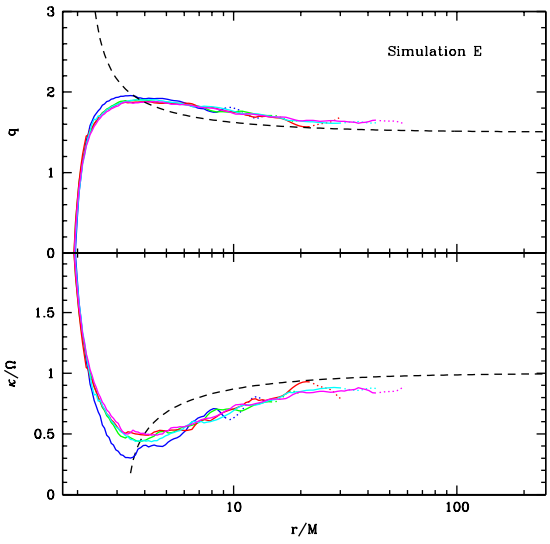

Fig. 4.12.— Same as Figure 4.6 but for simulation E.

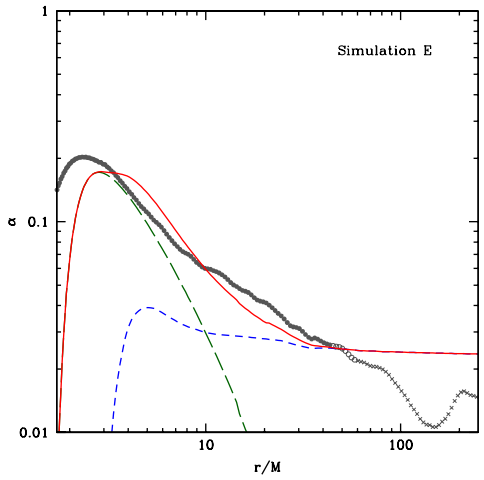

Fig. 4.13.— Same as Figure 4.1 but for simulation E.

same parameters that gave a good fit to simulation A: $\alpha_0 = 0.025$, $\alpha_1 = 1$, $n = 6$, and $r_B = r_{\rm ISCO}$. The parameters $\alpha_0 = 0.025$ and $n = 6$ governing the turbulent part of $\alpha(r)$ are the same across all four simulations we have considered so far, suggesting these parameters do not depend strongly on disk thickness.

4.6.3 Simulation C

Simulation C is the same as simulation A except the resolution is lower: $256 \times 64 \times 32$ versus $256 \times 128 \times 64$ and the disk is thinner ($h/r \sim 0.05$ instead of $h/r \sim 0.1$). The data from this simulation has a lower α than the $\alpha(r)$ prescription with our fiducial choice of parameters $\alpha_0 = 0.025$ and $n = 6$. This suggests we are under-resolving the MRI at this resolution. To infer whether the values $\alpha_0 = 0.025$ and $n = 6$ are robust, higher resolution simulations would be useful.

The results are shown in the right panel of Figure 4.14.

4.6.4 Simulation F

Simulation F differs from simulation D in one crucial respect. The initial torus of gas is threaded with a single poloidal magnetic field loop rather than multiple loops. The center of the initial loop is centered at $r = 300M$ and gas from this radius does not reach the black hole over the duration of the simulation. So the polarity of the flux that reaches the black hole is approximately constant and a large net flux builds up on the hole. Narayan et al. (2012) give a detailed account of the convergence in time and radius, and the role of outflows, in simulations D and F.

The large net flux carried by the gas in simulation D has a dramatic effect: the flow remains mostly laminar at all radii. Figure 4.15 shows the fluid frame magnetic field in the $r - \theta$ plane at $t = 100,000M$, the final snapshot of the simulation. The eddies and turbulent twisting of the field are all but gone on every scale, in marked contrast to the other five simulations we considered (see, e.g., Figure 4.2).

Following Narayan et al. (2012), we divide the simulation data into five time chunks. The time periods and estimated convergence radii for each time chunk are summarized in Table 4.6.

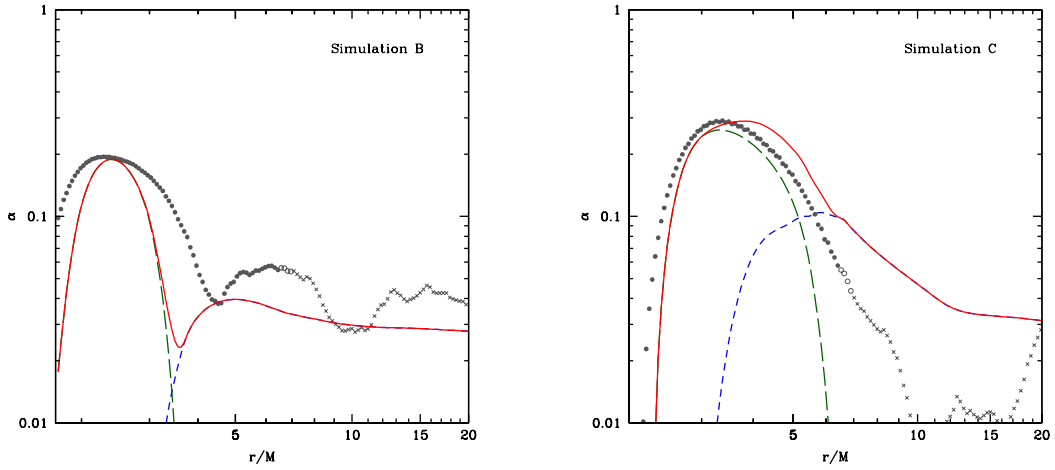

Fig. 4.14.— Same as Figure 4.1 except for simulations B (left panel) and C (right panel).

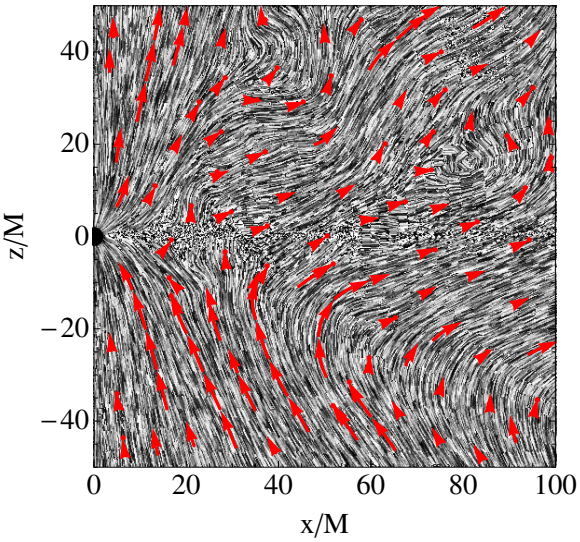

Fig. 4.15.— Same as Figure 4.2 but for Simulation F. The magnetic field structure does not show turbulent twisting on any scale; the flow is mostly laminar.

This simulation has the largest radial velocity of any of the simulations (see Figure 4.16), so the estimated convergence radii are the largest. The final time chunk has $r_{\rm strict} = 170M$ and $r_{\rm loose} = 207M$.

Simulation F also has the most sub-Keplerian angular velocity of the six simulations (Figure 4.16). The angular velocity drops by a factor of a few between time chunks I and III, but it is consistent across the final three time chunks to within a few percent.

The ratio of Maxwell stress to Reynolds stress has a much clumpier distribution in the $r - \theta$ plane than any of the other simulations. A large, magnetized, z-shaped clump, where the Maxwell stress is enhanced, extends throughout the flow (bottom panel of Figure 4.17). The irregular shape of the clump suggests it is a non-equilibrium structure. Perhaps if the duration of the simulation was longer it would be smoothed out. The appearance of the magnetized clump suggests $r_{\rm strict} = 170M$ is a better estimate for the radii of convergence for this simulation than $r_{\rm loose} = 207$.

The shear parameter of the flow (top panel of Figure 4.18) varies by about 50% between time chunks. Outside the ISCO, the shear parameter is roughly constant with radius. The epicyclic frequency (bottom panel of Figure 4.18) has its minimum near $r = 20M$, rather than at the ISCO. The minimum itself is very broad and shallow, not extending much below $\kappa/\Omega = 1$. In other words, the inner edge of the disk has moved well outside the ISCO and is highly smeared out.

The profiles of α as a function of radius for the five time chunks are shown in the top panel of Figure 4.19. Outside $r \approx 20M$, the profiles of α are constant with radius, even increasing slightly. The other simulations have α decreasing with radius. This suggests the turbulent contribution to α is not dominating even at the largest converged radii, which is consistent with the laminar structure of the magnetic field lines.

The bottom panel of Figure 4.19 shows the ratio of Maxwell to Reynolds stress as a function of radius for the five time chunks. For the first two time chunks, the Maxwell stress is an order of magnitude larger than the Reynolds stress at all radii. During the final three time chunks, the ratio appears to have stabilized out to $r = 40M$. At larger radii, the Maxwell stress is enhanced by the non-equilibrium, magnetized, z-shaped clump noted earlier.

Table 4.6: Time chunks for simulation F

Chunk	Time Range (M)	$t_{\rm chunk}/M$	$r_{\rm strict}/M$	$r_{\rm loose}/M$
I	3,000-6,000	3,000	35	52
II	6,000-12,000	6,000	37	65
III	12,000-25,000	13,000	69	90
IV	25,000-50,000	25,000	109	128
V	50,000-100,000	50,000	170	207

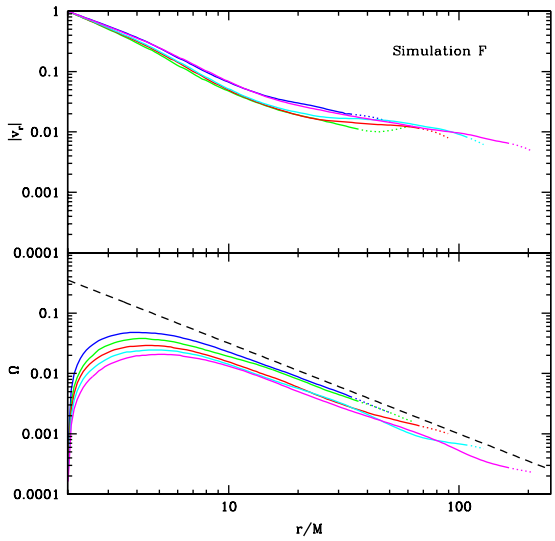

Fig. 4.16.— Same as Figure 4.5 but for simulation F. Of the six simulations we consider, this simulation has the largest radial velocity and is the most sub-Keplerian.

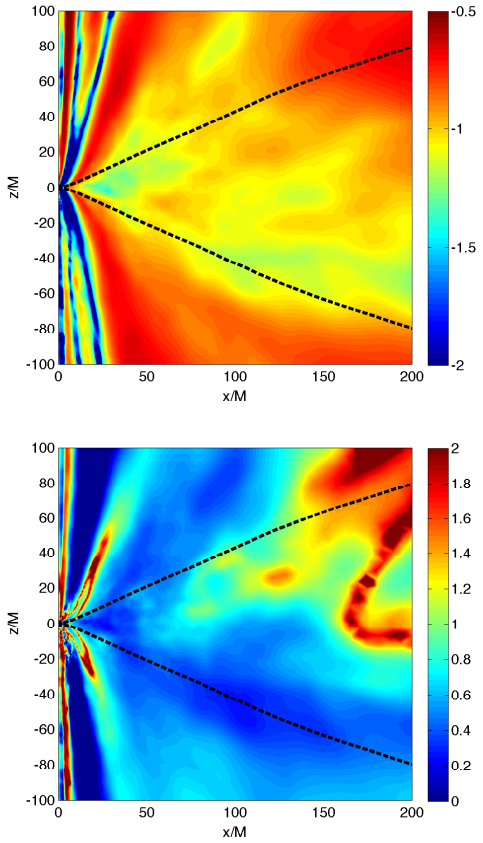

Fig. 4.17.— Same as Figure 4.3 but for simulation F. A large, highly-magnetized, z-shaped clump persists over most of the flow inside $r_{\rm loose}$. The magnetized clump increases α and the ratio of Maxwell to Reynolds stress.

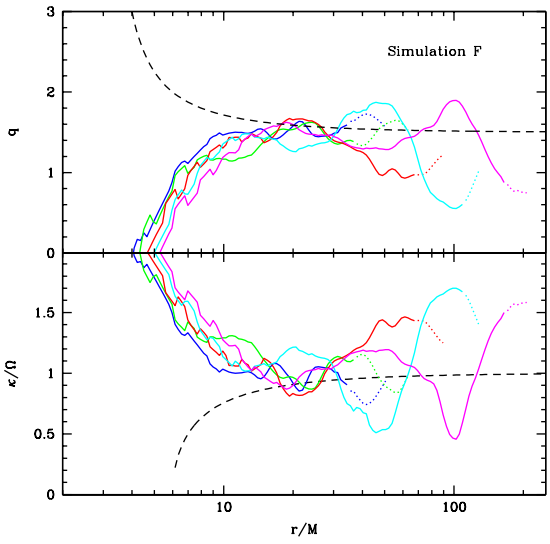

Fig. 4.18.— Same as Figure 4.6 but for simulation F.

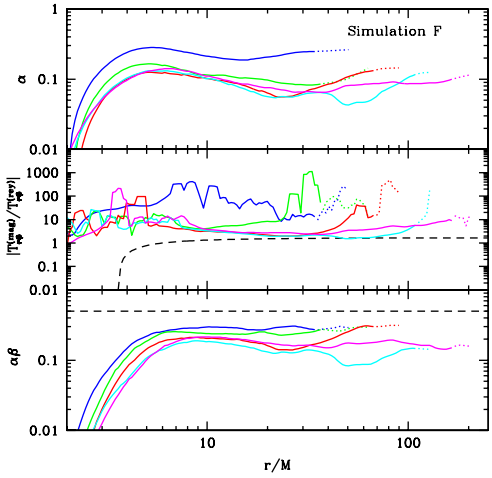

Fig. 4.19.— Same as Figure 4.8 but for simulation F.

Our $\alpha(r)$ prescription does not appear to give a good fit to the simulation F results (Figure 4.20). This is probably because the simulation is mostly laminar at all radii (as shown by Figure 4.15), whereas our $\alpha(r)$ prescription assumes turbulence dominates the stress beyond the innermost radii. For simulations A–E, this is a good assumption provided the disk region of the flow is distinguished from the coronal regions. However, the entire domain of simulation F is mostly laminar and highly magnetized, and so it should perhaps be considered entirely coronal gas. It appears a different $\alpha(r)$ prescription is needed to describe such highly magnetized flows.

4.7 α-disk solutions with variable $\alpha(r)$

In this section, we evaluate the dependence of α-disk solutions on the $\alpha(r)$ prescription. The particular α-disks we consider are "slim disks" (Abramowicz et al. 1988; Sądowski 2011). We compare slim disk solutions with constant $\alpha = \alpha_0$ to solutions with varying $\alpha(r)$, where $\alpha(r)$ is defined by equation (4.30) and the parameters inferred from simulation A (cf. Table 4.4). That is, we consider a non-spinning, 10 solar mass black hole, threaded with a magnetic flux $\Upsilon = 0.6$. The viscosity parameters are $\alpha_0 = 0.025$, $n = 6$, $\alpha_1 = 100$, and $r_B = 6M$. We consider two different accretion rates: 30% Eddington and Eddington.

Figure 4.21 shows our results. At large radii, $\alpha(r)$ converges to α_0, so the solutions with constant and varying $\alpha(r)$ are the same to within a percent. Inside the ISCO, the fluid plunges toward the black hole with little dissipation, so in the innermost regions the solutions are again insensitive to the α prescription. Only in an intermediate zone, between the ISCO and $r \approx 20M$, does the shape of $\alpha(r)$ have a significant effect. For solar mass black holes, this region emits predominately in X-rays and is relevant for black hole spin measurements (Gou et al. 2011).

In this zone, the $\alpha(r)$ prescription has a larger α than the constant $\alpha = \alpha_0$ prescription. So the $\alpha(r)$ prescription increases the disk's radial velocity by a factor of $2 - 3$ and lowers its central (mid-plane) temperature by about 50%. In fact, a solution accreting at the Eddington limit with varying $\alpha(r)$ has the same central temperature as a solution accreting at 30% Eddington with constant α (cf. Figure 4.21). So the $\alpha(r)$ prescription has a significant effect on central

temperature. Central temperature depends on both effective temperature and optical depth, so the effect is really due to changes in surface density.

At low accretion rates, the disk is radiatively efficient and the effect of $\alpha(r)$ on the radiated fluxed is negligible. At high accretion rates, advection becomes important and the radiated flux shows its dependence on $\alpha(r)$. At the Eddington limit, the flux from the solution with varying $\alpha(r)$ is about 50% lower than the flux from the solution with constant α. So flux is only affected by the $\alpha(r)$ prescription at high accretion rates.

4.8 Discussion and summary

The $\alpha(r)$ prescription of §4.3 must be computed numerically. However, for all practical purposes, the function $\alpha(r)$ for thin disks can be reduced to a simple analytical formula. Our simulations suggest

$$\alpha(r) = 0.025 \left[\frac{q(r)}{3/2}\right]^6, \quad (q > 0), \tag{4.42}$$

where $q(r)$ is given analytically by equation (4.24). The constant coefficient and exponent in equation (4.42) are the values favored by our GRMHD simulations (cf. Table 4.4). They will change as better simulation data becomes available. The free parameters are the mass and spin of the black hole, which enter through equation (4.24) for $q(r)$. The contribution from mean magnetic fields can be ignored in this approximation because mean field stresses are only significant inside the ISCO, and thin disks are not sensitive to $\alpha(r)$ in this region. Equations (4.24) and (4.42) thus give an analytical $\alpha(r)$ prescription that can be used for thin disk models (see Figure 4.22). The more general $\alpha(r)$ prescription of §4.3 is needed for thick disks.

To summarize our main results, we have constructed a one-dimensional prescription for $\alpha(r)$ and estimated parameters for this prescription based on data from GRMHD simulations. The fact that α varies with radius had been anticipated long ago (Pringle & Rees 1972; Shakura & Sunyaev 1973) but global MHD simulations provide the first quantitative information about the shape of $\alpha(r)$ (Papaloizou & Nelson 2003; Penna et al. 2010, 2012b; Fromang et al. 2011).

Our modified $\alpha(r)$ prescription, equation (4.30), is the sum of two components. The first

component describes mean field stresses. It is important in the laminar, inner regions of accretion disks, where the plunging fluid stretches the frozen-in field. Our description of this component is based on the model of Gammie (1999), which supplies the magnetic stress as a function of radius and two free parameters: black hole spin and the amount of magnetic flux threading the horizon.

The second component of the $\alpha(r)$ prescription describes turbulent stresses. As emphasized by Pessah et al. (2006b), α depends on the shear parameter, q. In Newtonian gravity, Keplerian flow has a constant shear parameter, $q = 3/2$, but general relativistic corrections give even Keplerian disks around black holes a varying $q(r)$, as discussed in §4.2. The shear parameter increases from $q = 3/2$ at the outer edge of the disk to $q = 2$ at the inner edge of the disk. This is a 25% change in q but it creates a larger variation in α, because α goes as q^n (for $q > 0$). Our GRMHD simulations are too noisy to infer n precisely, but the data seem to prefer $n \approx 6$. This is consistent with the simulations of Pessah et al. (2006b), which resulted in n between 2 and 8. Analytical MHD closure models for the MRI also allow n between 2 and 8 (Kato & Yoshizawa 1993, 1995; Ogilvie 2003; Pessah et al. 2006a,b, 2008).

Simple extensions of the standard α prescription and some closure models predict negative α for $q < 0$ (Kato & Yoshizawa 1993, 1995; Ogilvie 2003). An exception is the closure model of Pessah et al. (2006a,b). Data from shearing box simulations show zero turbulent stress for $q < 0$ (Pessah et al. 2008). Our simulations are consistent with this data, although they are not as decisive on this point because negative shear parameters are only found inside roughly the photon orbit, where mean field stresses are large. Our prescription for $\alpha(r)$ is always positive and the turbulent contribution vanishes for $q < 0$. The mean field term in our $\alpha(r)$ prescription gives a good description of our simulation data in regions near the black hole where $q < 0$.

We have discussed accretion onto black holes. When a disk accretes onto a star, a boundary layer forms between the star and disk. It can generate half the accretion luminosity in soft X-rays (Pringle 1977). The boundary layer in stellar accretion is similar to the region inside the ISCO in black hole accretion. In both regions, the angular velocity is non-Keplerian and the shear amplifies the magnetic field (Armitage 2002; Steinacker & Papaloizou 2002). Steinacker & Papaloizou (2002) found $\alpha(r)$ profiles in MHD simulations of boundary layers that are similar to our $\alpha(r)$ profiles

inside the ISCO. It would be interesting to extend the $\alpha(r)$ prescription to these cases.

We analyzed data from six GRMHD accretion disk simulations. Three of the simulations are thin, radiatively efficient accretion disks (simulations A, B, and C). The other three are geometrically thick, radiatively inefficient accretion flows (simulations D, E, and F). The simulations vary in resolution from $256 \times 64 \times 32$ to $256 \times 128 \times 64$. Two of the simulations describe spinning black holes, with spin parameter $a/M = 0.7$ (simulations B and E) and the others describe non-spinning black holes. MRI driven turbulence and large scale magnetic fields generate stresses in the simulated disks self-consistently, so the α viscosity prescription is not assumed. Instead, we measure $\alpha(r)$ from the simulation data.

For each simulation, we measure $\alpha(r) = T_{\hat{r}\hat{\phi}}/p_{\rm tot}$ and compare it against the $\alpha(r)$ prescription. Thin accretion disks are easier to describe with the $\alpha(r)$ prescription than thick accretion disks because they have a sharp transition at the ISCO that creates two distinct regions: a magnetically dominated region inside the ISCO, and a weakly magnetized, turbulent region outside the ISCO. This distinction is blurred in thick accretion disks by the large radial velocity of the flow. So some of the simplifications in the $\alpha(r)$ prescription are less applicable. Simulation F, in which a large magnetic flux was allowed to build up on the hole, is particularly difficult to interpret because turbulence is almost completely absent.

We were careful to only include fluid which has reached a quasi-steady state. The timescale to reach quasi-steady state scales as the inverse of radial velocity, and is thus an increasing function of radius. So the inner regions of disks converge before the outer regions. Thin accretion disks have smaller radial velocities than thick accretion disks, so thin disk simulations are only converged out to $r \approx 10M$ rather than $r \approx 100M$.

For further insight into the simulations, we analyzed their shear parameters and epicyclic frequencies. Outside the ISCO, the shear parameters of the simulations are usually within 20% of the Keplerian prediction. Inside the ISCO, the shear parameter turns over, going to zero near the photon orbit at $r = 3M$ where the angular velocity peaks. So the turbulent contribution to α, which scales as q^n (for $q > 0$), is unimportant near the black hole.

The epicyclic frequency of the flow is also close to the Keplerian value outside the ISCO. The

inner edge of the flow can be identified with the minimum in $\kappa(r)$, the radius where the flow is most unstable. This is usually near the ISCO, although when the disk is thick the inner edge is smeared out by the large radial velocity of the flow.

Finally, we considered the effect of the $\alpha(r)$ prescription on α-disk solutions. We compared solutions with varying $\alpha(r)$ to solutions with constant $\alpha = \alpha_0$. We fixed the free parameters α_0, α_1, n, and r_B using the values inferred from simulation A (cf. Table 4.4). The differences between varying and constant α are only significant in the region between the ISCO and $r \approx 20M$. At smaller radii, the gas is plunging too quickly for stresses to act, so α does not enter, and at larger radii the varying $\alpha(r)$ prescription is converging to $\alpha = \alpha_0$. In the intermediate zone between the ISCO and $r \approx 20M$, the solutions with varying $\alpha(r)$ have larger α than the solutions with constant α. This increases their radial velocity and lowers their central temperature and radiant flux. The effect on central temperature is most significant. A solution accreting at the Eddington rate with radially varying $\alpha(r)$ has the same central temperature as a solution accreting at 30% Eddington with constant α. Central (mid-plane) temperature depends on both the effective temperature and the optical depth, so the effect is really due to changes in surface density. The effect of α on the radiant flux is only important at high accretion rates.

The main shortcomings of our $\alpha(r)$ prescription are the absence of gas pressure in the prescription for the mean magnetic field component, and the absence of magnetic fields in the prescription for the turbulent component. For thin, weakly magnetized disks these are better assumptions than for thick or highly magnetized disks because the two components do not overlap significantly in the disk.

The simulations are limited by their duration, which prevents a large range of radii from reaching quasi-steady state. They are also limited by their resolution. The fastest growing mode of the MRI is usually not resolved by more than about 10 grid cells (Penna et al. 2010; Narayan et al. 2012) which is only marginally acceptable (Shiokawa et al. 2012; Sorathia et al. 2012). Despite these limitations, these are among the best GRMHD accretion disk simulations available at present. Shearing box simulations can resolve the local physics of the MRI better, but cannot obtain the dependence of α on radius explicitly. Nonetheless, the shearing box simulations of Pessah et al.

(2008) should be revisited with higher resolution (they used $32 \times 192 \times 32$), as these are the best way to measure the dependence of α on q.

Our results suggest that relativistic corrections to q partly contribute to the higher α's measured in GRMHD simulations (Penna et al. 2010, 2012b) compared to Newtonian simulations (Papaloizou & Nelson 2003; Fromang et al. 2011). Assuming $\alpha \propto q^6$ (for $q > 0$), we infer that α is six times larger in the relativistic inner regions of GRMHD disks than in Newtonian disks. This partly resolves the discrepancy but does not go far enough, as the α's measured from GRMHD simulations are over an order of magnitude larger than the α's measured from Newtonian MHD simulations. More work is needed to understand this discrepancy.

Switching from a constant α to a radially varying $\alpha(r)$ would have a small effect on black hole spin estimates. Gou et al. (2011) considered the effect on continuum fitting measurements of the spin of the black hole in Cyg X-1 if one assumes $\alpha = 0.01$ versus $\alpha = 0.1$. The black hole spin decreases slightly, from $a/M = 0.9988$ to 0.9985, as α is increased. Switching from a constant α to the $\alpha(r)$ prescription will have a similar effect. This is well below the current observational sources of error in black hole spin measurements (Kulkarni et al. 2011a; Zhu et al. 2012), so it is not a concern for now.

Black hole spin estimates are restricted to observations of disks radiating below 30% of the Eddington limit, which corresponds to thin disks ($h/r \sim 0.1$, Kulkarni et al. 2011a). Observations based on models of thick disks will be more sensitive to the shape of $\alpha(r)$.

Acknowledgments

We thank Eric Blackman for discussions. This work was supported in part by NASA grant NNX11AE16G and NSF grant AST-0805832. The simulations presented in this work were performed in part on the Pleiades supercomputer, using resources provided by the NASA High-End Computing (HEC) Program through the NASA Advanced Supercomputing (NAS) Division at Ames Research Center. We also acknowledge NSF support via XSEDE resources at NICS Kraken and LoneStar.

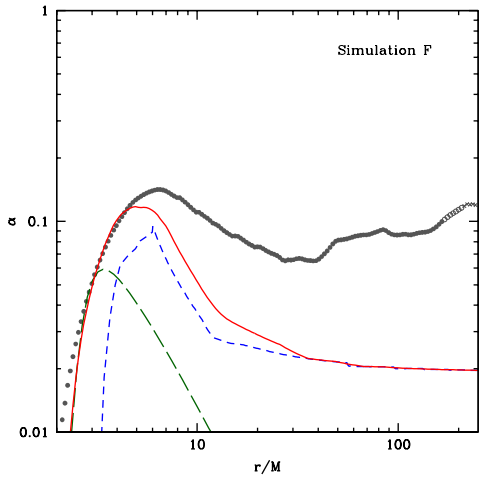

Fig. 4.20.— The dimensionless viscosity parameter, α, of simulation F as a function of radius. We have been unable to find a good fit to the simulation data using our $\alpha(r)$ prescription.

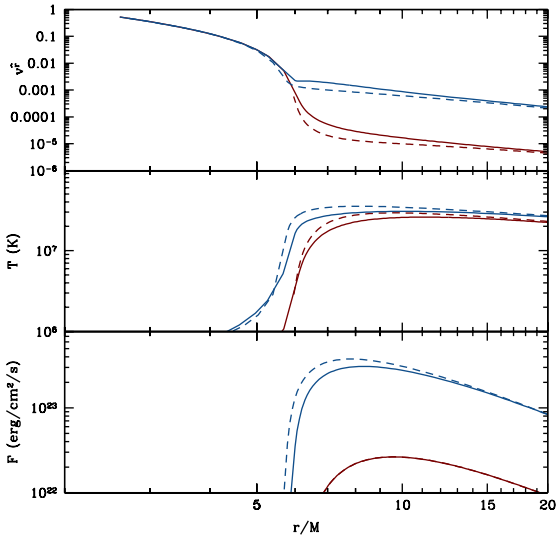

Fig. 4.21.— Slim disk solutions with varying $\alpha(r)$ (solid curves) and with constant $\alpha = 0.025$ (dashed curves), for the parameters inferred from simulation A (cf. 4.4). Solutions are shown at the Eddington accretion rate (blue curves) and at 30% Eddington (red curves). *Top panel:* Radial velocity as a function of radius. Solutions with varying $\alpha(r)$ have larger radial velocities. *Middle panel:* Midplane temperature (not effective temperature) as a function radius. Solutions with varying $\alpha(r)$ are colder in the X-ray emitting portions of the flow. *Bottom panel:* Radiant flux as a function of radius. Radiant flux is affected by $\alpha(r)$ only at high accretion rates.

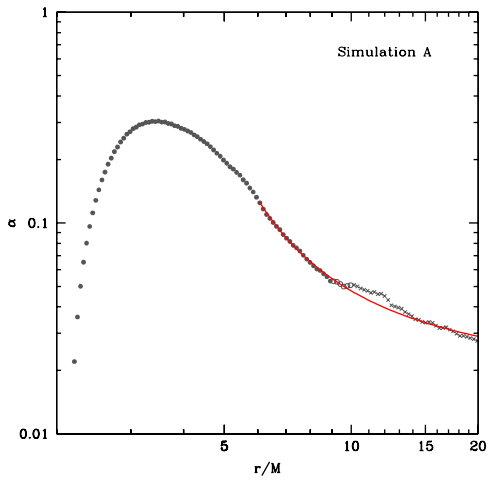

Fig. 4.22.— Analytical $\alpha(r)$ prescription defined by equation (4.42) for $a/M = 0$ (solid red curve). This model gives a good fit to data from Simulation A. Data from inside $r_{\rm strict}$ are marked with filled circles, data from between $r_{\rm strict}$ and $r_{\rm loose}$ are marked with open circles, and data from outside $r_{\rm loose}$ are marked with crosses (cf. §4.5.5).

Chapter 5

Black Hole Jets: Simulations and the Blandford-Znajek Model

5.1 Introduction

In this chapter, we revisit our GRMHD simulations of jets from accreting, spinning black holes. We have three main results. First, we quantify the error introduced into the BZ jet power prediction (1.20) by the standard approximations (maximum efficiency, uniform magnetic fields on the horizon, no disk thickness, and no gas accretion). Second, we check that the underlying physics generating simulated jets (torques, dissipation, and electromagnetic fields at the horizon) is correctly described by the membrane formulation of the BZ model. Third, we compute the effective resistance of the load region, where magnetic energy is converted into bulk gas motion. This analysis supports the prediction $\Omega_F/\Omega_H \approx 1/2$ of simple load region models (Lovelace et al. 1979; MacDonald & Thorne 1982; Phinney 1983).

This chapter is organized as follows. In §5.2, we give an overview of the membrane formalism and our GRMHD simulations. In §5.3, we show that the simulated jet power is consistent with the BZ formula (1.20) and quantify the main sources of discrepancy. In §5.4 and §5.5, we show that the torques, dissipation, and electromagnetic fields at the horizon in the GRMHD simulations are in

excellent agreement with the BZ model. In §5.6, we discuss the conversion of magnetic energy into bulk gas motion in the load region, which is what determines Ω_F/Ω_H. We summarize our results in §5.7. Appendix A re-derives the BZ jet power prediction (1.20). Appendix B gives 3D visualizations of the membrane torques, dissipation, and electromagnetic fields of our GRMHD simulations.

5.2 Preliminaries

5.2.1 GRMHD simulations

Our GRMHD simulations have been described in detail elsewhere (Narayan et al. 2012; Penna et al. 2013; Sądowski et al. 2013), so we can be brief. We use the GRMHD code HARM (Gammie et al. 2003; McKinney 2006a) to evolve a magnetized, turbulent accretion disk in the Kerr metric. The code conserves energy to machine precision, so any energy lost at the grid scale by e.g. turbulent dissipation or numerical magnetic reconnection is returned to the fluid, increasing its entropy. The stress-energy tensor of the fluid is

$$T_{\mu\nu} = T^{\rm gas}_{\mu\nu} + T^{\rm mag}_{\mu\nu}, \tag{5.1}$$

where

$$T^{\rm gas}_{\mu\nu} = (\rho_0 + u)u_\mu u_\nu + p h_{\mu\nu}, \tag{5.2}$$

$$T^{\rm mag}_{\mu\nu} = \frac{1}{2}\left(b^2 u_\mu u_\nu + b^2 h_{\mu\nu} - 2 b_\mu b_\nu\right). \tag{5.3}$$

The notation is standard: ρ_0, u, p, and u_μ are the fluid rest mass density, internal energy, pressure, and four-velocity. The field b^μ is the fluid frame magnetic field and $h_{\mu\nu} = g_{\mu\nu} + u_\mu u_\nu$ is the projection tensor. The equation of state for the gas is $p = (\Gamma - 1)u$, where $\Gamma = 5/3$. There is no radiative cooling, so the disk becomes thick and hot. It is similar to an advection dominated accretion flow (Narayan & Yi 1994, 1995; Narayan et al. 2012).

The Kerr metric in Boyer-Lindquist (t, r, θ, ϕ) coordinates is:

$$ds^2 = -\left(1 - 2Mr/\rho^2\right)dt^2 - \left(4Mar\sin^2\theta/\rho^2\right)dtd\phi + \left(\rho^2/\Delta\right)dr^2 \tag{5.4}$$

$$+ \rho^2 d\theta^2 + \left(r^2 + a^2 + 2Ma^2 r\sin^2\theta/\rho^2\right)\sin^2\theta d\phi^2. \tag{5.5}$$

We have defined the metric functions

$$\Delta = r^2 - 2Mr + a^2, \tag{5.6}$$

$$\rho^2 = r^2 + a^2 \cos^2\theta, \tag{5.7}$$

$$\Sigma^2 = (r^2 + a^2)^2 - a^2 \Delta \sin^2\theta. \tag{5.8}$$

Our notation follows Thorne et al. (1986). The simulations do not evolve the metric (self-gravity is ignored). We consider four black hole spins: $a_* = a/M = 0, 0.7, 0.9$, and 0.98.

HARM uses Kerr-Schild coordinates and Boyer-Lindquist coordinates. These coordinates have a couple of advantages over the membrane formulation for numerical computations. First, unlike the membrane formulation, they make Lorentz invariance manifest, so it is easier to impose energy and momentum conservation numerically. Second, computing in Kerr-Schild coordinates makes it trivial to impose boundary conditions at the inner edge of the numerical grid; the coordinates are horizon penetrating, so we simply place the inner boundary of the grid between the inner and outer black hole horizons and the black hole behaves as an event horizon. A major part of our work in this chapter is converting the simulation results from Kerr-Schild and Boyer-Lindquist coordinates to the membrane formalism. It is only possible to give a local description of black hole energy extraction in the membrane formalism.

We use a logarithmically spaced radial grid and put the outer boundary of the grid at $r \sim 10^5 M$: far enough away that nothing reaches it over the course of the simulation (so we do not need to worry about boundary conditions there). The θ coordinate runs from 0 to π and the ϕ coordinate runs from 0 to 2π. The duration of the simulations varies from as short as $t = 25,000M$ to as long as $t = 200,000M$. The typical resolution is $256 \times 128 \times 64$ in (r, θ, ϕ). The simulations are summarized in Table 5.1.

Initially, the fluid is in a hydrostatic equilibrium torus outside $r = 20M$. The fluid is threaded with a weak poloidal ($\beta = p^{\rm gas}/p^{\rm mag} = 100$) magnetic field. We consider two initial field geometries: multiple, smaller poloidal loops (we call these runs SANE, for Standard and Normal Evolution) and a single, large poloidal loop (we call these runs MAD, for Magnetically Arrested Disk). During the first few orbits of the fluid torus, the magnetic field is sheared and the magnetorotational instability is triggered (Velikhov 1959; Chandrasekhar 1960; Balbus & Hawley 1991, 1998). This causes the

fluid to become turbulent, leading to outward angular momentum transport and allowing fluid to accrete inwards and form an accretion disk. The accretion disk feeds the black hole and threads it with magnetic field lines. These magnetic fields tap the rotational energy of the black hole and drive jets. The remainder of this chapter is an analysis of these jets.

5.3 Simulation jets and jet power

In this section, we first verify that the simulations described in the previous section are generating jets. Then we show that the jet power matches the BZ prediction (1.20). In subsequent sections, we will show that the underlying physics producing jets in GRMHD simulations is indeed described by the BZ model in its membrane formulation.

5.3.1 Jet Lorentz factor

The easiest way to detect jets in the simulations is to look at the gas Lorentz factor, γ, in the x-z plane (where $z = r\cos\theta$ is along the black hole spin axis, and $x = r\sin\theta$ is along the equatorial plane). This is plotted in Figures 5.1 (for the SANE runs) and 5.2 (for the MAD runs). We have time-averaged the simulation data over the last $10,000M$ of each run. The jets show up as bright, collimated outflows along the black hole spin axes. Collimation of the jet is provided by the accretion disk. The accretion disk is invisible in these images because accreting gas has $\gamma \sim 1$.

There are already several hints of a connection between jet power and black hole spin in these images. Jets only appear when the black hole is spinning; the two non-spinning black hole simulations have no jets. The Lorentz factor (a proxy for jet power) increases slightly with spin, from $\gamma \sim 3$ at low spins to $\gamma \sim 4$ at high spins. These Lorentz factors should be interpreted with some caution. HARM uses density floors to avoid the high magnetizations and low densities that lead to inversion failures. The floors are mostly activated in the highly magnetized, low density regions along the jet axes, and could affect γ (Tchekhovskoy et al. 2011; McKinney et al. 2012).

The Lorentz factor peaks near the edges of the jets rather than along the axes: there is a low Lorentz factor core. This is consistent with the BZ model. Magnetic torques extracting black hole

Table 5.1: GRMHD simulations

Simulation	Initial field	a/M	h/r	Resolution (r, θ, ϕ)	Duration	$\Delta t_{\rm steady}$
1.	SANE	0	0.3	$256 \times 128 \times 64$	200,000M	$30,000M$
2.	SANE	0.7	0.3	$256 \times 128 \times 64$	100,000M	$30,000M$
3.	SANE	0.9	0.3	$256 \times 128 \times 64$	50,000M	$10,000M$
4.	SANE	0.98	0.3	$256 \times 128 \times 64$	25,000M	$10,000M$
5.	MAD	0	0.3	$264 \times 126 \times 60$	100,000M	$80,000M$
6.	MAD	0.7	0.3	$264 \times 126 \times 60$	91,500M	$80,000M$
7.	MAD	0.9	0.3	$264 \times 126 \times 60$	44,000M	$10,000M$

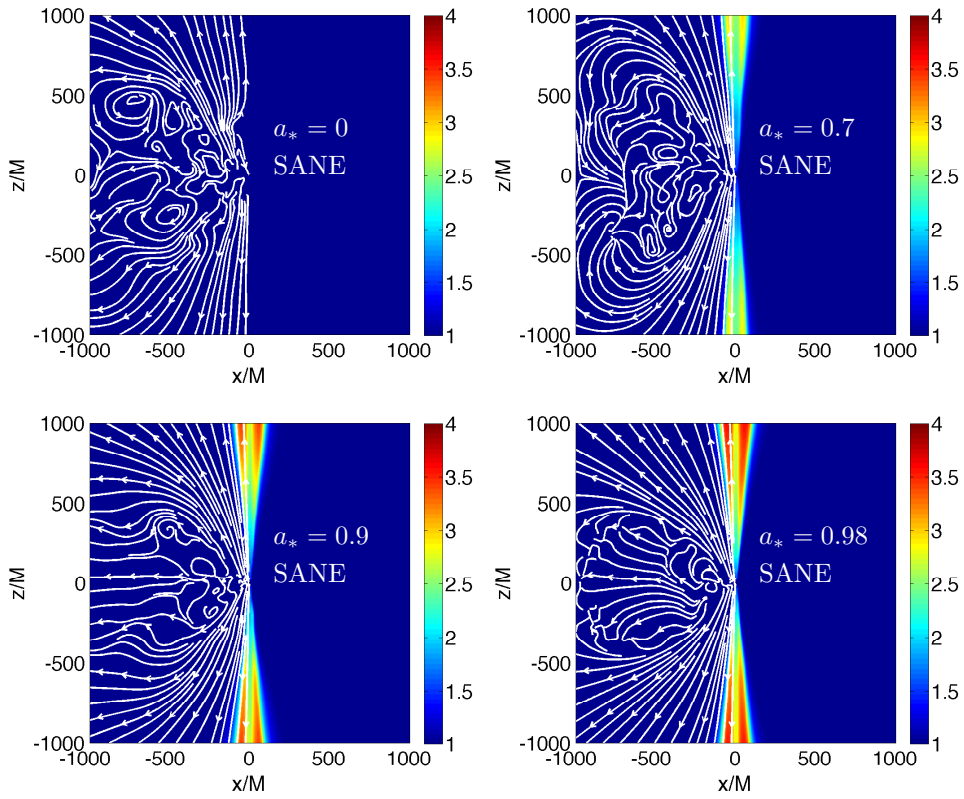

Fig. 5.1.— GRMHD simulation Lorentz factor and velocity streamlines for SANE runs. The spinning black holes power jets. Note that the jets are converged out much farther than the disks because the velocities are much larger in the jets.

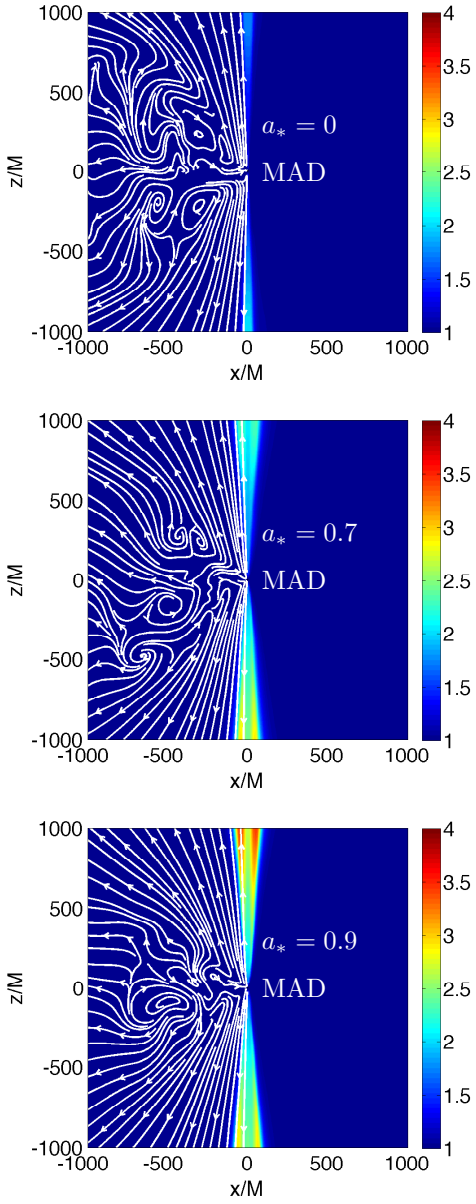

Fig. 5.2.— Same as Figure 5.1 but for MAD runs.

rotational energy scale with the lever arm radius, ϖ (roughly the cylindrical distance from the black hole spin axis to the black hole membrane) as $\tau = \varpi \times \mathbf{F}$. Near the axes, ϖ (and so also torque) goes to zero, so the cores of the jets are less accelerated than the edges.

5.3.2 Jet power vs. time

We introduce two proxies for jet power. The first is

$$P^{\rm mag} = -\int_{\mathcal{H}} \alpha T^{\rm mag}_{nt} dA, \quad (r = r_H), \tag{5.9}$$

where $dA = (r_H^2 + a^2)\sin\theta d\theta d\phi$ is an area element on the membrane and $\alpha = \rho/\Sigma\sqrt{\Delta}$ is the lapse function. The outward normal vector is $e_n = \sqrt{\Delta}/\rho(\partial/\partial r)$ and $T_{nt} = e^\mu_n T_{\mu t}$. As usual, t is the Boyer-Lindquist time coordinate. The integral is over the entire black hole horizon, $\mathcal{H}$, so it includes the jet and the accretion disk in the integral over θ.

The accretion disk might extract energy from the black hole, but only the energy extracted into the jet is directly relevant for observations of black hole jets. (The jets observed by Narayan & McClintock 2012 and Steiner et al. 2013 are at $r \sim 10^{10}M$ so can be observationally distinguished from the accretion disk.) We thus introduce a second proxy for jet power:

$$P^{\rm tot}_{\rm jet} = -\left.\frac{dM}{dt}\right|_{\mathcal{A}_{\rm jet}} = \int_{\mathcal{A}_{\rm jet}} \alpha T_{nt} dA. \quad (r = r_H). \tag{5.10}$$

Now we have restricted the integral to the *jet region*, $\mathcal{A}_{\rm jet}$, defined to be the region of the horizon where $-T_{nt} > 0$ (net energy leaving the hole). In other words, we do not include the accretion disk in the integral over θ. We have also switched from including only the magnetic energy flux, $T^{\rm mag}_{nt}$, to including the combined magnetic and gas energy flux, T_{nt}.

We expect $P^{\rm mag}$ to give the best fit to the BZ model, because the BZ prediction (1.20) includes the entire horizon and considers only magnetic torques. We expect $P^{\rm tot}_{\rm jet}$ to be more relevant for jet observations.

Our simulations with non-spinning black holes always have $-T_{nt} < 0$ across the entire horizon, meaning the black hole never loses energy. So $\mathcal{A}_{\rm jet}$ is empty and $P^{\rm tot}_{\rm jet} = 0$, always.

The simulations with spinning black holes are more lively. We show $P^{\rm mag}$ and $P^{\rm tot}_{\rm jet}$ vs. time

for these runs in Figure 5.3. Initially, none of the simulations have jets. The MAD simulations develop jets quickly, after just a few $1000M$, and soon thereafter the jet power saturates around a quasi-steady value. Remaining fluctuations in the jet power arise from turbulent fluctuations in the accretion disk feeding the black hole. The SANE simulations develop jets much more slowly. Even by the end of this set of runs the jet power has probably not converged to a quasi-steady value. The different onset time of jets in the SANE and MAD runs is easily understood. MAD runs begin with a single magnetic loop. This loop is so big that less than half of it is dragged onto the hole over the duration of the simulation. So the accretion flow is continually depositing magnetic flux of the same polarity on the horizon and a large mean field builds up. In the SANE runs on the other hand, the initial magnetic field is a series of small poloidal loops. The sign of the magnetic flux arriving on the hole is alternating with time and it is difficult for the hole to build up a large mean field. Nonetheless, at late times the SANE runs appear to be converging to what is perhaps the same quasi-steady jet power as the MAD runs.

It is interesting to compare $P^{\rm mag}$ (solid red and blue curves) and $P^{\rm tot}_{\rm jet}$ (dotted red and blue curves) in Figure 5.3. The former is always $\sim 2-3$ times larger than the latter. There are two reasons for this. First, $P^{\rm tot}_{\rm jet}$ does not include the accretion disk, so it is limited to a smaller region of the horizon. Second, even the jet regions, $\mathcal{A}_{\rm jet}$, are not devoid of gas. In the polar regions of the flow, gas within a few gravitational radii of the horizon is falling onto the black hole. This gas torques the hole in the opposite sense as the magnetic fields, so the total jet power is lower than the magnetic jet power. The BZ prediction (1.20) (black lines) gives an acceptable fit to the magnetic jet power, $P^{\rm mag}$, but overestimates the total jet power, $P^{\rm tot}_{\rm jet}$. The neglect of gas accretion is the main shortcoming of the BZ model identified in this chapter. To quantify this effect, we first need to time-average the data.

5.3.3 Time-averaging

Time averaging eliminates (or at least reduces) the imprint of accretion disk variability on the jets. The duration of the time interval used for averaging depends on the run's duration and jet onset time. We begin time-averaging when $P_{\rm jet}(t)$ appears to become roughly independent of t,

and we continue time averaging until the end of the run. The smallest time averaging interval is $\Delta t_{\rm steady} = 10,000M$. Table 5.1 gives $\Delta t_{\rm steady}$ for each of our simulations. The runs with $a_* = 0.9$ and $a_* = 0.98$ have shorter time averaging intervals because the duration of these runs was shorter.

5.3.4 Jet power vs. black hole spin

We now come to the main result of this section, the dependence of jet power on black hole spin. This is shown in Figure 5.4 for the five simulations with spinning black holes. The magnetic power, $P^{\rm mag}$, (filled circles) agrees with the BZ prediction (1.20) to within 10%. This is consistent with earlier simulation results (Tchekhovskoy et al. 2010a, 2012). (Our $P^{\rm mag}$ is similar to the η parameter of Tchekhovskoy et al. 2010a and Tchekhovskoy et al. 2012.)

Discrepancies between $P^{\rm mag}$ and the BZ model can be traced to approximations in the BZ prediction (1.20). First, the standard BZ model assumes the angular velocity of magnetic field lines is half the angular velocity of the horizon: $\Omega_F/\Omega_H = 1/2$. This ratio maximizes the jet power. As we will show in §5.6, our simulations have $\Omega_F/\Omega_H \approx 0.35$. For general Ω_F/Ω_H, the BZ model predicts (Blandford & Znajek 1977; Thorne et al. 1986):

$$P^{\rm BZ} = \frac{1}{6\pi} 4\Omega_F/\Omega_H(1-\Omega_F/\Omega_H)\Omega_H^2\Phi^2, \tag{5.11}$$

where Φ is the magnetic flux threading the black hole. So switching from $\Omega_F/\Omega_H = 1/2$ to $\Omega_F/\Omega_H = 0.35$ lowers the jet power by 8%. In other words, assuming $\Omega_F/\Omega_H = 1/2$ introduces an 8% error into the jet power estimate for our simulations.

The BZ jet power (1.20) also assumes uniform B_n over the horizon (see Appendix A). This assumption breaks down at high black hole spins, for which the magnetic field tends to bunch up near the polar axes (Tchekhovskoy et al. 2010a). However, Figure 5.4 shows $P^{\rm BZ}$ and $P^{\rm mag}$ continue to agree to within 10% even at $a_* = 0.98$. We conclude that the assumptions $\Omega_F/\Omega_H = 1/2$ and uniform B_n together create a $\sim 10\%$ discrepancy between the BZ prediction (1.20) and our simulations.

The jet power proxy $P^{\rm mag}$ measures the electromagnetic energy extracted across the entire black hole horizon. Not all of this energy is extracted into the jet: some of it is extracted into the

accretion disk. We expect $P^{\rm tot}_{\rm jet}$ to be more relevant for jet observations than $P^{\rm mag}$ because the former is restricted to the jet region. Figure 5.4 shows $P^{\rm tot}_{\rm jet}$ (crosses) is about a factor of three lower than $P^{\rm mag}$ (filled circles). There are two reasons for this reduction. First, $P^{\rm tot}_{\rm jet}$ is restricted to a smaller region of the horizon, the jet region. Second, even within the jet region, there are gas torques counteracting the magnetic torques, further lowering $P^{\rm tot}_{\rm jet}$.

To isolate the relative importance of these two effects, we introduce a third proxy for jet power

$$P^{\rm mag}_{\rm jet} = -\int_{\mathcal{A}_{\rm jet}} \alpha T^{\rm mag}_{nt} dA, \quad (r = r_H), \tag{5.12}$$

which is intermediate between $P^{\rm mag}$ and $P^{\rm tot}_{\rm jet}$ (Figure 5.4, open circles). It is limited to the jet region, but it does not include gas torques. So the discrepancy between $P^{\rm mag}$ and $P^{\rm mag}_{\rm jet}$ measures the effect of restricting the jet power to the jet region. The discrepancy between $P^{\rm mag}_{\rm jet}$ and $P^{\rm tot}_{\rm jet}$ measures the importance of gas torques within the jet region. Figure 5.4 shows that these two effects are comparable: each contributes about 25% to the discrepancy between $P^{\rm mag}$ and $P^{\rm tot}_{\rm jet}$.

To summarize, the jet power proxy which is probably most relevant for jet observations, $P^{\rm tot}_{\rm jet}$, is roughly 60% lower than the BZ prediction (1.20). Simply lowering $P^{\rm BZ}$ by 60% gives a good fit to our simulations. The main sources of discrepancy between the simulations and the BZ model are that the simulated jets do not cover the whole horizon and, within the jet region, there are gas torques partially counteracting the electromagnetic torques. Tchekhovskoy et al. (2010a) have previously considered restricting the BZ model to a subregion of the full horizon and our power estimates are consistent with theirs. Our estimate for the importance of gas torques in the jet region should be considered an upper limit, as numerical floor activations in the polar regions introduce more gas there than should otherwise be present. More work is needed to isolate the effect of the numerical floors and better determine the importance of gas torques in the jet region.

We have found that assuming $\Omega_F/\Omega_H = 1/2$ and uniform horizon B_n introduces order 10% discrepancies between the BZ jet power estimate and our simulations. It is worth noting that simulations of thicker ($h/r \sim 1$), more magnetized accretion flows have found $\Omega_F/\Omega_H \approx 0.2$ (McKinney et al. 2012; Beskin & Zheltoukhov 2013). Reducing Ω_F/Ω_H from 0.5 to 0.2 lowers the jet power by 40% (equation 5.11). This example serves to emphasize that details of the accretion flow can change jet power estimates by order unity factors. This suggests it will be difficult in

practice to predict the power of astrophysical jets to better than a factor of order unity.

5.4 Energy extraction at the horizon

In the previous section, we found good agreement between the simulated and BZ jet power. In this section and the next, we turn to the underlying physics. We show that the torques and electromagnetic fields acting on the black hole membrane in our GRMHD simulations are in excellent agreement with the BZ model in its membrane formulation. All of the numbered equations in this section can be found in Thorne et al. (1986).

5.4.1 First law of black hole thermodynamics

The black hole membrane has mass M, angular momentum J, angular velocity Ω_H, Bekenstein-Hawking temperature T_H, and Bekenstein-Hawking entropy S_H. These are related by the first law of black hole thermodynamics:

$$dM = \Omega_H dJ + T_H dS_H. \tag{5.13}$$

The left hand side is the total energy entering ($dM > 0$) or leaving ($dM < 0$) the membrane. It is related to jet power by $P_{\rm jet} = -dM/dt$. The right hand side splits dM into contributions from torques on the membrane, $\Omega_H dJ$, and dissipation in the membrane $T_H dS_H$. It is impossible to extract energy from a nonspinning black hole because $\Omega_H = 0$. The torque is negative when black hole rotational energy is being extracted and positive otherwise. The dissipation is always positive, as demanded by the second law of black hole thermodynamics.

In the BZ model, torques and dissipation have similar magnitudes. This might seem surprising: the Bekenstein-Hawking temperature $T_H \sim \hbar$ is miniscule. However, the Bekenstein Hawking entropy $S_H \sim 1/\hbar$ is huge, so the product $T_H dS_H$ is finite and astrophysically relevant. The importance of the dissipation term is a key distinction between black holes and pulsars. Pulsars are perfect conductors, so $dM_{\rm pulsar} = \Omega_{\rm pulsar} dJ_{\rm pulsar}$. Black holes are not perfect conductors, so jet power is a combination of torques and dissipation on the membrane. This explains why a pulsar magnetosphere has $\Omega_F = \Omega_{\rm pulsar}$ while a black hole magnetosphere has $\Omega_F < \Omega_H$: pulsar field lines

are frozen into the star, but black hole field lines slip with respect to the membrane because the latter is not a perfect conductor.

5.4.2 Torques and dissipation on the membrane

We have shown that GRMHD simulations of jets and the BZ model have the same $P^{\rm mag}$. Now we will show they produce the same torques and dissipation on the membrane. Energy flow, torques, and dissipation on the membrane are related to the GRMHD stress energy tensor by:

$$\frac{dM}{dt} = -\int \alpha T_{nt} dA, \quad (r = r_H), \tag{5.14}$$

$$\Omega_H \frac{dJ}{dt} = \Omega_H \int \alpha T_{n\phi} dA, \quad (r = r_H), \tag{5.15}$$

$$T_H \frac{dS_H}{dt} = -\int \alpha^2 T_{n\hat{t}} dA, \quad (r = r_H), \tag{5.16}$$

where $\hat{t}$ is the proper time of a ZAMO. The mathematical distinction between dM/dt and $T_H dS_H/dt$ is that the former is related to the Boyer-Lindquist energy flux, T_{nt}, and the later is related to the ZAMO energy flux, $T_{n\hat{t}}$. Boyer-Lindquist and ZAMO time are related at the membrane by

$$\vec{e}_{\hat{t}} = \frac{1}{\alpha}\left(\frac{\partial}{\partial t} + \Omega_H \frac{\partial}{\partial \phi}\right). \tag{5.17}$$

The first law of black hole thermodynamics is equivalent to equations (5.14)-(5.17), as an easy calculation shows:

$$T_H \frac{dS_H}{dt} = -\int \alpha^2 T_{n\hat{t}} dA = -\int \alpha T_{nt} dA - \Omega_H \int \alpha T_{n\phi} dA = \frac{dM}{dt} - \Omega_H \frac{dJ}{dt}. \tag{5.18}$$

The second law of black hole thermodynamics, $T_H dS_H \geq 0$, is equivalent to the right hand side of equation (5.16) by the weak energy condition: $-T_{n\hat{t}} \geq 0$ because ZAMOs are orthonormal observers.

The energy flow, torques, and dissipation on the membrane in the GRMHD simulations are shown in Figure 5.10 (for the SANE runs) and Figure 5.11 (for the MAD runs). We have normalized each time-averaged quantity to the time-averaged accretion rate, $\dot{m}$. The membrane is depicted as a spherical surface with coordinates on the sphere corresponding to Boyer-Lindquist coordinates

(θ, ϕ) in the usual way. The membrane is gaining energy at blue regions and losing energy at red regions.

The blue band near the equator is the accretion disk and the thickness of this band is set by the thickness of the disk. The accretion disk adds energy to the black hole. The yellow and red bands wrapping around the poles are the jet regions, $\mathcal{A}_{\rm jet}$, where the black hole is losing rotational energy. In the BZ model there is no accretion disk (so there would be no blue band) and the jet regions extend to the equator. In the GRMHD simulations the jet region is limited to areas outside the disk. The disk thickness in our simulations is $h/r \sim 0.3$ and this reduction in $\mathcal{A}_{\rm jet}$ lowers the jet power by a factor of $2-3$. Physically this is not a particularly interesting distinction between GRMHD simulations and BZ jets, as it is easily absorbed into the BZ model by simply restricting the BZ jet power to $\mathcal{A}_{\rm jet}$.

The torques and dissipation on the membrane in the GRMHD simulations pass basic consistency checks. The torque on nonspinning black holes is zero everywhere. Dissipation is always positive as demanded by the second law of black hole thermodynamics (except possibly at the last couple grid cells near the poles where HARM has trouble with floors on magnetization). The net energy flux is always smaller than the torque because there is dissipation. Torques decrease near the poles as the lever arm radius ϖ goes to zero. This causes the dissipation and total energy flux to drop as well. Everything is amplified by black hole spin.

Figures 5.12 and 5.13 provide a more fine grained look at the membrane energy flux, torques, and dissipation in the GRMHD simulations. Each quantity is split into electromagnetic and hydrodynamic components. We find that the hydrodynamic torques are everywhere positive, so the extraction of black hole energy is a purely electromagnetic process. We also find that electromagnetic torques become negligible in the accretion disk region. The accretion disk's magnetic fields are extracting energy from the spin of the black hole, but it is small compared to the energy in the accretion flow.

The crucial test of the BZ model is that it makes a specific prediction for the relative strength of torques and dissipation. The standard BZ model predicts:

$$\Omega_H dJ = -2T_H dS_H, \quad (\text{for } \Omega_F/\Omega_H = 1/2). \tag{5.19}$$

Figure 5.5 shows the ratio $-\Omega_H dJ/(T_H dS_H)$ as a function of θ for our GRMHD simulations. The ratio is roughly independent of θ except near the polar axes, where numerical floor activations make the simulation results untrustworthy. The simulations have $\Omega_H dJ \approx -1.5 T_H dS_H$, meaning they produce about 25% less torque per unit dissipation than the standard BZ model (equation 5.19). This can be traced back to the fact that the standard BZ model assumes maximum efficiency ($\Omega_F/\Omega_H = 1/2$). For general Ω_F/Ω_H, the BZ model predicts (Thorne et al. 1986)

$$-\frac{\Omega_H dJ}{T_H dS_H} = \left(1 - \frac{\Omega_F}{\Omega_H}\right)^{-1}. \tag{5.20}$$

Our simulations have $\Omega_F/\Omega_H \approx 0.35$ (see §5.6), for which equation (5.20) gives $-\Omega_H dJ/(T_H dS_H) \approx 1.5$, just as we observe in Figure 5.5. Note that while assuming maximum efficiency introduces a 25% error into $-\Omega_H dJ/(T_H dS_H)$, it only introduces an 8% error into $P_{\rm jet}^{\rm tot}$, as discussed in §5.3.4.

5.5 Electromagnetic fields at the horizon

In the previous section, we showed that membrane torques and dissipation in the GRMHD simulations are related as the BZ model predicts: $\Omega_H dJ \approx -2 T_H dS_H$. We also showed that extraction of black hole energy is a purely electromagnetic process mediated by electric and magnetic fields and currents acting on the black hole membrane. We now turn to the study of these fields and currents.

5.5.1 Membrane formalism

First, we review the necessary pieces of the membrane formalism (Thorne et al. 1986).

The electric and magnetic fields measured by ZAMOs are computed from the GRMHD Faraday tensor according to

$$\vec{E} = F^{i\hat{t}}, \quad \vec{B} = F^{*i\hat{t}}, \tag{5.21}$$

where ZAMO time, $\hat{t}$, is given by equation (5.17). These electric and magnetic fields are three-dimensional vectors.

At the black hole membrane, we split these electric and magnetic fields into their components perpendicular and parallel to the membrane. The perpendicular component of the magnetic field is B^n, where the outward normal vector is related to $\partial/\partial r$ by $e_n = \sqrt{\Delta}/\rho(\partial/\partial r)$.

The perpendicular component of the electric field is

$$\sigma_H = E^n, \quad (r = r_H) \tag{5.22}$$

and called the membrane's charge density, for the following reason. An observer outside a black hole never sees a field line cross the membrane, because gravitational redshifting causes everything falling in to appear to freeze just outside. Thus field lines appear to terminate on the membrane. As a result, ZAMOs infer a charge distribution on the membrane, σ_H, sourcing the radial electric fields. The inferred distribution of positive and negative charges on the membrane sums to Q, the charge of the black hole. Our simulations use the Kerr metric, so $Q = 0$ even when σ_H is nonzero. [1]

For the same reason, an observer outside the black hole believes the parallel components of $\vec{E}$ and $\vec{B}$ are terminated at the membrane. To ZAMOs, the membrane is a conductor endowed with just the right fields to terminate $\vec{E}^{\parallel}$ and $\vec{B}^{\parallel}$. This defines the membrane fields:

$$\vec{E}_H = \alpha\vec{E}^{\parallel}, \quad \vec{B}_H = \alpha\vec{B}^{\parallel}, \quad (r = r_H), \tag{5.23}$$

where $\alpha = \rho/\Sigma\sqrt{\Delta}$ is the lapse function. These electric and magnetic fields are two-dimensional vectors.

We have now packaged the six degrees of freedom of $F_{\mu\nu}$ into the set $B_n, \sigma_H, \vec{E}_H$, and $\vec{B}_H$. From this set, we can compute the horizon current, $\vec{J}_H$. The horizon behaves as a resistor with $R_H = 1\,(= 377\,\text{ohms in physical units})$ and the current is

$$\vec{J}_H = \vec{E}_H/R_H. \tag{5.24}$$

In these variables, the power generated by electromagnetic torques and dissipation on the

[1] Reasoning by analogy, B_n is sometimes called the membrane's magnetic monopole distribution.

horizon (5.15)-(5.16) are

$$\Omega_H \frac{dJ}{dt} = \Omega_H \int \varpi \left[\sigma_H E^\phi + (\vec{J}_H \times \vec{B}_n)^\phi\right] dA, \tag{5.25}$$

$$T_H \frac{dS_H}{dt} = \int R_H J_H^2 dA. \tag{5.26}$$

These are familiar expressions from ordinary three-dimensional mechanics for the electromagnetic torque on a membrane, $\vec{\varpi} \times \vec{F}_L$, and dissipation in a resistor, $R_H J_H^2$. This simplicity is an advantage of the membrane formalism.

5.5.2 Comparison of GRMHD and BZ electromagnetic fields

In §5.4, we showed that the BZ model and GRMHD simulations produce the same torques and dissipation on the membrane. We now show that the underlying electromagnetic fields are also the same.

There are six degrees of freedom: B_n, σ_H, $\vec{E}_H$, and $\vec{B}_H$. The BZ model leaves B_n a free parameter. The remaining degrees of freedom are predictions we can test against our GRMHD simulations. The (t,ϕ)-averaged electromagnetic fields of our simulations are shown in Figures 5.14 (SANE runs) and 5.15 (MAD runs). The accretion rate varies from run to run, so we plot the fields in units of $\sqrt{\dot{m}}$, where $\dot{m}$ is the (t,θ,ϕ)-averaged accretion rate.

First consider the radial magnetic field, B_n. This is a free parameter of the BZ model. In our GRMHD simulations, it is spontaneously generated by the accretion disk. The relaxed field geometry has a simple structure. It is roughly uniform over the jet regions and the sign of the field is reversed in the northern and southern hemispheres. So it is similar to a split monopole, the simplest possible field.

Now consider the membrane electric field, $\vec{E}_H$. The BZ model assumes axisymmetry, which implies (Thorne & MacDonald 1982):

$$E_H^{\hat{\phi}} = 0. \tag{5.27}$$

Our GRMHD simulations do not enforce axisymmetry, but the time-averaged fields become roughly axisymmetric at the membrane. Figures 5.14 and 5.15 show $E_H^{\hat{\phi}} \approx 0$ and the membrane electric field runs north-south.

The standard BZ model fixes the $\hat{\theta}$-component of the electric field by winding up B_n:

$$E_H^{\hat{\theta}} = -\frac{1}{2} v_H B_n, \quad (\Omega_F/\Omega_H = 1/2), \tag{5.28}$$

where $v_H = \varpi\Omega_H$ is the velocity of the membrane (note $v_H = 1$ at the equator when $a_* = 1$). Figure 5.5 (middle panel) shows $-E_H^{\hat{\theta}}/(v_H B_n)$ as a function of θ for our GRMHD simulations. The simulations have $E_H^{\hat{\theta}} \approx -0.65 v_H B_n$, so the simulated electric field is about 30% larger than predicted by the standard BZ model (equation 5.28). This is because the simulations do not achieve perfect efficiency. For general Ω_F/Ω_H, the BZ model predicts (Thorne et al. 1986)

$$E_H/(v_H B_n) = -(1 - \Omega_F/\Omega_H). \tag{5.29}$$

Our simulations have $\Omega_F/\Omega_H \approx 0.35$ (see §5.6), for which equation (5.29) predicts $E_H/(v_H B_n) \approx -0.65$, in excellent agreement with our results in Figure 5.5.

The magnetic field, $\vec{B}_H$, is not really an independent variable, because the black hole metric enforces

$$\vec{B}_H = \hat{n} \times \vec{E}_H \tag{5.30}$$

at the membrane. Figures 5.14 and 5.15 show that our GRMHD simulations pass this basic consistency test: the magnetic field runs east-west around the membrane and $|B_H| = |E_H|$.

The final degree of freedom is $\sigma_H = E_n$. The BZ model assumes force-free fields, $\vec{E} \cdot \vec{B} = 0$, which implies

$$\sigma_H = 0, \tag{5.31}$$

because $E_H^{\hat{\phi}} = B_H^{\hat{\theta}} = 0$. Our GRMHD simulations enforce $\vec{E} \cdot \vec{B} = 0$, so they do not give an independent test of this assumption. Figures 5.14 and 5.15 show $\sigma_H \approx 0$ in our simulations, as expected.

In summary, the GRMHD simulations' membrane fields, B_n, σ_H, $\vec{E}_H$, and $\vec{B}_H$, are correctly described by the BZ model. The BZ solution with $\Omega_F/\Omega_H = 1/2$ differs from the simulations' membrane fields by as much as 30%. The BZ solution with $\Omega_F/\Omega_H \approx 0.35$ gives an excellent fit to the simulations.

5.6 The load region

We have compared the BZ predictions for jet power and torques, dissipation, and electromagnetic fields on the membrane with our GRMHD simulations. A crucial assumption of the standard BZ model is $\Omega_F/\Omega_H = 1/2$. In this section we compute Ω_F/Ω_H from our simulations and relate it to the physics of gas acceleration in the load region.

In the absence of gas, many field geometries are possible, each with their own angular velocity, Ω_F/Ω_H. For example, a slowly rotating split monopole has $\Omega_F/\Omega_H = 1/2$, while a slowly rotating paraboloidal field has $\Omega_F/\Omega_H \approx 0.4$ (Blandford & Znajek 1977). Beskin & Zheltoukhov (2013) have found solutions with $\Omega_F/\Omega_H \approx 0.2$.

In simulations with gas (such as our's), Ω_F/Ω_H is not a free parameter. It is fixed self-consistently by the interaction of the magnetic field threading the black hole with gas in the jet. The region in the jet where magnetic energy is converted into bulk gas motion is called the load region. Simple models for the load region suggest (to within factors of order unity) $\Omega_F/\Omega_H \approx 1/2$ (Lovelace et al. 1979; MacDonald & Thorne 1982; Phinney 1983). In this section, we connect these load region models to our GRMHD simulations.

A current, I, flowing along the membrane, draws energy from the black hole's rotation. The black hole acts as a battery with EMF, V, given by (Znajek 1978; Blandford 1979; MacDonald & Thorne 1982; Phinney 1983; Thorne et al. 1986)

$$IV = \Omega_H \frac{dJ}{dt}. \tag{5.32}$$

Less than half of this energy is available for powering the jet. The remainder is dissipated by the membrane's internal resistance, R_H. In physical units, $R_H = 377$ ohms, while in the dimensionless units of this chapter, $R_H = 1$. So the membrane's internal resistance creates a potential drop, V_H, given by

$$IV_H = T_H \frac{dS_H}{dt}. \tag{5.33}$$

As the current circulates through the magnetosphere, the magnetic energy extracted at the membrane is converted into bulk gas motion in the load region. The potential drop through the

load region, V_L, is related to V and V_H by energy conservation:

$$V = V_H + V_L. \tag{5.34}$$

The effective resistance of the load region is

$$R_L = V_L/I. \tag{5.35}$$

In the BZ model, the effective resistance of the load region fixes Ω_F/Ω_H (Thorne et al. 1986):

$$\Omega_F/\Omega_H = \frac{R_L/R_H}{1 + R_L/R_H}. \tag{5.36}$$

Simple load region models (Lovelace et al. 1979; Phinney 1983) suggest the load and black hole achieve near perfect impedance matching, $R_L/R_H \approx 1$, in which case equation (5.36) gives $\Omega_F/\Omega_H = 1/2$.

This analysis can be applied to our simulations. Figure 5.6 shows the structure of the magnetosphere currents of the $a_* = 0.7$ MAD simulation. Currents flow out from the black hole into the jet, loop around the boundary of the jet, and return to the black hole through the accretion disk's corona. The boundary of the jet is marked in Figure 5.6 with heavy black lines. It is defined by following streamlines of energy flux, $-T^\mu_t$, outward from $\mathcal{A}_{\rm jet}$ (the region of the horizon where $-T_{nt} > 0$).

The voltage drop along a current streamline, $\mathcal{L}$, through the load region, is

$$V_L = \int_{\mathcal{L}} \vec{E} \cdot d\vec{l}. \tag{5.37}$$

In the load region, the electric field is predominantly along θ. So $R_L = V_L/I$ peaks at turning points of the current, where $\vec{j}$ is along θ. Figure 5.6 shows $dV/dl \sim R_L$ is concentrated at turning points of the current, as expected. The integral curves of $\vec{j}$ through the magnetosphere behave like wires with resistors, R_L, at their turning points.

Numerically evaluating the line integral (5.37) for the loop $\mathcal{L}$ highlighted in red in Figure 5.6, gives $V_L \approx 0.9$. Connecting the footpoints of this current loop across the membrane, we find $V_H \approx 2$. So

$$\frac{R_L}{R_H} = \frac{V_L}{V_H} \approx 0.45. \tag{5.38}$$

Plugging $R_L/R_H = 0.45$ into equation (5.36) gives $\Omega_F/\Omega_H = 0.31$. The load resistance does not appear to depend strongly on the choice of current loop or black hole spin, but we save a detailed investigation for the future.

We can test this analysis by computing the field line angular velocity directly:

$$\Omega_F = \frac{\alpha}{\varpi}\left(v^{\hat{\phi}} - v^n \frac{B^{\hat{\phi}}}{B^n}\right), \tag{5.39}$$

where $\vec{v}$ is the gas velocity in the ZAMO frame. Figure 5.7 shows that the simulated Ω_F/Ω_H is roughly constant over the horizon (except near the poles, where numerical floor activations make the simulations unreliable).

For all five of our simulations with spinning black holes, the (t,θ,ϕ)-averaged field line velocity is $\Omega_F/\Omega_H \approx 0.35$ (see Figure 5.8), close to the value estimated from R_L/R_H. This supports the idea that the angular velocity of magnetic field lines is controlled by the effective resistance of the load region, R_L/R_H. Furthermore, the simulated R_L/R_H is within a factor of order unity of estimates from simple load region models (Lovelace et al. 1979; Phinney 1983).

It is interesting that the load and membrane achieve near perfect impedance matching (within a factor of order unity). MacDonald & Thorne (1982) suggest an intuitive explanation. The minimum velocity of particles sliding along magnetic field lines is (MacDonald & Thorne 1982)

$$v_{\rm min} = \frac{\Omega_F/\Omega_H}{1 - \Omega_F/\Omega_H}. \tag{5.40}$$

If $\Omega_F/\Omega_H \ll 1/2$, then matter sliding along field lines has little inertia and the field tends to spin up. If $\Omega_F/\Omega_H \gg 1/2$, then matter is flung off of field lines and the resulting backreaction tends to spin down the field. This suggests the field is driven towards $\Omega_F/\Omega_H \approx 1/2$ in equilibrium.

Figure 5.9 shows the gas and magnetic energy fluxes in the jet for the $a_* = 0.7$ MAD simulation. The conversion of magnetic energy into gas energy is a gradual process and the load is a broad region, beginning a few gravitational radii from the black hole and continuing to $r \sim 10,000M$. The gas energy flux first exceeds the magnetic energy flux around $r \sim 300M$, at which point roughly half of the magnetic energy has been converted into gas energy. By $r \sim 10,000M$ the energy in the jet is carried almost entirely by the gas.

The fact that the load region is concentrated far from the black hole, where frame dragging is

unimportant, may go some way towards explaining why Ω_F/Ω_H is roughly independent of black hole spin (see Figure 5.8).

5.7 Summary and conclusions

We have discussed GRMHD simulations of jets from accreting ($h/r \sim 0.3$), spinning ($0 \leq a_* \leq 0.98$) black holes, and their relationship with the BZ model in its membrane formulation. We showed that the simulated magnetic jet power, $P^{\rm mag}$, integrated over the entire horizon, agrees with the standard BZ prediction (1.20) to within 10%. This is consistent with earlier simulations (Tchekhovskoy et al. 2010a, 2012). We traced the order 10% discrepancies between the BZ model and our simulated $P^{\rm mag}$ to the standard BZ assumptions $\Omega_F/\Omega_H = 1/2$ and uniform B_n.

The jet power proxy $P^{\rm mag}$ is integrated over the entire horizon, so it also includes power extracted into the accretion disk. We have separately considered the power extracted into the jet alone, $P^{\rm tot}_{\rm jet}$, and found this to be roughly 50% lower than $P^{\rm mag}$. This quantity is probably more relevant for jet observations. Simply lowering the standard BZ prediction (1.20) by 60% gives a good fit to the simulated $P^{\rm tot}_{\rm jet}$.

We then turned to the physics underlying jet power. We showed that the torques, dissipation, and electromagnetic fields at the horizon are correctly described by the BZ model in its membrane formulation. This extends earlier GRMHD tests of the BZ model in its Boyer-Lindquist formulation (McKinney & Gammie 2004; McKinney et al. 2012). We showed that the BZ model with $\Omega_F/\Omega_H = 1/2$ correctly describes our simulations to within factors of order unity. The BZ solution with $\Omega_F/\Omega_H = 0.35$ gives the best fit to our simulations.

Finally, we computed the effective resistance of the load region for the $a_* = 0.7$ MAD simulation. We found $R_L/R_H \approx 0.45$, for which the BZ model implies $\Omega_F/\Omega_H \approx 0.31$. This is close to the actual field line angular velocity of this simulation: $\Omega_F/\Omega_H \approx 0.33$. This supports the idea that Ω_F/Ω_H is controlled by the physics of gas acceleration in the load region. This load resistance agrees (within a factor of order unity) with simple load region models (Lovelace et al. 1979; Phinney 1983). The load region extends to $r \sim 10,000M$, at which point the energy in the

jet is almost entirely in the gas (rather than the magnetic fields). The fact that the load region is far from the black hole, where frame dragging is unimportant, may explain why Ω_F/Ω_H is found to be roughly independent of spin.

Acknowledgments

We thank Jon McKinney and Sasha Tchekhovskoy for discussions. R.N. and A.S. were supported in part by NASA grant NNX11AE16G.

5.A Blandford-Znajek jet power

In this Appendix, we derive the BZ jet power equation (1.20). The magnetic flux, $d\Phi$, through a circular ribbon on the horizon between θ and $\theta + d\theta$ is (Blandford & Znajek 1977; Thorne et al. 1986)

$$d\Phi = 2\pi B_n (r_H^2 + a^2) \sin\theta d\theta. \tag{5.41}$$

The jet power from the ribbon is (Blandford & Znajek 1977; Thorne et al. 1986)

$$dP_{\rm jet} = 2\pi\lambda\Omega_H^2 B_n^2 (r_H^2 + a^2)^3 \frac{\sin^3\theta}{r_H^2 + a^2\cos^2\theta} d\theta, \tag{5.42}$$

where

$$\lambda = \Omega_F/\Omega_H(1 - \Omega_F/\Omega_H) \tag{5.43}$$

is the efficiency factor.

Now we assume $\Omega_F/\Omega_H = 1/2$ and uniform B_n. Integrating (5.41) gives the total flux threading the jet:

$$\Phi = 2\pi B_n (r_H^2 + a^2). \tag{5.44}$$

Plugging this into (5.42) and integrating gives the total jet power:

$$P = \frac{1}{8\pi}\Omega_H^2 \Phi^2 (1 + 4\Omega_H^2) \int_0^\pi \frac{\sin^3\theta}{1 + 4\Omega_H^2\cos^2\theta} d\theta. \tag{5.45}$$

For all spins, equation (5.45) is approximately

$$P^{\rm BZ} \approx \frac{1}{6\pi}\Omega_H^2 \Phi^2. \tag{5.46}$$

This is the BZ model's prediction for jet power. We compare it with the jet power of GRMHD simulations in §5.3.4.

5.B 3D visualizations of GRMHD membranes

On the following pages we give 3D visualizations of our GRMHD simulation data. We show the simulated torques, dissipation, and electromagnetic fields on the black hole membranes.

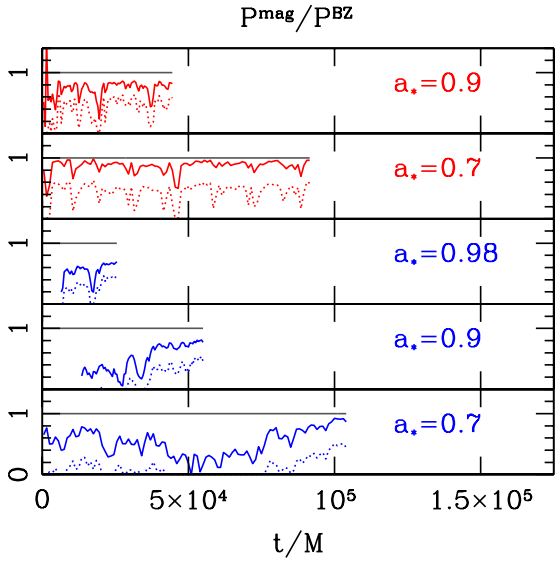

Fig. 5.3.— Jet power vs. time for our five GRMHD simulations with spinning black holes. $P^{\rm mag}$ (solid) and $P^{\rm tot}_{\rm jet}$ (dotted) are shown separately. SANE (blue) and MAD (red) simulations are shown. The standard BZ prediction (1.20) is also shown (solid black lines).

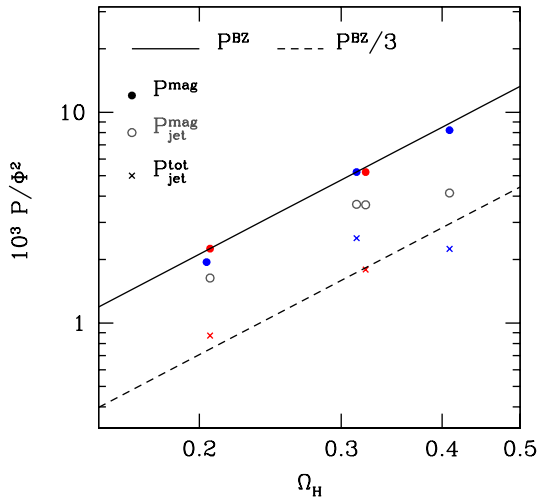

Fig. 5.4.— Jet power versus black hole spin for SANE (blue) and MAD (red) GRMHD simulations. $P^{\rm mag}$ (filled circles), $P^{\rm mag}_{\rm jet}$ (open circles), and $P^{\rm tot}_{\rm jet}$ (crosses) are shown separately. The BZ model (solid line) gives a good fit to $P^{\rm mag}$. Reducing the BZ jet power by a factor of 3 gives a good fit to $P^{\rm tot}_{\rm jet}$. We have normalized the jet power by the magnetic flux, Φ, threading the simulated black holes. The steady state magnetic flux on the hole varies from simulation to simulation, so this normalization is necessary to bring out the spin dependence of the jet power most clearly. Data for the MAD runs has been shifted slightly to the right for readability.

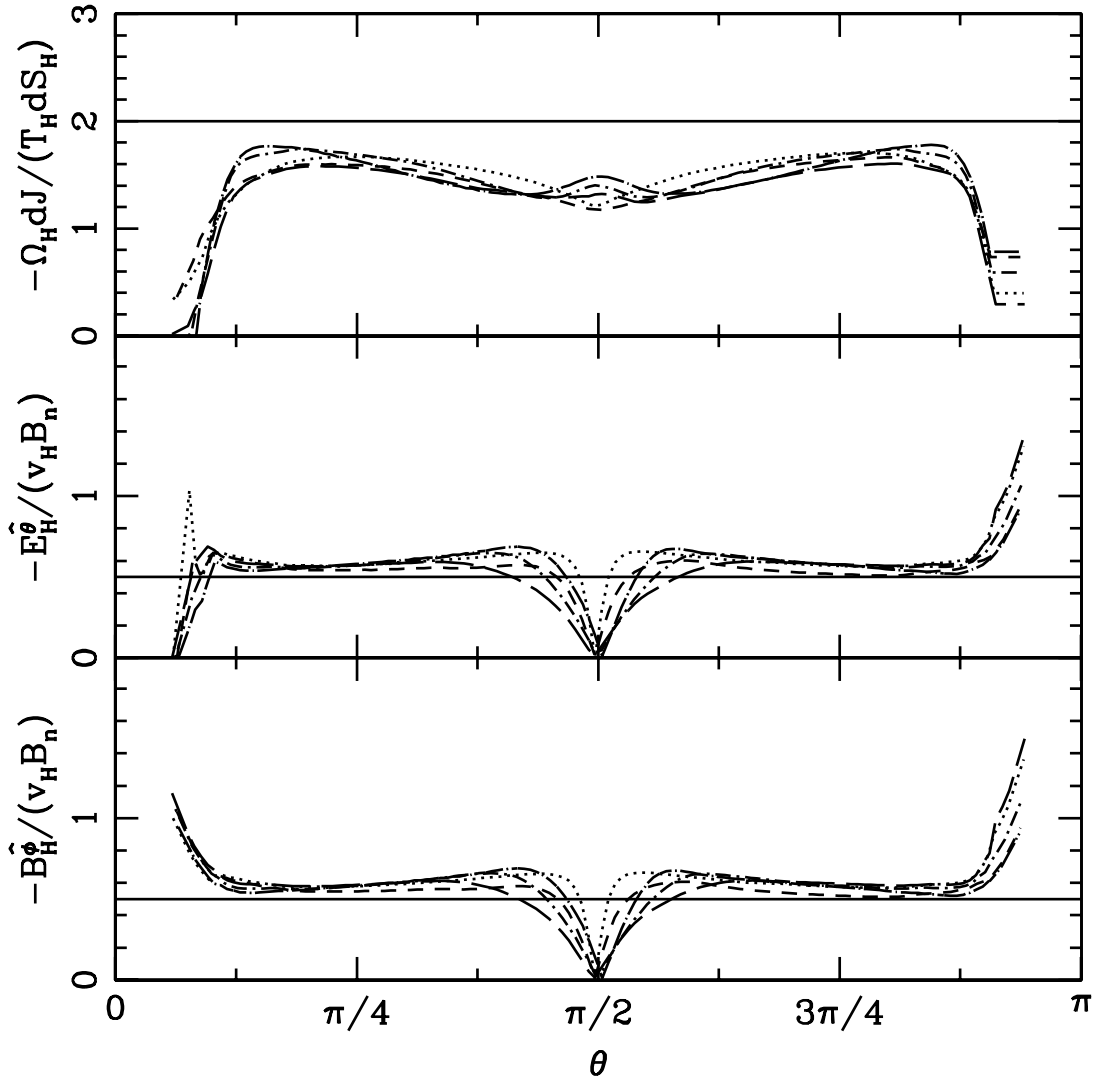

Fig. 5.5.— Torques and electromagnetic fields at the membrane as a function of θ. The line types are as follows. SANE runs: $a_* = 0.7$ (long dashed), $a_* = 0.9$ (dot-dashed), and $a_* = 0.98$ (dot-long dashed). MAD runs: $a_* = 0.7$ (dotted) and $a_* = 0.9$ (dashed). Solid lines indicate the standard BZ prediction.

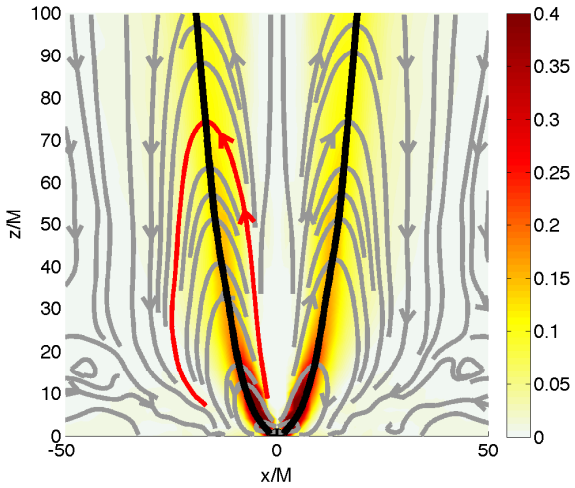

Fig. 5.6.— ZAMO frame currents (silver streamlines) and the effective resistance, dV_L/dl, (yellow-red) of the current carrying "wires." The jet boundary is indicated with heavy black lines.

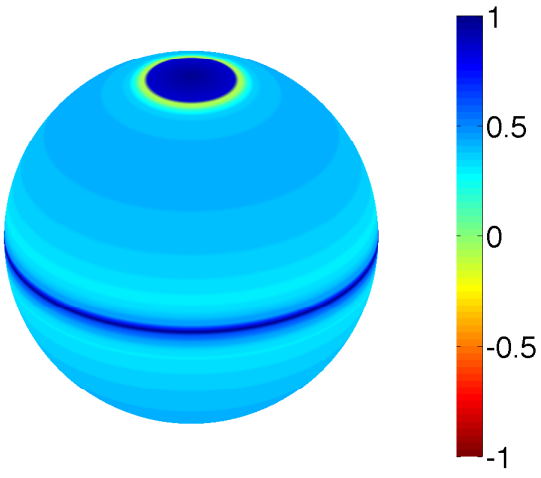

Fig. 5.7.— Angular velocity of magnetic fields lines, Ω_F/Ω_H, at the membrane of our $a_* = 0.7$ MAD simulation.

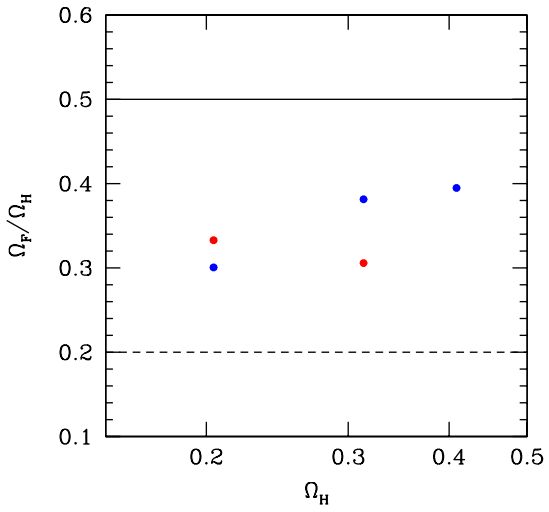

Fig. 5.8.— (t, θ, ϕ)-averaged field line angular velocity, Ω_F/Ω_H, as a function of Ω_H for SANE (blue) and MAD (red) simulations.

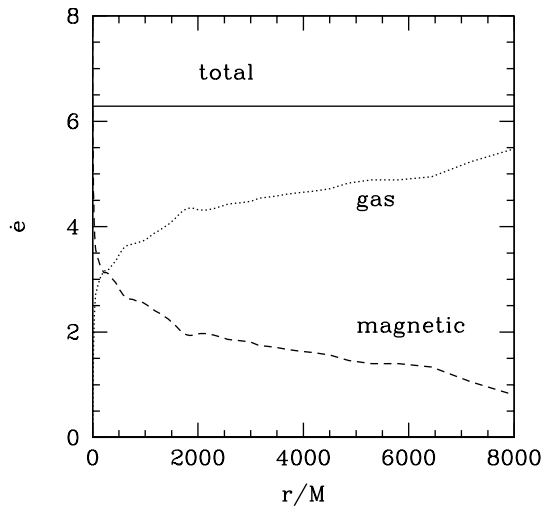

Fig. 5.9.— Gas and magnetic energy fluxes in the jet.

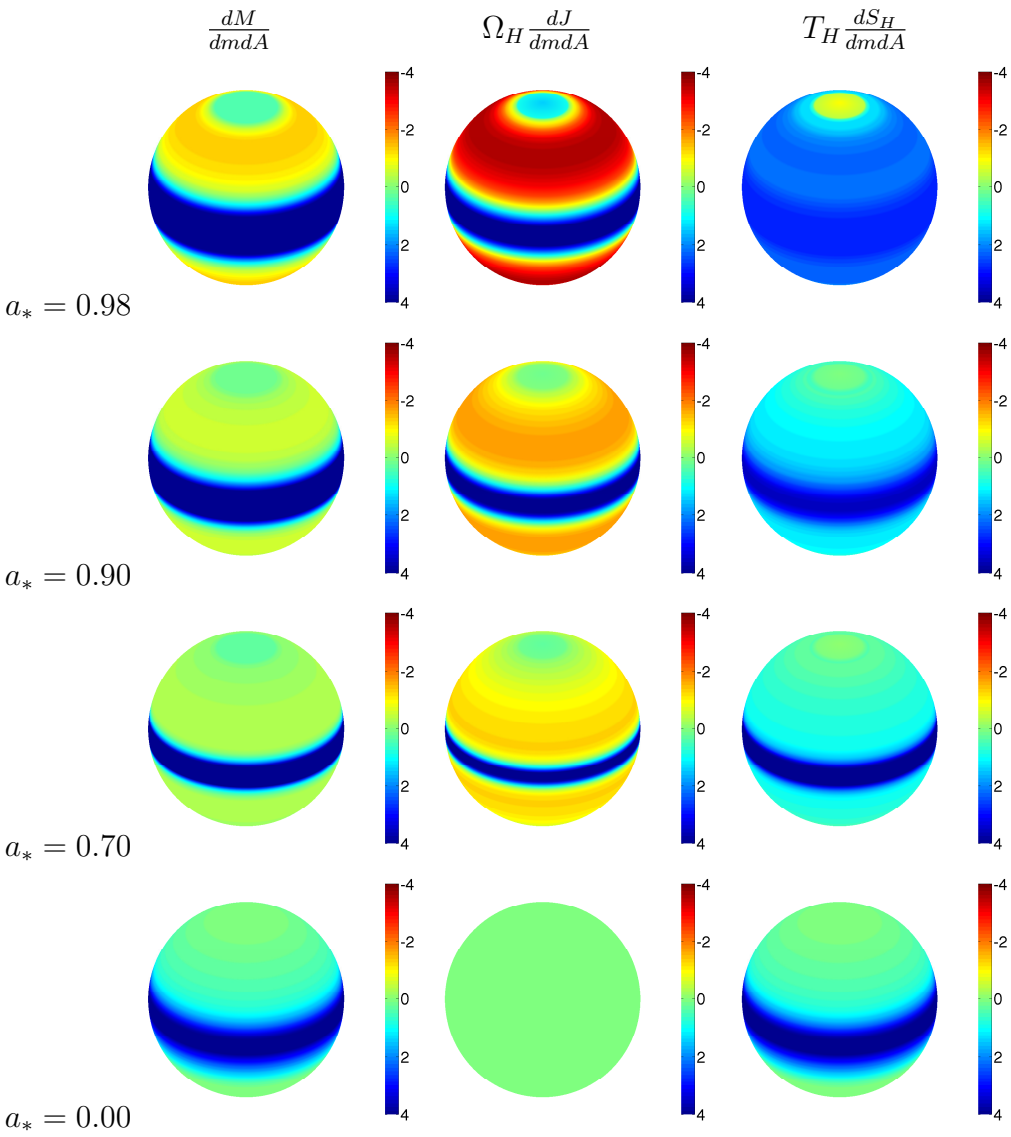

Fig. 5.10.— Energy flow (first column), torques (second column), and dissipation (third column) on the membrane for our GRMHD simulations with SANE initial conditions. Rows correspond to different simulations: $a_* = 0, 0.7, 0.9, 0.98$ (bottom to top). In all three columns, the membrane is losing energy at yellow-red regions (jets) and gaining energy at blue regions (accretion disk).

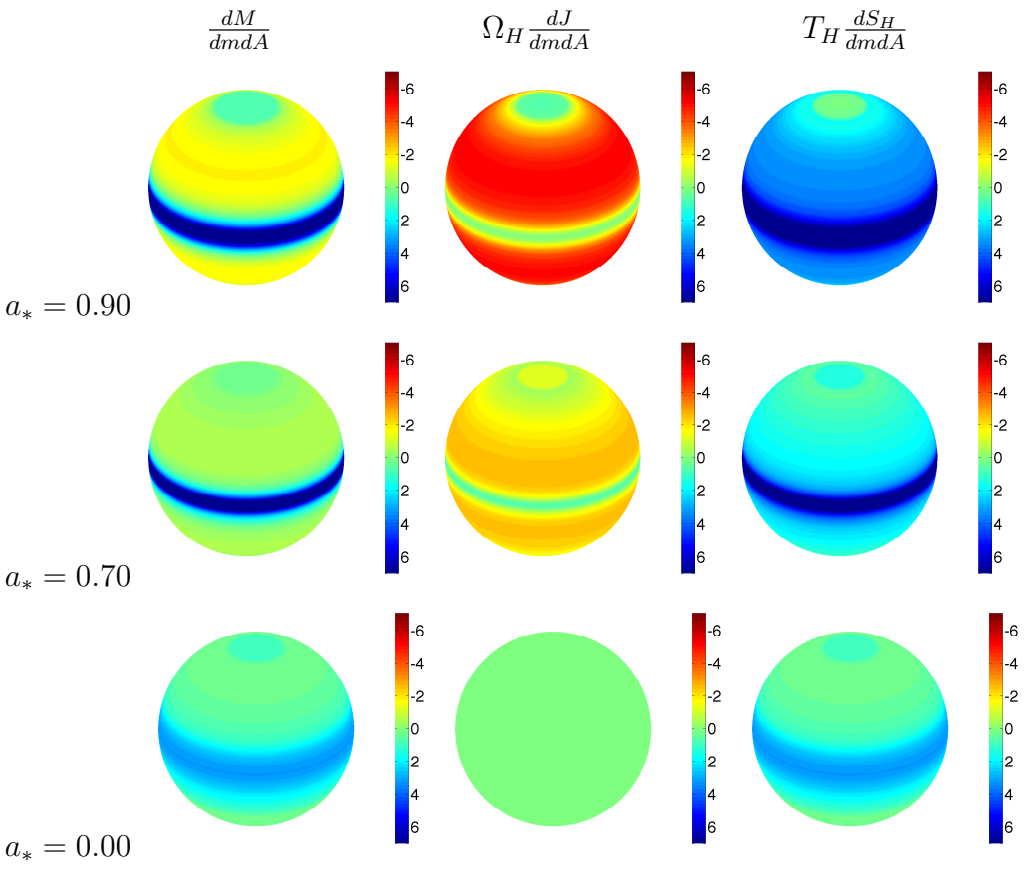

Fig. 5.11.— Same as Figure 5.10 but for MAD runs.

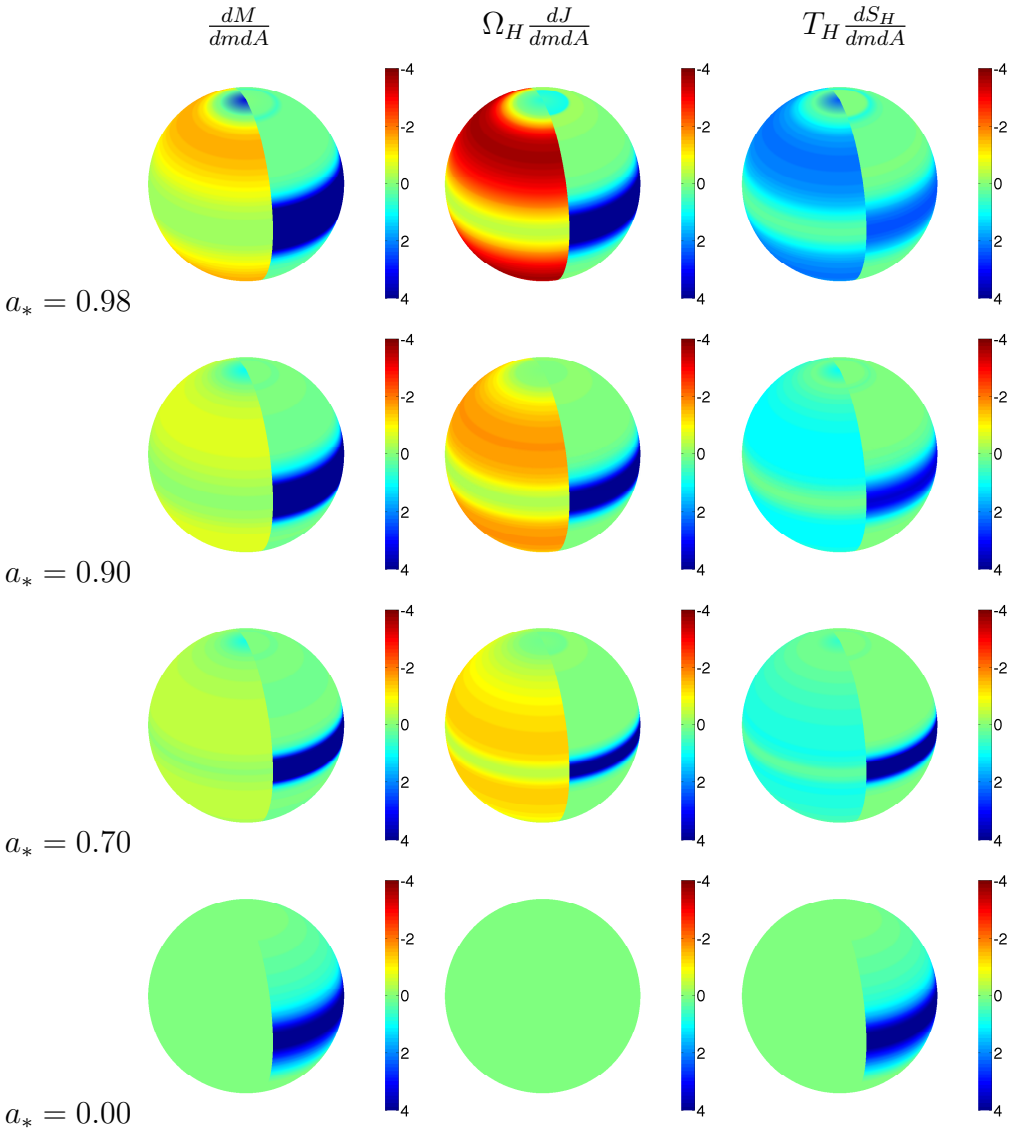

Fig. 5.12.— Same as Figure 5.10, except each term is split into its magnetic (left hemisphere) and hydrodynamic (right hemisphere) components.

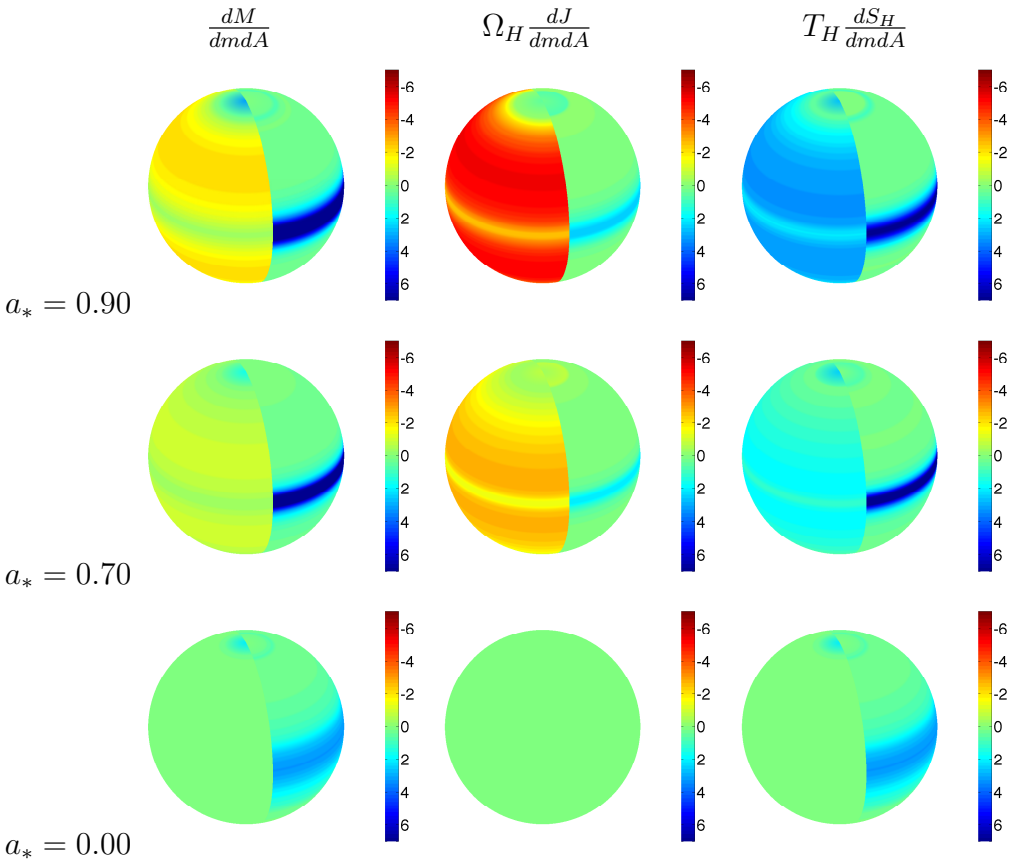

Fig. 5.13.— Same as Figure 5.12 but for MAD runs.

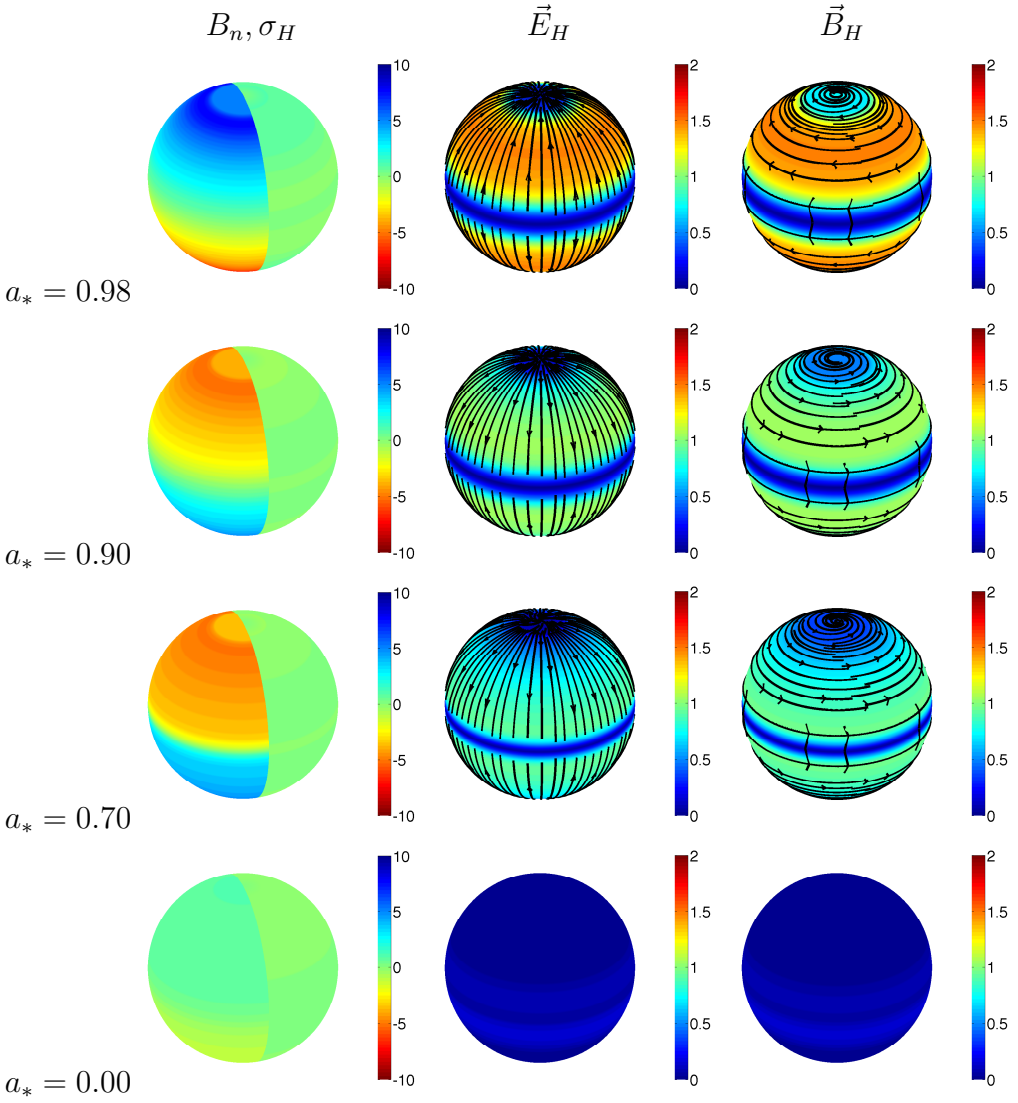

Fig. 5.14.— Electromagnetic fields at the membrane for our GRMHD simulations with SANE initial conditions. Membrane B_n (first column, left hemisphere), electric charge density (first column, right hemisphere), electric field (second column), and magnetic field (third column) are shown. On the membrane $\vec{J}_H = \vec{E}_H$, so the second column is also the membrane's current density. The GRMHD simulation results shown here are correctly described by the BZ model.

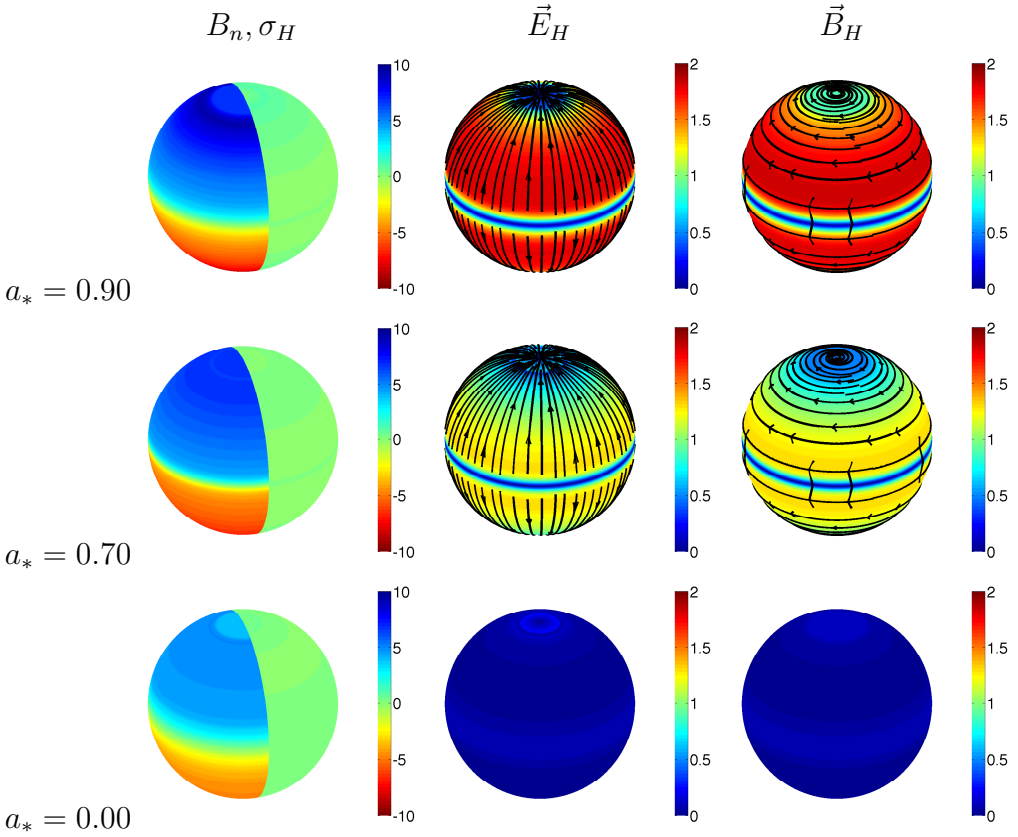

Fig. 5.15.— Same as Figure 5.14 but for MAD runs.

Chapter 6

Summary and Future Directions

6.1 Summary

In this thesis, we presented GRMHD simulations of thin and thick accretion disks around spinning and non-spinning black holes. We compared the simulations to standard analytical models of accretion disks and black hole jets. This work is motivated by recent observational efforts to study the spins of astrophysical black holes using observations of black hole disks and jets. We have demonstrated that the Novikov-Thorne solution gives a good description of thin GRMHD accretion disks and the Blandford-Znajek solution gives a good description of GRMHD jets. In particular, the Novikov-Thorne zero-torque boundary condition is satisfied in the thin disk limit and is a good approximation for $h/r \lesssim 0.1$. The standard Blandford-Znajek assumption that jets maximize efficiency provides a good fit to the simulation data. The simulated jet power is a factor $2-3$ lower than the Blandford-Znajek prediction because the latter ignores the accretion disk. The accretion disk partially counteracts the jet torques in the GRMHD simulations.

The discrepancies between the simulated thin disks and the Novikov-Thorne disk model are probably too small to be of interest for even the most sensitive accretion disk theory applications (such as black hole spin measurements), at present. However, improvements in observational data will eventually demand better accretion disk models. So we have taken steps to bring analytical

accretion disk theory closer to the simulations. In particular, we found an analytical generalization of the Novikov-Thorne model which allows a nonzero stress at the ISCO. The stress at the ISCO is proportional to disk thickness. Our solution extends throughout the plunging region. We have also found a physically motivated generalization of the usual constant α viscosity prescription.

6.2 Future directions

There are a number of interesting open problems for the future.

In Chapter 2 and Chapter 5, we compared the simulations with the Novikov-Thorne thin disk model and the Blandford-Znajek jet model. This work was crucial for gaining a physical understanding of the simulations. In addition to black hole jets, the simulations of geometrically thick accretion flows show disk-driven winds. It would be interesting to compare the simulated winds with the analytical Blandford-Payne model. One could perform a step-by-step comparison, just as we did for the Blandford-Znajek model in Chapter 5. The magnetic field structure, torques, and energy and angular momentum fluxes at the surface of the simulated accretion flows can be computed and compared against the Blandford-Payne prediction.

In Chapters 2 and 4, we found that the Gammie (1999) model gave a useful, one-dimensional model for the simulated flow inside the ISCO. The Gammie (1999) model ignores gas and magnetic pressure: it assumes a cold, geometrically thin disk. It would be valuable to generalize this model to hot, thick accretion flows. It should be relatively straightforward to add pressure terms back into the model's equations. One could then supplement the model with an equation for hydrostatic equilibrium. This would allow one to replace the pressure with the disk scale height. The disk scale height would be a new free parameter. This generalized inflow model could be a starting point for a one-dimensional model for the luminosity inside the ISCO. It could also be used to build a better $\alpha(r)$ model, along the same lines as we followed in Chapter 4.

We showed in Chapter 4 that switching from constant α to our $\alpha(r)$ prescription has a small effect on disk solutions. Even black hole spin measurements, perhaps the most sensitive application of accretion disk theory, would not discriminate between constant and radially varying $\alpha(r)$, given

current observational sources of error. A more interesting application of radially varying $\alpha(r)$ may be time-dependent phenomenon. Real accretion disks are highly variable. During episodes of variability, the magnetic field structure and shear rate are probably changing, which can be expected to modify α. This should be possible to understand using the ideas we have presented in Chapter 4. It would be interesting to revisit the early, un-converged portion of the simulation data (say, $t \leq 5000M$), and see if the time-variability of α during this transient period can be understood. It has been pointed out to us (by Fred Bagonoff) that the inner regions of quasar disks are more much more variable than the outer regions. Constant α accretion disks do not seem able to explain the level at which the disk variability depends on radius. The radial varying $\alpha(r)$ prescription may be relevant here.

In Chapter 5, we showed that the field line angular velocity, Ω_F/Ω_H is related to the effective resistance of the load region, R_L. The load resistance is related to the conversion of gas to magnetic energy. More work is needed to understand the nature of the energy conversion and gas acceleration in the load region. The simulations assume ideal MHD, although there is numerical resistivity at the grid scale, which allows for some level of Ohmic-like dissipation. It is unclear whether the load resistance, R_L, should be understood as an Ohmic-like dissipation or something else. One might clarify the physical interpretation of R_L by looking at force-free MHD simulations, which have no gas. In these simulations, the jet is confined by walls which are imposed by hand as boundary conditions. At the walls, the current and electric field are normal to the wall surface. So one can formally compute R_L along the walls. It would be interesting to better understand how R_L varies along the walls and how the shape of the walls affects the jet.

In Chapter 5, we found that SANE and MAD simulations of spinning black holes converged to a similar final state. These simulations differ only in their initial magnetic field geometry. The SANE simulations start with multiple poloidal loops and the MAD simulations start with a single poloidal loop. Nonetheless, the black hole ultimately acquires a large net flux in both cases, at least when the black hole is spinning. Understanding this behavior is important for interpreting the magnetization of astrophysical black holes. It is possible that the saturated flux on the black hole is controlled by a dynamo process. By this we mean there may be a mechanism which causes flux of one sign to preferentially build up on the hole, while flux of the other sign is ejected from the disk

into a wind. This would explain why the SANE simulations, with multiple initial magnetic loops and zero net flux, eventually deposit a large net flux on the black hole. Unlike jets and disk winds, there is no standard analytical models for dynamos. Even the origin of the solar dynamo, which has been observed in great detail, remains a subject of debate. This may represent an opportunity for the simulations to make a significant contribution to analytical theory. Furthermore, dynamos are typically only studied in non-relativistic flows. If a dynamo is present, it will be an interesting project to understand how it is modified by relativity and general relativity. The first step is to simply check whether the simulations require one to invoke a dynamo at all, by comparing the initial and final magnetic fluxes in the simulations.

More work is needed to understand the nature of the instability driving turbulence in the simulations. Throughout our work, we have assumed the magnetorotational instability (MRI) is the underlying mechanism. We presented some evidence for this in Chapter 4, where we showed $\alpha\beta \approx 0.5$, and $T^{\rm max}/T^{\rm rey} \approx 4$ in the turbulent regions of the accretion flows. These are widely regarded as empirical signatures of the MRI on the basis of shearing box simulations. The MRI is only understood analytically in the early, linear stages of its growth. So perhaps the most definitive way to identify the MRI in the GRMHD simulations would be to study the growth rates of magnetic field modes in the early stages of the simulations and compare with linear theory. Mean field dynamo theory has had some success capturing nonlinear features of dynamos (Blackman 2012). Guided by the simulations, perhaps a mean field theory of the MRI could be developed which could shed some light on the mysterious scaling laws such as $\alpha\beta \approx 0.5$.

It is possible that convective instabilities are also operating in the thick disks. There are two self-similar solutions for hot, geometrically thick accretion flows: advection dominated accretion flows (ADAFs) and convection dominated accretion flows (CDAFs). ADAFs appear to be convectively unstable, so nature might prefer CDAFs. There is some evidence that convection is important in at least some of the GRMHD simulations of hot accretion flows (Narayan et al. 2012). It will take more work to determine what role convection plays in these flows. There is some debate about how the MRI and convective instabilities interact when both are present. The simulations could probably shed some light on this issue.

We have focused this discussion on projects which do not require too much machinery beyond the work presented in this paper. Of course, given more substantial development time, the possible extensions are all but endless. For example, one of the most interesting, and challenging, developments on the horizon is ongoing work to add radiation to the GRMHD simulations. This is necessary to obtain truly realistic models for the luminosity inside the ISCO, simulate radiation dominated accretion flows near the Eddington limit, investigate radiation and thermal instabilities, and would probably lead to the discovery of entirely new phenomena. There are also efforts to incorporate numerical relativity into the simulations and evolve the metric. This would open up the study of accretion onto binary black holes and the electromagnetic counterparts to gravitational wave emission.

6.2.1 Tilted disks

Frame-dragging causes an accretion disk that is tilted with respect to the equatorial plane of the black hole to experience differential precession around the black hole spin axis. This is the so-called Lense-Thirring precession. The differential precession is believed to induce a shear stress in the vertical direction which drives the disk into alignment with the equatorial plane. This is called the Bardeen-Petterson (BP) effect.

The precession of tilted and warped disks could be an important source of accretion disk variability. It is unclear how effectively the BP effect actually works in disks. There have been a few studies so far on this problem, viz., Fragile et al. (2007); Fragile (2009); Dexter & Fragile (2011). These authors simulated a tilted thick disk and found that it did not align by the BP effect. Hydrodynamic calculations (Papaloizou & Lin 1995) suggest their disks may have been too thick for the BP effect to operate. In particular, if the disk opening angle is larger than the dimensionless viscosity parameter, resonant forces can prevent the BP effect from aligning the disk.

Based on the hydrodynamic calculations of Papaloizou & Lin (1995), one expects the disk to align if it is thin in the sense that the disk opening angle is less than the dimensionless viscosity parameter. However, this has never been tested with a GRMHD simulation. One should simulate accretion disks that are initially tilted with respect to the black hole spin axis and investigate the

timescale for the disk to align. The inner parts will align before the outer parts, so the disk will become warped. The precession of the warped disk might produce a variability related to X-ray observations of quasi-periodic oscillations.

Analytical models predict that retrograde disks always align with the BH. This effect was observed by Ivanov & Illarionov (1997) in a Newtonian context and by Zhuravlev & Ivanov (2011) using linearized general relativity, however the effect has never been confirmed in a full GRMHD simulation.

It would be interesting to analyze simulations of tilted disks using the membrane paradigm. The formalism for describing the torques on tilted disks using the membrane paradigm has already been developed. This formalism can give concrete and beautiful pictures for the disk alignment process, similar to the pictures it gave for black hole energy extraction by jets in Chapter 5.

Clearly there is no shortage of exciting open questions!

Appendix A

A New Equilibrium Torus Solution

A.1 Introduction

An early model for geometrically thick accretion disks were the equilibrium tori of Fishbone & Moncrief (1976); Fishbone (1977); Kozlowski et al. (1978); Abramowicz et al. (1978) and (Chakrabarti 1985a). In these models, a fluid entropy and angular momentum distribution are chosen arbitrarily. The equations of motion and the assumption of hydrostatic equilibrium then fix the fluid's density, velocity, and everything else. The fluid rotates in a doughnut shaped ring centered on the black hole and its velocity is purely azimuthal. The direct applications of these models to observational astronomy are limited by the arbitrariness of the entropy and angular momentum distributions.

In recent years, these models have often been used as the initial conditions for general relativistic magnetohydrodynamic (GRMHD) accretion disk simulations. Many simulations begin with the Fishbone & Moncrief (1976) fluid torus, an analytical solution for an equilibrium torus in the Kerr metric with a constant angular momentum distribution. Simulations using this torus as their initial condition have been applied to many problems, including black hole spin evolution (Gammie et al. 2004), radio emission from Sgr A* (Noble et al. 2007), black hole jets (McKinney 2006b, 2005a; Nagataki 2009), computations of spectra using coupled Monte-Carlo radiation

and GRMHD (Hilburn et al. 2010), magnetized accretion including neutrino losses (Barkov & Baushev 2011; Shibata et al. 2007; Barkov 2008), pair production in low luminosity galactic nuclei (Mościbrodzka et al. 2011), numerical convergence studies (Shiokawa et al. 2012), and magnetically arrested disks (McKinney et al. 2012).

The more general equilibrium solution of Chakrabarti (1985a) has also become a standard initial condition for GRMHD simulations. In this solution, the angular momentum distribution is no longer a constant, it becomes a tunable power law function of radius. Simulations using the Chakrabarti (1985a) solution have also found many applications, including magnetically driven accretion flows in the Kerr metric (De Villiers et al. 2003), tilted disk evolution and behaviour (Fragile et al. 2007; Fragile & Blaes 2008; Henisey et al. 2012), tests of analytical thin disk models (Shafee et al. 2008a; Noble et al. 2009; Penna et al. 2010), binary black hole mergers in gaseous (Farris et al. 2011) and magnetized (Farris et al. 2012) disks, black hole jets from prograde (Tchekhovskoy et al. 2011) and retrograde disks (Tchekhovskoy & McKinney 2012), the relation between disk scale height and jet power (Fragile et al. 2012), and polarized radiative transport (Shcherbakov et al. 2012) and radiative cooling (Dibi et al. 2012) in the accretion flow of Sgr A*.

These initial conditions require an arbitrary choice for the entropy and angular momentum of the initial fluid torus[1]. The onset of the magnetorotational instability (MRI) drives turbulence (Balbus & Hawley 1991, 1998). It would be nice if the final state of the disk did not depend on the initial conditions. But there is no evidence for this because all simulations to date have used variations of the same equilibrium torus solution (Chakrabarti 1985a; De Villiers et al. 2003).

McKinney et al. (2012) studied accretion disk winds with GRMHD simulations. In their simulations, the initial equilibrium torus is thick (scale height $|h/r| \sim 0.9$) and has a positive Bernoulli parameter $Be \sim 0.25c^2$: it is an energetically unbound cylinder extending radially outward to infinity. Our equilibrium torus solution is energetically bound at scale heights for which the standard solution is unbound. So as a GRMHD initial condition, it will likely produce weaker (or non-existent) winds. Equilibrium tori with intermediate Bernoulli parameter are of course

[1]Another arbitrariness in the initial conditions is the initial magnetic field topology and strength. The final results depend on these choices (Beckwith et al. 2008b; Penna et al. 2010; Tchekhovskoy et al. 2011; McKinney et al. 2012).

possible.

It will be important to check which results of GRMHD simulations depend on the properties of the initial torus. The rotation rate of the initial torus can be varied independently of the Bernoulli parameter and thickness. It is conceivable that simulations which start from slowly rotating tori end up more convectively unstable than simulations which start from rapidly rotating tori, because rotation stabilizes accretion flows against convection. A preliminary look suggests that even the longest duration GRMHD simulations retain some memory of their initial conditions. Figure A.1 shows that the final Bernoulli parameter of two of the longest duration simulations in the literature appear to be related to the Bernoulli parameters of the initial tori.

In §A.2, we construct the new equilibrium torus solution. In §A.3, we discuss several properties of the solution, giving simple formulas for the radius of the outer edge, the radius of the pressure maximum, the Bernoulli parameter, and the geometrical thickness, as a function of the free parameters. We compare the Bernoulli parameter and thickness of our solution to the standard solution. We show that it is possible to make an unbound torus thinner than a bound torus. In §A.4, we summarize our results. In the Appendix, we describe a possible magnetic field configuration for the torus and discuss the Bernoulli parameter of the magnetized torus. The magnetic field consists of multiple poloidal loops and is constructed so that the magnetic flux and gas-to-magnetic pressure ratio are the same in each loop. This setup could be useful for GRMHD simulations.

A.2 New torus solution

A rotating fluid is in hydrostatic equilibrium when the pull of gravity is exactly balanced by pressure gradients and centrifugal forces. An equilibrium torus is a fluid in hydrostatic equilibrium around a Kerr black hole.

We work in Boyer-Lindquist coordinates (t, r, θ, ϕ) and units for which $G = c = 1$. The solution is a function of r and θ only. Five free parameters appear in the solution: r_{in}, r_1, r_2, ξ, and κ. The inner edge of the torus is at r_{in}. There are breaks in the angular momentum distribution at r_1 and r_2 (cf. eq. (A.7)). The rotation rate is controlled by ξ. The entropy is a constant, κ.

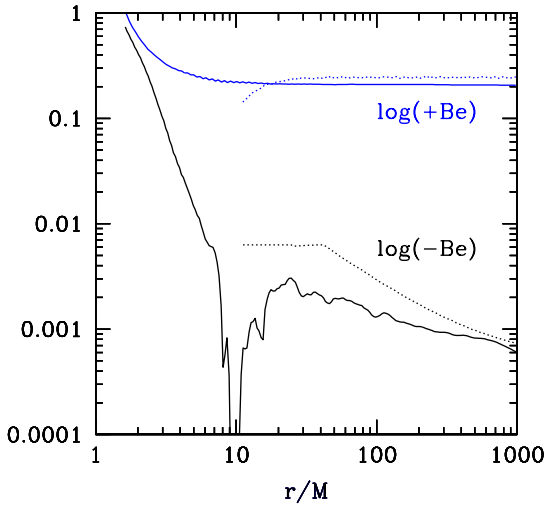

Fig. A.1.— The initial (dotted) and final (solid) midplane Bernoulli parameters, Be, of two GRMHD accretion disk simulations. The energetically unbound disk (blue) is model A0.0BtN10 of McKinney et al. (2012). The energetically bound disk (black) is the "ADAF/SANE" model of Narayan et al. (2012). The unbound disk was run to $t = 96,796M$ and the bound disk was run to $t = 200,000M$. In both cases, the saturated Be appears to be related to the initial Be.

Let $\Sigma = r^2 + a^2 \cos^2\theta$. Then the components of the Kerr metric we need are

$$g_{tt} = -1 + 2Mr/\Sigma, \quad g_{t\phi} = -2Mar\sin^2\theta/\Sigma, \tag{A.1}$$

$$g_{\phi\phi} = \left(r^2 + a^2\left(1 + 2Mr\sin^2\theta/\Sigma\right)\right)\sin^2\theta. \tag{A.2}$$

The angular momentum density, $\ell_K \equiv u_\phi/|u_t|$, of circular, equatorial geodesics is (Novikov & Thorne 1973)

$$\ell_K = \sqrt{Mr}\,\mathcal{F}/\mathcal{G}, \tag{A.3}$$

where,

$$\mathcal{F} = 1 - 2a_*/r_*^{3/2} + a_*^2/r_*^2, \quad \mathcal{G} = 1 - 2/r_* + a_*/r_*^{3/2}, \tag{A.4}$$

$$r_* = r/M, \quad a_* = a/M. \tag{A.5}$$

We are going to set the angular momentum distribution in the equatorial plane using (A.3). The angular momentum off the equatorial plane is obtained by holding ℓ constant on von Zeipel cylinders (Abramowicz 1971). The radius, λ, of a von Zeipel cylinder with angular momentum ℓ is (Chakrabarti 1985a):

$$\lambda^2 = -\ell(\lambda)\frac{\ell(\lambda)g_{t\phi} + g_{\phi\phi}}{\ell(\lambda)g_{tt} + g_{t\phi}}. \tag{A.6}$$

In Newtonian gravity, $\lambda = r\sin\theta$, the usual cylindrical radius. In the Schwarzschild metric, $\lambda = \sqrt{-g_{\phi\phi}/g_{tt}}$.

Our choice for the angular momentum distribution is

$$\ell(\lambda) = \begin{cases} \xi\ell_K(\lambda_1) & \text{if } \lambda < \lambda_1 \\ \xi\ell_K(\lambda) & \text{if } \lambda_1 < \lambda < \lambda_2 \\ \xi\ell_K(\lambda_2) & \text{if } \lambda > \lambda_2. \end{cases} \tag{A.7}$$

The equilibrium torus has three regions. There is an intermediate zone where the angular momentum tracks the Keplerian distribution. The torus is sub-Keplerian for $\xi < 1$. On either side of this zone are regions where the angular momentum distribution is constant. (The Boyer-Linquist break radii, r_1 and r_2 have been converted to von Zeipel break radii, λ_1 and λ_2.) At a given (r, θ), one finds the von Zeipel radius and angular momentum density iteratively, using (A.6) and (A.7).

The angular velocity of the torus is fixed by its angular momentum and the condition $u_\mu u^\mu = -1$:

$$\Omega = \frac{u^\phi}{u^t} = -\frac{g_{t\phi} + \ell g_{tt}}{g_{\phi\phi} + \ell g_{t\phi}}. \tag{A.8}$$

Assuming the angular momentum distribution (A.7) and constant entropy κ, we can work out the enthalpy, internal energy, and everything else the torus needs to maintain hydrostatic equilibrium. The relativistic Euler equation is (Abramowicz et al. 1978):

$$\frac{\nabla p}{p + \epsilon} = \nabla \ln A - \frac{\ell \nabla \Omega}{1 - \Omega \ell}, \tag{A.9}$$

where p and ϵ are the gas pressure and total energy density in the fluid frame. The gradient of the redshift factor,

$$A \equiv \frac{dt}{d\tau} = \left(-g_{tt} - 2\Omega g_{t\phi} - \Omega^2 g_{\phi\phi}\right)^{-1/2}, \tag{A.10}$$

supplies the gravitational force. Equation (A.9) has the same interpretation as the nonrelativistic Euler equation: equilibrium pressure gradients (LHS) balance the sum of gravitational and centrifugal forces (RHS). The RHS of eq (A.9) is minus the gradient of the effective potential (Kozlowski et al. 1978)

$$W(r, \theta) = -\ln(FA), \tag{A.11}$$

where,

$$\ln F(r, \theta) \equiv -\int_{r_{in}}^{r_{\lambda \mathrm{m}}(r,\theta)} \frac{d\Omega}{dr} \frac{\ell dr}{1 - \Omega \ell}. \tag{A.12}$$

The boundary of the torus is the isopotential surface $W(r, \theta) = W(r_{in}, \pi/2) \equiv W_{in}$, where r_{in} is the radius of the inner edge of the torus, a free parameter.

The outer limit of integration in eq (A.12), $r_{\lambda m}(r, \theta)$, is the radius at which the Von Zeipel cylinder containing (r, θ) intersects the equatorial plane. That is, $r_{\lambda m}$ is the Boyer-Lindquist radius that solves (A.6) with $\theta = \pi/2$ for the current value of λ and ℓ. In the midplane, $r_{\lambda m}(r, \pi/2) = r$.

For an isentropic torus, the specific enthalpy is fixed by the effective potential:

$$w = e^{-(W - W_{in})}. \tag{A.13}$$

Let us assume the equation of state $p = (\Gamma - 1)U$. Then the total energy density, internal energy

density, and rest mass density are

$$\epsilon = (w-1)/\Gamma, \quad U = \rho_0 \epsilon,$$
$$\rho_0 = \left((\Gamma-1)\epsilon/\kappa\right)^{1/(\Gamma-1)}. \tag{A.14}$$

To summarize, the equilibrium torus is defined by the angular momentum distribution (A.7), the assumption $\kappa =$ constant, and the equation of state. These assumptions fix $\Omega, W, w, \epsilon, \rho_0$ and U (cf. eqs (A.8), (A.11), (A.13)-(A.14)). There are five free parameters: the radius of the inner edge of the torus, r_{in}, the break radii in the angular momentum distribution, r_1 and r_2, the normalization of the angular momentum, ξ, and the entropy, κ. The entropy is not fundamental since there is no self-gravity, it only appears in eq (A.14) where it sets the density scale.

A.3 Properties of the solution

In this section we obtain simple formulas for a few properties of the torus. We determine the radius of the outer edge, the position of the pressure maximum, the geometrical thickness, and the Bernoulli parameter as a function of the free parameters r_{in}, r_1, r_2, and ξ. Some of the formulas are approximate but they give insight into the full solution.

The most complicated term in the equations to be solved is the integral in eq (A.12). It is helpful to rewrite this integral as

$$F = (1-\Omega\ell)\exp\left(\int_{r_{in}}^{r_{\lambda m}} \frac{\Omega}{1-\Omega\ell}\frac{d\ell}{dr}dr\right), \tag{A.15}$$

which follows from the identity $\ell d\Omega = d(\Omega\ell) - \Omega d\ell$.

In the inner regions of the torus, $\lambda < \lambda_1$, the angular momentum is constant, the integrand in eq (A.15) vanishes, and

$$F = 1-\Omega\ell, \quad \lambda < \lambda_1. \tag{A.16}$$

In the outer regions of the torus, $\lambda > \lambda_2$, the integral picks up a contribution from the break radii:

$$F \approx (1-\Omega\ell)\, I, \quad \lambda > \lambda_2, \tag{A.17}$$

where,

$$I \equiv \left(\frac{1 - \xi^2/\lambda_2}{1 - \xi^2/\lambda_1} \right)^{1/2}. \tag{A.18}$$

Equation (A.17) is approximate because we ignored special relativistic contributions to ℓ and Ω, but in the outer regions of the torus these are usually small.

A.3.1 Radius of the outer edge

The boundary of the torus is the isopotential surface $W(r, \theta) = W_{in}$. We can simplify W at the outer edge by using a Newtonian description there. The equation for the outer radius, r_{out}, becomes

$$W_{in} \approx -\frac{M}{r_{out}} + \frac{\xi^2 M r_2}{2 r_{out}^2} - \ln I. \tag{A.19}$$

The solution for the outer radius is

$$r_{out}/M \approx \frac{1 + \sqrt{1 - \xi^2 \lambda_2 \varpi}}{\varpi}, \tag{A.20}$$

where,

$$\varpi \equiv 2 \ln \left(\frac{A}{I} \left(1 - \frac{\ell^2}{\lambda^2} \right) \right)_{r = r_{in}}. \tag{A.21}$$

The top left panel of Figure A.2 shows the variation of r_{out} with ξ for several choices of r_{in} and fixed $r_1 = 42M$ and $r_2 = 1000M$. The outer radius increases as the inner radius decreases because the boundary of the torus is moving to larger isopotential surfaces. In the region of parameter space shown in Figure A.2, the Bernoulli parameter is small and negative, as we will see below. When the Bernoulli parameter is small and negative, the outer radius is very sensitive to ξ. This is because solutions with positive Bernoulli parameter become cylinders with infinite r_{out}. Solutions with infinite r_{out} are not very physical. They are energetically unbound but a nonzero pressure at infinity keeps them confined.

A.3.2 Pressure maximum

The pressure gradient term in the Euler equation (A.9) vanishes at the pressure maximum. So the only possible motion at the pressure maximum is geodesic flow. In other words, the pressure

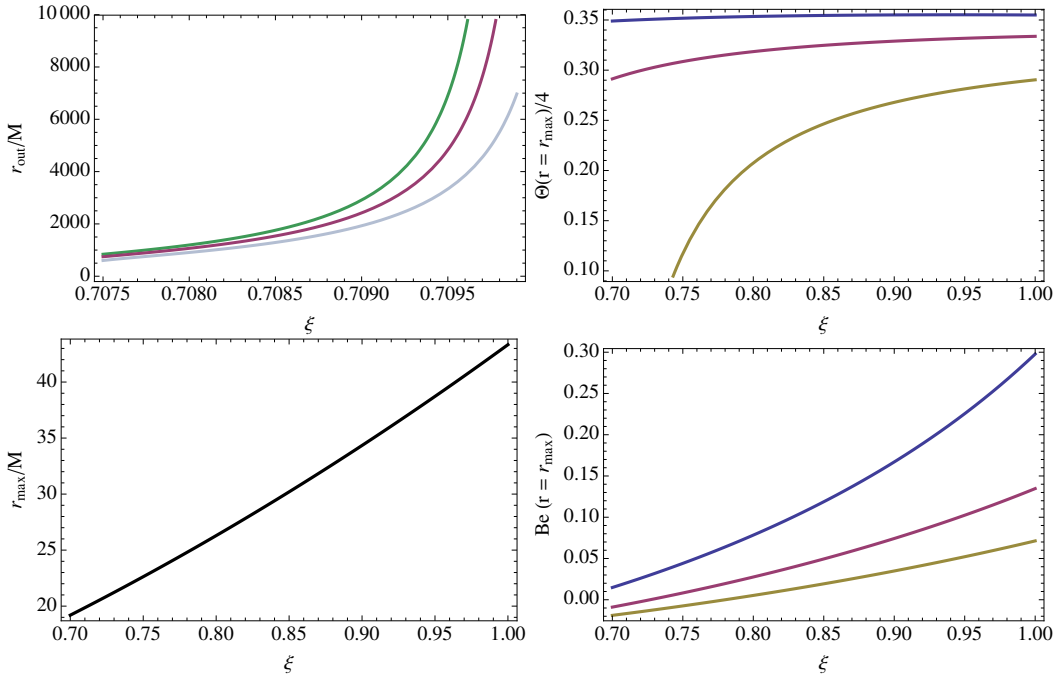

Fig. A.2.— Counterclockwise from the upper left panel, we show the radius of the outer edge of the torus, the radius of the pressure maximum, the Bernoulli parameter at the pressure maximum, and the geometrical thickness at the pressure maximum as a function of the rotation parameter, ξ, for several choices of r_{in}/M: 8 (blue), 9.993 (green), 10 (red), 10.01 (gray), and 12 (yellow). The pressure maximum position, r_{max}/M, is independent of r_{in}. The horizontal scale of the upper left panel is different from the other panels because r_{out} is only finite when $Be < 0$.

maximum is at the radius solving

$$\ell(r_{max}) = \ell_K(r_{max}), \tag{A.22}$$

where ℓ_K is the angular momentum of circular, equatorial geodesics defined by eq (A.3). For $\xi < 1$, the pressure maximum must be in the inner regions of the torus because the angular momentum of the torus is strictly sub-Keplerian for $r > r_1$.

Equation (A.22) gives

$$r_{max}(\xi, \lambda_1) \approx \xi^2 \ell_K(\lambda_1)^2 - 4M. \tag{A.23}$$

The lower left panel of Figure A.2 shows the dependence of r_{max} on ξ for $\lambda_1 = 42M$. Note that r_{max} is independent of r_{in} and λ_2. As $\xi \to 1$, the pressure maximum approaches r_1. As ξ becomes sub-Keplerian, the pressures maximum approaches r_{in}.

A.3.3 Bernoulli parameter

The relativistic Bernoulli parameter is (Novikov & Thorne 1973)

$$Be = -u_t w - 1. \tag{A.24}$$

Tori with $Be > 0$ are energetically unbound and tori with $Be < 0$ are energetically bound. For $r < r_1$, the Bernoulli parameter is:

$$Be = -(g_{tt} + g_{t\phi}\Omega) A^2 (1 - \Omega\ell) (A (1 - \Omega\ell))^{-1}_{r=r_{in}} - 1. \tag{A.25}$$

The lower right panel of Figure A.2 shows the dependence of Be at the pressure maximum on ξ for several choices of $r_{\rm in}$ and fixed $r_1 = 42M$ and $r_2 = 1000M$. The outer edge of the torus $r_{out} \to \infty$ as $Be \to 0$ from below. Note that by adjusting $r_{\rm in}$ and λ_1, any combination of Be and ξ is possible.

A.3.4 Thickness

We can find the thickness of the torus as a function of r the same way we found r_{out}, by using the fact that the boundary of the torus has $W(r, \theta) = W_{in}$. In the inner regions, $r < r_1$, the surface of the torus is at

$$\sin\theta = -g_{tt} \frac{\ell^2}{r^2} \left(1 + g_{tt} \left(A (1 - \Omega\ell)\right)_{r=r_{in}}\right)^{-1}. \tag{A.26}$$

The angle θ is measured with respect to the polar axis. The scale height of the torus with respect to the midplane is $\Theta = \pi/2 - \theta$. In the upper right panel of Figure A.2, the scale height at r_{max} is plotted as a function of ξ for several choices of r_{in}.

A.3.5 Comparison with Chakrabarti's solution

In Figure A.3, we illustrate the Bernoulli parameter of one of our solutions.[2] The torus is energetically bound: $Be < 0$. In the same figure, we show the Bernoulli parameter of an equilibrium torus from the standard family of solutions used by GRMHD simulations (Chakrabarti 1985a).[3] This torus is energetically unbound.

In the bottom panels of Figure A.3, we show the density scale heights,

$$|h/r| = \frac{\int |\theta - \pi/2| \, \rho_0 \sqrt{-g} d\theta d\phi}{\int \rho_0 \sqrt{-g} d\theta d\phi}, \tag{A.27}$$

of both solutions as a function of radius. Note that the unbound torus is actually thinner than the bound torus! As GRMHD initial conditions, the unbound torus might produce stronger disk winds than the bound torus.

This shows that equilibrium tori with significantly different Bernoulli parameters are possible, even after fixing $|h/r|$. The strength of disk winds in GRMHD disk simulations thus might depend on the choice of initial equilibrium torus solution.

A.4 Conclusions

We have constructed a new equilibrium torus solution. It provides an alternative initial condition for GRMHD disk simulations to the solution of Chakrabarti (1985a). The angular momentum is constant in the inner and outer regions of the torus. In intermediate regions, the angular momentum follows a sub-Keplerian distribution. The angular momentum is constant on von Zeipel cylinders. The entropy is constant everywhere.

[2]The free parameters are $r_{in} = 10M$, $r_1 = 42M$, $r_2 = 1000M$, $\kappa = 0.00766$, and $\xi = 0.708$.

[3]The free parameters are $r_{in} = 10M$, $\kappa = 0.00136M$, $d \log \ell / d \log \lambda = 0.4$, and pressure maximum at $r_{\rm max} = 40$.

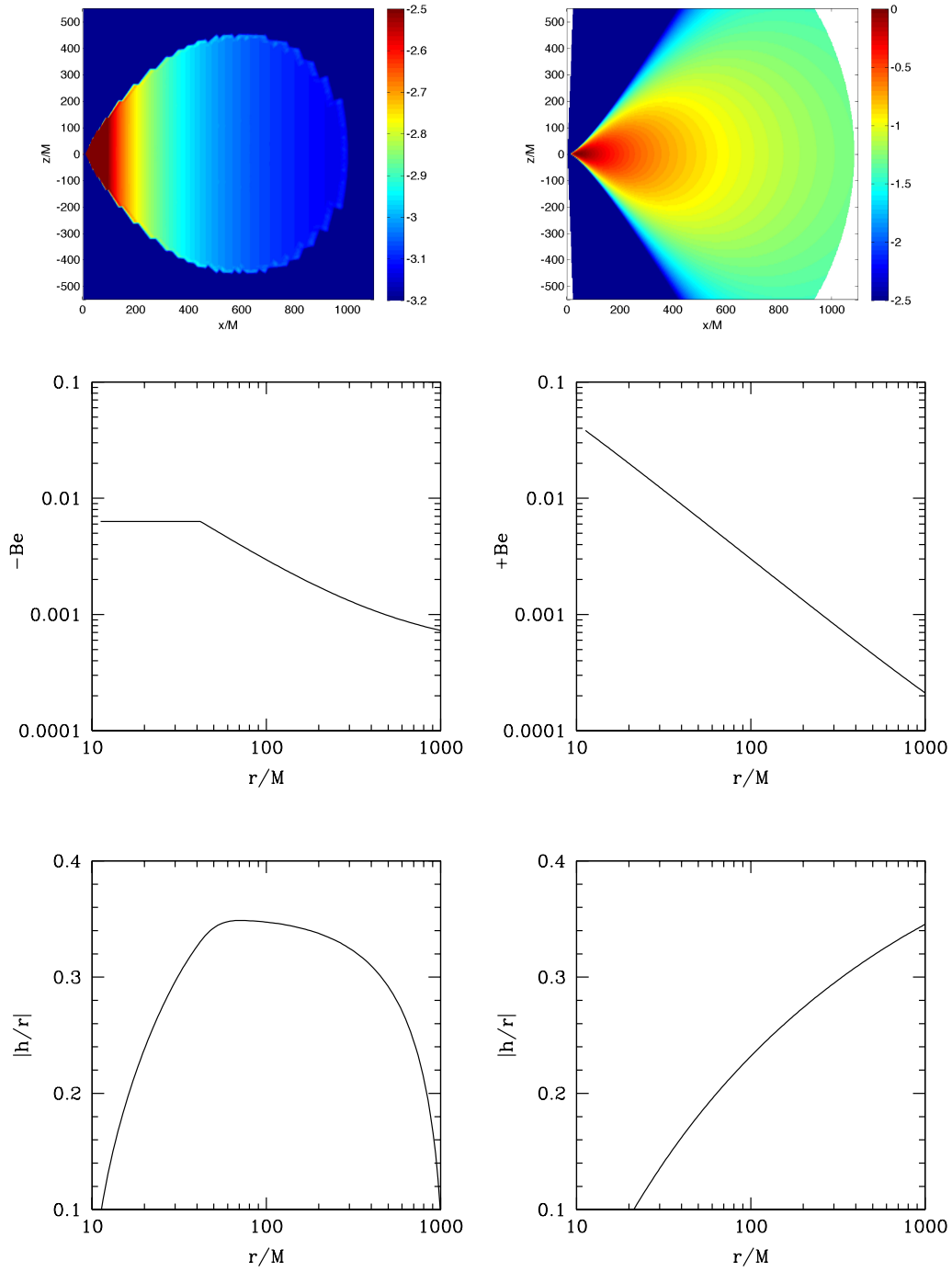

Fig. A.3.— The panels in the left column show $\log(-Be)$ and $|h/r|$ for the new equilibrium torus solution described in the text. The panels in the right column show $\log(Be)$ and $|h/r|$ for a solution of Chakrabarti (1985a) which is energetically unbound, i.e., $Be > 0$.

The Bernoulli parameter, rotation rate, and geometrical thickness of the solution can be varied independently. The torus tends to be more energetically bound than the solutions of Chakrabarti (1985a), even for the same $|h/r|$. In fact, we have shown that it is possible to generate equilibrium tori with the same $|h/r|$, but for which one is bound and the other unbound. Of course intermediate Bernoulli parameters are also possible. So as GRMHD initial conditions, the new solutions might lead to weaker (or non-existent) disk winds. Future GRMHD simulations will need to explore how the results depend on the Bernoulli parameter, rotation rate, and geometrical thickness of the initial equilibrium torus.

A.A Adding a magnetic field

Implementing the new equilibrium torus as a GRMHD initial condition requires adding a magnetic field to the torus. Here we record one possible magnetic field, a series of poloidal magnetic loops. We discuss the Bernoulli parameter of the magnetized torus in §A.A.2.

A.A.1 Magnetic field solution

We construct the magnetic field so that each loop carries the same magnetic flux and $\beta = p_{\rm gas}/p_{\rm mag}$ is roughly constant. Simulations often require initial conditions that minimize secular variability during the run, so these features can be useful.

Three free parameters appear in the solution: $r_{\rm start}$, $r_{\rm end}$, and λ_B. The first two set the inner and outer boundaries of the magnetized region and the third controls the size of the poloidal loops.

We define the field through the vector potential, A_μ. The magnetic loops are purely poloidal, so only A_ϕ is nonzero. To keep β close to a constant, the magnetic field strength tracks the fluid's internal energy density. Define

$$q = \begin{cases} \sin^3\theta \left(U_c/U_{cm} - 0.2\right)/0.8 & \text{if } r_{\rm start} < r < r_{\rm end} \\ 0 & \text{otherwise,} \end{cases} \tag{A.28}$$

where,

$$U_c(r,\theta) = U(r,\theta) - U(r_{\rm end}, \pi/2), \tag{A.29}$$

$$U_{cm}(r) = U(r,\pi/2) - U(r_{\rm end}, \pi/2). \tag{A.30}$$

The function q is defined to give $q = 1$ at the midplane and $q \to 0$ away from the midplane. The factor $\sin^3\theta$ smooths the vector potential as it approaches the edges of the torus. Dropping this factor leads to a torus with highly magnetized edges.

Further define

$$f(r) = \lambda_B^{-1}\left(r^{2/3} + 15r^{-2/5}/8\right). \tag{A.31}$$

The vector potential is then

$$A_\phi = \begin{cases} q\sin\left(f(r) - f(r_{\rm start})\right) & \text{if } q > 0 \\ 0 & \text{otherwise,} \end{cases} \tag{A.32}$$

$$\text{all other } A_\mu = 0. \tag{A.33}$$

The sinusoidal factor in A_ϕ breaks the poloidal field into a series of loops. The function $f(r)$ gives each loop the same magnetic flux. The number of loops is controlled by λ_B. The overall normalization of A_ϕ has not been specified so it can be tuned to give any field strength.

We give an example in Figure A.4. The equilibrium torus is as in Figure A.3 and the field parameters are $r_{\rm start} = 25$, $r_{\rm end} = 550$, and $\lambda_B = 15/4$. In this example there are eight magnetic loops. The magnetic flux, A_ϕ, peaks at the center of each loop, measures the flux carried by the loop, and is the same across the torus. The magnetization $\beta = p_{\rm gas}/p_{\rm mag}$ peaks at loop edges and drops at loop centers, but is roughly constant across the torus. In this example $\beta \sim 100$.

A.A.2 MHD Bernoulli parameter

The stress energy tensor of a magnetized fluid is

$$T_{\mu\nu} = \left(\rho_0 + U + \frac{b^2}{2}\right)u_\mu u_\nu + \left(p_{\rm gas} + \frac{b^2}{2}\right)h_{\mu\nu} - b_\mu b_\nu,$$

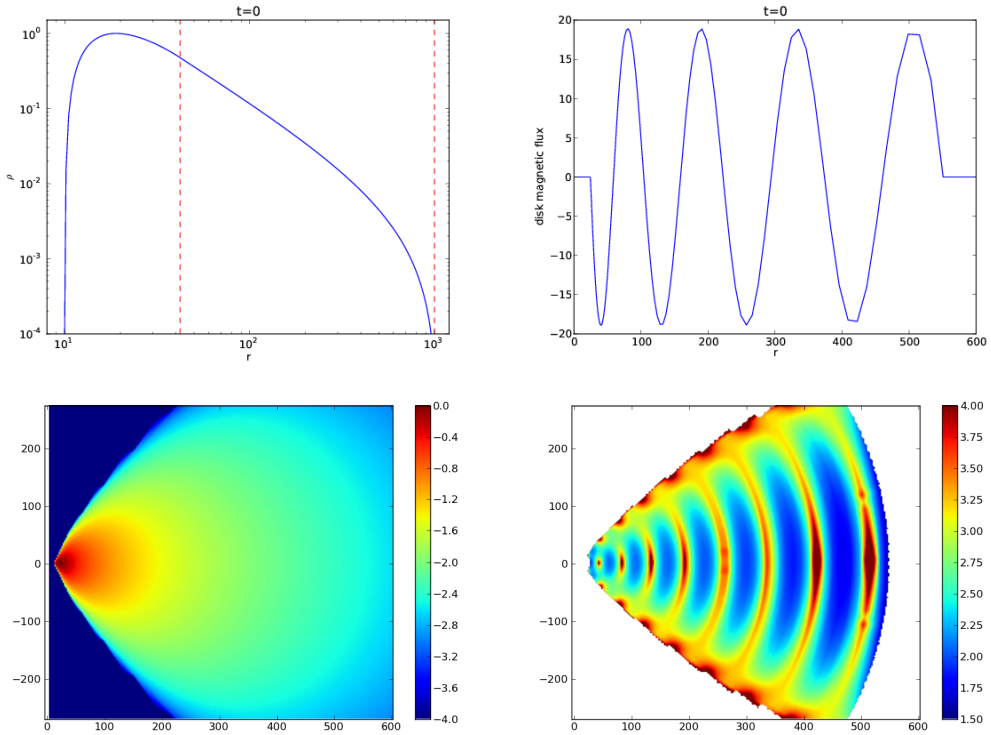

Fig. A.4.— The top two panels show the mid-plane density and the enclosed magnetic flux as a function of radius. The lower two panels show the density and the magnetization parameter β of the torus in the poloidal plane. Each loop carries the same magnetic flux. The magnetization is roughly constant throughout the torus.

where b_μ is the magnetic field in the fluid's rest frame and $h_{\mu\nu} = g_{\mu\nu} + u_\mu u_\nu$ is the projection tensor. The magnetic field contributes $b^2/2$ to the total internal energy and $b^2/2$ to the total pressure, and introduces a stress term, $-b_\mu b_\nu$.

The Euler equations, $h \cdot (\nabla \cdot T) = 0$, become:

$$\left(\rho_0 + U + p_{\rm gas} + b^2\right) a = -h \cdot \nabla \left(p_{\rm gas} + \frac{b^2}{2}\right) h - h \cdot (b \cdot \nabla)\, b,$$

where $a = \nabla_u u$ is the fluid's acceleration. We have used $\nabla \cdot b = 0$ to simplify the last term on the RHS.

Assume the flow is stationary and adiabatic, project the Euler equations along $\xi = \partial_t$, and combine terms using the first law of thermodynamics. This leads to:

$$\frac{d}{d\tau}\left(\frac{\rho_0 + U + p_{\rm gas} + b^2}{\rho_0} u_t\right) = -\frac{1}{\rho_0} \xi \cdot h \cdot (b \cdot \nabla)\, b.$$

For the field configuration of §A.A.1, b is purely poloidal and $\xi \cdot h$ is purely toroidal. So the RHS is zero.

We thus obtain a straightforward generalization of equation (A.24):

$$Be = -\left(1 + \frac{U + p_{\rm gas} + b^2}{\rho_0}\right) u_t - 1. \tag{A.34}$$

The unmagnetized torus has $Be \sim -w_{\rm gas}$. Adding magnetic fields to the torus, with gas-to-magnetic pressure ratio $\beta = p_{\rm gas}/p_{\rm mag}$, changes the Bernoulli parameter by terms of order $1/\beta$. Simulations typically have initial $\beta \sim 100$, in which case the magnetic contribution to the Bernoulli parameter is of order 1%.

References

Abramowicz, M., Brandenburg, A., & Lasota, J. P. 1996, MNRAS, 281, L21

Abramowicz, M., Jaroszynski, M., & Sikora, M. 1978, A&A, 63, 221

Abramowicz, M. A. 1971, Acta Astron., 21, 81

Abramowicz, M. A., Czerny, B., Lasota, J. P., & Szuszkiewicz, E. 1988, ApJ, 332, 646

Abramowicz, M. A., Jaroszynski, M., Kato, S., et al. 2010, ArXiv e-prints, arXiv:1003.3887

Abramowicz, M. A., Lanza, A., & Percival, M. J. 1997, ApJ, 479, 179

Afshordi, N., & Paczyński, B. 2003, ApJ, 592, 354

Agol, E., & Krolik, J. H. 2000, ApJ, 528, 161

Armitage, P. J. 1998, ApJ, 501, L189

—. 2002, MNRAS, 330, 895

Armitage, P. J., Reynolds, C. S., & Chiang, J. 2001, ApJ, 548, 868

Balbus, S. A. 2012, MNRAS, 423, L50

Balbus, S. A., & Hawley, J. F. 1991, ApJ, 376, 214

—. 1998, Rev. Mod. Phys., 70, 1

Bardeen, J. M. 1970, ApJ, 161, 103

Bardeen, J. M., Press, W. H., & Teukolsky, S. A. 1972, ApJ, 178, 347

Barkov, M. V. 2008, in American Institute of Physics Conference Series, Vol. 1054, American Institute of Physics Conference Series, ed. M. Axelsson, 79–85

Barkov, M. V., & Baushev, A. N. 2011, New Astron., 16, 46

Barkov, M. V., & Komissarov, S. S. 2008a, International Journal of Modern Physics D, 17, 1669

—. 2008b, MNRAS, 385, L28

—. 2010, MNRAS, 401, 1644

Barrabes, C., Israel, W., & Poisson, E. 1990, Classical and Quantum Gravity, 7, L273

Beckwith, K., Hawley, J. F., & Krolik, J. H. 2008a, ApJ, 678, 1180

—. 2008b, MNRAS, 390, 21

Bekenstein, J. D., & Oron, E. 1978, Phys. Rev. D, 18, 1809

Berti, E., & Volonteri, M. 2008, ApJ, 684, 822

Beskin, V., & Tchekhovskoy, A. 2005, A&A, 433, 619

Beskin, V. S., & Zheltoukhov, A. A. 2013, ArXiv e-prints, arXiv:1303.1644

Blackman, E. G. 2012, arXiv:1203.0823, arXiv:1203.0823

Blackman, E. G., Penna, R. F., & Varnière, P. 2008, New Astron., 13, 244

Blandford, R. D. 1976, MNRAS, 176, 465

—. 1979, Accretion disc and black hole electrodynamics (Cambridge University Press), 241–254

Blandford, R. D., & Znajek, R. L. 1977, MNRAS, 179, 433

Brandenburg, A. 2001, ApJ, 550, 824

Brandenburg, A., Nordlund, A., Stein, R. F., & Torkelsson, U. 1995, ApJ, 446, 741

Cantrell, A. G., Bailyn, C. D., Orosz, J. A., et al. 2010, ApJ, 710, 1127

Chakrabarti, S. K. 1985a, ApJ, 288, 1

—. 1985b, ApJ, 294, 383

Chandrasekhar, S. 1960, Proceedings of the National Academy of Science, 46, 253

—. 1992, The Mathematical Theory of Black Holes (1992), NY, OUP (Oxford University Press, USA)

Colella, P., & Woodward, P. R. 1984, J. Comp. Phys., 54, 174

Davis, S. W., Done, C., & Blaes, O. M. 2006, ApJ, 647, 525

Davis, S. W., & Hubeny, I. 2006, ApJS, 164, 530

Davis, S. W., Stone, J. M., & Pessah, M. E. 2010, ApJ, 713, 52

De Villiers, J.-P., Hawley, J. F., & Krolik, J. H. 2003, ApJ, 599, 1238

De Villiers, J.-P., Hawley, J. F., Krolik, J. H., & Hirose, S. 2005, ApJ, 620, 878

Dexter, J., & Fragile, P. C. 2011, ApJ, 730, 36

Dibi, S., Drappeau, S., Fragile, P. C., Markoff, S., & Dexter, J. 2012, MNRAS, 426, 1928

Eardley, D. M., & Lightman, A. P. 1975, ApJ, 200, 187

Farris, B. D., Gold, R., Paschalidis, V., Etienne, Z. B., & Shapiro, S. L. 2012, Physical Review Letters, 109, 221102

Farris, B. D., Liu, Y. T., & Shapiro, S. L. 2011, Phys. Rev. D, 84, 024024

Fender, R. P., Belloni, T. M., & Gallo, E. 2004, MNRAS, 355, 1105

Fishbone, L. G. 1977, ApJ, 215, 323

Fishbone, L. G., & Moncrief, V. 1976, ApJ, 207, 962

Font, J. A., Ibáñez, J. M. ., & Papadopoulos, P. 1998, ApJ, 507, L67

Fragile, P. C. 2009, ApJ, 706, L246

Fragile, P. C., & Blaes, O. M. 2008, ApJ, 687, 757

Fragile, P. C., Blaes, O. M., Anninos, P., & Salmonson, J. D. 2007, ApJ, 668, 417

Fragile, P. C., Wilson, J., & Rodriguez, M. 2012, MNRAS, 424, 524

Frank, J., King, A., & Raine, D. 1992, Accretion power in astrophysics. (Cambridge University Press, Cambridge, UK)

Fromang, S., Lyra, W., & Masset, F. 2011, A&A, 534, A107

Fromang, S., & Papaloizou, J. 2007, A&A, 476, 1113

Gammie, C. F. 1999, ApJ, 522, L57

—. 2004, ApJ, 614, 309

Gammie, C. F., McKinney, J. C., & Tóth, G. 2003, ApJ, 589, 444

Gammie, C. F., Shapiro, S. L., & McKinney, J. C. 2004, ApJ, 602, 312

Godon, P. 1995, MNRAS, 277, 157

Goldreich, P., & Julian, W. H. 1969, ApJ, 157, 869

Gou, L., McClintock, J. E., Steiner, J. F., et al. 2010, ArXiv e-prints, arXiv:1002.2211

Gou, L., McClintock, J. E., Liu, J., et al. 2009, ApJ, 701, 1076

Gou, L., McClintock, J. E., Reid, M. J., et al. 2011, ApJ, 742, 85

Greene, J., Bailyn, C. D., & Orosz, J. A. 2001, ApJ, 554, 1290

Guan, X., Gammie, C. F., Simon, J. B., & Johnson, B. M. 2009, ApJ, 694, 1010

Hawking, S. W. 1974, Nature, 248, 30

Hawley, J. F. 2000, ApJ, 528, 462

Hawley, J. F., & Balbus, S. A. 1991, ApJ, 376, 223

Hawley, J. F., Balbus, S. A., & Winters, W. F. 1999, ApJ, 518, 394

Hawley, J. F., Gammie, C. F., & Balbus, S. A. 1995, ApJ, 440, 742

—. 1996, ApJ, 464, 690

Hawley, J. F., & Krolik, J. H. 2001, ApJ, 548, 348

—. 2006, ApJ, 641, 103

Henisey, K. B., Blaes, O. M., & Fragile, P. C. 2012, ApJ, 761, 18

Hilburn, G., Liang, E., Liu, S., & Li, H. 2010, MNRAS, 401, 1620

Hirose, S., Krolik, J. H., De Villiers, J.-P., & Hawley, J. F. 2004, ApJ, 606, 1083

Hughes, S. A., & Blandford, R. D. 2003, ApJ, 585, L101

Igumenshchev, I. V. 2009, ApJ, 702, L72

Igumenshchev, I. V., Narayan, R., & Abramowicz, M. A. 2003, ApJ, 592, 1042

Ivanov, P. B., & Illarionov, A. F. 1997, MNRAS, 285, 394

Kato, S., & Yoshizawa, A. 1993, PASJ, 45, 103

—. 1995, PASJ, 47, 629

Kerr, R. P. 1963, Physical Review Letters, 11, 237

Komissarov, S. S. 2001, MNRAS, 326, L41

—. 2005, MNRAS, 359, 801

—. 2012, MNRAS, 422, 326

Komissarov, S. S., & Barkov, M. V. 2009, MNRAS, 397, 1153

Komissarov, S. S., Barkov, M. V., Vlahakis, N., & Königl, A. 2007, MNRAS, 380, 51

Komissarov, S. S., & McKinney, J. C. 2007, MNRAS, 377, L49

Kozlowski, M., Jaroszynski, M., & Abramowicz, M. A. 1978, A&A, 63, 209

Krolik, J. H. 1999, ApJ, 515, L73

Krolik, J. H., & Hawley, J. F. 2002, ApJ, 573, 754

Krolik, J. H., Hawley, J. F., & Hirose, S. 2005, ApJ, 622, 1008

Kulkarni, A. K., Penna, R. F., Shcherbakov, R. V., et al. 2011a, MNRAS, 414, 1183

—. 2011b, MNRAS, 620

Lee, H. K., Wijers, R. A. M. J., & Brown, G. E. 2000, Phys. Rep., 325, 83

Lesur, G., & Longaretti, P. Y. 2007, MNRAS, 378, 1471

Li, L. 2002, Phys. Rev. D, 65, 084047

Li, L., Zimmerman, E. R., Narayan, R., & McClintock, J. E. 2005, ApJS, 157, 335

Liu, J., McClintock, J. E., Narayan, R., Davis, S. W., & Orosz, J. A. 2008, ApJ, 679, L37

Lovelace, R. V. E., MacAuslan, J., & Burns, M. 1979, in American Institute of Physics Conference Series, Vol. 56, Particle Acceleration Mechanisms in Astrophysics, ed. J. Arons, C. McKee, & C. Max, 399–415

MacDonald, D., & Thorne, K. S. 1982, MNRAS, 198, 345

MacDonald, D. A. 1984, MNRAS, 211, 313

Machida, M., Hayashi, M. R., & Matsumoto, R. 2000, ApJ, 532, L67

Matsumoto, R. 1999, in Astrophysics and Space Science Library, Vol. 240, Numerical Astrophysics, ed. S. M. Miyama, K. Tomisaka, & T. Hanawa, 195

McClintock, J. E., Narayan, R., Gou, L., et al. 2009, ArXiv e-prints, arXiv:0911.5408

McClintock, J. E., Narayan, R., & Steiner, J. F. 2013, ArXiv e-prints, arXiv:1303.1583

McClintock, J. E., Shafee, R., Narayan, R., et al. 2006, ApJ, 652, 518

McClintock, J. E., Narayan, R., Davis, S. W., et al. 2011, Classical and Quantum Gravity, 28, 114009

McKinney, J. C. 2005a, arXiv:astro-ph/0506369

—. 2005b, ApJ, 630, L5

—. 2006a, MNRAS, 367, 1797

—. 2006b, MNRAS, 368, 1561

McKinney, J. C., & Blandford, R. D. 2009, MNRAS, 394, L126

McKinney, J. C., & Gammie, C. F. 2004, ApJ, 611, 977

McKinney, J. C., & Narayan, R. 2007a, MNRAS, 375, 513

—. 2007b, MNRAS, 375, 531

McKinney, J. C., Tchekhovskoy, A., & Blandford, R. D. 2012, MNRAS, 423, 3083

Meier, D. L. 2001, ApJ, 548, L9

Mignone, A., & McKinney, J. C. 2007, MNRAS, 378, 1118

Mościbrodzka, M., Gammie, C. F., Dolence, J. C., & Shiokawa, H. 2011, ApJ, 735, 9

Nagataki, S. 2009, ApJ, 704, 937

Narayan, R., Igumenshchev, I. V., & Abramowicz, M. A. 2003, PASJ, 55, L69

Narayan, R., Kato, S., & Honma, F. 1997, ApJ, 476, 49

Narayan, R., & McClintock, J. E. 2012, MNRAS, 419, L69

Narayan, R., McClintock, J. E., & Shafee, R. 2008, in American Institute of Physics Conference Series, Vol. 968, Astrophysics of Compact Objects, ed. Y.-F. Yuan, X.-D. Li, & D. Lai, 265–272

Narayan, R., Sądowski, A., Penna, R. F., & Kulkarni, A. K. 2012, MNRAS, 426, 3241

Narayan, R., & Yi, I. 1994, ApJ, 428, L13

—. 1995, ApJ, 444, 231

Noble, S. C., Gammie, C. F., McKinney, J. C., & Del Zanna, L. 2006, ApJ, 641, 626

Noble, S. C., & Krolik, J. H. 2009, ApJ, 703, 964

Noble, S. C., Krolik, J. H., & Hawley, J. F. 2009, ApJ, 692, 411

—. 2010, ArXiv e-prints, arXiv:1001.4809

Noble, S. C., Leung, P. K., Gammie, C. F., & Book, L. G. 2007, Classical and Quantum Gravity, 24, 259

Novikov, I. D., & Thorne, K. S. 1973, in Black holes (Les astres occlus), p. 343 - 450, 343–450

Ogilvie, G. I. 2003, MNRAS, 340, 969

Orosz, J. A. 2003, in IAU Symposium, Vol. 212, A Massive Star Odyssey: From Main Sequence to Supernova, ed. K. van der Hucht, A. Herrero, & C. Esteban, 365

Orosz, J. A., McClintock, J. E., Aufdenberg, J. P., et al. 2011a, ApJ, 742, 84

Orosz, J. A., Steiner, J. F., McClintock, J. E., et al. 2011b, ApJ, 730, 75

Orosz, J. A., McClintock, J. E., Narayan, R., et al. 2007, Nature, 449, 872

Orosz, J. A., Steeghs, D., McClintock, J. E., et al. 2009, ApJ, 697, 573

Özel, F., Psaltis, D., Narayan, R., & McClintock, J. E. 2010, ApJ, 725, 1918

Paczyński, B. 2000, astro-ph/0004129, astro-ph/0004129

Page, D. N., & Thorne, K. S. 1974, ApJ, 191, 499

Papadopoulos, P., & Font, J. A. 1998, Phys. Rev. D, 58, 024005

Papaloizou, J. C. B., & Lin, D. N. C. 1995, ApJ, 438, 841

Papaloizou, J. C. B., & Nelson, R. P. 2003, MNRAS, 339, 983

Penna, R. F., Kulkarni, K., & Narayan, R. 2012a, Submitted to A&A

Penna, R. F., McKinney, J. C., Narayan, R., et al. 2010, MNRAS, 408, 752

Penna, R. F., Sądowski, A., Kulkarni, A. K., & Narayan, R. 2013, MNRAS, 428, 2255

Penna, R. F., Sądowski, A., & McKinney, J. C. 2012b, MNRAS, 420, 684

Penrose, R. 1969, Nuovo Cimento Rivista Serie, 1, 252

Pessah, M. E., Chan, C. K., & Psaltis, D. 2006a, Physical Review Letters, 97, 221103

—. 2006b, MNRAS, 372, 183

—. 2007, ApJ, 668, L51

—. 2008, MNRAS, 383, 683

Pessah, M. E., & Psaltis, D. 2005, ApJ, 628, 879

Phinney, E. S. 1983, in Astrophysics and Space Science Library, Vol. 103, Astrophysical Jets, ed. A. Ferrari & A. G. Pacholczyk, 201–212

Popham, R., & Gammie, C. F. 1998, ApJ, 504, 419

Pringle, J. E. 1977, MNRAS, 178, 195

Pringle, J. E., & King, A. R. 2007, Astrophysical flows (CUP)

Pringle, J. E., & Rees, M. J. 1972, A&A, 21, 1

Remillard, R. A., & McClintock, J. E. 2006, ARA&A, 44, 49

Reynolds, C. S., & Armitage, P. J. 2001, ApJ, 561, L81

Reynolds, C. S., & Fabian, A. C. 2008, ApJ, 675, 1048

Riffert, H., & Herold, H. 1995, ApJ, 450, 508

Ruffini, R., & Wilson, J. R. 1975, Phys. Rev. D, 12, 2959

Sano, T., Inutsuka, S., Turner, N. J., & Stone, J. M. 2004, ApJ, 605, 321

Sądowski, A. 2009, ApJS, 183, 171

Sądowski, A., Abramowicz, M., Bursa, M., et al. 2011, A&A, 527, A17

Schnittman, J. D., Krolik, J. H., & Hawley, J. F. 2006, ApJ, 651, 1031

Shafee, R., McClintock, J. E., Narayan, R., et al. 2006, ApJ, 636, L113

Shafee, R., McKinney, J. C., Narayan, R., et al. 2008a, ApJ, 687, L25

Shafee, R., Narayan, R., & McClintock, J. E. 2008b, ApJ, 676, 549

Shakura, N. I., & Sunyaev, R. A. 1973, A&A, 24, 337

Shapiro, S. L. 2010, Phys. Rev. D, 81, 024019

Shapiro, S. L., & Teukolsky, S. A. 1983, Black holes, white dwarfs, and neutron stars: The physics of compact objects (Research supported by the National Science Foundation. New York, Wiley-Interscience, 1983, 663 p.)

Shcherbakov, R. V., Penna, R. F., & McKinney, J. C. 2012, ApJ, 755, 133

Shibata, M., Sekiguchi, Y.-I., & Takahashi, R. 2007, Progress of Theoretical Physics, 118, 257

Shiokawa, H., Dolence, J. C., Gammie, C. F., & Noble, S. C. 2012, ApJ, 744, 187

Simon, J. B., & Hawley, J. F. 2009, ApJ, 707, 833

Sądowski, A. 2011, PhD thesis, Nicolaus Copernicus Astronomical Center, Warsaw, Poland

Sądowski, A., Narayan, R., & Penna, R. F. 2013, MNRAS submitted

Sorathia, K. A., Reynolds, C. S., & Armitage, P. J. 2010, ApJ, 712, 1241

Sorathia, K. A., Reynolds, C. S., Stone, J. M., & Beckwith, K. 2012, ApJ, 749, 189

Steeghs, D., McClintock, J. E., Parsons, S. G., et al. 2013, ArXiv e-prints, arXiv:1304.1808

Steinacker, A., & Papaloizou, J. C. B. 2002, ApJ, 571, 413

Steiner, J. F., McClintock, J. E., & Narayan, R. 2013, ApJ, 762, 104

Steiner, J. F., McClintock, J. E., & Reid, M. J. 2012, ApJ, 745, L7

Steiner, J. F., McClintock, J. E., Remillard, R. A., Narayan, R., & Gou, L. 2009, ApJ, 701, L83

Steiner, J. F., Reis, R. C., McClintock, J. E., et al. 2011, MNRAS, 416, 941

Stewart, J. 1994, Advanced General Relativity (CUP)

Stone, J. M., & Balbus, S. A. 1996, ApJ, 464, 364

Straub, O., Bursa, M., Sądowski, A., et al. 2011, A&A, 533, A67+

Susskind, L., Thorlacius, L., & Uglum, J. 1993, Phys. Rev. D, 48, 3743

Takahashi, M., Nitta, S., Tatematsu, Y., & Tomimatsu, A. 1990, ApJ, 363, 206

Taylor, G. I. 1936, Royal Society of London Proceedings Series A, 157, 546

Tchekhovskoy, A., & McKinney, J. C. 2012, MNRAS, 423, L55

Tchekhovskoy, A., McKinney, J. C., & Narayan, R. 2007, MNRAS, 379, 469

—. 2008, MNRAS, 388, 551

—. 2009a, ApJ, 699, 1789

—. 2012, Journal of Physics Conference Series, 372, 012040

Tchekhovskoy, A., Narayan, R., & McKinney, J. C. 2009b, astro-ph/0909.0011, arXiv:0909.0011

—. 2010a, ApJ, 711, 50

—. 2010b, New Astron., 15, 749

—. 2011, MNRAS, 418, L79

Thorne, K. S. 1974, ApJ, 191, 507

Thorne, K. S., & MacDonald, D. 1982, MNRAS, 198, 339

Thorne, K. S., Price, R. H., & MacDonald, D. A. 1986, Black holes: The membrane paradigm (Yale Univ. Press)

Velikhov, E. P. 1959, J. Exptl. Theoret. Phys., 36, 1398

Wald, R. M. 1974, Phys. Rev. D, 10, 1680

Wang, M. T., & Yau, S. T. 2009, Physical Review Letters, 102, 021101

Zhang, S. N., Cui, W., & Chen, W. 1997, ApJ, 482, L155+

Zhu, Y., Davis, S. W., Narayan, R., et al. 2012, MNRAS, 424, 2504

Zhuravlev, V. V., & Ivanov, P. B. 2011, MNRAS, 415, 2122

Znajek, R. L. 1978, MNRAS, 185, 833